

## Abstract

## Measurement of ( $\pi^-$ -Ar) and ( $K^+$ -Ar) total hadronic cross sections in the LArIAT experiment

Elena Gramellini

2018

The Liquid Argon Time Projection Chamber (LArTPC) represents one of the most advanced experimental technologies for physics at the Intensity Frontier due to its full 3D-imaging, excellent particle identification and precise calorimetric energy reconstruction. By deploying a LArTPC in a dedicated calibration test beam line at Fermilab, LArIAT (Liquid Argon In A Testbeam) aims to experimentally calibrate this technology in a controlled environment and to provide physics results key to the neutrino oscillation physics and proton decay searches of the Short Baseline Neutrino and Long Baseline Neutrino programs.

<sup>14</sup> LArIAT's physics program entails a vast set of topics with a particular focus on  
<sup>15</sup> the study of nuclear effects such as pion and kaon characteristic interaction modes.

This thesis presents two world's first measurements: the measurement of ( $\pi^-$ -Ar) total hadronic cross section in the 100-1050 MeV kinetic energy range and the measurement of the ( $K^+$ -Ar) total hadronic cross section in the 100-650 MeV kinetic energy range. The analyses devised for these measurements use both the core elements of LArIAT: beamline and TPC. The first step in each analysis is the development of an event selection based on beamline and TPC information geared towards the identification of the hadron of interest. We then proceed to match the beamline candidate to a suitable TPC track. Finally, we apply the “thin slice method” technique and measure the cross section, correcting for background and detector effects. The thin slice technique is a new method to measure hadron-argon cross sections possible only thanks to the combination of the tracking and calorimetry capability of the

27 LArTPC technology. Albeit never on argon, the hadronic cross section of pions has  
28 been measured before on several different elements in thin target experiments, leading  
29 to solid predictions in the argon case. Through the use of a different technique, our  
30 measurement of the ( $\pi^-$ -Ar) total hadronic cross section is in general agreement with  
31 the prediction by the Geant4 Bertini Cascade model which are based on data from  
32 thin target experiments. On the contrary, cross section measurements for kaons are  
33 extremely rare, thus more difficult to model. Not surprisingly, our measurement of  
34 the ( $K^+$ -Ar) total hadronic cross section is mostly in disagreement with the Geant4  
35 prediction.

36 This thesis also reports two ancillary detector physics measurements necessary  
37 for the cross section analyses: the measurements of the LArIAT electric field and  
38 calorimetry constants. We developed a technique to measure the LArIAT electric field  
39 using cathode-anode piercing tracks with cosmic data. We applied a new technique  
40 for the measurement of the calorimetry calibration constants based on the particles'  
41 momentum measurement.

42 The ( $\pi^-$ -Ar) and the ( $K^+$ -Ar) total hadronic cross measurements are the first  
43 physics results of the LArIAT experiment and will be the basis for the future LArIAT  
44 measurements of pion and kaon cross sections in the exclusive channels.

45

# Measurement of ( $\pi^-$ -Ar) and ( $K^+$ -Ar) total hadronic cross sections in the LArIAT experiment

46

47

48

A Dissertation  
Presented to the Faculty of the Graduate School  
of  
Yale University  
in Candidacy for the Degree of  
Doctor of Philosophy

49

50

51

52

53

54

55

by  
Elena Gramellini

56

Dissertation Director: Bonnie T. Fleming

57

Date you'll receive your degree

58

Copyright © 2018 by Elena Gramellini

59

All rights reserved.

60

*A mia mamma e mio babbo,*

61

*grazie per le radici e grazie per le ali.*

62

*To my mom and dad,*

63

*thank you for the roots and thank you for the wings.*

# <sup>64</sup> Contents

<sup>65</sup>	<b>Acknowledgements</b>	<b>viii</b>
<sup>66</sup>	<b>Introduction</b>	<b>xi</b>
<sup>67</sup>	<b>1 The theoretical framework</b>	<b>1</b>
<sup>68</sup>	1.1 The Standard Model . . . . .	1
<sup>69</sup>	1.2 Neutrinos: tiny cracks in the Standard Model . . . . .	4
<sup>70</sup>	1.2.1 Neutrinos in the Standard Model . . . . .	4
<sup>71</sup>	1.2.2 Neutrino Oscillations . . . . .	6
<sup>72</sup>	1.2.3 Make up of Neutrino Interactions . . . . .	7
<sup>73</sup>	1.3 Beyond the Standard Model . . . . .	9
<sup>74</sup>	1.3.1 Open Questions in Neutrino Physics . . . . .	11
<sup>75</sup>	1.3.2 Towards a more fundamental theory: GUTs . . . . .	15
<sup>76</sup>	1.4 Motivations for Hadronic Cross Sections in Argon . . . . .	18
<sup>77</sup>	1.4.1 Pion-Argon Total Hadronic Cross Section . . . . .	18
<sup>78</sup>	1.4.2 Kaon-Argon Total Hadronic Cross Section . . . . .	29
<sup>79</sup>	<b>2 Liquid Argon Detectors at the Intensity Frontier</b>	<b>34</b>
<sup>80</sup>	2.1 The Liquid Argon Time Projection Chamber Technology . . . . .	34
<sup>81</sup>	2.1.1 TPCs, Neutrinos & Argon . . . . .	35
<sup>82</sup>	2.1.2 LArTPC: Principles of Operation . . . . .	37

83	2.1.3	Liquid Argon: Ionization Charge . . . . .	40
84	2.1.4	Liquid Argon: Scintillation Light . . . . .	45
85	2.1.5	Signal Processing and Event Reconstruction . . . . .	49
86	2.2	The Intensity Frontier Program . . . . .	53
87	2.2.1	Prospects for LArTPCs in Neutrino Physics: SBN and DUNE	54
88	2.2.2	Prospects for LArTPCs in GUT Physics: DUNE . . . . .	55
89	2.2.3	Enabling the next generation of discoveries: LArIAT . . . . .	57
90	<b>3</b>	<b>LArIAT: Liquid Argon In A Testbeam</b>	<b>60</b>
91	3.1	The Particles' Path to LArIAT . . . . .	60
92	3.2	LArIAT Tertiary Beam Instrumentation . . . . .	62
93	3.2.1	Bending Magnets . . . . .	63
94	3.2.2	Multi-Wire Proportional Chambers . . . . .	65
95	3.2.3	Time-of-Flight System . . . . .	67
96	3.2.4	Punch-Through and Muon Range Stack Instruments . . . . .	68
97	3.2.5	LArIAT Cosmic Ray Paddle Detectors . . . . .	70
98	3.3	In the Cryostat . . . . .	71
99	3.3.1	Cryogenics and Argon Purity . . . . .	71
100	3.3.2	LArTPC: Charge Collection . . . . .	74
101	3.3.3	LArTPC: Light Collection System . . . . .	77
102	3.4	Trigger and DAQ . . . . .	80
103	3.5	Control Systems . . . . .	81
104	<b>4</b>	<b>Total Hadronic Cross Section Measurement Methodology</b>	<b>87</b>
105	4.1	Event Selection . . . . .	88
106	4.1.1	Selection of Beamline Events . . . . .	88
107	4.1.2	Particle Identification in the Beamline . . . . .	89
108	4.1.3	TPC Selection: Halo Mitigation . . . . .	89

109	4.1.4	TPC Selection: Shower Removal . . . . .	90
110	4.2	Beamline and TPC Handshake: the Wire Chamber to TPC Match . .	91
111	4.3	The Thin Slice Method . . . . .	93
112	4.3.1	Cross Sections on Thin Target . . . . .	93
113	4.3.2	Not-so-Thin Target: Slicing the Liquid Argon Volume . . . . .	94
114	4.3.3	Corrections to the Raw Cross Section . . . . .	96
115	4.4	Procedure testing with MC truth quantities . . . . .	98
116	<b>5</b>	<b>Data and MC preparation for the Cross Section Measurements</b>	<b>100</b>
117	5.1	Cross Section Analyses Data Sets . . . . .	100
118	5.2	Construction of a Monte Carlo Simulation for LArIAT . . . . .	102
119	5.2.1	G4Beamline . . . . .	102
120	5.2.2	Data Driven MC . . . . .	106
121	5.3	Estimate of Backgrounds in the Pion Cross Section . . . . .	108
122	5.3.1	Background from Pion Capture and Decay . . . . .	110
123	5.3.2	Contributions from the Beamline Background . . . . .	113
124	5.4	Estimate of Energy Loss before the TPC . . . . .	117
125	5.5	Tracking Studies . . . . .	119
126	5.5.1	Angular Resolution . . . . .	121
127	5.6	Calorimetry Studies . . . . .	128
128	5.6.1	Kinetic Energy Measurement . . . . .	128
129	<b>6</b>	<b>Negative Pion Cross Section Measurement</b>	<b>131</b>
130	6.1	Raw Cross Section . . . . .	131
131	6.1.1	Statistical Uncertainty . . . . .	133
132	6.1.2	Treatment of Systematics . . . . .	135
133	6.2	Corrections to the Raw Cross Section . . . . .	136
134	6.2.1	Background subtraction . . . . .	137

<sup>135</sup>	6.2.2 Correction for Reconstruction Effects . . . . .	138
<sup>136</sup>	6.3 Results . . . . .	144
<sup>137</sup>	<b>7 Positive Kaon Cross Section Measurement</b>	<b>146</b>
<sup>138</sup>	7.1 Raw Cross Section . . . . .	146
<sup>139</sup>	7.2 Corrections to the Raw Cross Section . . . . .	148
<sup>140</sup>	7.3 Results . . . . .	152
<sup>141</sup>	<b>8 Conclusions</b>	<b>153</b>
<sup>142</sup>	<b>A Measurement of LArIAT Electric Field</b>	<b>155</b>
<sup>143</sup>	<b>B Additional Tracking Studies for LArIAT Cross Section Analyses</b>	<b>163</b>
<sup>144</sup>	B.0.1 Study of WC to TPC Match . . . . .	164
<sup>145</sup>	B.0.2 Tracking Optimization . . . . .	166
<sup>146</sup>	<b>C Energy Calibration</b>	<b>169</b>

# <sup>147</sup> Acknowledgements

<sup>148</sup>

*“Dunque io ringrazio tutti quanti.*

<sup>149</sup>

*Specie la mia mamma che mi ha fatto così funky.”*

<sup>150</sup>

– Articolo 31, Tanqi Funky, 1996 –

<sup>151</sup>

*“At last, I thank everyone.*

<sup>152</sup>

*Especialiy my mom who made me so funky.”*

<sup>153</sup>

– Articolo 31, Tanqi Funky, 1996 –

<sup>154</sup> Mom, you are and will always be the hero of my story; I know this has been  
<sup>155</sup> challenging for you, thanks for being there for me at every hour of the day and the  
<sup>156</sup> night, for being always honest with me and for somehow handling this whole US-Italy  
<sup>157</sup> thing gracefully. I can't believe you still haven't met Bonnie. Ah, and don't worry,  
<sup>158</sup> I'll always translate things for you.

<sup>159</sup> Bonnie Fleming, my advisor, I don't even know where to start in thanking you.  
<sup>160</sup> Thanks for listening to me before I proved I was worth be listened to; thanks for  
<sup>161</sup> always believing I could make it, even at the bottom of my doubts; thanks for all  
<sup>162</sup> the laughters, for all the freedom, for all the great advices; thanks for leading by  
<sup>163</sup> example; thanks for being always supportive of all my crazy side projects; thanks  
<sup>164</sup> for choosing each and every person in the most wonderful research group ever and  
<sup>165</sup> thanks for letting me be part of it. Thanks for showing me that even Bonnie Freaking  
<sup>166</sup> Fleming is human, has her downs and still she strives.

167 Flavio Cavanna, my co-advisor, working with you has been one of the greatest  
168 pleasures of my academic life; the extent of your knowledge never ceases to amaze me  
169 and the freshness of your enthusiasm is always contagious. Thanks for all the time  
170 spent in your office banging our heads on these cross section analyses and thanks for  
171 convincing me to join LArIAT in the first place.

172 Ornella Palamara, after a particularly heated exchange at a wine and cheese, I  
173 once told Andrzej I think of you as my spirit animal: fierce, knowledgeable and direct;  
174 he replied I still need to walk many miles to get there and I can't agree more.

175 A big thank you to my academic sisters, from the youngest to the oldest (again  
176 academically speaking): Supraja Balasubramanian, you worked the magic of enriching  
177 my past, thank you from the bottom of my heart; Brooke Morrison, the depth of your  
178 knowledge, your drive and love for our field has been and will always be a constant  
179 inspiration; Ariana Hackenburg, thanks for keeping me sane for the last four years,  
180 if you run for president – as you should – remember to delete our Skype chats, love  
181 and hugs to you dudette; and last but not least Xiao Luo, Fermilab has given me lots  
182 of extraordinary gifts, but no one bigger than your friendship.

183 Jen Raaf and Jonathan Asaadi, these analyses would have not seen the light of  
184 day without you. Thanks for your many inputs and for letting your door open to talk  
185 about physics and/or my latest paranoia. Thanks for the patience and understanding.  
186 And thanks for leading that small experiment with a big heart called LArIAT and all  
187 its crazy ponies. Speaking of which, thanks to all my collaborators, especially Irene  
188 Nutini, who started the path for the pion analysis, Greg Pulliam, who suffered with  
189 me at the end of said path, Dan the Man, Jason, Johnny, Will Fo and Mr Bojangles.  
190 A special token of gratitude goes to Roberto Acciarri and Andrzej M. Szelc, you are  
191 so much more to me than collaborators and previous car owners, you know you'll  
192 always have a home in Chicago.

193 To all the members of the NPG, thanks for all the laughters and all the wise

194 insights. You're the smartest bunch of idiots I've ever met, I love y'all.

195 Thanks to the MicroBooNE collaboration Sam kazu and kirby

196 Shany Danieli and Louise Laage, you're the piece of heart I left in New Haven.

197 Shany, I don't know what made you think I was the cool kid in the group, but I'm so

198 glad you stuck with me. I'm not sure I would have survived my first semester at Yale

199 without you: you shine in your smartness and lift other people with you – it's a rare

200 quality in our field. Louise, my dear, thanks for always finding the time to listen, for

201 your attuned spirit and for the magnolias.

202 Thanks to all the people which helped me make Chicago and Fermilab my new

203 home, in particular David Caratelli, Mateus Carneiro, Pilar Coloma, Ciaran Hughes,

204 Gordan Krnjaic, Seyda Ipek, Kiel Howe and Rob Fine.

205 To the extraordinary people who stayed close, even with an ocean in between: la

206 Tasso, Marci, la Bea, la Kittirn, Alvin, la Viola e Brogna, Sighi, Eleonora and all the

207 people from the "La Chiappia Nuova" group, thanks for making me feel like I never

208 left.

209 Finally, thanks to Anto, my husband, my topo and my adventure companion,

210 cause people might think I'm nice and easy, but you know I'm not... And still, you

211 followed me across half the world and you're still here, so that I could never feel alone.

# <sup>212</sup> Introduction

<sup>213</sup> This thesis work concerns the first measurement of the ( $\pi^-$ -Ar) total hadronic cross  
<sup>214</sup> section in the 100-1000 MeV kinetic energy range and the first measurement of the  
<sup>215</sup> ( $K^+$ -Ar) total hadronic cross section in the 100-650 MeV kinetic energy range. We  
<sup>216</sup> performed these measurements at the LArIAT experiment, a small (0.25 ton) Liquid  
<sup>217</sup> Argon Time Projection Chamber (LArTPC) on a beam of charged particles at the  
<sup>218</sup> Fermilab Test Beam Facility. Albeit particle and nuclear physics have a long history  
<sup>219</sup> of hadronic cross section measurements, the work outlined in this thesis presents a  
<sup>220</sup> new methodology – the “thin slice method” – for cross section measurements in argon,  
<sup>221</sup> possible only thanks to the detection capabilities of the LArTPC technology. The  
<sup>222</sup> combination of fine-grained tracking and excellent calorimetric information provided  
<sup>223</sup> by the LArTPC technology allows to see unprecedented details of particle interactions  
<sup>224</sup> in argon and, in LArIAT, to measure the kinetic energy of a hadron at each step  
<sup>225</sup> of the tracking. A renewed interest for precision measurements of hadronic cross  
<sup>226</sup> sections, particularly in argon, arises from the current panorama of experimental  
<sup>227</sup> particle physics at the intensity frontier.

<sup>228</sup> The discovery of the Higgs boson in 2012 marked the triumph of the Standard  
<sup>229</sup> Model of Particle Physics; exploring what lays beyond is the real challenge in our field  
<sup>230</sup> today. Since their formulation in 1930, neutrinos have been a source of surprises (and  
<sup>231</sup> Nobel Prizes) for particle physicists, tiny cracks in our understanding of Nature. In  
<sup>232</sup> particular, the discovery of neutrino oscillation represents the first evidence of physics

233 Beyond the Standard Model (BSM). From a theoretical point of view, the field is  
234 developing new theories to account for the small but non-zero mass of neutrinos,  
235 while trying to remain consistent with the rest of the Standard Model. From an  
236 experimental point of view, we are developing technologies and huge collaborations  
237 to probe these theories. As we enter the era of precision measurements of neutrino  
238 interaction, neutrinos might hold the key to the next generation of discoveries in  
239 particle physics.

240 Experimentally, precision measurements can be achieved only if the detector tech-  
241 nology is able to resolve the fine details of a neutrino interaction and to record a  
242 statistically relevant number of neutrinos. With “fine details” here we mean the abil-  
243 ity to distinguish the many products of the neutrino interaction, such as protons,  
244 pions, muons and electrons, and to measure their energy. Historically, bubble cham-  
245 ber neutrino detectors were the first revolution in neutrino detection: for example,  
246 the spatial resolution of Gargamelle allowed the discovery of neutrino neutral current  
247 interaction. Despite the high precision of bubble chambers images, this technology  
248 is hard to scale to massive size, making statistical analyses on neutrino interactions  
249 almost impossible to perform. To make up for the small neutrino interaction cross  
250 section, neutrino experiments moved to very large size, at the expenses of spatial  
251 precision. This is the case for the detectors which discovered neutrino oscillation:  
252 both Super-Kamiokande and SNO are massive Cherenkov detectors. With LArT-  
253 PCs, the field is gaining again bubble-chamber like precision but at massive scales.  
254 Following the recommendations of the latest Particle Physics Project Prioritization  
255 Panel [106], the US particle physics panorama is directing a substantial effort to-  
256 wards the exploration of the intensity frontier through the construction of massive  
257 LArTPCs. In particular, the near future will see the development of a Short Baseline  
258 Neutrino Program (SBN) and long baseline neutrino program (DUNE), both based  
259 on the LArTPC detector technology. The US liquid argon program has the potential

260 to answer many of the fundamental open questions in particle physics today, such  
261 as: is there a fourth generation neutrino? is CP violated in the lepton sector? are  
262 there any additional symmetries? and, can we find an indication of Grand Unified  
263 Theories?

264 The SBN program at Fermilab is tasked with conclusively addressing the existence  
265 of a fourth neutrino generation in the  $\Delta m^2 = \Delta m_{14}^2 \sim [0.1 - 10] \text{ eV}^2$  parameter space.  
266 The SBN program entails three surface LArTPCs positioned on the Booster Neutrino  
267 Beam at different distances from the neutrino production in oder to fully exploit the  
268 L/E dependence of the oscillation pattern: SBND (100 m from the decay pipe),  
269 MicroBooNE (450 m), and ICARUS (600 m). SBN will also perform an extensive  
270 program of neutrino cross section measurements, fundamental to abate systematics  
271 in the oscillation analyses in both SBN and DUNE.

272 DUNE has a vast neutrino and non-accelerator physics reach. For what it concerns  
273 neutrino physics, oscillation analyses in DUNE have the capability of solving the mass  
274 hierarchy and octant problem, and discovering CP violation in the neutrino sector.  
275 Besides its neutrino program, DUNE can open an experimental window on Grand  
276 Unified Theories (GUTs). GUTs could potentially answer fundamental questions  
277 such as the existence of non-zero neutrino masses and matter-antimatter asymmetry,  
278 explaining some “accidents” in the Standard Models, such as the exact cancellation of  
279 the proton and the electron charge. Directly probing GUTs at the unification energy  
280 scale is impossible by any foreseeable collider experiment. We then need an indirect  
281 proof such as baryon number violation, which is predicted by almost every GUT in the  
282 form of proton decay, bounded nucleon decay or  $n - \bar{n}$  oscillations on long time-scales.  
283 Historically, the main technology used in these searches has been water Cherenkov  
284 detectors, with Super-Kamiokande setting all the current experimental limits on the  
285 decay lifetimes at the order of  $\sim 10^{34}$  years. The DUNE far detector and its non-  
286 accelerator physics program is a interesting new actor on this stage. LArTPCs can in

287 fact complement nucleon decay searches in modes where water Cherenkov detectors  
288 are less sensitive, especially  $p \rightarrow K^+ \bar{\nu}$  [11].

289 Such a diverse physics program speaks to the versatility of the LArTPC technol-  
290 ogy. LArTPCs provide excellent electron/photon separation [9] lacking in Cherenkov  
291 detectors which can be leveraged to abate the photon background from neutral cur-  
292 rent interactions in  $\nu_e$  searches. LArTPCs also share superb tracking capability with  
293 bubble chamber detectors, with several additional benefits. They are electronically  
294 read out and self triggered detectors; they provide full 3D-imaging with millimeter  
295 resolution, precise calorimetric reconstruction and excellent particle identification.

296 The amount of information a LArTPC can provide makes these detectors rather  
297 complex: a series of dedicated measurements is necessary to obtain meaningful physics  
298 results from a LArTPC. The complexity of the LArTPC technology for neutrino  
299 detection is due to several reasons. Argon is a fairly heavy element, which means that  
300 nuclear effects play an important role in the looks of the interaction topology. For  
301 example, pions are one of the main products of neutrino interactions; yet, since data  
302 on charged particle interaction in argon is scarce, neutrino event generators have big  
303 uncertainties in the re-scattering simulation of pion in argon. The amount of details  
304 in an LArTPC event is easily parsed by human eye, but can make automatic event  
305 reconstruction rather challenging. Thus, reconstruction algorithms in LArTPC need  
306 to be tune to recognize the different topologies of the neutrino interaction products in  
307 argon. This is particularly true for pions, since they are an abundant product of the  
308 neutrino interactions: the occurrence of a pion interaction in argon can modify the  
309 topology of the neutrino event, causing a misidentification of the neutrino interaction.

310 The LArIAT [38] experiment is performing precise cross section measurements of  
311 charged particles in argon to bridge this gap of knowledge. The LArIAT LArTPC sits  
312 on a beam of charged particles at the Fermilab Test Beam Facility which provides  
313 charge particles of the type and energy range relevant for neutrino interaction of

314 both SBN and DUNE. The ( $\pi^-$ -Ar) hadronic cross section is a fundamental input for  
315 neutrino detectors in liquid argon, as pion interactions can modify the topology and  
316 energy reconstruction of neutrino events in the GeV range, where pion production  
317 is abundant. The ( $K^+$ -Ar) total hadronic differential cross section in LArIAT is  
318 particularly relevant for a high identification efficiency in the context of proton decay  
319 searches in DUNE in the  $p \rightarrow K^+ \bar{\nu}$  channel. In fact, the kaon-argon cross section  
320 affects the kaon topology by modifying the kaon tracking and energy reconstruction,  
321 impacting the basis for kaon identification in a LArTPC.

322 The cross section analyses exploit the totality of LArIAT’s experimental handles;  
323 they rely on beam line detector information as well as both calorimetry and tracking  
324 in the TPC. These analyses are LArIAT’s first physics results. In order to measure  
325 total hadronic argon cross sections, several steps are necessary. The analyses start by  
326 identifying a sample of the hadron of interest in the beam line and assessing the beam  
327 line contaminations. It proceeds with tracking the hadron candidates in the TPC and  
328 measuring their kinetic energy at each point in the tracking: the fine sampling of an  
329 hadron in the TPC forms the set of “incident” hadrons. Then, the hadronic interac-  
330 tion point is identified and the raw cross section is calculated. Two corrections are  
331 then applied to the raw cross section – a background subtraction and a correction  
332 for detector effects – to obtain the true cross section measurement.

333

334 This body of work is organized in 8 chapters. We provide a description of the  
335 theoretical framework for the measurements in Chapter 1. Chapter 2 outlines the  
336 LArTPC detector technology, while Chapter 3 describes LArIAT experimental setup.  
337 We present the event selection for both the pion and kaon analyses, as well as the  
338 “thin slice method” in Chapter 4. Chapter 5 describes the work done on the data  
339 and Monte Carlo samples in preparation of the cross section analyses. Chapter 6  
340 shows the results for the ( $\pi^-$ -Ar) total hadronic cross section measurement. Chapter

<sup>341</sup> 7 shows the results for the ( $K^+$ -Ar) total hadronic cross section measurement. We  
<sup>342</sup> draw the final remarks on this work in Chapter 8

<sup>343</sup> A series of additional studies and calibrations were necessary to perform the cross  
<sup>344</sup> section analyses. Appendix A shows a measurement of the LArIAT LArTPC electric  
<sup>345</sup> field using cosmic data. Appendix B shows an optimization of the tracking algorithms  
<sup>346</sup> geared towards maximizing the efficiency of finding the hadronic interaction point.  
<sup>347</sup> Appendix C shows the calorimetry calibration of the LArIAT LArTPC, which is a  
<sup>348</sup> pivotal measurement to enable any physics analysis with TPC data.

349 **Chapter 1**

350 **The theoretical framework**



351 – J. S. Bach, 1720 ca. –

352 In this chapter, we set the ( $\pi^-$ - Ar) and ( $K^+$ - Ar) total hadronic cross section  
353 measurements into the greater theoretical and phenomenological framework. We start  
354 by briefly describing the Standard Model (Section 1.1), with particular attention to  
355 neutrinos and neutrino interactions (Section 1.2). We then describe some of the  
356 open questions in neutrino physics today and Beyond Standard Model theories (1.3)  
357 setting the stage for the measurements reported in this work (Section 1.4).

358 **1.1 The Standard Model**

359 The Standard Model (SM) of particle physics is the most accurate theoretical descrip-  
360 tion of the subatomic world and, in general, one of the most precisely tested theories  
361 in the history of physics. The SM describes the strong, electromagnetic and weak  
362 interactions among elementary particles in the framework of quantum field theory,

363 accounting for the unification of electromagnetic and weak interactions for energies  
364 above the vacuum expectation value (VEV) of the Higgs field. The SM does not  
365 describe gravity or general relativity.

366 The Standard Model is a gauge theory based on the local symmetry group

$$G_{SM} = SU(3)_C \otimes SU(2)_L \otimes U(1)_Y \quad (1.1)$$

367 where the subscripts C indicates the conserved strong charge (color), and the  
368 subscripts Y indicates the conserved hypercharge. If we indicated with T the weak  
369 isospin T and with T3 its third component, hypercharge can be related to the electric  
370 charge Q through the Gell-Mann-Nishijima relation:

$$Q = \frac{Y}{2} + T_3. \quad (1.2)$$

371 In the quantum field framework, the SM fields correspond to the irreducible rep-  
372 resentations of the  $G_{SM}$  symmetry group. In particular, the particles are divided in  
373 two categories, fermions and bosons, according to their spin-statistics. Described by  
374 the Fermi-Dirac statistics, fermions have half-integer spin and are sometimes called  
375 “matter-particles”. Bosons or “force carriers” have integer spin, follow the Bose-  
376 Einstein statistics and mediate the interaction between fermions. The fundamental  
377 fermions and their quantum numbers are listed in Tab 1.1.

378 Quarks can interact via all three the fundamental forces; they are triplets of  
379  $SU(3)_C$ , that is they can exist in three different colors. If one chooses a base where  
380  $u$ ,  $c$  and  $t$  quarks are simultaneously eigenstates of both the strong and the weak  
381 interactions, the remaining eigenstates are usually written as  $d$ ,  $s$  and  $b$  for the strong  
382 interaction and  $d'$ ,  $s'$  and  $b'$  for the weak interaction, because the latter ones are  
383 the result of a CKM rotation on the first ones. Charged leptons interact via the  
384 weak and the electromagnetic forces, while neutrinos only interact via the weak force.

Generation	I	II	III	T	Y	Q
Leptons	$\begin{pmatrix} \nu_e \\ e \end{pmatrix}_L$	$\begin{pmatrix} \nu_\mu \\ \mu \end{pmatrix}_L$	$\begin{pmatrix} \nu_\tau \\ \tau \end{pmatrix}_L$	1/2 -1/2	-1 -1	0 -1
	$e_R$	$\mu_R$	$\tau_R$	0	-2	1
Quarks	$\begin{pmatrix} u \\ d' \end{pmatrix}_L$	$\begin{pmatrix} c \\ s' \end{pmatrix}_L$	$\begin{pmatrix} t \\ b' \end{pmatrix}_L$	1/2 -1/2	1/3 1/3	2/3 -1/3
	$u_R$ $d'_R$	$c_R$ $s'_R$	$t_R$ $b'_R$	0 0	4/3 -2/3	2/3 -1/3

Table 1.1: SM elementary fermionic fields. The subscripts L and R indicate respectively the negative chirality (left-handed) and the positive chirality (right-handed).

385 The gauge group univocally determines the number of gauge bosons that carry the  
 386 interaction; the gauge bosons correspond to the generators of the group: eight gluons  
 387 (g) for the strong interaction, one photon ( $\gamma$ ) and three bosons ( $W^\pm$ ,  $Z^0$ ) for the  
 388 electroweak interaction. A gauge theory by itself cannot provide a description of  
 389 massive particles, but it is experimentally well known that most of the elementary  
 390 particles have non-zero masses. The introduction of massive fields in the Standard  
 391 Model lagrangian would make the theory not gauge invariant, resulting ill-defined.  
 392 This problem is solved in the SM by the introduction of a scalar iso-doublet  $\Phi(x)$ , the  
 393 Higgs field, which gives mass to  $W^\pm$  and  $Z^0$  gauge bosons through the electroweak  
 394 symmetry breaking mechanism and to the fermions through Yukawa coupling [75, 76].  
 395 The discovery of the Higgs boson in 2012 by the LHC experiments [41, 42] marked  
 396 the ultimate confirmation of a long history of successful predictions by the SM.

## 397 1.2 Neutrinos: tiny cracks in the Standard Model

398 To our current knowledge, neutrinos are the most abundant fermion in the Universe.  
399 And yet, they are maybe the most mysterious particle in the SM: they generate  
400 theoretical puzzles and experimental challenges. In this section, we treat neutrinos  
401 within and beyond the SM and describe the make up of their interaction with matter.

### 402 1.2.1 Neutrinos in the Standard Model

403 Neutrino can be introduced in the SM as left-handed massless Weyl spinors. The  
404 Dirac equation of motion for a free field

$$(i\gamma^\mu \partial_\mu - m)\psi = 0 \quad (1.3)$$

405 for a fermionic field

$$\psi = \psi_L + \psi_R \quad (1.4)$$

406 is equivalent to the equations

$$i\gamma^\mu \partial_\mu \psi_L = m\psi_R \quad (1.5)$$

407

$$i\gamma^\mu \partial_\mu \psi_R = m\psi_L \quad (1.6)$$

408 for the chiral fields  $\psi_R$  and  $\psi_L$ , whose evolution in space and time is coupled  
409 through the mass  $m$ . If the fermion is massless, the chiral fields decouple and the  
410 fermion can be described by a single Weyl spinor with two independent compo-  
411 nents [116]. Pauli initially rejected the description of a physical particle through  
412 a single Weyl spinor because of its implication of parity violation. In fact, since  
413 the spatial inversion operator throws  $\psi_R \leftrightarrow \psi_L$ , parity is conserved only if both chi-  
414 ral components exist at the same time. For the neutrino introduction in the SM,  
415 experiments came in help of the theoretical description. The constraint of parity

<sup>416</sup> conservation weakened after Wu's experiment in 1957 [119]. Additionally, there was  
<sup>417</sup> no experimental indication for massive neutrinos, nor evidence of interaction via the  
<sup>418</sup> neutrino right-handed component.

<sup>419</sup> The symmetry group  $SU(2)_L \otimes U(1)_Y$  is the only group relevant for neutrino  
<sup>420</sup> interactions. The SM electroweak lagrangian is the most general renormalizable la-  
<sup>421</sup> grangian invariant under the local symmetry group  $SU(2)_L \otimes U(1)_Y$ . The lagrangian  
<sup>422</sup> couples the weak isotopic spin doublets and singlets described in Table 1.1 with the  
<sup>423</sup> gauge bosons  $A_a^\mu$  ( $a = 1, 2, 3$ ) and  $B^\mu$ , and Higgs doublet  $\Phi(x)$ :

$$\begin{aligned} \mathcal{L} = & i \sum_{\alpha=e,\mu,\tau} \bar{L}'_{\alpha L} \not{D} L'_{\alpha L} + i \sum_{\alpha=1,2,3} \bar{Q}'_{\alpha L} \not{D} Q'_{\alpha L} \\ & + i \sum_{\alpha=e,\mu,\tau} \bar{l}'_{\alpha R} \not{D} l'_{\alpha R} + i \sum_{\alpha=d,s,b} \bar{q}'^D_{\alpha R} \not{D} q'^D_{\alpha R} + i \sum_{\alpha=u,c,t} \bar{q}'^U_{\alpha R} \not{D} q'^U_{\alpha R} \\ & - \frac{1}{4} A_{\mu\nu} A^{\mu\nu} - \frac{1}{4} B_{\mu\nu} B^{\mu\nu} \\ & + (D_\rho \Phi)^\dagger (D^\rho \Phi) - \mu^2 \Phi^\dagger \Phi - \lambda (\Phi^\dagger \Phi)^2 \\ & - \sum_{\alpha,\beta=e,\mu,\tau} \left( Y_{\alpha\beta}^l \bar{L}'_{\alpha L} \Phi l'_{\beta R} + Y_{\alpha\beta}^{l*} \bar{l}'_{\beta R} \Phi^\dagger L'_{\alpha L} \right) \\ & - \sum_{\alpha=1,2,3} \sum_{\beta=d,s,b} \left( Y_{\alpha\beta}^D \bar{Q}'_{\alpha L} \Phi q'^D_{\beta R} + Y_{\alpha\beta}^{D*} \bar{q}'^D_{\beta R} \Phi^\dagger Q'_{\alpha L} \right) \\ & - \sum_{\alpha=1,2,3} \sum_{\beta=u,c,t} \left( Y_{\alpha\beta}^U \bar{Q}'_{\alpha L} \tilde{\Phi} q'^U_{\beta R} + Y_{\alpha\beta}^{U*} \bar{q}'^U_{\beta R} \tilde{\Phi}^\dagger Q'_{\alpha L} \right). \end{aligned} \quad (1.7)$$

<sup>424</sup> The first two lines of the lagrangian summarize the kinetic terms for the fermionic  
<sup>425</sup> fields and their coupling to the gauge bosons  $A_a^{\mu\nu}$ ,  $B^{\mu\nu}$ <sup>1</sup>. The third line describes  
<sup>426</sup> the kinetic terms and the self-coupling terms of the gauge bosons. The forth line is  
<sup>427</sup> the Higgs lagrangian, which results in the spontaneous symmetry breaking. The last  
<sup>428</sup> three lines describe the Yukawa coupling between fermions and the Higgs field, origin  
<sup>429</sup> of the fermions' mass.

---

1. In gauge theories the ordinary derivative  $\partial_\mu$  is substituted with the covariant derivative  $D_\mu$ . Here  $D_\mu = \partial_\mu + igA_\mu \cdot I + ig'B_\mu \frac{Y}{2}$ , where  $I$  and  $Y$  are the  $SU(2)_L$  and  $U(1)_Y$  generators, respectively.

430        The coupling between left-handed and right-handed field generates the mass term  
431    for fermions. The SM assumes only left-handed components for neutrinos, thus im-  
432    plying zero neutrino mass. Since any linear combination of massless fields results in a  
433    massless field, the flavor eigenstates are identical to the mass eigenstates in the SM.

### 434    1.2.2 Neutrino Oscillations

435    The determination of the flavor of a neutrino dynamically arises from the correspond-  
436    ing charged lepton associated in a change current interaction; for example, a  $\nu_e$  is a  
437    neutrino which produces an  $e^-$ , a  $\bar{\nu}_\mu$  is a neutrino which produces a  $\mu^+$ , etc. The  
438    neutrino flavor eigenstates  $|\nu_\alpha\rangle$ , with  $\alpha = e, \mu, \tau$ , are orthogonal to each other and  
439    form a base for the weak interaction matrix.

440        Overwhelming experimental data show that neutrinos change flavor during their  
441    propagation [101]. This phenomenon, called “neutrino oscillations”, was predicted  
442    first by Bruno Pontecorvo in 1957 [102]. Neutrino oscillations are possible only if  
443    the neutrino flavor eigenstate are not identical to the mass eigenstates. Thus, the  
444    observation of neutrino oscillation results in the first evidence of physics beyond the  
445    Standard Model. A minimal extension of the SM introduces three mass eigenstates,  
446     $|\nu_i\rangle$  ( $i = 1, 2, 3$ ), whose mass  $m_i$  is well defined. The unitary Pontecorvo-Maki-  
447    Nakagawa-Sakata matrix transforms the mass base into the flavor base as follows

$$|\nu_\alpha\rangle = U_{PMNS} |\nu_i\rangle, \quad (1.8)$$

448        with

$$U_{PMNS} = \begin{bmatrix} c_{12} & s_{12} & 0 \\ -s_{12} & c_{12} & 0 \\ 0 & 0 & 1 \end{bmatrix} \begin{bmatrix} c_{13} & 0 & s_{13}e^{-i\delta} \\ 0 & 1 & 0 \\ -s_{13}e^{-i\delta} & 0 & c_{13} \end{bmatrix} \begin{bmatrix} 1 & 0 & 0 \\ 0 & c_{23} & s_{23} \\ 0 & -s_{23} & c_{23} \end{bmatrix} \begin{bmatrix} e^{i\alpha_1} & 0 & 0 \\ 0 & e^{i\alpha_2} & 0 \\ 0 & 0 & 1 \end{bmatrix} \quad (1.9)$$

449 where  $c$  e  $s$  stand respectively for cosine and sine of the corresponding mixing  
 450 angles ( $\theta_{12}$ ,  $\theta_{23}$  and  $\theta_{13}$ ),  $\delta$  is the Dirac CP violation phase,  $\alpha_1$  and  $\alpha_2$  are the eventual  
 451 Majorana CP violation phases. Experimental results on neutrino oscillations are  
 452 generally reported in terms of the mixing angles and of the squared mass splitting  
 453  $\Delta m_{ab}^2 = m_a^2 - m_b^2$ , where  $a$  and  $b$  represent the mass eigenstates. A summary of the  
 454 current status of experimental results, albeit partial, is given in table 1.2.

Table 1.2: Summary of experimental results on neutrino oscillation parameters. **ADD CITATIONS**

	Value	Precision	Experiment
$\theta_{23}$	$45^\circ$	9.0%	Super Kamiokande, MINOS,
$-\Delta m_{32}^2$	$2.5 \cdot 10^{-3} \text{ eV}^2$	1.8%	Nova, MACRO
$\theta_{12}$	$34^\circ$	5.8%	SNO, Gallex,
$-\Delta m_{12}^2$	$7.4 \cdot 10^{-5} \text{ eV}^2$	2.8%	SAGE, KamLAND
$\theta_{13}$	$9^\circ$	4.7%	DAYA Bay,
$-\Delta m_{32}^2$	$2.5 \cdot 10^{-3} \text{ eV}^2$	1.8%	RENO

### 455 1.2.3 Make up of Neutrino Interactions

456 All neutrino experiments involving the detection of single neutrinos are concerned  
 457 with neutrino interactions (and neutrino cross sections) on nuclei. Given the invisible  
 458 nature of the neutrino, characterizing the products of its interaction is the only  
 459 method to a) assess the neutrino presence, b) detect its flavor in case of a charge  
 460 current interaction and c) eventually reconstruct its energy.

461 Historically, neutrino interactions with the nucleus in the GeV region are divided  
 462 into three categories into three categories whose contributions change as a function

463 of increasing neutrino energy:: quasi elastic (QE), resonant (RES), and deep inelastic  
464 (DIS) scattering. All current and forthcoming oscillation experiments on neutrino  
465 beams live in the 0.1-10 GeV transition region, which encompasses the energy where  
466 the QE neutrino-nucleus interaction transitions into RES and then into DIS. For  
467 scattering off free nucleons, neutrino and antineutrino QE charge current scattering  
468 refers to the process  $\nu_l n \rightarrow l^- p$  and  $\bar{\nu}_l p \rightarrow l^+ n$  where a charged lepton and single  
469 nucleon are ejected in the elastic interaction. Resonant scattering refers to an inelas-  
470 tic collision producing a nucleon excited state ( $\Delta, N^*$ ) – the resonance – which then  
471 quickly decays, most often to a nucleon and single-pion final state. DIS refers to the  
472 head-on collision between the neutrino and a parton inside the nucleon, producing  
473 hadronization and subsequent abundant production of mesons and nucleons. In addi-  
474 tion to such interactions between the neutrino and a single component of the nucleus,  
475 neutrinos can also interact with the nucleus as a whole, albeit more rarely, a well  
476 documented process called coherent meson production scattering [58]; the signature  
477 of such process is the production of a distinctly forward-scattered single meson final  
478 state, most often a pion. This simple picture of neutrino interactions works rather  
479 well for scattering off of light nuclear targets, such as the H<sub>2</sub> and D<sub>2</sub> of bubble cham-  
480 ber experiments [64], but the complexity of the nuclear structure for heavier nuclei  
481 such as argon complicates this model.

482 As we will discuss in Chapter 2, the properties of argon make it a good candidate  
483 for an interacting medium in neutrino experiments; in particular the density of its  
484 interaction centers increases the yield of neutrino interactions and allows for relatively  
485 compact detectors. Though, the choice of a relatively heavy nuclear target comes at  
486 the cost of enhancing nuclear effects which modify the kinematic and final state of  
487 the neutrino interaction products.

488 Nuclear effects can potentially affect neutrino event rates, final state particle emis-  
489 sion, neutrino energy reconstruction, and the neutrino/antineutrino ratios, carrying

490 deep implications for oscillation experiments. Even in the case of “simple” QE scat-  
491 tering, intra-nuclear hadron rescattering and correlation effects between the target  
492 nucleons can cause the ejection of additional nucleons in the final state, modifying  
493 the final state kinematics and topology. In the case of resonant and DIS scattering,  
494 the hadronic interactions of meson and nucleons produced in the decay of the res-  
495 onance or during hadronization complicate this picture even more. A large source  
496 of uncertainty in modeling nuclear effects in neutrino interactions come from mesons  
497 interactions (and re-interactions) in the nucleus, e.g., pion re-scattering, charge ex-  
498 change, and absorption.

499 A renewed interest for neutrino cross section measurements surged in recent years,  
500 along with a lively discussion on the data reporting; the historical method of reporting  
501 the neutrino cross section as a function of the neutrino energy or momentum trans-  
502 fered shakes under the weight of its dependency on the chosen nuclear model. On one  
503 hand, correcting for nuclear effects in neutrino interaction can introduce unwanted  
504 sources of uncertainty and model dependency especially due to the mis-modeling of  
505 the meson interactions. On the other, avoiding this correction makes a comparison  
506 between neutrino interactions on different target nuclei extremely difficult.

507 Data on neutrino scattering off many different nuclei are available for both charged  
508 current (CC) and neutral current (NC) channels, as summarized in [64]. A summary  
509 of the results on QE, resonant and DIS scattering for neutrinos and antineutrinos from  
510 accelerators on different target is reported in Figure 1.1, where the (NUANCE) [37]  
511 event generator is used as comparison with the theory.

### 512 **1.3 Beyond the Standard Model**

513 The discovery of neutrino oscillation and its implication of non-zero neutrino mass  
514 mark the beginning of a new, exciting era in neutrino physics: the era of physics Be-

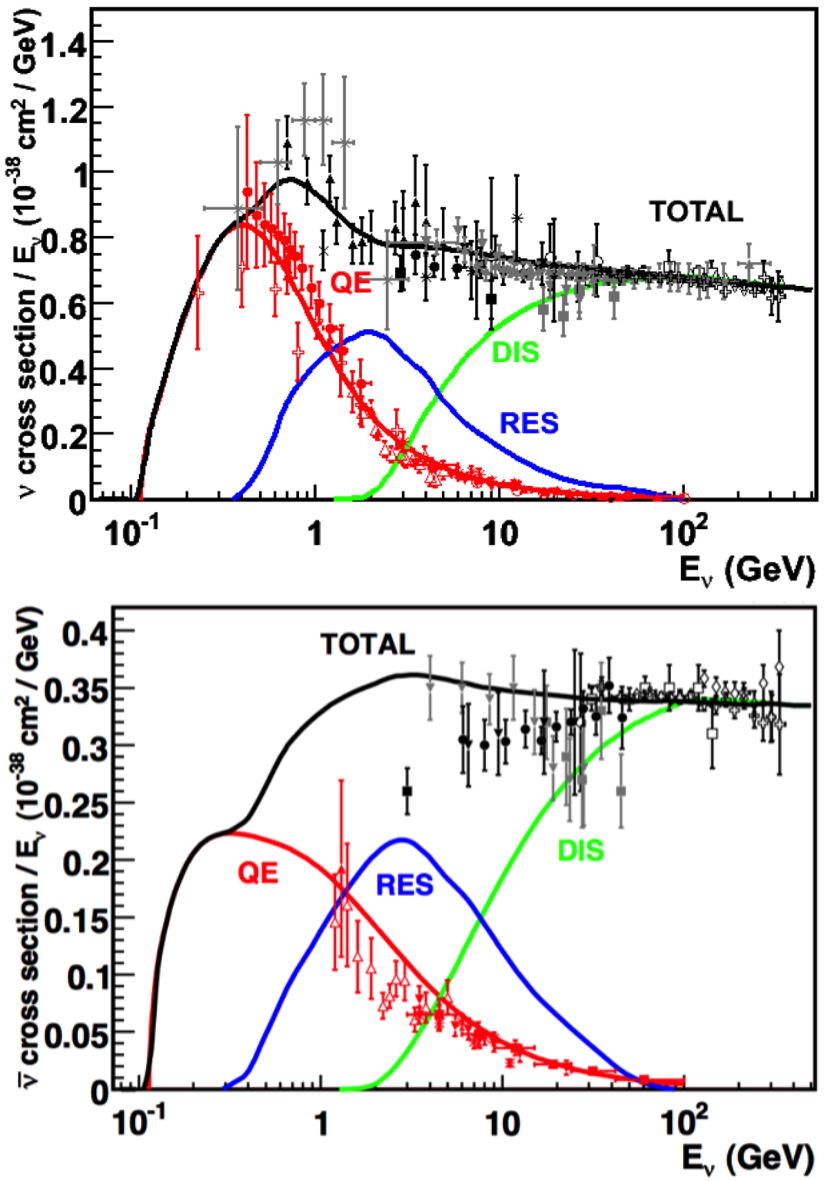


Figure 1.1: Total neutrino (top) and antineutrino (bottom) CC cross sections per nucleon divided by neutrino energy as a function of energy as reported in [64]. Predictions for the total (black), the QE (red), resonant (blue) and DIS (green) are provided by the NUANCE generator. The quasi-elastic scattering data and predictions have been averaged over neutron and proton targets (isoscalar target).

515 yond the Standard Model (BSM) at the intensity frontier. We are currently searching  
516 for new, deeper theories that can accommodate neutrinos with tiny but non-zero  
517 masses, while remaining consistent with the rest of the Standard Model.

### 518 1.3.1 Open Questions in Neutrino Physics

519 On one hand, the last three decades of experiments in neutrino oscillations brought  
520 spectacular advancements in the understanding of the oscillations pattern, measuring  
521 the neutrino mixing angles and mass splitting with a precision of less than 10%. On  
522 the other, they opened the field for a series of questions needing experimental answers.

523 **Sterile neutrinos.** Hints to the existence of at least one additional neutrino,  
524 in the form of various anomalies, have been puzzling physicists almost from the be-  
525 ginning of neutrino oscillation searches. Originally designed to look for evidence of  
526 neutrino oscillation, the Liquid Scintillator Neutrino Detector (LSND) [54] provided  
527 a first conflicting result with the Standard Model expectation of only three neutrinos.

528 A second conflicting result has also been provided by the MiniBooNE experiment [50].

529 The LSND and MiniBooNE  $\nu_e$  and  $\bar{\nu}_e$  appearance results, known as the “LSND and  
530 MiniBooNE anomalies” [14, 15, 23], may be interpreted under the assumption of a new  
531 right-handed neutrino. The additional neutrino needs to be “sterile”, i.e needs not  
532 to couple with the electroweak force carriers, in order to meet the constraint imposed  
533 by the measurement of the width of the Z boson [2]. The new sterile neutrino would  
534 mainly be composed of a heavy neutrino  $\nu_4$  with mass  $m_4$  such that  $m_1, m_2, m_3 \ll m_4$   
535 and  $\Delta m^2 = \Delta m_{14}^2 \sim [0.1 - 10] \text{ eV}^2$ . The introduction of sterile neutrinos is an ap-  
536 pealing line of thinking, since this renormalizable generalization of the SM has the  
537 potential to impact long standing questions in high energy physics and cosmology:  
538 light sterile neutrinos are candidates for dark matter particles and there are ideas  
539 that the theory could be adjusted to explain the baryon asymmetry of the Universe  
540 via leptogenesis [71].

541       **CP Violation In Lepton Sector.** The measurement of non-zero value for the  
542 oscillation parameter  $\theta_{13}$  allows the exploration of low-energy CP violation in the lep-  
543 ton sector at neutrino long baseline oscillation experiments, enabling the possibility  
544 to measure the Dirac CP-violating phase  $\delta$ . Exciting theoretical results tie  $\delta$  directly  
545 to the generation of the baryon asymmetry of the Universe at the Grand Unified  
546 Theory scale **a couple of cit would be nice**. According to the theoretical model de-  
547 scribed in [100], for example, leptogenesis can be achieved if  $|\sin \theta_{13} \sin \delta| > 0.11$ , i.e.  
548  $\sin \delta > 0.7$ .

549       The asymmetry in the oscillation probability of neutrinos and antineutrinos is the ob-  
550 servable sensitive to the Dirac CP-violating phase  $\delta$  leveraged in neutrino oscillation  
551 experiments. Using the parameterization of the PMNS matrix shown in Equation  
552 1.9, the difference between the probability of  $\nu_e \rightarrow \nu_\mu$  oscillation and the probability  
553 of  $\bar{\nu}_e \rightarrow \bar{\nu}_\mu$  oscillation can be parametrized as follows [39],

$$P_{\nu_e \rightarrow \nu_\mu} - P_{\bar{\nu}_e \rightarrow \bar{\nu}_\mu} = J \cos \left( \pm \delta - \frac{\Delta_{31} L}{2} \right) \sin \left( \frac{\Delta_{21} L}{2} \right) \sin \left( \frac{\Delta_{31} L}{2} \right) \quad (1.10)$$

554       where

$$J = \cos \theta_{13} \sin 2\theta_{13} \sin 2\theta_{12} \sin 2\theta_{23} \quad (1.11)$$

555       is the Jarlskog invariant [81],  $L$  the neutrino baseline, i.e. the distance between  
556 the neutrino production and detection points, and  $\Delta_{ab}$  a factor proportional to the  
557 sign and magnitude of the mass splitting. From these equations, it is clear how the  
558 relative large value of  $\theta_{13}$  is a happy accident necessary not to completely suppress  
559 the sensitivity to CP violation. The equations also show how the sensitivity to  $\delta$  is  
560 tied to the measurement of the least precisely measured mixing angle,  $\theta_{23}$  (via the  
561  $\sin 2\theta_{23}$  term) and to an other unknown quantity, the neutrino “mass hierarchy” (via  
562 the  $\Delta_{ab}$  terms). The precise determination of  $\theta_{23}$  is often referred as to “the octant  
563 problem”. Current experimental results [3, 12] are consistent with  $\theta_{23} = 45^\circ$ , which

564 would imply maximal mixing between  $\nu_\mu$  -  $\nu_\tau$ , hinting to an intriguing new symmetry.  
565 Therefore, a precise measurement of  $\theta_{23}$  is of great interest for theoretical models of  
566 quark-lepton universality [74, 92, 105], whose quark and lepton mixing matrices are  
567 proportional to the deviation of  $\theta_{23}$  from 45°.

568       **Neutrino mass hierarchy.** The “mass hierarchy” problem refers to the unknown  
569 ordering of the value of absolute mass of the neutrino mass eigenstates. Current  
570 oscillation experiments are sensitive only to the magnitude of the mass splitting, and  
571 not directly to its sign. In a framework where the lightest neutrino mass (arbitrarily)  
572 corresponds to the first eigenstate  $m_1$ , it is unknown whether  $m_2 - m_1 < m_3 - m_1$   
573 (Normal Hierarchy) or  $m_2 - m_1 > m_3 - m_1$  (Inverted Hierarchy). The mass hierarchy  
574 affects not only the sensitivity to CP violation searches in long baseline oscillation  
575 experiments, but also the sensitivity to determine whether neutrinos are Majorana  
576 particles in neutrinoless double beta decay experiments.

577       **Majorana or Dirac?** Evidence of neutrino oscillations demands the introduction  
578 of a mechanism which can give mass to the neutrinos. This mechanism should possibly  
579 also explain why neutrino masses are at least six orders of magnitude lower than the  
580 electron mass (the second lightest SM fermion). In a description of neutrinos as Dirac  
581 4-component spinors, the neutrino field acquires mass via the Higgs mechanism as  
582 any other fermion of the SM. In this case, the neutrino mass is given by  $m_a = \frac{y_a^\nu v}{\sqrt{2}}$ ,  
583 where  $v$  is the Higgs VEV and  $y_a^\nu$  is the Yukawa coupling between the Higgs and the  
584 neutrino. The smallness of neutrino masses can only be pinned on a tiny Yukawa  
585 coupling which is not justified by the theory.

586 In 1937, Majorana demonstrated that the introduction of a two components spinor is  
587 sufficient to describe a massive fermion [91]. The Dirac equations of motion for the  
588 chiral fields (equations 1.5 and 1.6) hold true in the case of two components spinor  
589 under the assumption that the chiral components  $\psi_R$  and  $\psi_L$  are correlated through  
590 the charge conjugation matrix  $\mathcal{C}$ ,  $\psi_R = \mathcal{C}\bar{\psi}_L$ . Therefore the theory is applicable only

591 to neutral fermions. Neutrinos are the only neutral elementary particles in the SM  
 592 – the only possible Majorana particle candidate. This theory constructs a neutrino  
 593 Majorana mass term  $\mathcal{L}_5$  of the following form in the Higgs unitary gauge

$$\mathcal{L}_5 = \frac{1}{2} \frac{gv^2}{\mathcal{M}} \nu_L^T \mathcal{C}^\dagger \nu_L, \quad (1.12)$$

594 where  $g$  is the coupling coefficient,  $v$  the Higgs VEV and  $\mathcal{M}$  a constant with the  
 595 dimension of the mass proportional to the scale of new physics. The  $\mathcal{L}_5$  term would  
 596 introduce a non-renormalizable term in the lagrangian, since it has dimensions of  
 597 energy to the fifth power. This is not allowed in the SM lagrangian; however, the  
 598 existence of such terms is plausible if we consider the SM as an effective theory  
 599 at low energy, manifestation of the symmetry breaking of a more general theory at  
 600 higher energy, e.g. a Grand Unified Theory (GUT), and not the definitive theory.  
 601 The mass term in eq 1.12 implies the neutrino mass to be  $m = \frac{gv^2}{\mathcal{M}}$ . The coupling  
 602 coefficient can be of the order of any other fermion's coupling coefficient, since the  
 603 smallness of neutrino masses is achieved by the big value of the new physics mass  
 604 scale alone. This vanilla formulation is the conceptual basis for many flavors of *see-*  
 605 *saw mechanism* [121], which we will not discuss here in any detail. However, it is  
 606 fascinating how the puzzle of the neutrino mass hints to the existence of a deeper and  
 607 more complete theory.

608 From a kinematic point of view, Dirac and Majorana neutrinos satisfy the same  
 609 energy-momentum dispersion relationship. Thus, it is impossible to discern the neu-  
 610 trino nature through kinematic effects such as neutrino oscillations. Neutrinoless  
 611 double beta decay searches are the most promising way to understand the nature of  
 612 the neutrino and are therefore subject of great theoretical and experimental interest.  
 613 Observation of the lepton number violating process  $0\nu\beta\beta$  would imply neutrinos have  
 614 a Majorana component. Depending on the mass hierarchy, the theory also predicts

615  $0\nu\beta\beta$  exclusion regions and confirmation of the sole Dirac component for neutrinos [44].

617

### 618 1.3.2 Towards a more fundamental theory: GUTs

619 Despite its highly predictive power, a number of conceptual issues arise in the SM  
620 which disfavor it to be a good candidate for a fundamental theory.

621 The SM does not include a suitable dark matter candidate and a mechanisms  
622 that accounts for the baryon asymmetry of the universe. Additionally, up to a total  
623 of 25 parameters remain seemingly arbitrary and need to be fitted to data: 3 gauge  
624 couplings, 9 charged fermion masses, 3 mixing angles and one CP phase in the CKM  
625 matrix, the Higgs mass and quartic coupling,  $\theta_{QCD}$ , 3 neutrino mixing angles, 1 Dirac  
626 phase and, eventually, 2 Majorana phases.

627 From a group theory perspective, the SM has a rather complex group structure,  
628 where a gauge group is formed with the direct product of other three groups as shown  
629 in eq. 1.1. Drawing a parallel with the electroweak symmetry breaking mechanism,  
630 where the  $SU(2)_L \otimes U(1)_Y$  is recovered from  $U(1)_{EM}$ , an interesting line of simplification  
631 for the SM group structure would be to devise a similar mechanism where  
632  $SU(3)_C \otimes SU(2)_L \otimes U(1)_Y$  is recovered from an hypothetical larger group. IS THIS  
633 CORRECT? Just as the electroweak unification becomes evident at energies higher  
634 than the Higgs VEV, a direct manifestation of Grand Unification Theories (GUTs)  
635 would occur at even higher energies.

636 As the smallness of neutrino masses suggests the existence of a higher mass scale,  
637 an other, even stronger, hint to Grand Unification comes from the slope of running  
638 of the coupling constants. The coupling constants for the electromagnetic, weak and  
639 strong interactions in the SM vary as a function of the interaction energy as shown  
640 in figure 1.2; they do not exactly meet under the current experimental constraints,

<sub>641</sub> but their trend is interesting enough to push for the construction of theories where  
<sub>642</sub> perfect unification is achieved through the addition of new particles.

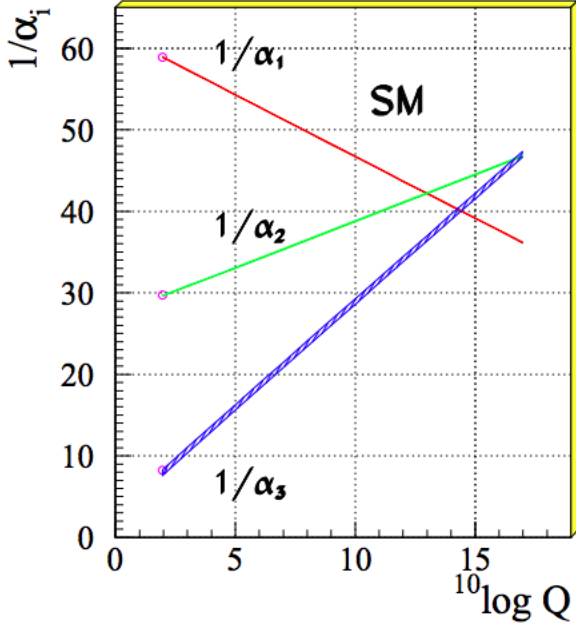


Figure 1.2: Evolution of the inverse of the three coupling constants in the Standard Model as a function of the momentum transferred, [85].

**SU(5).** The smallest simple group containing  $SU(3)_C \otimes SU(2)_L \otimes U(1)_Y$  is SU(5), as shown first by Georgi and Glashow in [68]. Quarks and leptons in this group fit the  $\bar{5}$  and 10 representations. The representation for left-handed fermions are the following

$$\bar{5} = (\nu_e, e^-)_L + \bar{d}_L \quad (1.13)$$

$$10 = e_L^+ + \bar{u}_L + (u, d)_L, \quad (1.14)$$

<sub>643</sub> while the boson structure gains a new couple of super heavy bosons (X,Y)

$$24 = \underbrace{(8, 1)}_{\text{gluons}} + \underbrace{(1, 3) + (1, 1)}_{W^\pm, Z, \gamma} + \underbrace{(3, 2) + (\bar{3}, 2)}_{X, Y \text{ bosons}}. \quad (1.15)$$

<sub>644</sub> Nice features such as charge quantization and the identity between the positron

and proton charge value come directly from the group structure. The new super heavy bosons are colored and form a weak doublet. Their are the mediator of the interaction that turns quarks into leptons, leading to predict the existence of processes that violate baryon number, such as  $p \rightarrow \pi^0 + e^+$  (see fig 1.8, right). The prediction for proton decay lifetime,  $\tau_p \sim \frac{M_X^4}{m_p^5} \sim 10^{30 \pm 1.5}$  years, is unfortunately experimentally disproved by IMB and Super-Kamiokande [4, 28].

**SO(10).** More complicated group structures, such as SO(10) are still viable candidates for GUT. SO(10) includes the same type of  $X$  and  $Y$  bosons as SU(5). Right-handed massive neutrinos are embedded in the construction of the irreducible representation of SO(10). Different patterns of SO(10) symmetry breaking to recover the SM are possible and lead to different predictions for the proton decay lifetime; some of these predictions are not excluded by the experiments [86].

**SUSY GUTs.** Supersymmetry theories allow for another family of GUTs. In SUSY, every fundamental particle in the SM has a “superpartner”, identical in each quantum number except for the spin-statistics: the fermion supersymmetric partners are bosons and vice versa. Collider experiments (mainly LHC) constrain the mass of the supersymmetric partners to be very heavy [?]. The SU(5), SU(10) groups with a SUSY twist are the basic groups for SUSY GUTs. From the phenomenology point of view, SUSY models tend to push the proton decay life time higher by a factor of four, they solve the “hierarchy problem”, and they also predict new channels for the proton decay. In particular they predict the presence of kaons in the final product, with a dominant mode of  $p \rightarrow K^+ \bar{\nu}$ . Predictions on the proton decay lifetime depend on the chosen SUSY model; again, some of the predictions are not excluded by the experiments [89, 90, 109].

669 **1.4 Motivations for Hadronic Cross Sections in Ar-**  
670 **gon**

671 Critical challenges await the next decade of high energy physics at the intensity  
672 frontier. Following the recommendation of the latest Particle Physics Project Priori-  
673 tization Panel [106], the US is dedicating substantial resources to the development of  
674 a short- and long- baseline neutrino program to address many of open questions in  
675 neutrino physics today. This program pivots on the Liquid Argon Time Projection  
676 Chamber (LArTPC) detector technology which will be described in Chapter 2.

677 The main goals of these research programs include:

- 678 - the assessment of the existence of right-handed sterile neutrinos via the study  
679 of accelerator neutrinos on a short baseline (SBN),
- 680 - the determination of the sign of  $\Delta m_{13}^2$  (or  $\Delta m_{23}^2$ ), i.e., the neutrino mass hier-  
681 archy via the study of accelerator neutrinos on a long baseline (DUNE),
- 682 - the determination of the octant, i.e. whether  $\theta_{23}$  is maximal, via the study of  
683 accelerator neutrinos on a long baseline (DUNE),
- 684 - the determination the status of CP symmetry in the lepton sector, via the study  
685 of accelerator neutrinos on a long baseline (DUNE),
- 686 - the search for observables predicted by GUTs, such as proton decay via the  
687 study of non accelerator physics in massive underground detectors (DUNE).

688 **1.4.1 Pion-Argon Total Hadronic Cross Section**

689 This section outlines the importance of the pion-argon total hadronic cross section in  
690 the context of the current and upcoming liquid argon neutrino experiments, SBN and  
691 DUNE. We describe the signal signature and historic measurements of pion-nucleus

692 cross section, as well as the implementation of these cross sections in the current  
693 version of the simulation package used by LArIAT.

694  **$\pi^-$ Ar Cross Section in the Context of Neutrino Searches**

695 As outlined in 1.2.3, neutrino experiments use the products of neutrino interactions  
696 to identify the energy and flavor of the incoming neutrino. Pions are a common  
697 product of neutrino interaction, especially in resonant scattering, DIS and coherent  
698 pion production. For neutrino experiments in argon, there are two main reasons  
699 why understanding pion hadronic interactions with argon is important: to model the  
700 behavior of the pion inside the target nucleus and to model the behavior of the pion  
701 during its propagation inside the detector medium.

702 Assumptions on the nuclear modeling and on the interaction of hadrons inside the  
703 nucleus performed at the level of the neutrino event generator bridge the measure-  
704 ment of the products of a neutrino interaction to the reconstruction of the neutrino  
705 energy and flavor. Thus, understanding pion hadronic interactions with the nucleus is  
706 particularly important to model correctly resonant, DIS and coherent pion production  
707 in neutrino interactions. For example, in case of resonant scattering,

$$\nu_l + N \rightarrow l + \Delta/N^* \rightarrow l + \pi + N', \quad (1.16)$$

708 the  $\Delta$  and  $N^*$  and excited states will decay hadronically in matters of  $\sim 10^{-24}$  s  
709 inside the nucleus producing pions which will have many chances to re-interact  
710 as they exit the target medium. The decay modes for the lower mass  $\Delta$  (1232) and  
711  $N^*(1440)$  are listed in table 1.3.

712 The key elements of a neutrino event generators for resonance and DIS events  
713 are the nuclear model and the hadron treatment (both production and transporta-  
714 tion). We illustrate here the conceptual basis of the GENIE Neutrino Generator [18]

715 as an example, since GENIE is one the most popular event generators for liquid ar-  
716 gon experiments. For example, the nuclear model used by GENIE for all processes  
717 is a Relativistic Fermi Gas (RFG) model modified to incorporate nucleon-nucleon  
718 correlations [30]. This means that the initial momentum and binding energy of the  
719 struck nucleon is determined by assuming nucleons inside the nucleus are quasi-free,  
720 acting independently in the mean field of the nucleus. For  $A > 20$  such as argon, the  
721 2-parameter Woods-Saxon shell model for density function is used. The GENIE mod-  
722 ule INTRANUKE [84] is used to simulate final-state interactions (FSI) which model  
723 hadron re-interactions inside the nucleus. This module places the outgoing parti-  
724 cles in the nucleus and propagates them using the “hA model”. In the INTRANUKE  
725 hA model, hadrons can undergo at most one FSI per event. When possible, external  
726 hadron-nucleus scattering data are used to tune INTRANUKE. Since no data is avail-  
727 able for Argon, GENIE uses an interpolation of data from heavier and lighter nuclei  
728 for the pion-argon cross section leading to large (10?s of %) resultant uncertainties in  
729 the INTRANUKE module.

730 Once the pion has left the target nucleus, the pion-argon hadronic cross section also  
731 plays an important role in the pion transportation inside the argon medium: processes  
732 such as pion absorption or pion charge exchange can greatly modify the topology of  
733 a neutrino interactions in the detector and lead to significant modifications in the  
734 event classification. Being able to reconstruct the details of pions inside the detector  
735 is an imperative for modern liquid argon neutrino experiment to achieve the design  
736 resolution for their key physics measurements.

### 737 $\pi^-$ -Ar Hadronic Interaction: Signal Signatures

738 Strong hadronic interaction models [49,69] predict the pion interaction processes with  
739 argon in the [100 - 1200] MeV energy range. The total hadronic  $\pi^-$ -Ar interaction  
740 cross section is defined as the one related to the single process driven only by the

741 strong interaction which is dominant in the considered energy range. In measuring  
742 the “total” cross section, we include both the elastic and reaction channels, regardless  
743 of the final state,

$$\sigma_{Tot} = \sigma_{Elastic} + \sigma_{Reaction}; \quad (1.17)$$

744 the reaction channel is further characterized by several exclusive channels with defined  
745 topologies,

$$\sigma_{Reaction} = \sigma_{Inelastic} + \sigma_{abs} + \sigma_{chex} + \sigma_{\pi prod}. \quad (1.18)$$

746 A summary of the pion final states in order of pion multiplicity for the reaction  
747 channel is given in table 1.4. Pion capture and pion decay at rest dominate the  
748 cross section under 100 MeV. We define pion capture as the process determining the  
749 formation of a pionic atom and the subsequent pion’s end of life. Stopping negative  
750 pions can form pionic argon, where the negative pion plays the role of an orbital  
751 electron. Since the pion mass is two orders of magnitude greater than the electron  
752 mass, the spatial wave form of the pion will overlap more with the nucleus compared  
753 to the electron case. After the electromagnetic formation of the pionic atom, the  
754 pion will get quickly absorbed by the nucleus, which is put in an excited state. The  
755 nucleus then de-excites with the emission of low energy nucleons and photons. Pion  
756 capture is dominant compared to pion decay, the other important process for very  
757 low energy pions. The decay of a pion is governed by the weak force; the pion decay  
758 life time is  $\tau_\pi = 2.6 \times 10^{-8}$  s and the main decay mode is  $\pi^- \rightarrow \mu^- + \bar{\nu}_\mu$  (BR 99.98%).  
759 Since pion capture can be considered an electromagnetic process and pion decay is a  
760 weak process, this energy region is purposely excluded from the hadronic cross section  
761 measurement.

762 **Previous measurements: Lighter and Heavier Nuclei**

763 Many experiments with pion beams have studied the hadronic interaction of pions on  
764 light and heavy materials, such as He, Li, C, Fe, Pb [36]. However, data on argon are  
765 rare: the total differential hadronic cross section has never been measured before on  
766 argon. Simulation packages such as Geant4 base their pion transportation for argon  
767 on data from lighter and heavier nuclei: the goal of LArIAT’s dedicated measurement  
768 on argon is to bridge this gap in data, thus reducing the uncertainties related to pion  
769 interactions in argon in both neutrino event generators and in simulation packages of  
770 pion transportation.

771 The shape of the pion-nucleus interaction cross section in the energy range con-  
772 sidered shows the distinct features indicating the presence of a resonance. In fact, the  
773 mean free path of a pion of kinetic energy between 100 and 400 MeV is much shorter  
774 than the average distance between nucleons (which is of the order of 1 fm). There-  
775 fore, the pion interacts with surface nucleons. A  $\Delta$  resonance is often produced in  
776 the interaction, which subsequently decays inside the nucleus. Experimental results  
777 on several nuclei as reported in [36] are shown in Figure 1.3; it is interesting to notice  
778 here how the shape of the  $\Delta$  resonance becomes less pronounced as a function of the  
779 mass number of the target nucleus. Pion interactions with heavier nuclei also shift the  
780 peak of the resonance at lower energy; this effect is due to kinematic considerations  
781 and to the difference in propagation of the  $\Delta$  inside the nucleus. Multiple scattering  
782 effect modify the resonance width, which is larger than the natural-decay width. As  
783 an example of a fairly well studied target, Figure 1.4 reports the negative pion cross  
784 section on Carbon for the elastic and reaction<sup>2</sup> channels, and their sum [55].

---

2. This paper calls “inelastic interaction” what we refer as to “reaction channel”.

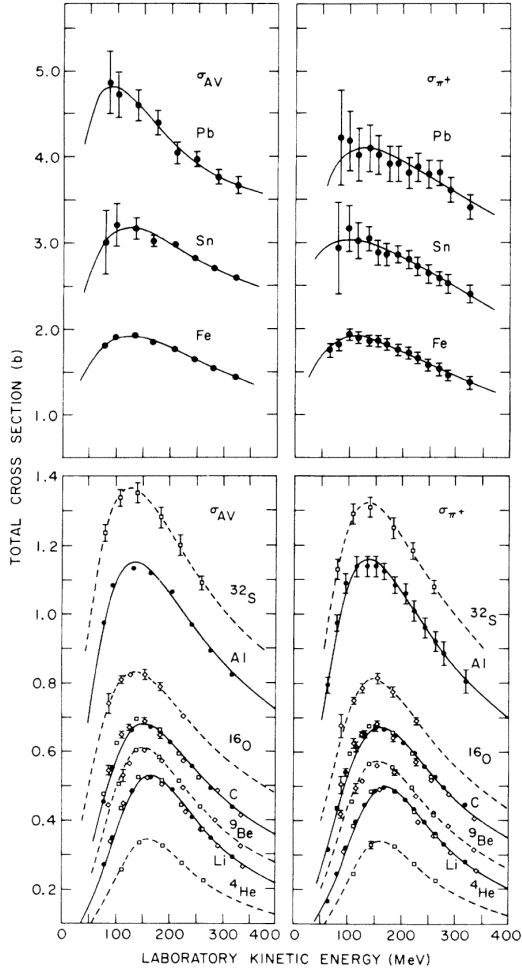


Figure 1.3: Pion-nucleus total cross sections:  $\sigma_{\pi^+}$  for positive pions (right) and  $\sigma_{AV}$  (left) for the average between positive and negative pions  $\sigma_{AV} = \frac{\sigma_{\pi^+} + \sigma_{\pi^-}}{2}$  in the  $\Delta$  resonance region. The error bars include estimates of systematic uncertainties. The curves are the results of fits to the data assuming a Breit-Wigner shape. This summary plot is reported in [36] and uses data from [52, 117].

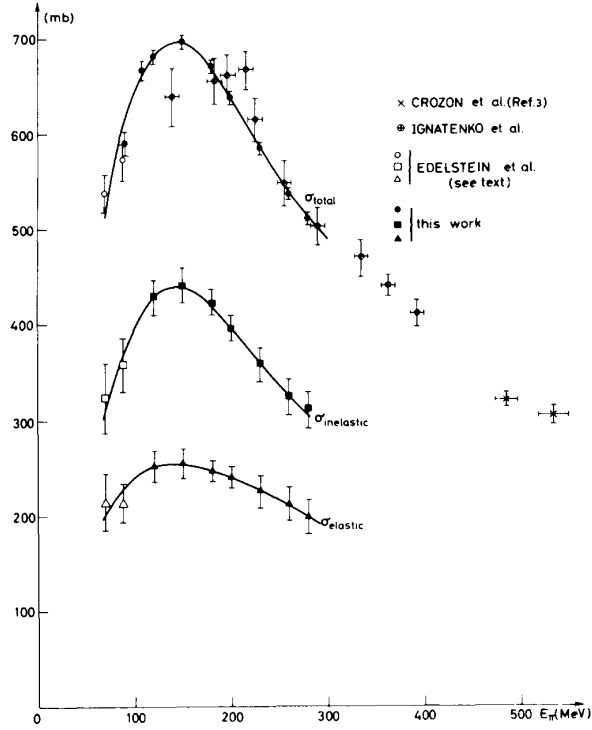


Figure 1.4: Negative pion nucleus total, elastic and reaction cross sections on  $^{12}\text{C}$  as from [55].

### 785 Negative Pion Interaction Cross Section in Simulation Packages

786 LArIAT uses Geant4 as the default simulation package. In particular, pions (and  
 787 kaons) transportation is achieved through the Geant4 FTFP\_BERT physics list. In  
 788 this physics list, Geant4 uses the Bertini cascade model [118] to simulate the products  
 789 of the pion-nucleus interaction as well as secondary hadronic re-interactions inside  
 790 the target nucleus (intra-nuclear cascade). The target nucleus is represented as a  
 791 continuous gas where the nuclear potential follows concentrical shells whose depths  
 792 approximate the Woods-Saxon shape. The CERN-HERA compilations [113, 114] of  
 793 hadron-nucleon interaction data is the data base used for the decision making process  
 794 after the cascade is invoked. The cross section model determines if the pion inter-  
 795 acts, the eventual type of interaction and the interaction multiplicity. For hadron  
 796 projectiles with energy less than 20 GeV, Geant4 reports the uncertainty on the cross

797 section model to be about the size of the error bars on the data used, or about 10%,  
798 increasing to 20-30% in energy regions where data is sparse.

799       The relevance of the GENIE generator for neutrino physics and its basic working  
800 principles have been outlined earlier in this section. Given GENIE’s modularity,  
801 information on hadron-nucleus interactions can be extracted from the INTRANUKE  
802 module and directly compared against the Geant4 predictions. The work in [97]  
803 reviews the current status of negative and positive pion simulation in Geant4 and  
804 GENIE for  $^{12}\text{C}$ ,  $^{56}\text{Fe}$ , and  $^{40}\text{Ca}$ . From that work, we report the results for  $^{12}\text{C}$  in  
805 Figure 1.5 as it allows a direct comparison between Geant4, GENIE and and pion  
806 re-scattering data. Geant4 predictions for  $\pi^-$  on Carbon are in good agreement with  
807 data over the entire spectrum spectrum, while GENIE predictions seem to show some  
808 features at around 500 MeV and 900 MeV, maybe due to higher resonances in the hA  
809 model. From the same work, we also report the negative pion cross section on  $^{40}\text{Ca}$   
810 in Figure 1.6, since this is the nuclear medium closest to argon. The predictions from  
811 both Geant4 and GENIE agree with data in the high energy region; the Geant4 and  
812 GENIE predictions diverge in the resonance region, where data is not available. These  
813 few examples highlight how cross section data for the specific nucleus considered in  
814 the neutrino experiments is fundamental to inform the Monte Carlo simulation.

815       For the LArIAT simulation of the MC sample used in the  $\pi^-$  argon total hadronic  
816 cross section measurement we use the Geant4 Bertini Cascade model, whose predic-  
817 tions for the total, elastic and reaction hadronic cross sections are show in Figure  
818 1.7.

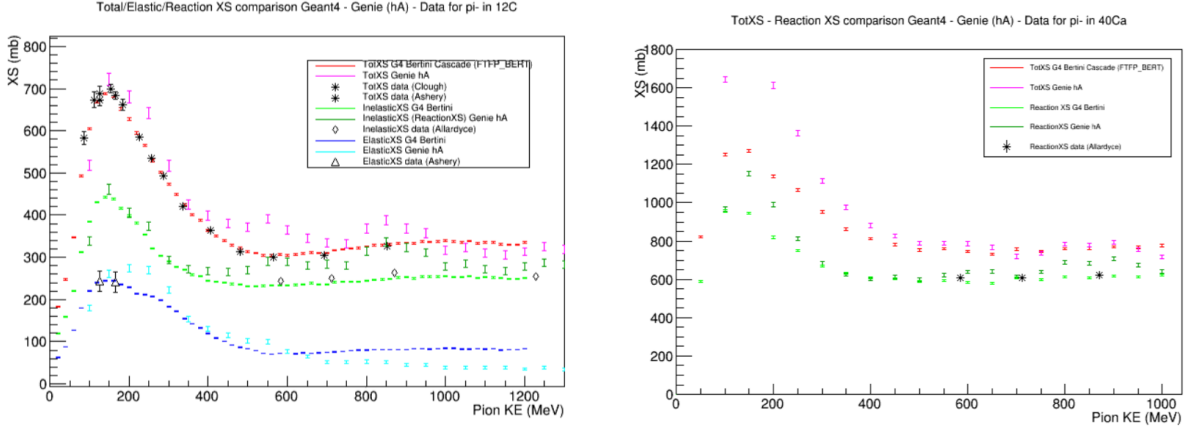


Figure 1.5: Total, elastic and reaction cross section for  $\pi^-$  on  $^{12}\text{C}$ . Comparison between results from Geant4 simulation (Bertini cascade model), Genie simulation (hA model), and experimental data [22, 52, 53, 108].

Figure 1.6: Total, elastic and reaction cross section for  $\pi^-$  on  $^{40}\text{Ca}$ . Comparison between results from Geant4 simulation (Bertini cascade model), Genie simulation (hA model), and experimental data [53].

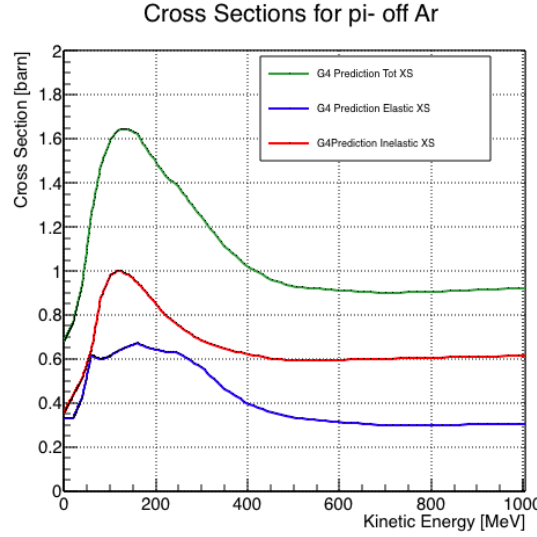


Figure 1.7: Total, elastic and reaction hadronic cross section for  $\pi^-$ -argon implemented in Geant4 10.01.p3.

Resonance	Decay Mode	Lifetime (s)
$\Delta$ (1232) $3/2^+$	$\Delta^{++}(\text{uuu}) \rightarrow p\pi^+$ $\Delta^+(\text{uud}) \rightarrow n\pi^+$ $\Delta^+(\text{uud}) \rightarrow p\pi^0$ $\Delta^0(\text{udd}) \rightarrow n\pi^0$ $\Delta^0(\text{udd}) \rightarrow p\pi^-$ $\Delta^-(\text{ddd}) \rightarrow n\pi^-$	$\sim 5.6 \times 10^{-24}$
$N^*$ (1440) $1/2^+$	$N^* \rightarrow N\pi$ $N^* \rightarrow N\pi\pi$	$\sim 2.2 \times 10^{-24}$

Table 1.3: Main decay modes of the lightest Delta resonance and Nucleon excited state.

N $\pi$ in FS	Channel Name	Reaction	Notes
0	Pion Absorption, $\sigma_{abs}$	$\pi^-(np) \rightarrow nn$ (2-body abs) $\pi^-(nnp) \rightarrow nnn$ (3-body abs) $\pi^-(npp) \rightarrow pnn$ (3-body abs) $\pi^-(nnpp) \rightarrow pmn$ (Multi-body abs)	Suppressed on single nucleon by energy conservation: the process occurs on at least two nucleons system.
1	Elastic Scattering, $\sigma_{el}$	$\pi^- + N \rightarrow \pi^- + N$	Scattering on nucleon or nucleus, the target is left in ground state
1	Charge Exchange, $\sigma_{chea}$	$\pi^- + p \rightarrow \Delta^0 \rightarrow \pi^0 + n$ $\pi^- + N \rightarrow \pi^+ +$ nucleons	Single charge exchange: charged pion converts into neutral pion  Double charge exchange: charged pion converts into opposite charge pion
1	Inelastic Scattering, $\sigma_{inel}$	$\pi^- + p \rightarrow \Delta^0 \rightarrow \pi^- + p$ (knock-out) $\pi^- + n \rightarrow \Delta^- \rightarrow \pi^- + n$ (knock-out)	Other possible reactions:  Pure Inelastic scattering: population of low energy bound excited states Nuclear break-up with nucleons or fragments knock-out
2+	Pion Production, $\sigma_{\pi prod}$	$\pi^- + N \rightarrow \geq 2\pi +$ nucleons	Possible if pion K.E $\geq 500$ MeV/c

Table 1.4: Summary of negative pion hadronic interactions of the reaction channel as a function of the pion multiplicity in the final state in the energy range [100-1200] MeV.

819 **1.4.2 Kaon-Argon Total Hadronic Cross Section**

820 This section outlines the importance of the kaon-argon total hadronic cross section.  
821 We start by discussing the measurement in the context of nucleon decay searches. We  
822 then describe the signal signature and historical measurements of kaon-nucleus cross  
823 section, as well as the implementation of this cross sections in the current version of  
824 the simulation package used by LArIAT.

825 **K<sup>+</sup>Ar Cross section in the Context of Nucleon Decay Searches**

826 Baryon number is accidentally conserved in the Standard Model. Even though no  
827 baryon number violation has been experimentally observed thus far, no underlying  
828 symmetry in line with the Noether paradigm [96] explains its conservation. As shown  
829 in section 1.3.2, almost all Grand Unified Theories predict at some level baryon num-  
830 ber violation in the form of nucleon decay on long time-scales. Given the impossibil-  
831 ity to reach grand unification energy scales with collider experiments (Energy Scale  
832 > 10<sup>15</sup> GeV), an indirect proof of GUTs is needed. The experimental observation of  
833 nucleon decay may be the only viable way to explore these theories.

834 In case of nucleon decay discovery, the dominant decay mode may uncover addi-  
835 tional information about the GUT type. Supersymmetric GUTs [24, 46] prefer the  
836 presence of kaons in the products of the decay, e.g.  $p \rightarrow K^+ \bar{\nu}$  (see fig 1.8, left).  
837 Gauge mediated GUTs, in which new gauge bosons are introduced that allow for the  
838 transformation of quarks into leptons, and vice versa, prefer the mode  $p \rightarrow e^+ \pi^0$  (see  
839 fig 1.8, right).

840 LArIAT tiny active volume makes it impossible for the experiment to place com-  
841 petitive limits on nucleon decay searches. However, LArIAT provides excellent data  
842 to characterize kaons in liquid argon for the “LAr golden mode”,  $p \rightarrow K^+ \bar{\nu}$ . The  
843 result of these studies will affect future proton decay searches in LArTPCs. Previous  
844 work has been done to assess the potential identification efficiency for different decay

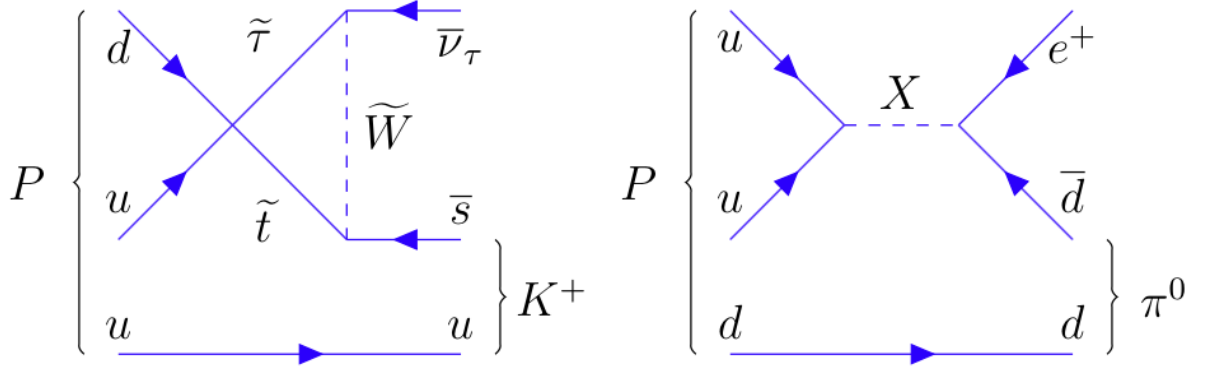


Figure 1.8: Feynman diagrams for proton decay “golden modes”:  $p \rightarrow K^+\bar{\nu}$  for supersymmetric GUTs on the left and  $p \rightarrow e^+\pi^0$  for gauge-mediated GUTs on the right.

845 modes in a LArTPC [51], but, as the time of this writing, no study of kaon selection  
 846 efficiency in LArTPCs has been performed on data. The  $K^+$ -Ar interaction cross  
 847 section has never been measured before and can affect the possibility of detecting  
 848 and measuring kaons when produced in a proton decay event. Kaon interactions with  
 849 argon can distort the kaon energy spectrum as well as change the topology of single  
 850 kaon events. In a LArTPC, non-interacting kaons appear as straight tracks with a  
 851 high ionization depositions at the end (Bragg peak). The topology of interacting  
 852 kaons can be quite different. In case of elastic scattering, a distinct kink will be  
 853 present in the track. In case of inelastic scattering the Bragg peak will not be present  
 854 and additional tracks will populate the event. Performing the total hadronic  $K^+$ -Ar  
 855 cross section measurement on data serves the double purpose of identifying the rate  
 856 of “unusual” topologies (kinks and additional tracks) and of developing tools for kaon  
 857 tracking in LAr.

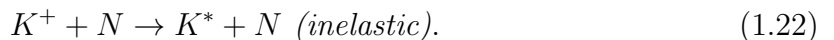
### 858 **$K^+$ Ar Hadronic Interaction: Signal Signatures**

The interaction of a mildly relativistic charged kaon with an argon nucleus is determined largely by the strong force. The total hadronic  $K^+$ -Ar interaction cross section

is defined as the one related to the single (hadronic) process driven only by the strong interaction. In this case, “total” indicates all strong interactions regardless of the final state. This condition purposefully includes both elastic and inelastic (reaction) channels. Indeed, the total cross section section can be then decomposed into

$$\sigma_{Tot} = \sigma_{Elastic} + \sigma_{Reaction}.$$

859        For the LArIAT cross section analysis, the kaons considered span a momentum  
 860      inside the TPC from 100 MeV/c to 800 MeV/c. In this energy range, the relevant  
 861      K-Nucleon interactions are according to [63]:



862      **Previous Measurements: Lighter and Heavier Nuclei**

863      In general, measurements on kaon cross sections are extremely scarce. The mea-  
 864      surement of the kaon interaction cross section would bring the additional benefit  
 865      of reducing the uncertainties associated with hadron interaction models adopted in  
 866      MC simulations for argon targets, beneficial for both proton decay studies and kaon  
 867      production from neutrino interaction studies, where the uncertainties for final state  
 868      interaction models are big [47].

869      Figure 1.9 shows a 1997 measurement on several elements as performed by Fried-  
 870      mann et al. [65]. As a reference, this paper measures a  $\sigma_{Tot}$  for Si of  $366.5 \pm 4.8$   
 871      mb and a  $\sigma_{Tot}$  for Ca of  $494.6 \pm 7.7$  mb at 488 MeV/c. The cross section for argon

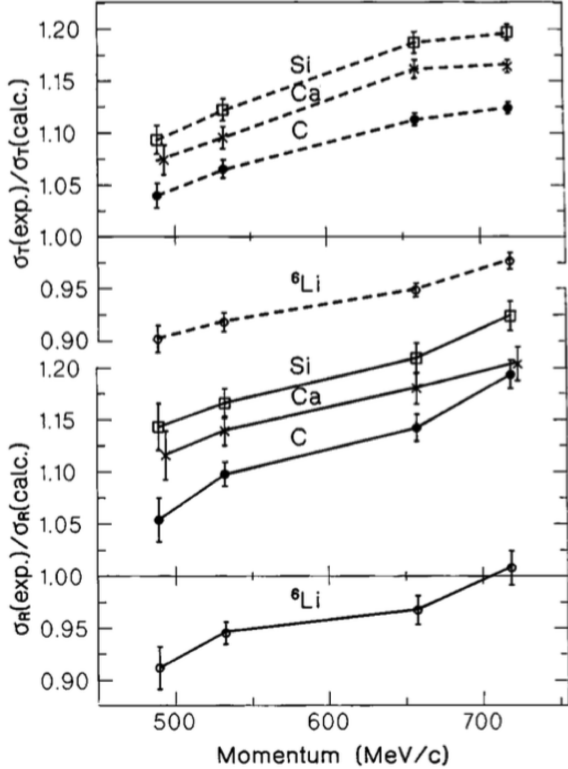


Figure 1.9: Ratios between experimental and calculated cross sections as from [65].  
Top: Total cross sections.  
Bottom: reaction cross sections.

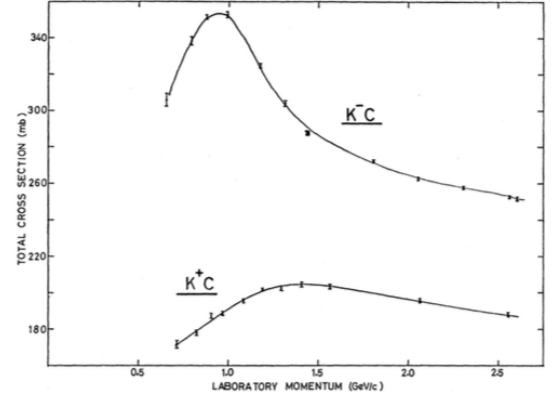


Figure 1.10: Total  $K^+$  and  $K^-$  cross sections on carbon as from [32].

is expected to lie in between these two measurements. Additional data on the kaon cross section are provided by Bugg et al. [32]. Bugg performs a measurement of the total  $K^+$  and  $K^-$  cross sections on protons and deuterons over the range of 0.6-2.65 GeV/c, as well as a measurement of the total  $K^+$  and  $K^-$  cross sections on carbon for a number of momenta; the results of this paper on carbon are reported in Figure 1.10.

### 878 Kaon Interaction Cross Section for thin target in Geant4

879 Since the kaon cross section in argon has never been measured before, simulation  
880 packages tune kaon transportation in argon by extrapolation from lighter and heavier  
881 nuclei. LArIAT uses the Geant4 suite for particle transportation. Since kaon data on

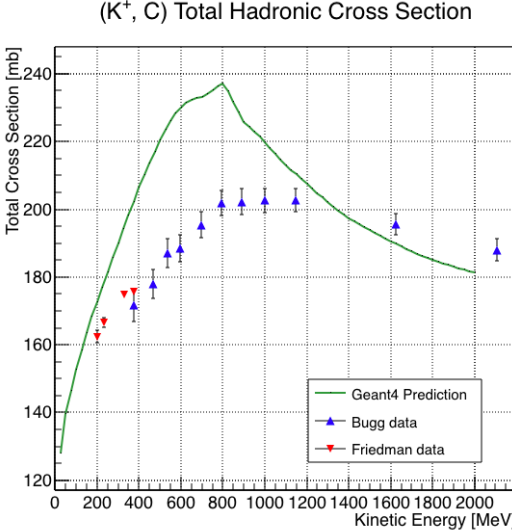


Figure 1.11: Total hadronic cross section for carbon implemented in Geant4 10.01.p3 with overlaid with the Bugg and Friedman data.

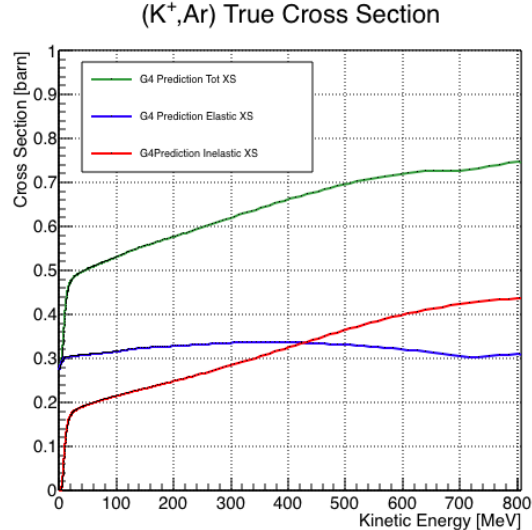


Figure 1.12: Total, elastic and reaction hadronic cross section for  $K^+$ -argon implemented in Geant4 10.01.p3.

carbon are available, we used it as a metric to evaluate the Geant4 prediction performances. Figure 1.11 shows the total hadronic cross section for carbon implemented in Geant4 10.01.p3 overlaid with the Bugg and Friedman data. Unfortunately, version 10.01.p3<sup>3</sup> of Geant4, which is the version used for the simulation in this work, does not reproduce the data for carbon closely. On one hand, this evidence makes us even more wary when using the Monte Carlo in simulating the kaon-argon interactions. On the other, it further highlights the importance of the kaon measurement. For the LArIAT simulation of the MC sample used in the  $K^+$  argon total hadronic cross section measurement we use the Geant4 Bertini Cascade model, whose predictions for the total, elastic and reaction hadronic cross sections are show in Figure 1.12.

---

3. It should be noted that the latest Geant4 version, 10.03.p3, uses a different parametrization for the kaon cross section and retrieves a better agreement with data.

892 **Chapter 2**

893 **Liquid Argon Detectors at the**  
894 **Intensity Frontier**

895 “*Don’t you know, honey,*  
896 *Ain’t nobody ever gonna love you, the way I try to do?*”  
897 – Janis Joplin, 1971 –

898 In the next few years, LArTPCs will be the tools to answer some of the burning  
899 questions in neutrino physics today. This chapter illustrates the operational principles  
900 of this detector technology, as well as the scope of the key detectors in the US liquid  
901 argon program – SBN, DUNE and LArIAT.

902 **2.1 The Liquid Argon Time Projection Chamber**  
903 **Technology**

904 In this section, we outline an extremely brief history of Time Projection Chambers  
905 as particle detectors, focusing on their incarnation as Argon detectors for neutrino  
906 physics. We further describe the working principles of Liquid Argon Time Projection

907 Chambers, leading to the description of the event reconstruction in LArTPC.

### 908 2.1.1 TPCs, Neutrinos & Argon

909 David Nygren designed the first Time Projection Chamber (TPC) in the late 1970s [98]  
910 for the PEP-4 experiment, a detector apt to study electron-positron collisions at the  
911 PEP storage ring at the SLAC National Accelerator Laboratory. From the original  
912 design in the seventies – a cylindrical chamber filled with methane gas – the TPC  
913 detector concept has seen many incarnations, the employment of several different  
914 active media and a variety of different particle physics applications, including, but  
915 not limited to the study of electron/positron storage rings (e.g. PEP4, TOPAZ,  
916 ALEPH and DELPHI), heavy ions collisions in fixed target and collider experiments  
917 (e.g. EOS/HISSL and ALICE ), dark matter (ArDM), rare decays and capture (e.g.  
918 TRIUMF, MuCap), neutrino detectors and nucleon decay (ICARUS, SBN, DUNE),  
919 and neutrino less double beta decay (Next). A nice review of the history of TPCs  
920 and working principles is provided in [77].

921 Several features of the TPC technology make these detectors a more versatile tool  
922 compared to other ionization detectors and explain such a wide popularity. TPCs are  
923 the only electronically read detector which deliver simultaneous three-dimensional  
924 track information and a measurement of the particle energy loss. Leveraging on both  
925 tracking and calorimetry, particle identification (PID) capabilities are enhanced over  
926 a wide momentum range.

927 Historically, the active medium in ionization detectors has been in the gaseous  
928 form. Carlo Rubbia first proposed the use of a Liquid Argon TPC for a neutrino  
929 experiment, ICARUS [107], in 1977. Using nobles elements in the liquid form for  
930 neutrino detectors is advantageous for several reasons. The density of liquids is  $\sim$ 1000  
931 times greater than gases, augmenting the number of targets for neutrino's interaction  
932 in the same volume, in a effort to balance the smallness of neutrino cross section. Since

Element	LAr	LXe
Atomic Number	18	54
Atomic weight A	40	131
Boiling Point Tb at 1 atm	87.3 K	165.0 K
Density	1.4 g/cm <sup>3</sup>	3.0 g/cm <sup>3</sup>
Radiation length	14.0 cm	2.8 cm
Moliere Radius	10.0 cm	5.7 cm
Work function	23.6 eV	15.6 eV
Electron Mobility at $E_{field} = 10^4$ V/m	0.047 m <sup>2</sup> /Vs	0.22 m <sup>2</sup> /Vs
Average dE/dx MIP	2.1 MeV/cm	3.8 MeV/cm
Average Scintillation Light Yield	40000 $\gamma$ /MeV	42000 $\gamma$ /MeV
Scintillation $\lambda$	128 nm	175 nm

Table 2.1: LAr, LXe summary of properties relevant for neutrino detectors.

the energy loss of charged particle is proportional to the target material density, as shown in the Bethe-Block equation (eq. 2.1), the increased density reflects into a proportionally higher energy loss, enhancing the calorimetry capability of detectors with a liquid active medium. Additionally, the ionization energy of liquids is smaller than gasses by the order of tens of eV. Thus, at the passage of charged particles, liquids generally produce more ionization electrons than gases for the same deposited energy, forcing the particles to deposit more energy in a shorter range. The downside of using noble liquid elements in experiments is that they require expensive cryogenic systems to cool the gas until it transitions to its the liquid form. The properties of liquid argon in comparison liquid xenon – a popular choice for dark matter and neutrinoless double beta decay detectors – are summarized in table 2.1. Albeit xenon would be more desirable than argon given some superior properties such as lower ionization energy and higher density and light yield, argon relative abundance abates the cost of argon compared to xenon, making argon a more viable choice for the construction of ton (and kilo-ton) scale neutrino detectors.

LArTPCs are some times referred as to “electronic” bubble-chambers, for the similarity in the tracking and energy resolution which is coupled with an electronic readout of the imaging information in LArTPCs. Compared to these historic detectors

951 however, LArTPC bestow tridimensional tracking and a self triggering mechanism  
 952 provided by the scintillation light in the liquid argon. An event display of a  $\nu_\mu$  CC  
 953 interaction candidate in the MicroBooNE detector is shown in picture 2.1 to display  
 954 the level of spatial details these detectors are capable of; the color scale of the image  
 955 is proportional to the energy deposited, hinting to these calorimetry capabilities of  
 the detectors.

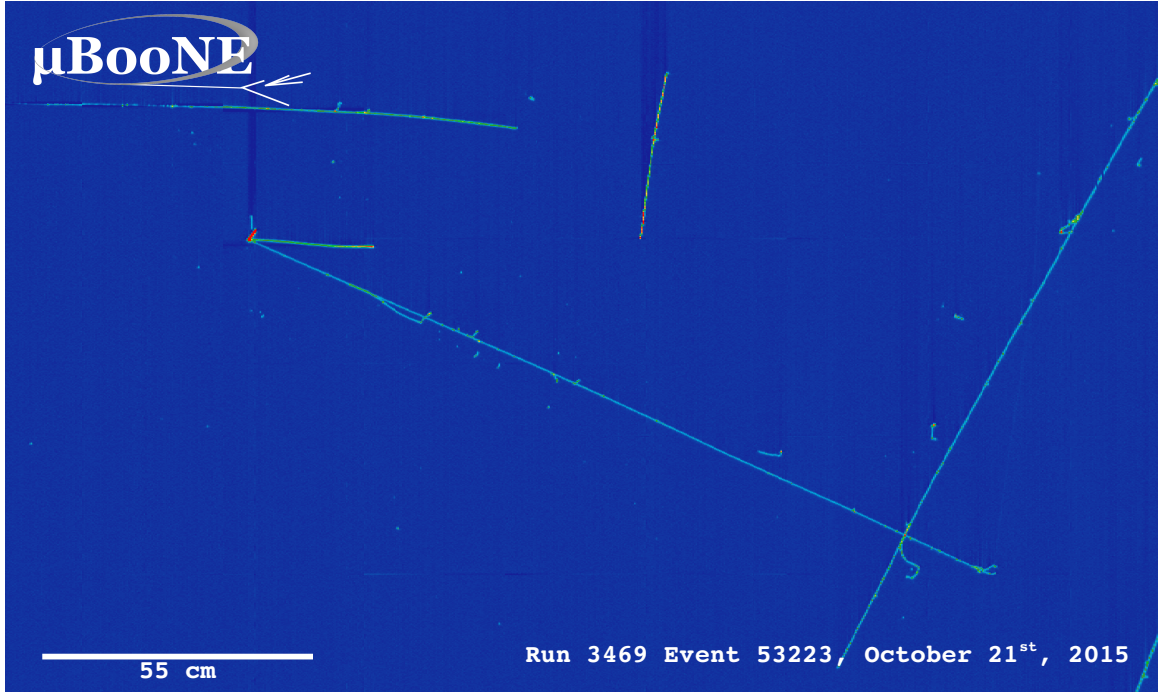


Figure 2.1: Event display of a  $\nu_\mu$  CC interaction candidate in the MicroBooNE detector.

956

### 957 2.1.2 LArTPC: Principles of Operation

958 To the bare bones, a LArTPC is a bulk of liquid argon sandwiched in a flat capacitor,  
 959 equipped with a light collection system, as the cartoon in 2.2 shows. A uniform  
 960 electric field of the order of 500 V/cm is maintained constant between the faces of the  
 961 capacitor. The anode is sensitive to ionization charge and it is usually made of two  
 962 or more planes segmented into several hundreds parallel sense wires a few millimeters  
 963 apart; different geometries for the anode segmentation are under study [48].

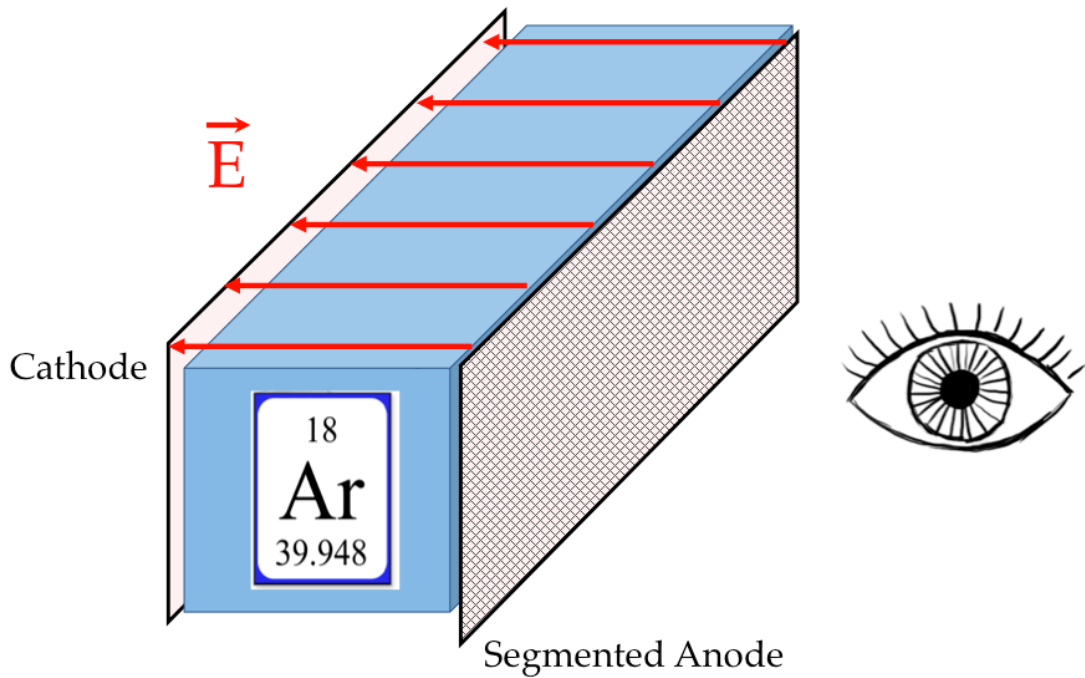


Figure 2.2: A cartoonish sketch of a LArTPC.

Argon ionization and scintillation are the processes leveraged to detect particles in the LArTPC active volume. When a ionizing radiation traverses the argon active volume it leaves a trail of ionization electrons along its trajectory and it excites the argon producing scintillation light – details on the production and detection of ionization charge and scintillation light are provided in 2.1.4 and 2.1.4 respectively. The optical detector sees the argon scintillation light in matters of nanoseconds. This flash of light determines the start time of an event in the chamber,  $t_0$ . The uniform electric field drifts the ionization electrons from the production point towards the anode in order of hundreds of microseconds or more depending on the chamber dimensions<sup>1</sup>. The anode sense wires see either an induced current by the drifting ionization charge (on induction planes) or an injection of such charge (collection

---

1. The ionized argon also drifts, but in the opposite directions compared to the electrons. Since the drift time is proportional to the particle mass, the ions' drift time is much longer than the electrons'. Ionized argon is collected on the cathode which is not instrumented, so it is not used to infer information about the interactions in the chamber.

975 plane). An appropriate choice of the voltage bias on each wire plane assures ideal  
976 charge transparency, so that all the ionization charge is collected on the collection  
977 plane and none on the induction planes.

978       The arrival time of the charge on the anode sense wires is used to measure the  
979 position of the original ionizing radiation in the drift direction. In fact, since the  
980 constant electric field implies that the drift velocity is also constant, the position of  
981 the original ionization is simply given by the multiplication of the drift velocity by the  
982 drift time, where the “drift time” is the difference between  $t_0$  and the charge arrival  
983 time on the wire planes. The spacial resolution on this dimension is limited by the  
984 time resolution of the electronics or by longitudinal diffusion of the electrons. The  
985 spatial information on the different wire planes maps a bi-dimensional projection of  
986 the interaction pattern in the plane perpendicular to the drift direction. The spacial  
987 resolution on this dimension is limited by the transverse electron diffusion in argon  
988 and by the grain of the anode segmentation, i.e. the spacing between the wires in  
989 the sense planes [45]. The off-line combination of the 2-D information on the wire  
990 planes with the timing information allows for the 3D reconstruction of the event in  
991 the chamber.

992       Since the charge deposited by the ionizing radiation is proportional to the de-  
993 posited energy and the charge collected on the sense plane is a function of the de-  
994 posited charge, LArTPCs allow the measurement of the energy deposit in the active  
995 volume. Effects due to the presence of free charge and impurities in the active vol-  
996 ume, such as a finite electron lifetime, recombination and space charge, complicate  
997 the relationship between deposited and collected charge affecting the measurement of  
998 the particle’s energy, as described in the next section.

### 999 2.1.3 Liquid Argon: Ionization Charge

1000 The mean rate of energy loss by moderately relativistic elementary charge particles  
 1001 heavier than electrons is well described by the modified Bethe-Bloch [101] equation

$$-\frac{dE}{dx} = K z^2 \frac{Z}{A} \varrho \frac{1}{\beta^2} \left[ \frac{1}{2} \ln \frac{2m_e c^2 \beta^2 \gamma^2 T_{max}}{I^2} - \beta^2 - \frac{\delta}{2} \right], \quad (2.1)$$

1002 where  $z$  is the number of unit charge of the ionizing radiation,  $Z$ ,  $A$  and  $\varrho$  are the  
 1003 atomic number, mass number and density of the medium,  $m_e$  is the electron mass,  
 1004  $\gamma = \frac{\beta}{\sqrt{1-\beta^2}}$  is the Lorentz factor of the ionizing radiation,  $T_{max}$  is the maximum kinetic  
 1005 energy which can be imparted to a free electron in a single collision,  $I$  is the mean  
 1006 excitation energy on eV,  $\delta$  is the density correction and  $K = 0.307075 \text{ MeV g}^{-1} \text{ cm}^2$  is  
 1007 a numerical conversion factor. The Bethe-Bloch treats the energy loss by an ionizing  
 1008 radiation via quantum-mechanical collisions producing ionization or an excitation in  
 1009 the medium as an uniform and continuous process. The density correction terms  
 1010 becomes relevant for incident particle with high energy, where screening effects due  
 1011 to the polarization of the medium by high energy particles occur.

1012 Excitation and ionization of the detector medium occur in similar amounts. Since  
 1013 the ionizing collisions occur randomly, we can parametrize their number  $k$  in a segment  
 1014 of length  $s$  along the track with a Poissonian function

$$P(k) = \frac{s^k}{k! \lambda^k} e^{-s/\lambda}, \quad (2.2)$$

1015 where  $\lambda = 1/N_e \sigma_i$ , with  $N_e$  being the electron density of  $\sigma_i$  the ionization cross-  
 1016 section per electron. About 66% of the ionizing collisions in Argon produce only  
 1017 a single electron/ion pair [77]; in the other cases, the transferred kinetic energy is  
 1018 enough for the primary electron to liberate one or more secondary electrons, which  
 1019 usually stay close to the original pair. Occasionally, electrons can receive enough

1020 energy to be ejected with high energy, forming a so-called “ $\delta$ -ray”: a detectable short  
1021 track off the particle trajectory, as shown in figure 2.3. The average number of  $\delta$ -ray  
1022 with energy  $E > E_0$  per cm follows the empirical form

$$P(E > E_0) \sim \frac{y}{\beta^2 E_0}, \quad (2.3)$$

1023 where  $y$  is an empirical factor depending on the medium (0.114 for gaseous Ar), and  
1024  $\beta$  is  $v/c$ .

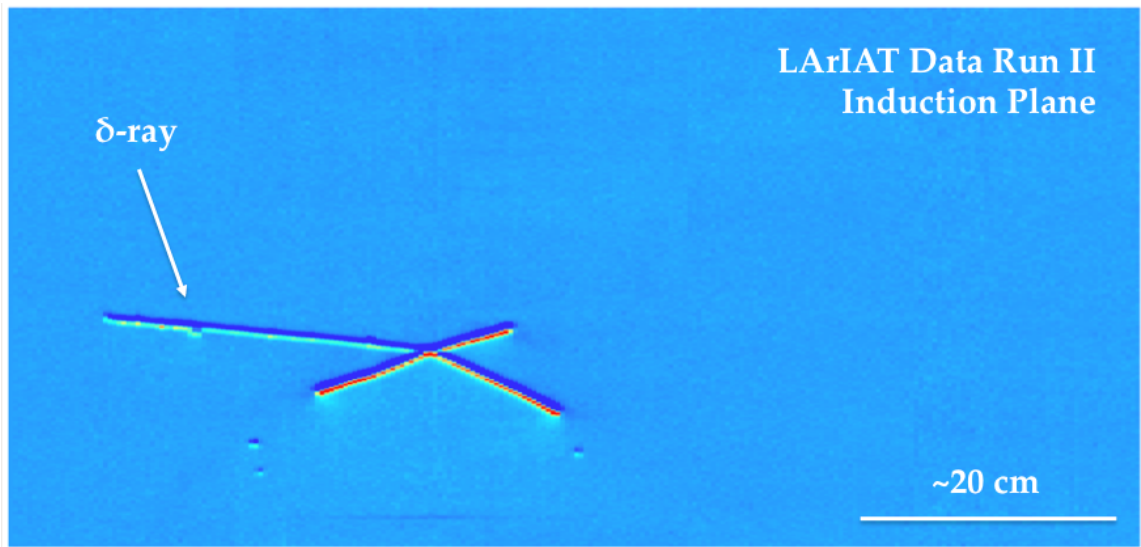


Figure 2.3: Events display for a LArIAT pion absorption candidate on the induction plane, with highlighted delta ray.

## 1025 Purity & Electron Life Time

1026 The presence of electronegative contaminants in liquid argon, such as oxygen  $O_2$   
1027 and water  $H_2O$ , is particularly pernicious, since these molecules quench the charge  
1028 produced by the ionizing radiation. Thus, amount of charge per unit of length  $dQ/dx$   
1029 collected on the collection plane depends on the charge's production point in the  
1030 detector: ionization produced close to the cathode will see more impurities along its  
1031 journey to the collection plane than ionization produced close to the anode, resulting

1032 in greater attenuation of its charge. As a result, the amount of charge collected on  
 1033 the sense wires as a function of the traveled distance follows an exponential decay  
 1034 trend. The traveled distance is generally measured in terms of drift time and the  
 1035 characteristic time constant of the exponential decay is called electron lifetime  $\tau_e$ .  
 1036 Figure 2.4 shows the typical life time for LArIAT data. The procedure to measure  
 1037 the electron lifetime in LArIAT is outlined in [104]. LArIAT small drift distance (47  
 1038 cm) allows for a relatively short electron life time. The life time for bigger detectors  
 1039 such as MicroBooNE, whose drift distance is 2.6 m, needs to be of the order of  
 1040 tens of milliseconds to allow a charge collection usable for physics analyses. Energy  
 1041 reconstruction in LArTPC applies a correction for the finite lifetime to calibrate the  
 1042 detector calorimetric response; details for LArIAT are provided in Section C.

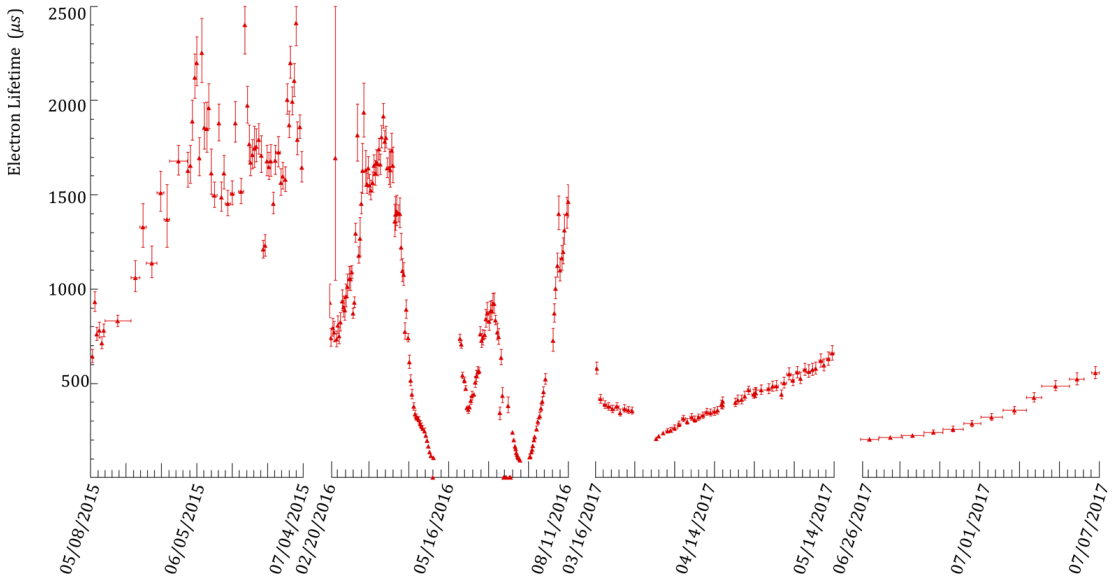


Figure 2.4: Electron lifetime during the LArIAT run period [43].

1043 LArTPCs use hermetically sealed and leak-checked vessels to abate the leakage  
1044 and diffusion of contaminants into the system. The liquid argon filling of the volume  
1045 occurs after the vessel is evacuated or purged with gaseous argon [10] to reduce re-  
1046 maining gases in the volume. Even so, the construction of a pure tank of argon is  
1047 unviable, as several sources of impurity remain. In particular, impurities can come  
1048 from the raw argon supply, the argon filtration system and from the outgassing from  
1049 internal surfaces. Outgassing is a continuous diffusive process producing contami-  
1050 nants, especially water, even after the vessel is sealed, particularly from materials in  
1051 the ullage region<sup>2</sup>. Since research-grade argon comes from the industrial distillation  
1052 of air, the impurities with the highest concentration are nitrogen, oxygen and water,  
1053 generally maintained under the 1 part per million level by the vendor. Even so, a  
1054 higher level of purity is necessary to achieve a free electron life time usable in meter  
1055 scale detectors. Thus, argon is constantly filtered in the cryogenic system, which  
1056 reduce the oxygen and water contamination to less than 100 parts per trillion. The  
1057 filtration system depends on the size and drift distance of the experiment and, for  
1058 experiments on several meters scale, it includes an argon recirculation system.

## 1059 Recombination Effect

1060 After production, ionization electrons thermalize with the surrounding medium and  
1061 may recombine with nearby ions. Recombination might occur either between the  
1062 electron and the parent ion through Coulomb attraction, as described in the geminate  
1063 theory [99], or thanks to the collective charge density of electrons and ions from  
1064 multiple ionizations in a cylindrical volume surrounding the particle trajectory, as  
1065 described in the columnar model [80]. Consideration on the average electron-ion  
1066 distance and the average ion-ion distance for argon show that the probability of

---

2. While the liquid argon low temperature reduces outgassing in the liquid, this process remains significant for absorptive material (such as plastic) above the surface of the liquid phase.

1067 geminate recombination is low; thus recombination in argon is mainly due to collective  
1068 effects [5]. Since protons, kaons and stopping particles present a higher ionization  
1069 compared to MIPs, recombination effects are more prominent when considering the  
1070 reconstruction of energy deposited by these particles.

1071 Theoretical descriptions of recombination based on the Birks model and the Box  
1072 model are provided in [29] and [112], respectively. The Birks model assumes a gaus-  
1073 sian spatial distribution around the particle trajectory during the entire recombina-  
1074 tion phase and identical charge mobility for ions and electrons. The Box model also  
1075 assumes that electron diffusion and ion mobility are negligible in liquid argon during  
1076 recombination. In these models, the fraction of ionization electrons surviving recom-  
1077 bination is a function of the number of ion-electron pairs per unit length, the electric  
1078 field, the average ion-electron separation distance after thermalization and the angle  
1079 of the particle with respect to the direction of the electric field – plus the diffusion  
1080 coefficient in the Birks model. Given the stringent assumptions, it is perhaps not sur-  
1081 prising that these models are in accordance to data only in specific regimes: the Birks  
1082 model is generally used to describe recombination for low  $dE/dx$ , the Box model for  
1083 high  $dE/dX$ . In LArTPC, the ICARUS and ArgoNeut experiments have measured  
1084 recombination in [16] and [5] respectively. Since LArIAT uses the refurbished Ar-  
1085 goNeut TPC and cryostat at the same electric field, LArIAT currently corrects for  
1086 recombination using the ArgoNeut measured recombination parameters in [5].

## 1087 Space Charge Effect

1088 Slow-moving positive argon ions created during ionization can build-up in LArTPC,  
1089 causing the distortion of the electric field within the detector. This effect, called  
1090 “space charge effect” leads to a displacement in the reconstructed position of the  
1091 signal ionization electrons. In surface LArTPCs the space charge effect is primarily  
1092 due to the rate of ionization produced by cosmic rays which is slowly drifting in the

1093 chamber at all times. Surface LArTPC of the size of several meters are expected  
1094 to be modestly impacted from the space charge effect, where charge build-up create  
1095 anisotropy of the electric field magnitude of the order of 5% at a drift field of 500  
1096 V/cm [93]. The smallness of the LArIAT drift volume and its relatively high electric  
1097 field are such that the effect of space charge is expected to be negligible.

### 1098 **2.1.4 Liquid Argon: Scintillation Light**

1099 Liquid argon emits scintillation light at the passage of charged particles. LArTPCs  
1100 leverage this property to determine when the ionization charge begins to drift towards  
1101 the anode plane.

#### 1102 **Scintillation Process**

1103 Scintillation light in argon peaks in the ultraviolet at a 128 nm, shown in comparison  
1104 to Xenon and Kypton in Figure 2.5, from [94]. The light yield collected by the optical  
1105 detector depends on the argon purity, the electric field, the dE/dx and particle type,  
1106 averaging at the tens of thousands of photons per MeV.

1107 The de-excitation of Rydberg dimers in the argon is responsible for the scintillation  
1108 light. Rydberg dimers exist in two states: singlets and a triplets. The time constant  
1109 for the singlet radiative decay is 6 ns, resulting in a prompt component for the scin-  
1110 tillation light. The decay of the triplet is delayed by intersystem crossing, producing  
1111 a slow component with a time constant of  $\sim$  1500 ns. “Self-trapped exciton lumines-  
1112 cence” and “recombination luminescence” are the two processes responsible for the  
1113 creation of the Rydberg dimers [83]. In the first process, a charged particle excites an  
1114 argon atom which becomes self-trapped in the surrounding bulk of argon, forming a  
1115 dimer; the dimer is in the singlet state 65% of the times and in the triplet state 35%  
1116 of the times. In case of recombination luminescence, the charged particle transfers  
1117 enough energy to ionize the argon. The argon ion forms a charged argon dimer state,

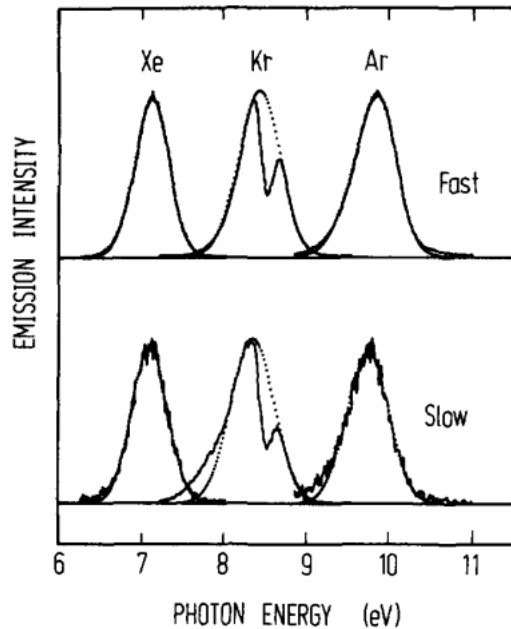


Figure 2.5: Emission spectra of the fast and slow emission components in Xenon, Krypton and Argon according to [94]. The dotted lines correspond to the Gaussian fits.

which quickly recombines with the thermalized free electron cloud. Excimer states  
 are produced in the recombination, roughly half in the singlet and half in the triplet  
 state. The light yield dependency on the electric field, on the  $dE/dx$  and particle  
 type derives from the role of free charge in the recombination luminescence process.  
 The spacial separation between the argon ions and the free electron cloud depends on  
 the electric field. On one hand, a strong electric field diminishes the recombination  
 probability, leading to a smaller light yield; on the other, it increases the free charge  
 drifting towards the anode plane. Hence, the amount of measurable charge and light  
 anti-correlates as a function of the electric field. Ionizing particles in the argon mod-  
 ify the local density of both free electrons and ions depending on their  $dE/dx$ . Since  
 the recombination rate is proportional to the square of the local ionization density,  
 highly ionizing particles boost recombination and the subsequent light yield compared  
 to MIPs. The possibility to leverage this dependency for pulseshape-based particle  
 identification has been shown in [31, 88].

1132 **Effects Modifying the Light Yield**

1133 The production mechanism through emission from bound excimer states implies that  
1134 argon is transparent to its own scintillation light. In fact, the photons emitted from  
1135 these metastable states are not energetic enough to re-excite the argon bulk, greatly  
1136 suppressing absorption mechanisms. In a LArTPC however, several processes modify  
1137 the light yield in between the location where light is produced and the optical detector.  
1138 In a hypothetical pure tank of argon, Rayleigh scattering would be the most important  
1139 processes modifying the light yield. Rayleigh scattering changes the path of light  
1140 propagation in argon, prolonging the time between light production and detection.  
1141 The scattering length has been measured to be 66 cm [78] , shorter than the theoretical  
1142 prediction of  $\sim 90$  cm [111]; this value is short enough to be relevant for the current  
1143 size of LArTPCs detectors. In fact, Rayleigh scattering worsen the resolution on  $t_0$ ,  
1144 the start time for charge drifting, and alters the light directionality, complicating the  
1145 matching between light and charge coming from the same object in case of multiple  
1146 charged particles in the detector.

1147 Traces of impurities in argon such as oxygen, water and nitrogen also affect the  
1148 light yield, mainly via absorption and quenching mechanisms. Absorption occurs as  
1149 the interaction of a 128 nm photon directly with the impurity dissolved in the liquid  
1150 argon. Differently, quenching occurs as the interaction of an argon excimer and an  
1151 impurity, where the excimer transfers its excitation to the impurity and dissociates  
1152 non-radiatively. Given this mechanism, it is evident how quenching is both a function  
1153 of the impurity concentrations and the excimer lifetime. Since the triplet states  
1154 live much longer than the singlet states, quenching occurs mainly on triplet states,  
1155 affecting primarily the slow component of the light, reducing the scintillation yield  
1156 and a shortening of the scintillation time constants.

1157 The stringent constraints for the electron life time limit the presence of oxygen and  
1158 water to such a low level that both absorption and quenching on these impurity is not

1159 expected to be significant. Contrarily, the nitrogen level is not bound by the electron  
1160 life time constraints – nitrogen being an inert gas, expensive to filter. Thus, nitrogen  
1161 is often present at the level provided by the vendor. The effects of nitrogen on argon  
1162 scintillation light have been studied in the WArP R&D program and at several test  
1163 stands. The quenching process induced by nitrogen in liquid Ar has been measured  
1164 to be proportional to the nitrogen concentration, with a rate constant of  $\sim 0.11$   
1165  $\mu\text{s}^{-1}$  ppm $^{-1}$ ; appreciable decreasing in lifetime and relative amplitude of the slow  
1166 component have been shown for contamination as high as a few ppm of nitrogen [6].  
1167 For a nitrogen concentration of 2 parts per million, typical of the current generation  
1168 of LArTPC, the attenuation length due to nitrogen has been measured to be  $\sim 30$   
1169 meters [82].

## 1170 **Wavelength Shifting of LAr Scintillation Light**

1171 Liquid argon scintillation light is invisible for most optical detectors deployed in a  
1172 LArTPC, such as cryogenic PMTs and SiPMs, since a wavelength of 128 nm is gen-  
1173 erally too short to be absorbed from most in glasses, polymers and semiconductor  
1174 materials. Research on prototype SiPMs absorbing directly VUV light and their  
1175 deployment in noble gasses experiment is ongoing but not mature [120]. Thus, ex-  
1176 periments need to shift the wavelength of scintillation light to be able to detect it.  
1177 Albeit deployed in different ways, neutrinos and dark matter experiments commonly  
1178 use 1,1,4,4-tetraphenyl-butadiene (TPB) to shift the scintillation light. TPB absorbs  
1179 the vacuum ultraviolet (VUV) light and emits in the visible at  $\sim 425$  nm [33], with  
1180 a ratio of visible photon emitted per VUV photon absorbed of  $\sim 1.2:1$  [66].

1181 Neutrino experiments typically coat their optical detector system evaporating a  
1182 layer of TPB either directly on the PMTs glass surface or on acrylic plates mounted in  
1183 front of the PMTs [60]; this technique allows the fast detection light coming directly  
1184 from the neutrino interaction. Dark matter experiments typically evaporate TPB on

1185 reflective foils mounted on the inside walls of the sensitive volume and detect the  
1186 light after it has been reflected; this technique leads to a higher and more uniform  
1187 light yield, though scattering effects for both the visible and VUV light augment  
1188 the propagation time and hinder directionality information [61]. In order to take  
1189 advantage of both these techniques, hybrid systems with PMT coating and foils are  
1190 being considered for the next generation of large neutrino detectors.

### 1191 2.1.5 Signal Processing and Event Reconstruction

1192 In this section we illustrate the processing and reconstruction chain of the TPC sig-  
1193 nals, from the pulses on the sense wire to the construction of three dimensional objects  
1194 with associated calorimetry. Different experiments can chose different software pack-  
1195 ages for their off line signal processing and event reconstruction, but a popular choice  
1196 for US based LArTPCs is LArSoft [40]. Based on the Art framework [72], LArSoft is  
1197 an event-based toolkit to perform simulation, analysis and reconstruction of LArT-  
1198 PCs events.

1199

1200 LArTPC signal processing develops in several consecutive stages that we summa-  
1201 rize here in the following categories: *Deconvolution, Hit Reconstruction, 2D Cluster-*  
1202 *ing, 3D Tracking, Calorimetry Reconstruction*. A visualization of the signal processing  
1203 workflow is shown in figure 2.6.

1204

1205 **Deconvolution.** Induction and collection planes have different field responses,  
1206 given the different nature of the signals on these planes: the wires on the induction  
1207 planes see the inductive signal of the drifting charge, while the wires on the collection  
1208 planes see the current derived from the charge entering the conductor. Thus, signals  
1209 on the induction plane are bi-polar pulse and signal on the collection plane are unipo-  
1210 lar pulses, see Figure 2.6 panel a). The first step in signal processing is deconvolution,

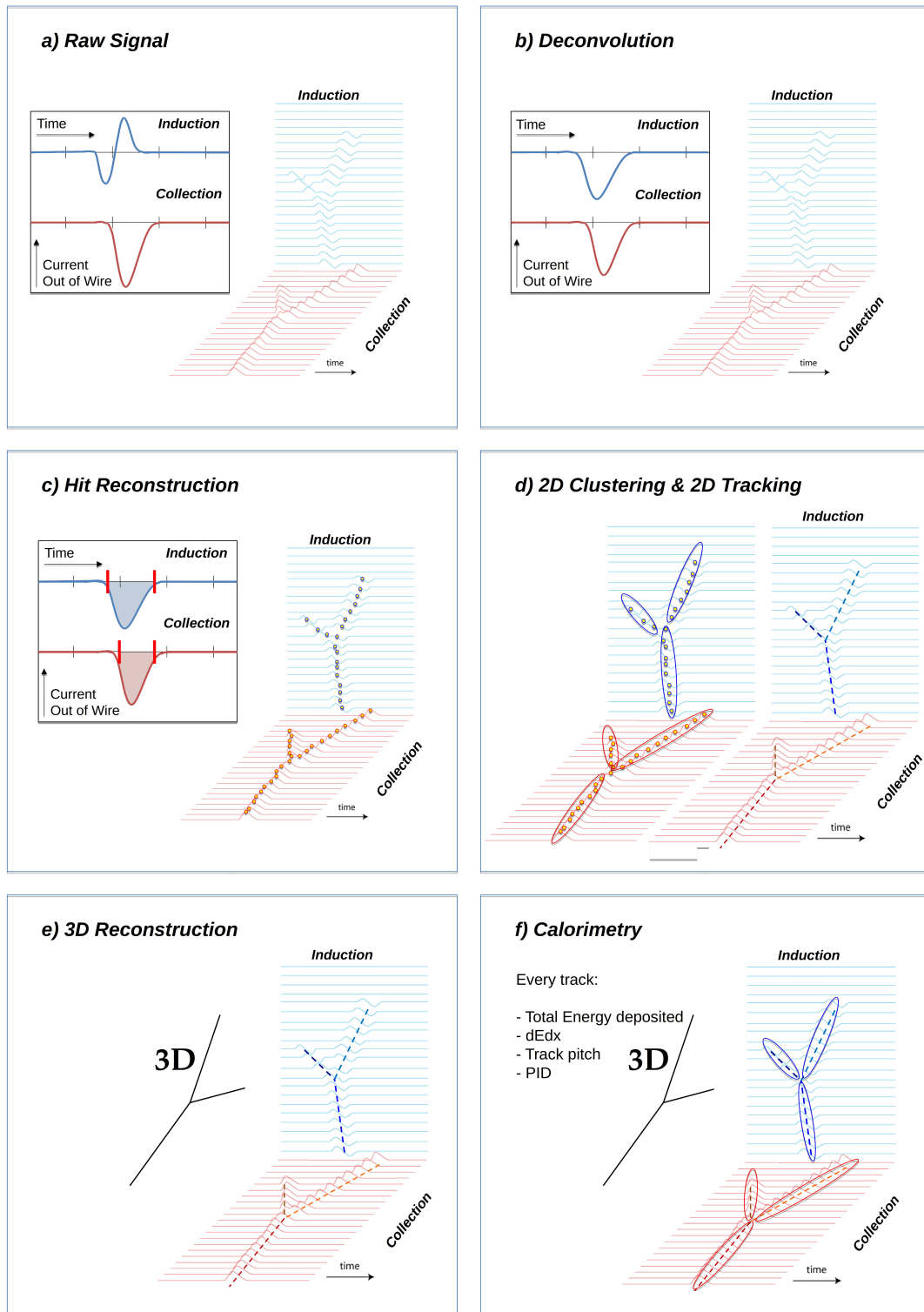


Figure 2.6: A scheme of a typical signal processing workflow in LArSoft.

1211 that is a series of off-line algorithms geared towards undoing the detector effects. The  
1212 result of the deconvolution step is the production of a comparable set waveforms on  
1213 all planes presenting unipolar, approximately gaussian-like pulses (Figure 2.6 panel  
1214 b). Signal from all planes are treated on equal footage beyond this point. Some  
1215 LArTPC apply noise filtering in the frequency domain just after the deconvolution  
1216 to clean up wire cross talk. Since signals from the LArIAT TPC are extremely clean,  
1217 noise filtering is not necessary.

1218

1219 **Hit Reconstruction.** The second stage of the signal processing is the recon-  
1220 struction of hits, indicating an energy deposition in the detector. A peak finder scans  
1221 the deconvolved TPC waveforms for each wire on the whole readout time looking for  
1222 spikes above the waveform’s baseline. It then fits these peaks with gaussian shapes  
1223 and stores the fit parameters such as the quality of the fit, the peak time, height and  
1224 area under the gaussian fit. The information resulting from this process on a single  
1225 spike form a single reconstructed “hit”, see Figure 2.6 panel c). The next steps in  
1226 the event reconstruction chain will then decide if rejecting hits with poor fits. It is  
1227 important to notice how the height and width of the hit depend on the topology of  
1228 the event: for example, a particle running parallel to the wire planes will leave a series  
1229 of sharp hits on many consecutive wires, while a particle traveling towards the planes  
1230 will leave a long, wide hit on very few wires. The height of the hits and their integral  
1231 is proportional to the charge collected on the wire, so it depends on the particle type.

1232

1233 The event reconstruction chain uses collection of hits to form more complex objects  
1234 associated with the particles in the detector. The development of different approaches  
1235 to accomplish this task is an extremely hot topic in LArTPC event reconstruction  
1236 which spans from more traditional approaches such as line-clustering [26] to the use of  
1237 machine learning tools [59]. Generally speaking, the scope of hit clustering and event

1238 reconstruction to provide shower-like or track like-objects with an associated energy  
1239 reconstruction. This is because different particles have different topology in the de-  
1240 tector – electrons and photon create electromagnetic showers, resulting in shower-like  
1241 topologies, while muons and hadrons leave track-like signals. For the scope of these  
1242 thesis, we will describe only LArIAT’s approach to track reconstruction even if we  
1243 recognize the breath of LArTPC event reconstruction is much wider. We are inter-  
1244 ested in the reconstruction of pions and kaons in the active volume, whose topology  
1245 is track-like.

1246

1247 **2D Clustering Reconstruction.** The LArIAT reconstruction of track-like ob-  
1248 jects starts by clustering hits on the collection and induction planes separately with  
1249 the use of the TrajCluster clustering package [25]. TrajCluster looks for a collection  
1250 of hits in the wire-time 2D space which can be described with a line-like 2D trajec-  
1251 tory. TrajCluster reconstructs trajectories by adding trajectory points to the leading  
1252 edge of the trajectory while stepping through the 2D space of hits. Several factors  
1253 determine whether a hit is added to the trajectory, including but not limited to

- 1254 1. the goodness of the fit of the single hit,
- 1255 2. the charge of the hit compared to the average charge and RMS of the hits  
1256 already forming the trajectory,
- 1257 3. the goodness of trajectory fit with and without the hit addition,
- 1258 4. the angle between the two lines formed by the collection of hits before and after  
1259 the considered hit in the trajectory.

1260 The final product of this reconstruction stage is the collection of bidimensional clusters  
1261 on each wire plane, see Figure 2.6 panel d).

1262 **3D Tracking.** The 3D tracking set of algorithms uses clusters close in time on  
1263 the induction and collection planes as starting point to form a 3D track. Firstly, it

1264 construct a tentative 3D trajectory using the edges of the clusters. Then, it projected  
1265 back the tentative trajectory on to the planes and adjusts the parameters of the 3D  
1266 track fit such that they minimize the distance between the fit projections and the  
1267 track hits in all wire planes simultaneously. Tridimensional tracking can use multiple  
1268 clusters in one plane, but it can never break them in smaller groups of hits. This  
1269 algorithm was first developed for the ICARUS collaboration [20]. The final product  
1270 of this reconstruction stage is the formation of tridimensional objects in the TPC  
1271 active volume, see Figure 2.6 panel e).

1272

1273 **Calorimetry.** The last step in the event reconstruction chain is to assign calorimetric  
1274 information to the track (or shower) objects. Calorimetry is performed separately on the different planes. A multi-step procedure is needed to retrieve the energy  
1275 deposited in the TPC from the charge seen by the wires. For each hit associated with  
1276 the track object, the calorimetry algorithms calculate the charge seen on every wire  
1277 using the area underneath the gaussian fit; then, they correct this raw charge by the  
1278 electron life time, the electronic noise on the considered wire and the recombination  
1279 effect. Lastly an overall calibration of the energy, explained in detail in section C,  
1280 is applied and the calorimetric information for the given track is assigned. Even if  
1281 calorimetry is done in 2D, it benefits from the 3D tracking information; typical information available after the calorimetric reconstruction are the total energy deposited  
1282 by the particle and its stopping power  $dE/dx$  at each “track pitch”, i.e. at each 2D  
1283 projection on the wire plane of the 3D trajectory.

## 1286 2.2 The Intensity Frontier Program

1287 This section highlights the role of Liquid Argon Time Projection Chambers at the  
1288 Intensity frontier. In particular, we show the prospects for the exploration of neutrino

1289 physics (Section 2.2.1) and GUT models (Section 2.2.2) in current and forthcoming  
1290 LAr experiments. In Section , we introduce LArIAT and its role in the Intensity  
1291 Frontier panorama.

1292 **2.2.1 Prospects for LArTPCs in Neutrino Physics: SBN and**  
1293 **DUNE**

1294 The ArgoNeut experiment [17] together the LAr R&D experiments TallBo and the  
1295 Yale TPC initiated the US LArTPC neutrino program. Following the success of the  
1296 ArgoNeut small TPC on the NuMI beam, a wide program of LArTPCs on neutrino  
1297 beams has flourished. The construction of LArTPCs as near and far detectors at  
1298 different baseline allows for the exploration of some of the fundamental questions in  
1299 neutrino physics today illustrated in section 1.3.1.

1300 The Short-Baseline Neutrino (SBN) [21] program at Fermilab is tasked with con-  
1301 clusively assess the nature of the “LSND and MiniBooNE anomalies” [14, 15, 23],  
1302 resolving the mystery of sterile neutrinos at the eV<sup>2</sup> scale. The SBN program entails  
1303 three surface LArTPCs positioned on the Booster Neutrino Beam at different dis-  
1304 tances from the neutrino production in oder to fully exploit the L/E dependence of  
1305 the oscillation pattern: SBND (100 m from the decay pipe), MicroBooNE (450 m),  
1306 and ICARUS (600 m). Within the oscillation context, the choice of the LArTPC tech-  
1307 nology for the SBN detectors changes the set of systematics with respect to LSND  
1308 and MiniBooNE, whose detection techniques were both based on Cherenkov light.  
1309 In particular, LArTPCs provide excellent electron/photon separation [9] lacking in  
1310 Cherenkov detectors which can be leveraged to abate the photon background from  
1311 neutral current interactions in  $\nu_e$  searches. MicroBooNE [8], the first detector of the  
1312 SBN program to be fully operational, started its first neutrino run in October 2015.  
1313 MicroBooNE is a 89 ton active volume LArTPC, single drift chamber with TPC di-  
1314 mensions of 2.6 m (drift) x 2.3 m (heigh) x 10.4 m (depth). MicroBooNE is positioned

1315 at a very similar L/E on the Booster neutrino beam as MiniBooNE has the scope to  
1316 directly cross check the MiniBooNE oscillation measurement. In case MicroBooNE  
1317 confirms the presence of the “low energy excess” anomaly, SBND and ICARUS will  
1318 provide the full measurement of the oscillation parameters. SBND and ICARUS are  
1319 both dual drift chambers, whose active volume is respectively 112 ton and 600 ton.  
1320 ICARUS is scheduled to become operational by the end of 2018 and SBND shortly  
1321 after. Besides the oscillation analysis, the second main goals of SBN is to perform  
1322 an extensive campaign of neutrino cross section measurements in argon. Given the  
1323 importance of nuclear effects in (relatively) heavy materials, as discussed in section  
1324 1.2.3, both the oscillation analysis of the SBN program and the measurements of  
1325 neutrino properties in DUNE will benefit from such a campaign.

1326 On a different neutrino beam and baseline, the DUNE experiment, née LBNE [11],  
1327 is the flagship experiment on the medium-long term of US-based neutrino physics,  
1328 scheduled to start data taking in 2026. Shooting neutrinos from Fermilab for 800 miles  
1329 to the SURF laboratory in South Dakota, DUNE is tasked with performing conclusive  
1330 measurements of CP violation in the lepton sector, the neutrino mass ordering and  
1331 the  $\theta_{23}$  octant. The DUNE far detector will count four 10 kton LArTPCs, roughly of  
1332 dimensions of 19 m (horizontally) x 18 m (vertically) x 66 m (depth).

### 1333 2.2.2 Prospects for LArTPCs in GUT Physics: DUNE

1334 The experimental exploration of a manifestation of Grand Unified Theory is possible  
1335 in DUNE thanks to its sheer mass. In particular, proton decay searches are a capital  
1336 topic of DUNE’s wide non-accelerator physics program. The key elements for a  
1337 rare decay experiment are: massive active volume, long exposure, high identification  
1338 efficiency and low background. Figure 2.7 shows the current best experimental limits  
1339 on nucleon decay lifetime over branching ratio (dots). Historically, the dominant  
1340 technology used in these searches has been water Cherenkov detectors: all the best

1341 experimental limits on every decay mode are indeed set by Super-Kamiokande [?, ?].  
 1342 As shown in section 1.3.2, different family of GUTs predict the proton to decay in  
 1343 different modes. In particular, SUSY flavored GUTs prefer the presence of kaons  
 1344 in the decay products, e.g.  $p \rightarrow K^+ \bar{\nu}$ . It is particularly important to notice that  
 1345 the kaon energy for the proton decay mode  $p \rightarrow K^+ \bar{\nu}$  is under Cherenkov threshold  
 1346 in water. Thus, Super-Kamiokande set the limit on the lifetime for the  $p \rightarrow K^+ \bar{\nu}$   
 1347 mode by relying on photons from nuclear de-excitation and on the muon tagging in  
 1348 the kaon decay leptonic mode. For this reason, an attractive alternative approach to  
 1349 identifying nucleon decay is the use of a LArTPCs, where the kaon is directly visible  
 1350 in the detector. According to [11], DUNE will have an active volume large enough,  
 1351 have sufficient shielding from the surface, and will run for lengths of time sufficient  
 1352 to compete with Hyper-K, opening up the opportunity for the discovery of nucleon  
 1353 decay.

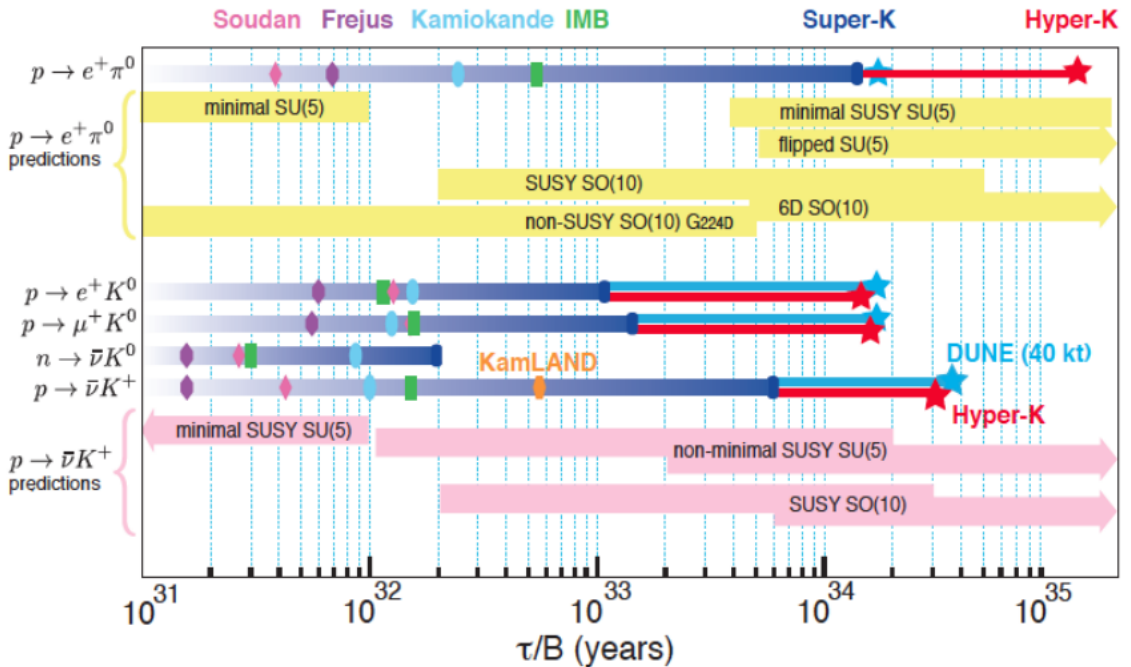


Figure 2.7: Proton decay lifetime limits from passed and future experiments.

### 1354 2.2.3 Enabling the next generation of discoveries: LArIAT

1355 LArIAT, a small LArTPC in a test beam, is designed to perform an extensive physics  
1356 campaign centered on charged particle cross section measurements while characteriz-  
1357 ing the detector performance for future LArTPCs. Since LArTPCs represent the most  
1358 advanced experiments for physics at the Intensity Frontier, their complex technology  
1359 needs a thorough calibration and dedicated measurements of some key quantities to  
1360 achieve the precision required for the next generation of discoveries. LArIAT’s goal  
1361 is to provide such calibration and dedicated measurements. The LArIAT LArTPC is  
1362 deployed in a dedicated calibration test beamline at Fermilab. We use the LArIAT  
1363 beamline to characterize the charge particles before they enter the TPC: the particle  
1364 type and initial momentum is known from beamline information. The precise calori-  
1365 metric energy reconstruction of the LArTPC technology enables the measurement of  
1366 the total differential cross section for tagged hadrons. The Pion-Nucleus and Kaon-  
1367 Nucleus total hadronic interaction cross section have never been measured before in  
1368 argon and they are a fundamental step to shed light on light meson interaction in nu-  
1369 clei per se, while providing a key input to neutrino physics and proton decay studies  
1370 in future LArTPC experiments like SBN and DUNE.

1371 In order to showcase LArIAT’s utility to SBN and DUNE, we illustrate briefly  
1372 two comparisons as examples: one regarding neutrino interactions and the second  
1373 regarding proton decay studies.

1374 The left side of figure 2.8 shows the distribution of products in momentum spectrum  
1375 and particle type as simulated in a  $\nu_e$  CC interaction in DUNE (according to [87]);  
1376 the range of these distribution is to compare with the momentum distribution of  
1377 light particles in the LArIAT beamline – shown on the right side of figure 2.8. The  
1378 momentum spectrum in the LArIAT beamline for electrons, muons and pions – the  
1379 most abundant particles produced in a  $\nu_e$  CC interaction – covers a wide range of the  
1380 expected momentum distribution in a neutrino event.

1381        The signature of a proton decay event in the “LAr golden mode” is the presence of  
 1382        a single kaon of about 400 MeV in the detector; the momentum spectrum of the kaon  
 1383        pre and post FSI in such an event as simulated by GENIE is shown on the left side  
 1384        of figure 2.9. The right side of figure 2.9 shows the momentum spectrum of kaons in  
 1385        the LArIAT beamline. Kaons arriving to the LArIAT TPC are ideal for proton decay  
 1386        studies, since their momentum in the beamline is just above the typical momentum  
 1387        for kaons in a proton decay event: the majority of LArIAT kaons slow down in the  
 1388        TPC enough to enter the desired momentum window.

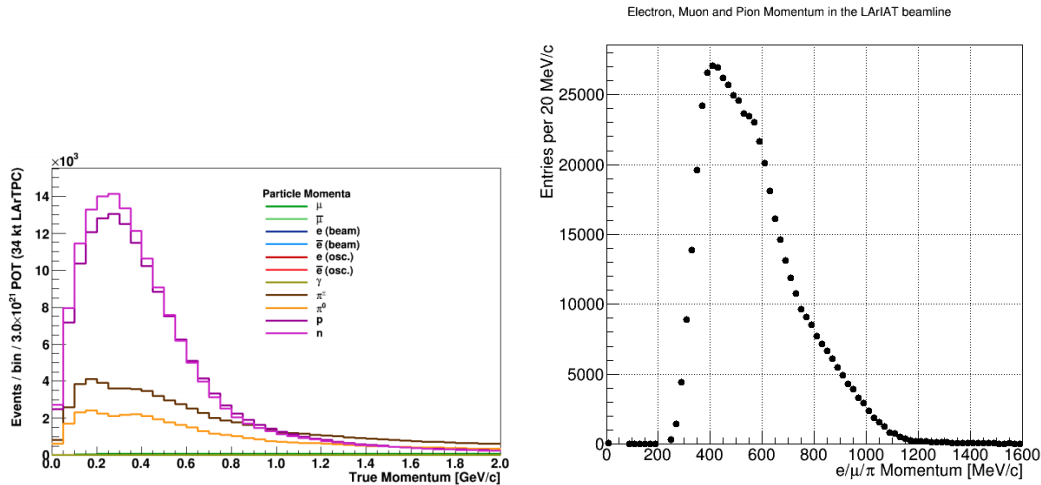


Figure 2.8: *Left.* Simulation of the products of a  $\nu_e$  CC interaction in DUNE, both in particles type and momentum.  
*Right.* Momentum spectrum for low mass particles ( $e, \mu, \pi$ ) in the LArIAT beamline, negative tune, Run II, Picky Tracks see section 3.2.2.

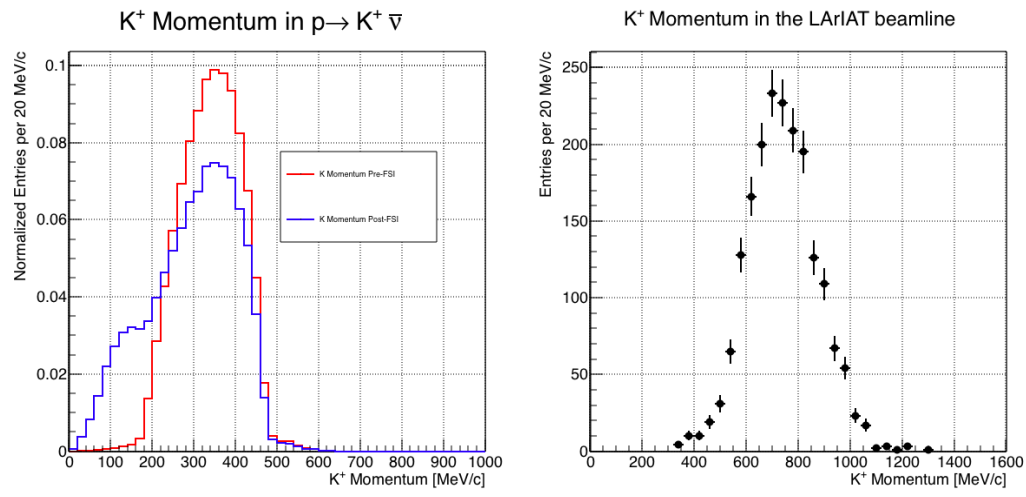


Figure 2.9: *Left.* Momentum of the kaon outgoing a proton decay  $p \rightarrow K^+ \bar{\nu}$  event as simulated by the Genie 2.8.10 event generator in argon. The red line represents the kaon momentum distribution before undergoing the simulated final state interaction inside the argon nucleus, while the blue line represents the momentum distribution after FSI.

*Right.* Positive Kaon momentum spectrum in the LArIAT beamline, positive tune, Run II, Picky Tracks see section 3.2.2.

1389 **Chapter 3**

1390 **LArIAT: Liquid Argon In A**

1391 **Testbeam**

1392 “*But, hey we need to be somewhat foolish...*”

1393 – Agnes Obel, 2010 –

1394 In this chapter, we describe the LArIAT experimental setup. We start by illus-  
1395 trating the journey of the charged particles in the Fermilab accelerator complex, from  
1396 the gaseous thermal hydrogen at the Fermilab ion source to the delivery of the LAr-  
1397 IAT tertiary beam at MC7. We then describe the LArIAT beamline detectors, the  
1398 LArTPC, the DAQ and the monitoring system.

1399 **3.1 The Particles’ Path to LArIAT**

1400 LArIAT’s particle history begins in the Fermilab accelerator complex with a beam of  
1401 protons. The process of proton acceleration develops in gradual stages (see picture  
1402 3.1): gaseous hydrogen is ionized in order to form  $H^-$  ions; these ions are boosted  
1403 to 750 keV by a Cockcroft-Walton accelerator and injected into the linear accelerator  
1404 (Linac) that increases their energy up to 400 MeV; then,  $H^-$  ions pass through a

1405 carbon foil and lose the two electrons; the resulting protons are then injected into a  
1406 rapid cycling synchrotron, called the Booster; at this stage, protons reach 8 GeV of  
1407 energy and are compacted into bunches; the next stage of acceleration is the Main  
1408 Injector, a synchrotron which accelerates the bunches up to 120 GeV; in the Main  
1409 Injector, several bunches are merged into one and are ready for delivery.

1410 The Fermilab accelerator complex works in supercycles of 60 seconds in duration.  
1411 A 120 GeV primary proton beam with variable intensity is extracted in four-second  
1412 “spills” and sent to the Meson Center beam line.

1413 LArIAT’s home at Fermilab is the Fermilab Test Beam Facility (FTBF), where  
1414 the experiment characterizes a beam of charged particles in the Meson Center beam  
1415 line. At FTBF, the primary beam is focused onto a tungsten target to create LAr-  
1416 IAT’s secondary beam. The secondary beamline is set such that the composition of  
1417 the secondary particle beam is mainly positive pions. The momentum peak of the  
1418 secondary beam was fixed at 64 GeV/c for the LArIAT data considered in this work,  
1419 although the beam is tunable in momentum between 8-80 GeV/c; this configuration  
1420 of the secondary beamline assured a stable beam delivery at the LArIAT experimental  
1421 hall.

1422 The secondary beam impinges then on a copper target within a steel collimator  
1423 inside the LArIAT experimental hall (MC7) to create the LArIAT tertiary beam,  
1424 (shown in Fig. 3.2). The steel collimator selects particles produced with a 13° pro-  
1425 duction angle. The particles are then bent by roughly 10° through a pair of dipole  
1426 magnets. By configuring the field intensity of the magnets we allow the particles of  
1427 LArIAT’s tertiary beam to span a momentum range from 0.2 to 1.4 GeV/c. The  
1428 polarity of the magnet is also configurable and determines the sign of the beamline  
1429 particles which are focused on the LArTPC. If the magnet polarity is positive the  
1430 tertiary beam composition is mostly pions and protons with a small fraction of elec-  
1431 trons, muons, and kaons. It is the job of the LArIAT beamline equipment to select the

## Fermilab Accelerator Complex

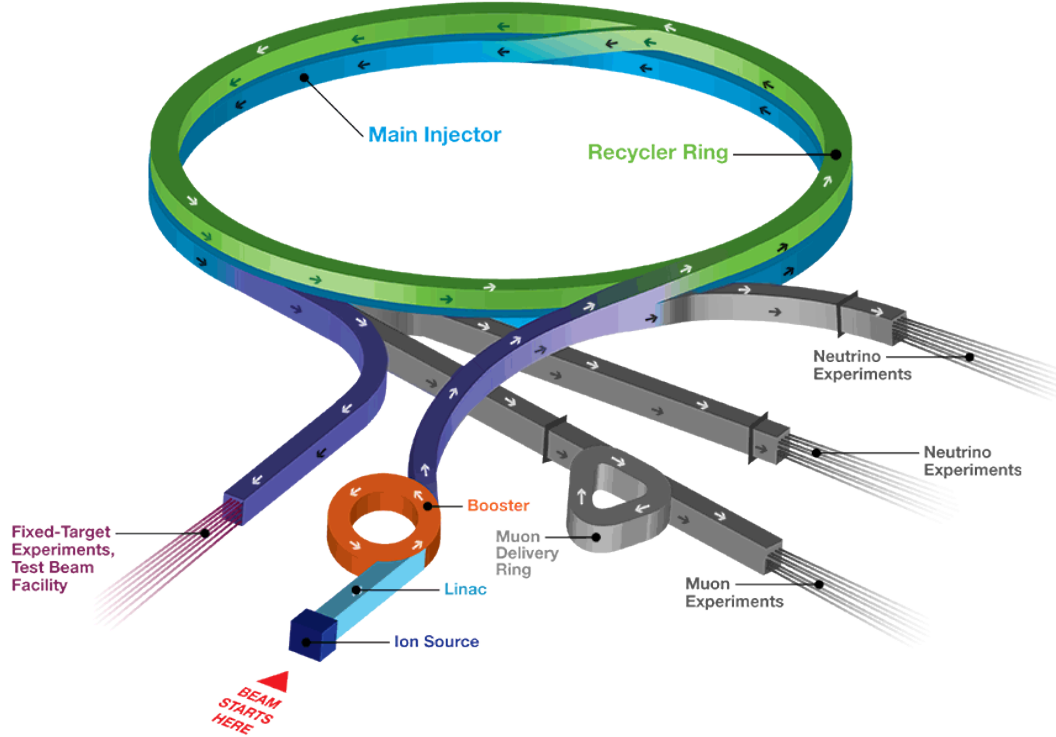


Figure 3.1: Layout of Fermilab Accelerator complex.

1432 particles polarity, to perform particle identification in the beamline and to measure  
1433 the momentum of the tertiary beam particles before they get to the LArTPC. The  
1434 LArIAT detectors are described in the following paragraphs.

### 1435 3.2 LArIAT Tertiary Beam Instrumentation

1436 The instrumentation of LArIAT tertiary beam and the TPC components have changed  
1437 several times during the three years of LArIAT data taking. The following paragraphs  
1438 describe the components operational during “Run II”, the data taking period relevant  
1439 to the hadron cross section measurements considered in this thesis.

1440 The key components of the tertiary beamline instrumentation for the hadron cross  
1441 section analyses are the two bending magnets, a set of four wire chambers (WCs)

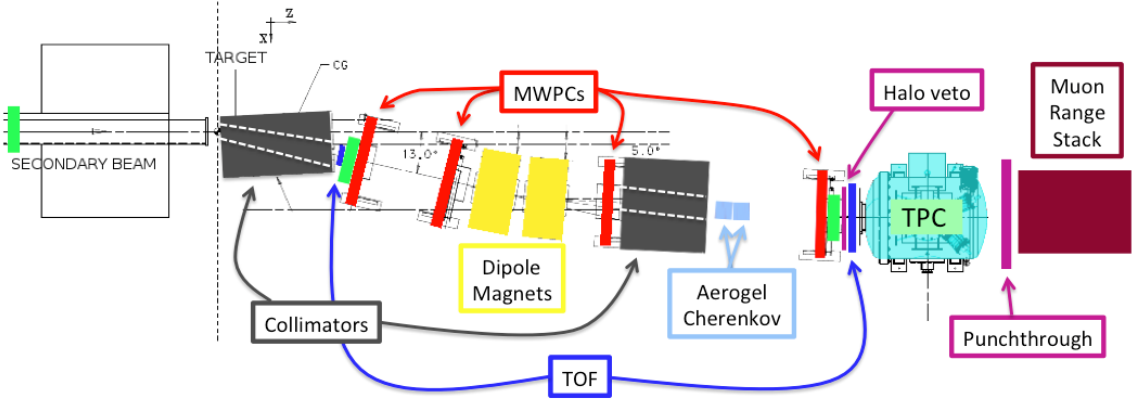


Figure 3.2: Bird’s eye view of the LArIAT tertiary beamline. In grey: upstream and downstream collimators; in yellow: bending magnets; in red: multi wire proportional chambers; in blue: time of flight; in green: liquid argon TPC volume; in maroon: muon range stack.

and two time-of-flight scintillating paddles (TOF) and, of course, the LArTPC. The magnets determine the polarity of the particles in the tertiary beam; the combination of magnets and wire chambers determines the particles’ momenta, which is used to determine the particle species in conjunction with the TOF. A muon range stack downstream from the TPC and two sets of cosmic paddles configured as a telescope surrounding the TPC are also used for calibration purposes. A couple of Aerogel Cherenkov counters, which we will not describe here as they are not used in the hadron cross section measurements, completes the beamline instrumentation.

### 3.2.1 Bending Magnets

LArIAT uses a pair of identical Fermilab type “NDB” electromagnets, recycled from the Tevatron’s anti-proton ring, in a similar configuration used for the MINERvA T-977 test beam calibration [56]. The magnets are a fundamental piece of the LArIAT beamline equipment, as they are used for the selection of the particle polarity and for the momentum measurement before the LArTPC. The sign of the current in the magnets allows us to select either positively or negatively charged particles; the value

1457 of the magnetic field is used in the momentum determination and in the subsequent  
1458 particle identification.

1459 We describe here the characteristics and response of one magnet, as the second one  
1460 has a similar response, given its identical shape and history. Each magnet is a box with  
1461 a rectangular aperture gap in the center to allow for the particle passage. The magnet  
1462 aperture measures 14.22 cm in height, 31.75 cm in width, and 46.67 cm in length.  
1463 Since the wire chambers aperture ( $\sim 12.8 \text{ cm}^2$ ) is smaller than the magnet aperture,  
1464 only the central part of the magnet gap is utilized. The field is extremely uniform  
1465 over this limited aperture and was measured with two hall probes, both calibrated  
1466 with nuclear magnetic resonance probes. The probes measured the excitation curve  
1467 shown in Figure 3.3.

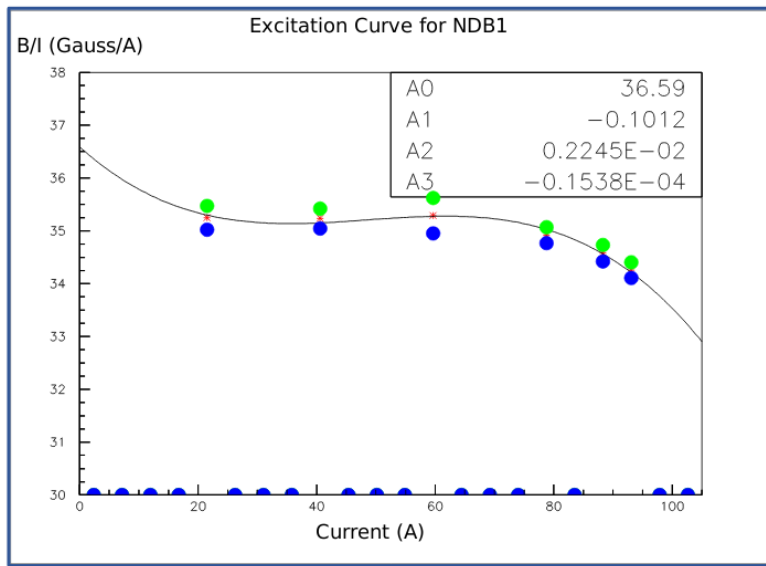


Figure 3.3: Magnetic field over current as a function of the current, for one NDB magnet (excitation curve). The data was collected using two hall probes (blue and green). We fit the readings with a cubic function (black) to average of measurements (red) given in the legend [43].

1468 The current through the magnets at a given time is identical in both magnets.  
1469 For the Run II data taking period, the current settings explored were 60A ( $B \sim 0.21$   
1470 T) and 100A ( $B \sim 0.35$  T) in both polarities. Albeit advantageous to enrich the  
1471 tertiary beam composition with high mass particles such as kaons, we never pushed

1472 the magnets current over 100 A, not to incur in overheating. During operation, we  
1473 operated an air and water cooling system on the magnets and we remotely monitored  
1474 the magnet temperatures.

### 1475 3.2.2 Multi-Wire Proportional Chambers



Figure 3.4: One of the four Multi Wire Proportional Chambers (WC) used in the LArIAT tertiary beamline and related read-out electronics.

1476 LArIAT uses four multi-wire proportional chambers, or wire chambers (WC) for  
1477 short, two upstream and two downstream from the bending magnets. The geometry of  
1478 one chamber is shown in Figure 3.4: the WC effective aperture is a square of 12.8 cm  
1479 perpendicular to the beam direction. Inside the chamber, the 128 horizontal and 128  
1480 vertical wires strung at a distance of 1 mm from each other in a mixture of 85% Argon  
1481 and 15% isobutane gas. The WC operating voltage is between 2400 V and 2500 V.  
1482 The LArIAT wire chambers are an upgraded version of the Fenker Chambers [62],  
1483 where an extra grounding improves the signal to noise ratio of the electronic readout.

1484 Two ASDQ chips [95] mounted on a mother board plugged into the chamber serve  
1485 as front end amplifier/discriminator. The chips are connected to a multi-hit TDC [73]  
1486 which provides a fast OR output used as first level trigger. The TDC time resolution  
1487 is 1.18 ns/bin and can accept 2 edges per 9 ns. The maximum event rate acceptable  
1488 by the chamber system is 1 MHz: this rate is not a limiting factor considering that

1489 the rate of the tertiary particle beam at the first wire chamber is estimated to be less  
1490 than 15 kHz. A full spill of data occurring once per supercycle is stored on the TDC  
1491 board memory at once and read out by a specially designed controller. We use LVDS  
1492 cables to carry both power and data between the controller and the TDCs and from  
1493 the controller to the rest of the DAQ.

1494 **Multi-Wire Proportional Chambers functionality**

1495 We use the wire chamber system together with the bending magnets to measure the  
1496 particle's momentum.

1497 In the simplest scenario, only one hit on each and every of the four wire chambers  
1498 is recorded during a single readout of the detector systems. Thus, we use the hit  
1499 positions in the two wire chambers upstream of the magnets to form a trajectory  
1500 before the bend, and the hit positions in the two wire chambers downstream of the  
1501 magnets to form a trajectory after the bend. We use the angles in the XZ plane  
1502 between the upstream and downstream trajectories to calculate the  $Z$  component of  
1503 the momentum as follows:

$$P_z = \frac{B_{eff}L_{eff}}{3.3(\sin(\theta_{DS}) - \sin(\theta_{US}))}, \quad (3.1)$$

1504 where  $B_{eff}$  is the effective maximum field in a square field approximation,  $L_{eff}$   
1505 is the effective length of both magnets (twice the effective length of one magnet),  
1506  $\theta_{US}$  is the angle off the  $z$  axis of the upstream trajectory,  $\theta_{DS}$  is the angle off the  
1507  $z$  axis of the downstream trajectory and  $3.3 c^{-1}$  is the conversion factor from [T·m]  
1508 to [MeV/c]. By using the hit positions on the third and fourth wire chamber, we  
1509 estimate the azimuthal and polar angles of the particle trajectory, and we are able to  
1510 calculate the other components of the momentum.

1511 The presence of multiple hits in a single wire chamber or the absence of hits in one  
1512 (or more) wire chambers can complicate this simple scenario. The first complication

is due to beam pile up, while the latter is due to wire chamber inefficiency. In the case of multiple hits on a single WC, at most one wire chamber track is reconstructed per event. Since the magnets bend particles only in the X direction, we assume the particle trajectory to be roughly constant in the YZ plane, thus we keep the combination of hits which fit best with a straight line. It is still possible to reconstruct the particle’s momentum even if the information is missing in either of the two middle wire chambers (WC2 or WC3), by constraining the particle trajectory to cross the plane in between the magnets.

Events satisfying the simplest scenario of one single hit in each of the four wire chambers form the “Picky Track” sample. We construct another, higher statistics sample, where we loosen the requirements on single hit and wire chamber efficiency: the “High Yield” sample. For LArIAT Run II, the High Yield sample is about three times the Picky Tracks statistics. We assume an uncertainty of 2% for four-point WC track, momentum uncertainty as reported for the same beamline in [56].

### 3.2.3 Time-of-Flight System

Two scintillator paddles, one upstream of the first set of WCs and one downstream of the second set of WCs form LArIAT time-of-flight (TOF) detector system.

The upstream paddle is made of a 10 x 6 x 1 cm scintillator piece, read out by two PMTs mounted on the beam left side which collect the light from light guides mounted on all four edges of the scintillator. The downstream paddle is a 14 x 14 x 1 cm scintillator piece read out by two PMTs on the opposite ends of the scintillator, as shown in figure 3.5. The relatively thin width in the beamline direction minimizes energy loss of beam particles traveling through the scintillator material.

The CAEN 1751 digitizer is used to digitize the TOF PMTs signals at a sampling rate of 1 GHz. The 12 bit samples are stored in a circular memory buffer. At trigger time, data from the TOF PMTs are recorded to output in a 28.7  $\mu$ s windows starting

1539 approximately 8.4  $\mu$ s before the trigger time.

1540 **TOF functionality**

1541 The TOF signals rise time (10-90%) is 4 ns and a full width, half-maximum of 9 ns  
1542 consistent in time. The signal amplitudes from the upstream TOF and downstream  
1543 TOF are slightly different: 200 mV for the upstream PMTs but only 50 mV for  
1544 downstream PMTs. The time of the pulses was calculated utilizing an oversampled  
1545 template derived from the data itself. We take the pulse pedestal from samples  
1546 far from the pulse and subtract it from the pulse amplitude. We then vertically  
1547 stretch a template to match the pedestal-subtracted pulse amplitude and we move  
1548 it horizontally to find the time. With this technique, we find a pulse time-pickoff  
1549 resolution better than 100 ps. The pulse pile up is not a significant problem given  
1550 the TOF timing resolution and the rate of the particle beam. Leveraging on the  
1551 pulses width uniformity of any given PMT, we flag events where two pulses overlap  
1552 as closely in time as 4 ns with a 90% efficiency according to simulation.

1553 We combine the pulses from the two PMTs on each paddle to determine the  
1554 particles' arrival time by averaging the time measured from the single PMT, so to  
1555 minimize errors due to optical path differences in the scintillator. However, a time  
1556 spread of approximately 300 ps is present in both the upstream and downstream  
1557 detectors, likely due to transit time jitter in the PMTs themselves.

1558 **3.2.4 Punch-Through and Muon Range Stack Instruments**

1559 The punch-through and the muon range stack (MuRS) detectors are located down-  
1560 stream of the TPC. These detectors provide a sample of TPC crossing tracks without  
1561 relying on TPC information and can be used to improve particle ID for muons and  
1562 pions with momentum higher than 450 MeV/c.

1563 The punch-through is simple sheet of scintillator material, read out by two PMTs.



Figure 3.5: Image of the down stream time of flight paddle, PMTs and relative support structure before mounting.

1564 The MuRS is a segmented block of steel with four slots instrumented with scintillation  
1565 bars. The four steel layers in front of each instrumented slot are 2 cm, 2 cm, 14 cm  
1566 and 16 cm deep in the beam direction. Each instrumented slot is equipped with  
1567 four scintillation bars each, positioned horizontally in the direction orthogonal to the  
1568 beam. Each scintillator bar measures  $\textcolor{red}{? \times ? \times 2}$  cm and it is read out by one PMT.

1569 The signals from both the punch-thorough and the MuRS PMTs are sent to a  
1570 NIM discriminator. If the signal crosses the discriminator threshold, it is digitized in  
1571 the CAEN V1740, same as the TPC. The sampling time of the CAEN V1740 is slow  
1572 (of the order of 128 ns) and that the pulse shape information from the PMT is lost.  
1573 A Punch-thorough and MuRS signal will then be simply a “hit” at a given time in  
1574 the beamline event.

1575 It is worth mentioning here the presence of an additional scintillation paddle  
1576 between WC4 and the downstream paddle of the TOF system, called halo. The  
1577 halo is a  $39 \times 38 \times 1$  cm $^3$  paddle with a 6.5 cm radius hole in the center, whose original  
1578 function was to reject beam particles slightly offset from the beamline center. Data

1579 from this paddle turned out to be unusable, so our data events include both particle  
1580 going through the halo scintillation material or through the halo hole.

1581 **3.2.5 LArIAT Cosmic Ray Paddle Detectors**

1582 LArIAT triggers both on beam events and on cosmic rays events. We perform this  
1583 latter trigger by using two sets of cosmic ray paddle detectors (a.k.a. “cosmic towers”.)  
1584 The cosmic towers frame the LArIAT cryostat, as one sits in the downstream left  
1585 corner and the other sits in the upstream right corner of the cryostat. Two paddle  
1586 sets of four scintillators pieces each make up each cosmic tower, an upper set and a  
1587 lower set per tower. Of the four paddles, a couple of two matched paddles stands  
1588 upright while the a second matched pair lies across the top of the assembly in the top  
1589 sets (or across the bottom of the assembly in the bottom sets). The horizontal couple  
1590 is used as a veto for particles traveling from inside the TPC out. The four signals  
1591 from the vertical paddles along one of the body diagonals of the TPC are combined  
1592 in a logical “AND”. This allows to select track due to cosmic muons at the ground  
1593 level crossing the TPC along one of its diagonals. Cosmic ray muons whose average  
1594 energy is in the few GeV range crossing both anode and cathode populate the events  
1595 triggered this way. This particularly useful sample of tracks is associated can be used  
1596 for many tasks; for example, we use anode-cathode piercing tracks to cross check  
1597 the TPC electric field on data (see Appendix A), to calibrate the charge response of  
1598 the TPC wires for the full TPC volume and to measure the electron lifetime in the  
1599 chamber [104].

1600 We retrieved the scintillation paddles from the decommissioning of the CDF de-  
1601 tector at Fermilab and we used only the paddles with a counting efficiency greater  
1602 than 95% and low noise at working voltage. The measured trigger rate of the whole  
1603 system is 0.032 Hz, corresponding to  $\sim 2$  muons per minute.



Figure 3.6: Photograph of one of the scintillation counters used in the cosmic towers.

### 1604 3.3 In the Cryostat

1605 The heart of the LArIAT experiment lives in the LArIAT cryostat. In this section,  
1606 we describe the cryogenic system and the argon purity (Section 3.3.1), the LArIAT  
1607 TPC (Section 3.3.2) and light collection system (3.3.3).

#### 1608 3.3.1 Cryogenics and Argon Purity

1609 LArIAT repurposed the ArgoNeuT cryostat [17] in order to use it in a beam of charged  
1610 particles, and added a new process piping and a new liquid argon filtration system in  
1611 FTBF. Inside the LArIAT experimental hall, the cryostat sits in the beam of charged  
1612 particles with its horizontal main axis oriented parallel to the secondary beam,  $3^\circ$   
1613 off axis from the tertiary beam

1614 Two volumes make up LArIAT cryostat, shown in Figure 3.7: the inner vessel and  
1615 the outer vessel. Purified liquid argon fills the inner vessel, while the outer volume  
1616 provides insulation through a vacuum jacket equipped with layers of aluminized mylar  
1617 superinsulation. The inner vessel is a cylinder of 130 cm length and 76.2 cm diameter,  
1618 containing about 550 L of LAr, corresponding to a mass of 0.77 ton. We run the signal  
1619 cables for the LArTPC and the high voltage feedthrough through a “chimney” at the  
1620 top and mid-length of the cryostat.

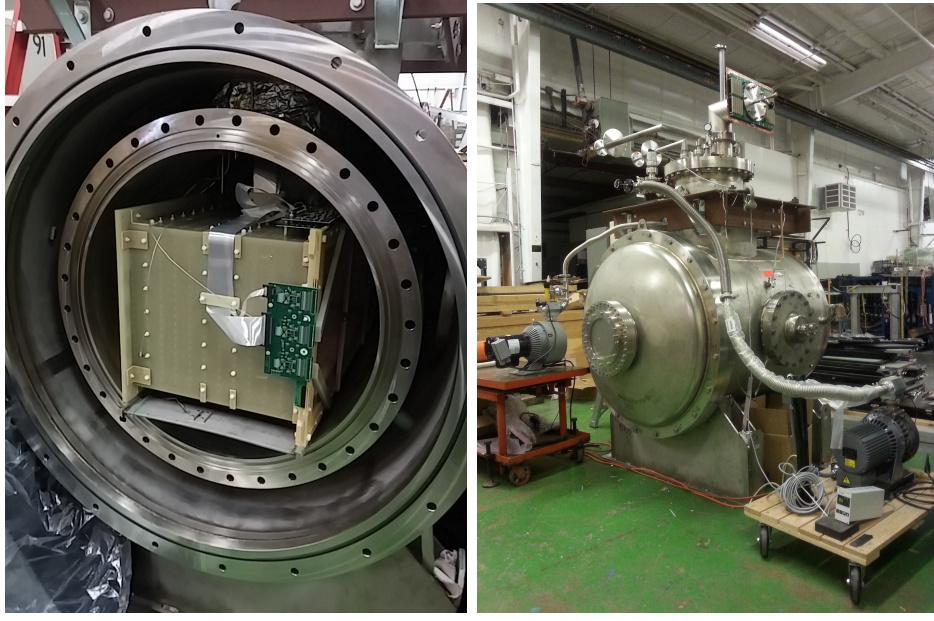


Figure 3.7: Left: the LArIAT TPC in the inner volume of the open cryostat. Right: cryostat fully sealed ready to be transported to FTBF.

Given the different scopes of the ArgoNeuT and LArIAT detectors, we made several modifications to the ArgoNeuT cryostat in order to use it in LArIAT. In particular, the modifications shown in Figure 3.8 were necessary to account for the beam of charged particles entering the TPC and to employ the new FTBF liquid argon purification system. We added a “beam window” on the front outer end cap and an “excluder” on the inner endcap, with the purpose of minimizing the amount of non-instrumented material upstream of the TPC’s active volume. The amount of non-instrumented material in front of the TPC for LArIAT corresponds to  $\sim 0.3$  electron radiation lengths ( $X_0$ ), to compare against the  $\sim 1.6X_0$  of ArgoNeuT. To allow studies of the scintillation light, we added a side port feedthrough which enables the mounting of the light collection system, as well as the connections for the corresponding signal and high-voltage cables (see Section 3.3.3). We modified the bottom of the cryostat adding Conflat and ISO flange sealing to connect the liquid argon transfer line to the new argon cooling and purification system.

As in any other LArTPC, argon purity is a crucial parameter for LArIAT. Indeed,



Figure 3.8: Main modifications to the ArgoNeuT cryostat: 1) outlet for connection to the purification system at the bottom of the cryostat; 2) the “beam-window” on the outer endcap and “excluder” which reduces the amount of non-instrumented material before the TPC; 3) the side port to host the light collection system.

1636 the presence of contaminants affects both the basic working principles of a LArTPC,  
 1637 as shown in section 2.1.2: electronegative contaminants such as oxygen and water de-  
 1638 crease the number of ionization electrons collected on the wires after drifting through  
 1639 the volume. In addition, contaminants such as Nitrogen decrease the light yield  
 1640 from scintillation light, especially in its slow component. In LArIAT, contaminations  
 1641 should not exceed the level of 0.2 parts per billion (ppb). We achieve this level of  
 1642 purity in several stages. The specifics required for the commercial argon bought for  
 1643 LArIAT are 2 parts per million (ppm) oxygen, 3.5 ppm water, and 10 ppm nitrogen.  
 1644 This argon is monitored with the use of commercial gas analyzer. Argon is stored in  
 1645 a dewar external to LArIAT hall and filtered before filling the TPC. LArIAT uses a  
 1646 filtration system designed for the Liquid Argon Purity Demonstrator (LAPD) [57]:  
 1647 half of a 77 liter filter contains a 4A molecular sieve (Sigma-Aldrich [110]) able to re-  
 1648 move mainly water, while the other half contains BASF CU-0226 S, a highly dispersed  
 1649 copper oxide impregnated on a high surface area alumina, apt to remove mainly oxy-

1650 gen [27]. A single pass of argon in the filter is sufficient to achieve the necessary  
1651 purity, unless the filter is saturated. In case the filter saturates, the media needs to  
1652 be regenerated by using heated gas; this happened twice during the Run II period<sup>1</sup>.  
1653 The electron lifetime during the full LArIAT data taking are shown in Figure 2.4.  
1654 The filtered argon reaches the inner vessel via a liquid feedthrough which is routed to  
1655 the bottom of the cryostat. Argon is not recirculated in the system; rather, it boils  
1656 off and vents to the atmosphere. During data taking, we replenish the argon in the  
1657 cryostat every 6 hours to keep the TPC high voltage feedthrough and cold electronics  
1658 always submerged. In fact, we constantly monitor the level, temperature, and pres-  
1659 sure of the argon both in the commercial dewar and inside the cryostat during data  
1660 taking.

### 1661 **3.3.2 LArTPC: Charge Collection**

1662 The LArIAT Liquid Argon Time Projection Chamber is a rectangular box of dimen-  
1663 sions 47 cm (drift) x 40 cm (height) x 90 cm (length), containing 170 liters of Liquid  
1664 Argon. The LArTPC three major subcomponents are

- 1665 1) the cathode and field cage,
- 1666 2) the wire planes,
- 1667 3) the read-out electronics.

#### 1668 **Cathode and field cage**

1669 A G10 plain sheet with copper metallization on one of the 40 x 90 cm inner surfaces  
1670 forms the cathode. A high-voltage feedthrough on the top of the LArIAT cryostat  
1671 delivers the high voltage to the cathode; the purpose of the high voltage system

---

1. We deemed the filter regeneration necessary every time the electron lifetime dropped under 100 μs.

1672 (Figure 3.9) is to drift ionization electrons from the interaction of charged particles  
 1673 in the liquid argon to the wire planes. The power supply used in this system is a  
 1674 Glassman LX125N16 [70] capable of generating up to -125 kV and 16 mA of current,  
 1675 but operated at -23.5kV during LArIAT Run-II. The power supply is connected via  
 1676 high voltage cables to a series of filter pots before finally reaching the cathode.

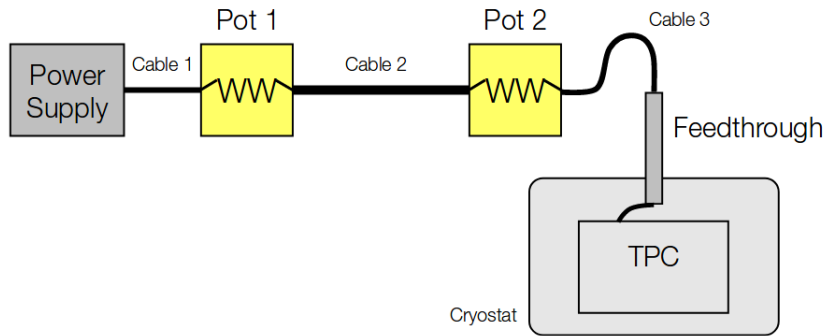


Figure 3.9: Schematic of the LArIAT high voltage system.

1677 The field cage is made of twenty-three parallel copper rings framing the inner walls  
 1678 of the G10 TPC structure. A network of voltage-dividing resistors connected to the  
 1679 field cage rings steps down the high voltage from the cathode to form a uniform electric  
 1680 field. The electric field over the entire TPC drift volume is 486 V/cm, as measured  
 1681 in appendix A. The maximum drift length, i.e. the distance between cathode and  
 1682 anode planes, is 47 cm.

### 1683 Wire planes

1684 LArIAT Run-II has three wire planes separated by 4 mm spaces: in order of increasing  
 1685 distance from the cathode, they are the shield, the induction and the collection plane.  
 1686 The “wire pitch”, i.e., the distance between two adjacent wires in a given plane, is  
 1687 4 mm. The shield plane counts 225 parallel wires of equal length oriented vertically.  
 1688 This plane is not connected with the read-out electronics; rather it shields the outer  
 1689 planes from extremely long induction signals due to the ionization in the whole drift

volume. As the shield plane acts almost like a Faraday cage, the resulting shape of signals in the first instrumented plane (induction) is easier to reconstruct. Both the induction and collection planes count 240 parallel wires of different length oriented at  $60^\circ$  from the vertical with opposite signs. Electrons moving past the induction plane will induce a bipolar pulse on its wires; the drifting electrons will be then collected on the collection plane's wires, forming a unipolar pulse.

The three wire planes and the cathode form three drift volumes, as shown in Figure 3.10. The main drift volume is defined as the region between the cathode plane and the shield plane (C-S). The other two drift regions are those between the shield plane and the induction plane (S-I), and between the induction plane and the collection plane (I-C). The electric field in these regions is chosen to satisfy the charge transparency condition and allow for 100% transmission of the drifting electrons through the shield and the induction planes.

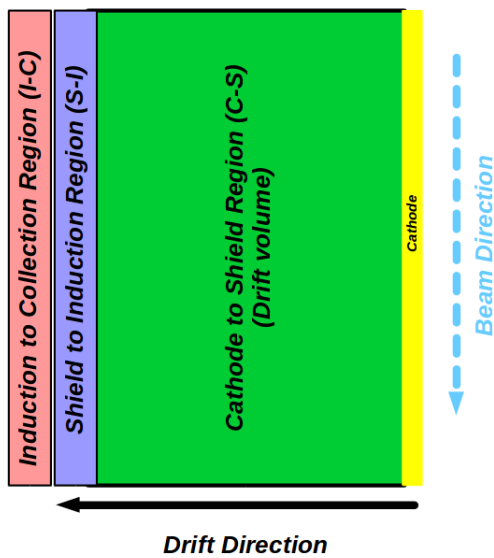


Figure 3.10: Schematic of the three drift regions inside the LArIAT TPC: the main drift volume between the cathode and the shield plane (C-S) in green, the region between the shield plane and the induction plane (S-I) in purple, and the region between the induction plane and the collection plane (I-C) in pink.

Table 3.1 provides the default voltages applied to the cathode and the shield,

1704 induction, and collection plane.

Table 3.1: Cathode and anode planes default voltages

Cathode	Shield	Induction	Collection
-23.17 kV	-298.8 V	-18.5 V	338.5 V

## 1705 Electronics

1706 Dedicated electronics read the induction and collection plane wires, for a total of  
1707 480-channel analog signal path from the TPC wires to the signal digitizers. A digital  
1708 control system for the TPC-mounted electronics, a power supply, and a distribution  
1709 system complete the front-end system. Figure 3.11 shows a block diagram of the  
1710 overall system. The direct readout of the ionization electrons in liquid argon forms  
1711 typically small signals on the wires, which need amplification in oder to be processed.  
1712 LArIAT performs the amplification stage directly in cold with amplifiers mounted  
1713 on the TPC frame inside the liquid argon. The BNL ASICs adopted in LArIAT are  
1714 designated as LArASIC, version 4-star and are the same used by the MicroBooNE  
1715 experiment [60]. The signal from the ASICs are driven to the other end of the readout  
1716 chain, to the CAEN V1740 digitizers [35]. The CAEN V1740 has a 12 bit resolution  
1717 and a maximum input range of 2 VDC, resulting in about 180 ADC count for a  
1718 crossing MIP.

### 1719 3.3.3 LArTPC: Light Collection System

1720 The collection of scintillation photons is the second mechanism of particle detection  
1721 in argon other than the ionization electrons. Over the course of LArIAT's three years  
1722 of data taking, the light collection system changed several times. We describe here  
1723 the light collection system for Run II. Two PMTs, a 3-inch diameter Hamamatsu  
1724 R-11065 and 2-inch diameter ETL D757KFL [7], as well as three SiPMs arrays (two  
1725 Hamamatsu S11828-3344M 4x4 arrays and one single-channel SensL MicroFB-60035)

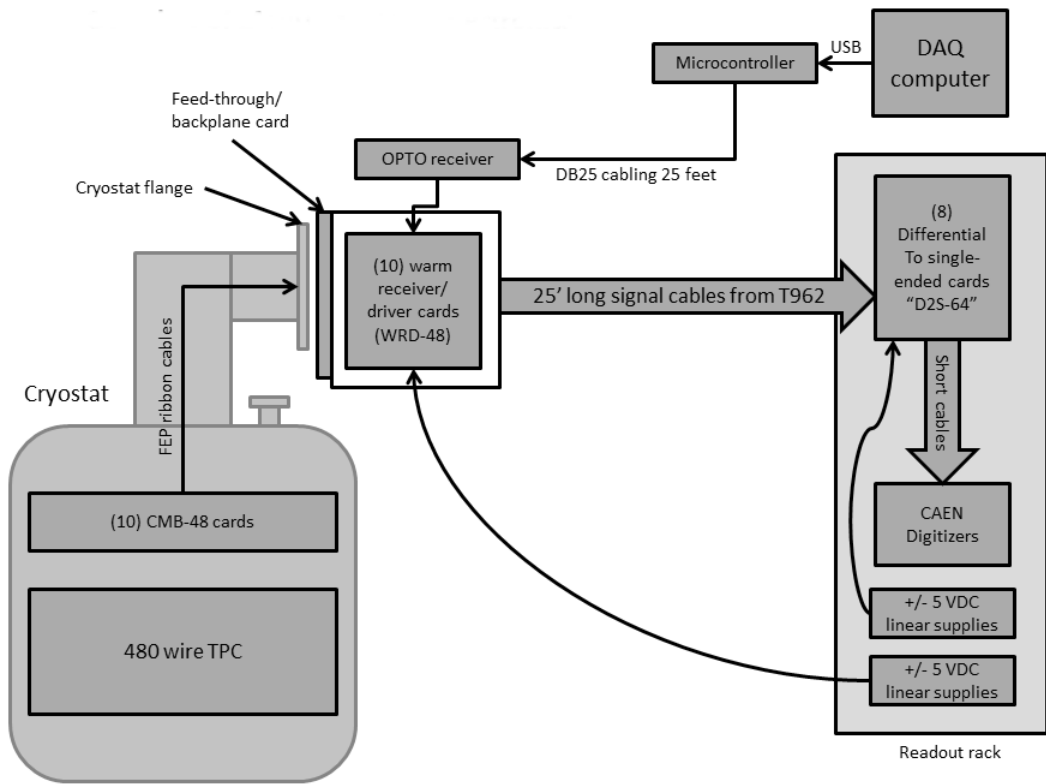


Figure 3.11: Overview of LArIAT Front End electronics.

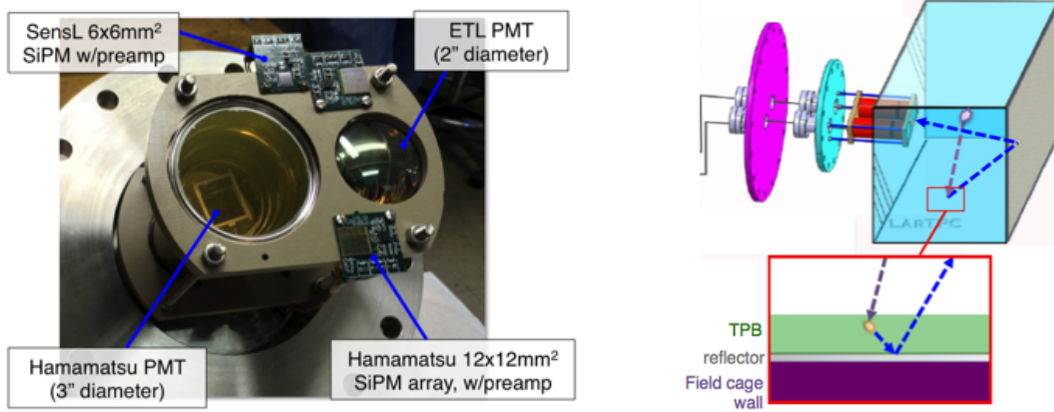


Figure 3.12: LArIAT’s photodetector system for observing LAr scintillation light inside the TPC (left), and a simplified schematic of VUV light being wavelength-shifting along the TPB-coated reflecting foils (right).

1726 are mounted on the PEEK support structure. PEEK screws into an access flange  
 1727 as shown in Figure 3.12, on the anode side, leaving approximately 5 cm of clearance  
 1728 from the collection plane.

1729 Liquid argon scintillates in vacuum-ultraviolet (VUV) range at 128 nm; since  
 1730 cryogenic PMTs are not sensitive to VUV wavelengths, we need to shift the light to a  
 1731 range that is visible to the PMTs. In LArIAT, the wavelength shifting is achieved by  
 1732 installing highly-reflective 3M VIKUITI dielectric substrate foils coated with a thin  
 1733 layer of tetraphenyl-butadiene (TPB) on the four unbiased walls of the TPC. The  
 1734 scintillation light interaction with the TPB emits one or more visible photons, which  
 1735 are then reflected into the chamber. Thus, the light yield increases and results in  
 1736 higher uniformity of light across the TPC active volume, allowing the possibility of  
 1737 light-based calorimetry, currently under study.

1738 For Run II, we coated the windows of the ETL PMT and the SensL SiPM with  
 1739 a thin layer of TPB. In doing so, some of the VUV scintillation light converts into  
 1740 visible right at the sensor faces, keeping information on the direction of the light  
 1741 source. Information about the light directionality is hindered for the light reflected  
 1742 on foils, as the reflection is uniform in angle.

## 1743 3.4 Trigger and DAQ

1744 The LArIAT DAQ and trigger system governs the read out of all the many subsystems  
1745 forming LArIAT. The CAEN V1495 module [34] and its user-programmable FPGA  
1746 are the core of this system. Every 10 ns, this module checks for matches between  
1747 sixteen logical inputs and user-defined patterns in the trigger menu; if it finds a match  
1748 for two consecutive clock ticks, that trigger fires.

1749 LArIAT receives three logic signals from the Fermilab accelerator complex related  
1750 to the beam timing which we use as input triggers: a pulse just before the beam, a  
1751 pulse indicating beam-on, and a beam-off pulse.

1752 The beam instruments, the cosmic ray taggers, and the light collection system  
1753 provide the other NIM-standard logic pulse inputs to the trigger decision. We auto-  
1754 matically log the trigger inputs configuration with the rest of the DAQ configuration  
1755 at the beginning of each run.

1756 Fundamental inputs to the trigger card come from the TOF (see section 3.2.3)  
1757 and the wire chambers (see section 3.2.2), as activity in these systems points to the  
1758 presence of a charged particle in tertiary beam line. In particular, the discriminated  
1759 pulses from the TOF PMTs form a NIM logic pulse for the trigger logic. We ask  
1760 for a coincidence within a 20 ns window for all the pulses from the PMTs looking at  
1761 the same scintillator block and use a delayed coincidence between the upstream and  
1762 downstream paddle to inform the trigger decision. In order to form a coincidence  
1763 between the upstream and downstream paddles, we delay the upstream paddle coin-  
1764 cidence by 20 ns and widen it by 100 ns. The delay and widening are necessary to  
1765 account for both lightspeed particles and slower particles (high-mass) to travel the  
1766 6.5 m between the upstream and the downstream paddles. For the read out of the  
1767 wire chambers, we use a total of sixteen multi-hit TDCs [73], four per chamber: two  
1768 TDC per plane (horizontal and vertical), sixty-four wires per TDC. In each TDC, we  
1769 keep the logical “OR” for any signal over threshold from the sixty-four wires. We

1770 then require a coincidence between the “OR” for the horizontal TDCs and the “OR”  
1771 for the vertical TDCs: with this logic we make sure that at least one horizontal wire  
1772 and one vertical wire saw significant signal in one wire chamber. The single logical  
1773 pulse from each of the four wire chambers feeds into the first four inputs to the V1495  
1774 trigger card. We require a coincidence within 20 ns of at least three logical inputs to  
1775 form a trigger.

1776 The cosmic towers (see Section 3.2.5) provide another primary input to the trigger,  
1777 in order to capture long tracks from cosmic muons crossing the TPC. We use NIM  
1778 modules to require coincidences between one upper and one lower paddle set of any  
1779 opposite cosmic towers. The OR all the opposite towers’ coincidences is fed as an  
1780 input to the trigger card.

1781 We use the signal from the cryogenic PMTs (see Section 3.3.3) to form several  
1782 interesting triggers. The coincidence of signals from all the PMT pulses within  $\sim$ 20 ns  
1783 is an indication of ionizing radiation in the TPC and forms a trigger input. The  
1784 coincidence of two subsequent scintillation logic pulses delayed by a maximum of  $7 \mu\text{s}$   
1785 forms the Michel electron trigger.

## 1786 3.5 Control Systems

1787 LArIAT is a complex ensemble of systems which needed to be monitored simultane-  
1788 ously during data taking. We performed the monitoring of the systems operations  
1789 with a slow control system, a DAQ monitoring system and a low level data quality  
1790 monitoring described in the following sections.

### 1791 Slow Control

1792 We used the Synoptic Java Web Start framework [19] as a real-time display of subsys-  
1793 tem conditions. Synoptic provides a Graphical User Interface that talks to the Fer-

milab Accelerator Control System via the ACNET protocol. Its simple GUI allowed us to change the operating parameters and to graph the trends of several variables of interest for all of the tertiary beam detectors. Among the most important quantities monitored by Synoptic there are the level of argon in both the inner vessel and the external dewar, the operating voltages of cathode and wire planes, of the PMTs and SiPMs, and of the four wire chambers, as well as the magnet temperatures. Figure 3.13 shows an example of the monitoring system. LArIAT uses the Accelerator Control NETwork system (ACNET) to monitor the beam conditions of the MCcenter beamline. For example, the horizontal and vertical position of the beam at the first two wire chambers (WC1 and WC2) are shown in 3.14 as seen by the shifter during data taking.

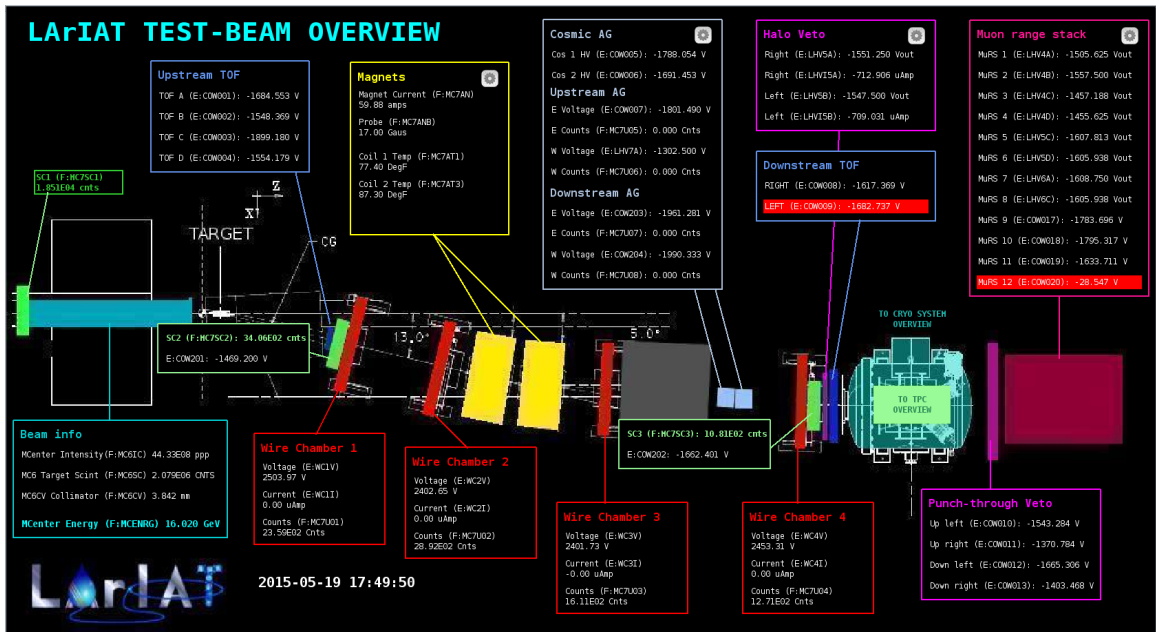


Figure 3.13: Interface of the Synoptic slow control system

## 1805 DAQ Monitoring

We monitor the data taking and the run time evolution with the Run Status Webpage (<http://lariat-wbm.fnal.gov/lariat/run.html>), a webpage updated in real-time. The

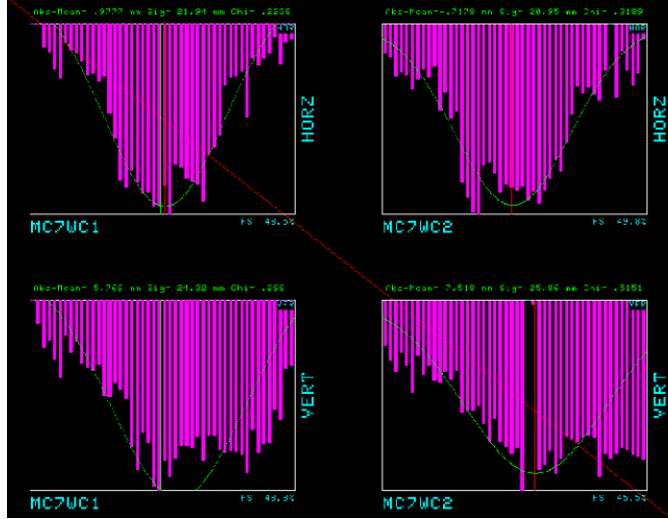


Figure 3.14: Beam position at the upstream wire chambers monitored with ACNET.

1808 page displays, among other information, the total number of triggers in the event,  
 1809 the total number of detectors triggered during a beam spill, the trigger patterns, the  
 1810 number of times a particular trigger pattern was satisfied during a beam spill, and  
 1811 the current time relative to the Fermilab accelerator complex supercycle. A screen  
 1812 shot of the page is show in figure 3.15.

### 1813 Data Quality Monitoring

1814 We employ two systems to ensure the quality of our data during data taking: the  
 1815 Near-Real-Time Data Quality Monitoring and the Event Viewer.

1816 The Near-Real-Time Data Quality Monitoring (DQM) is a webpage which receives  
 1817 updates from all the VME boards in the trigger system and displays the results of  
 1818 a quick analysis of the DAQ stream of raw data on a spill-by-spill basis. The DQM  
 1819 allows the shifter to monitor almost in real time (typically with a 2-minute delay)  
 1820 a series of low level-quantities and compare them to past collections of beam spills.  
 1821 Some of the variables monitored in the DQM are the pedestal mean and RMS on  
 1822 CAEN digitizer boards of the TPC wires and PMTs of the beamline detectors, the  
 1823 hit occupancy and timing plots on the wire chambers, and number of data fragments

1824 recorded that are used to build a TPC event. Abnormal values for low-level quantity  
1825 in the data activates a series of alarms in the DQM; this quick feedback on the DAQ  
1826 and beam conditions is fundamental to assure a fast debugging of the detector and a  
1827 very efficient data taking during beam uptime.

1828 The online Event Viewer displays a two dimensional representation (Wire vs Time)  
1829 of LArIAT TPC events on both the Induction and the Collection planes in near real  
1830 time. The raw pulses collected by the DAQ on each wire are plotted as a function  
1831 of drift time, resulting in an image of the TPC event easily readable by the shifter.  
1832 This tool guarantees a particularly good check of the TPC operation which activate  
1833 an immediate feedback for troubleshooting a number of issues. For example, it is  
1834 easy for the shifter to spot high occupancy events and request a reduction of the  
1835 primary beam intensity, or to spot a decrease of the argon purity which requires the  
1836 regeneration of filters, or to catch the presence of electronic noise and reboot the  
1837 ASICs. An example of high occupancy event is shown in 3.16.

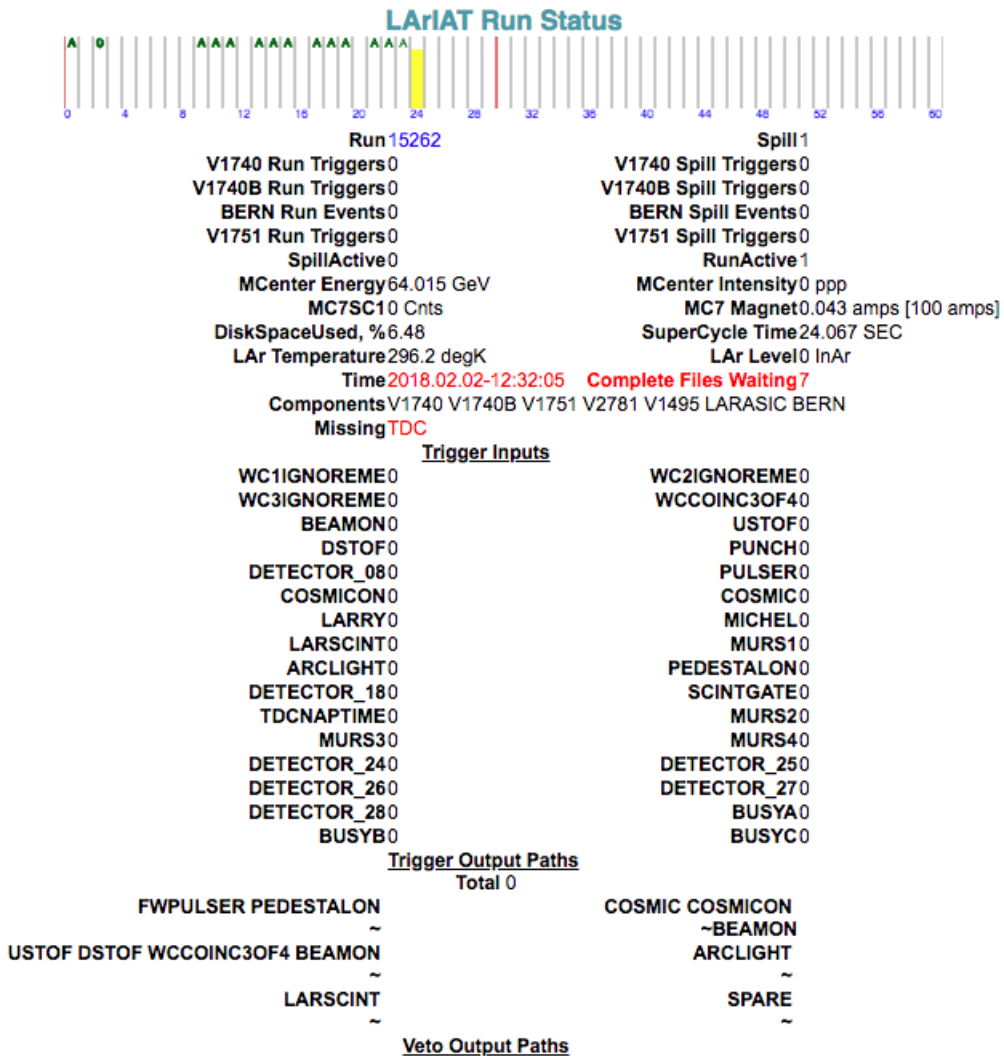


Figure 3.15: Run Status page at LArIAT downtime. At the top the yellow bar displays the current position in the Fermilab supercycle. Interesting information to be monitored by the shifter were the run number and number of spills, time elapsed from data taking (here in red), the energy of the secondary beam and the trigger paths.

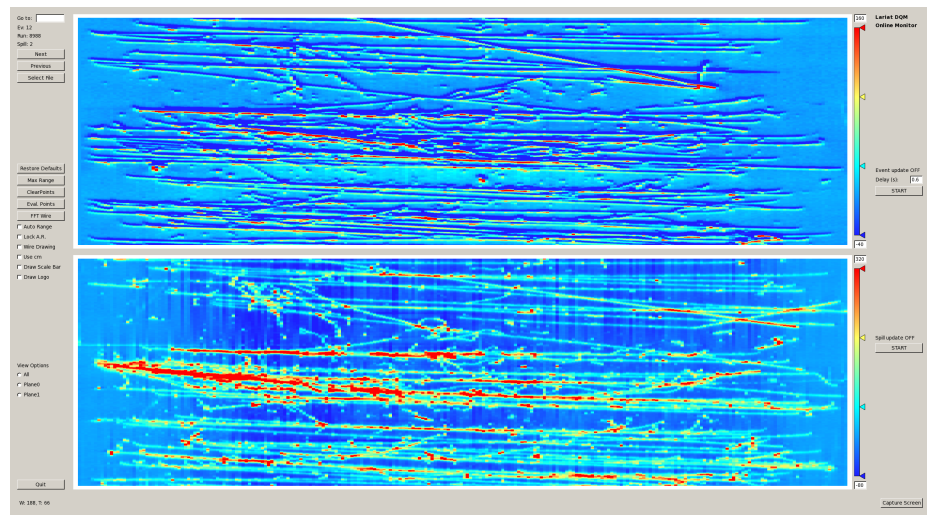


Figure 3.16: High occupancy event display: induction plane (top) and collection plane (bottom).

1838 **Chapter 4**

1839 **Total Hadronic Cross Section**

1840 **Measurement Methodology**

1841 “Like a lemon to the lime and the bubble to the bee”

1842 – Eazy-E, 1993 –

1843 This chapter describes the general procedure employed to measure total hadronic  
1844 interaction cross sections on Ar in LArIAT. Albeit with small differences, both the  
1845 ( $\pi^-$ ,Ar) and ( $K^+$ ,Ar) total hadronic cross section measurements rely on the same  
1846 procedure. We start by selecting the particle of interest using a combination of  
1847 beamline detectors and TPC information (Section 4.1). We then perform a handshake  
1848 between the beamline information and the TPC tracking to assure the selection of  
1849 the correct TPC track (Section 4.2) associated to the corresponding beam particle.  
1850 We then apply the “thin slice” method to measure the “raw” hadronic cross section  
1851 (Section 4.3). A series of corrections are then evaluated and applied to obtain the  
1852 final cross section (Section 4.3.3).

1853 At the end of this chapter, we show a sanity check of the methodology by apply-  
1854 ing the thin slice method employing only MC truth information and retrieving the  
1855 expected MC cross section for pions and kaons (Section 4.4).

## 1856 4.1 Event Selection

1857 The measurement of the ( $\pi^-$ ,Ar) and ( $K^+$ ,Ar) total hadronic cross section in LArIAT  
1858 starts by selecting the pool of pion or kaon candidates and measuring their momentum  
1859 before they enter the LAr volume. This is done through the series of selections on  
1860 beamline and TPC information described in the next sections. The summary of the  
1861 event selection in data is reported in Table 4.1.

### 1862 4.1.1 Selection of Beamline Events

1863 We leverage the beamline particle identification and momentum measurement before  
1864 entering the TPC as an input to evaluate the kinetic energy for the hadrons used in  
1865 the cross sections measurements. To this end, we select the LArIAT data to keep  
1866 only events whose wire chamber and time of flight information is registered (line 1 in  
1867 in Table 4.1). Additionally, we perform a check of the plausibility of the trajectory  
1868 inside the beamline detectors: given the position of the hits in the four wire chambers,  
1869 we make sure the particle's trajectory does not cross any impenetrable material such  
1870 as the collimator and the magnets steel (line 2 in in Table 4.1).

	Run-II Neg Pol	Run-II Pos Pol
1. Events Reconstructed in Beamline	158396	260810
2. Events with Plausible Trajectory	147468	240954
3. Beamline $\pi^-/\mu^-/e^-$ Candidate	138481	N.A.
4. Beamline $K^+$ Candidate	N.A	2837
5. Events Surviving Pile Up Filter	108929	2389
6. Events with WC2TPC Match	41757	1081
7. Events Surviving Shower Filter	40841	N.A.
8. Available Events For Cross Section	40841	1081

Table 4.1: Number of data events for Run-II Negative and Positive polarity

1871 **4.1.2 Particle Identification in the Beamline**

1872 In data, the main tool to establish the identity of the hadron of interest is the LArIAT  
1873 tertiary beamline, in its function of mass spectrometer. We combine the measurement  
1874 of the time of flight,  $TOF$ , and the beamline momentum,  $p_{Beam}$ , to reconstruct the  
1875 invariant mass of the particles in the beamline,  $m_{Beam}$ , as follows

$$m_{Beam} = \frac{p_{Beam}}{c} \sqrt{\left(\frac{TOF * c}{l}\right)^2 - 1}, \quad (4.1)$$

1876 where  $c$  is the speed of light and  $l$  is the length of the particle's trajectory between  
1877 the time of flight paddles.

1878 Figure 4.1 shows the mass distribution for the Run II negative polarity runs on  
1879 the left and positive polarity runs on the right. We perform the classification of events  
1880 into the different samples as follows:

- 1881 •  $\pi/\mu/e$ : mass  $< 350 \text{ MeV}/c^2$   
1882 • kaon:  $350 \text{ MeV} < \text{mass} < 650 \text{ MeV}/c^2$   
1883 • proton:  $650 \text{ MeV} < \text{mass} < 3000 \text{ MeV}/c^2$ .

1884 Lines 3 and 4 in Table 4.1 show the number of negative  $\pi/\mu/e$  and positive  $K$   
1885 candidates which pass the mass selection for LArIAT Run-II data.

1886 **4.1.3 TPC Selection: Halo Mitigation**

1887 The secondary beam impinging on LArIAT secondary target produces a plethora of  
1888 particles which propagates downstream. The presence of upstream and downstream  
1889 collimators greatly abates the number of particles tracing down the LArIAT tertiary  
1890 beamline. However, it is possible that more than one particle sneaks into the LArTPC  
1891 during its readout time: the TPC readout is triggered by the particle firing the series

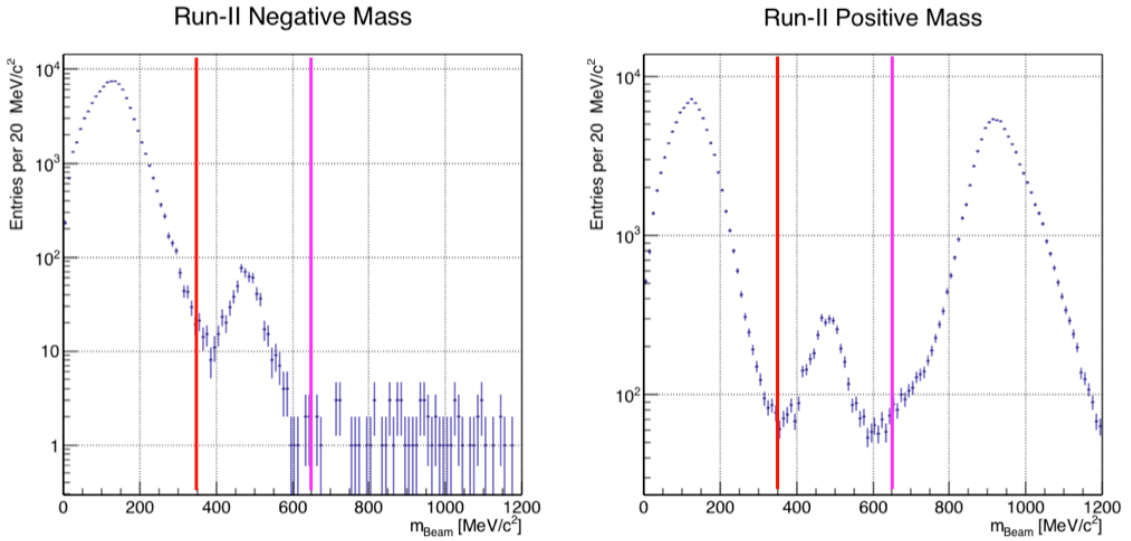


Figure 4.1: Distribution of the beamline mass as calculated according to equation 4.1 for the Run-II events reconstructed in the beamline, negative polarity runs on the left and positive polarity runs on the right. The classification of the events into  $\pi^\pm/\mu^\pm/e^\pm$ ,  $K^\pm$ , or (anti)proton is based on these distributions, whose selection cut are represented by the vertical colored lines.

1892 of beamline detectors along our tertiary beamline, but particles from the beam halo  
 1893 might also be present in the TPC at the same time. We call “pile up” the additional  
 1894 traces in the TPC. We adjusted the primary beam intensity between LArIAT Run I  
 1895 and Run II to reduce the presence of events with high pile up particles in the data  
 1896 sample. For the cross section analyses, we remove events with more than 4 tracks in  
 1897 the first 14 cm upstream portion of the TPC from the sample (line 5 in Table 4.1).

#### 1898 **4.1.4 TPC Selection: Shower Removal**

1899 In the case of the  $(\pi^-, \text{Ar})$  cross section, the resolution of beamline mass spectrometer  
 1900 is not sufficient to select a beam of pure pions. In fact, muons which are close in mass  
 1901 to the pions and relativistic electrons survive the selection on the beamline mass. It  
 1902 is important to notice that the composition of the negative polarity beam is mostly  
 1903 pions, as will be discussed in section 5.2.1. Still, we devise a selection on the TPC

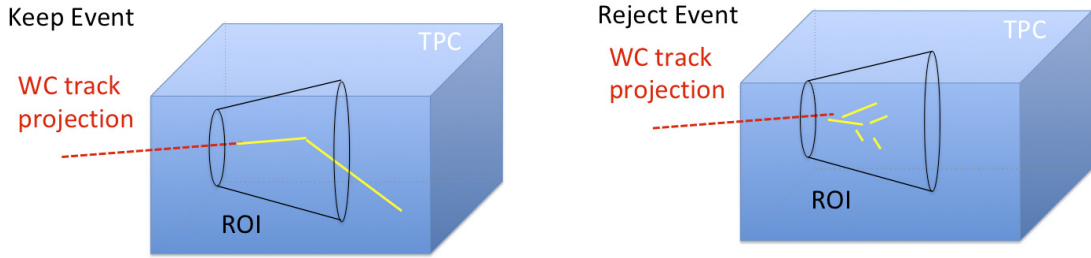


Figure 4.2: Visual rendering of the shower filter. The ROI is a cut cone, with a small radius of 4 cm, a big radius of 10 cm and an height of 42 cm (corresponding to 3 radiation lengths for electrons in Argon).

1904 information to mitigate the presence of electrons in the sample used for the pion  
 1905 cross section. The selection relies on the different topologies of a pion and an electron  
 1906 event when propagating in liquid argon: while the former will trace a track inside the  
 1907 TPC active volume, the latter will tend to “shower”, i.e. interact with the medium,  
 1908 producing bremsstrahlung photons which pair convert into several short tracks. In  
 1909 order to remove the shower topology, we create a region of interest (ROI) around the  
 1910 TPC track corresponding to the beamline particle. We look for short tracks contained  
 1911 in the ROI, as depicted in figure 4.4: if more than 5 tracks shorter than 10 cm are  
 1912 in the ROI, we reject the event. Line 7 in Table 4.1 shows the number of events  
 1913 surviving this selection.

## 1914 4.2 Beamlne and TPC Handshake: the Wire Cham- 1915 ber to TPC Match

1916 For each event passing the selection on its beamline information, we need to identify  
 1917 the track inside the TPC corresponding to the particle which triggered the beamline  
 1918 detectors, a procedure we refer to as “WC to TPC match” (WC2TPC for short). In  
 1919 general, the TPC tracking algorithm can reconstruct more than one track in the event,  
 1920 partially due to the fact that hadrons interact in the chamber and partially because

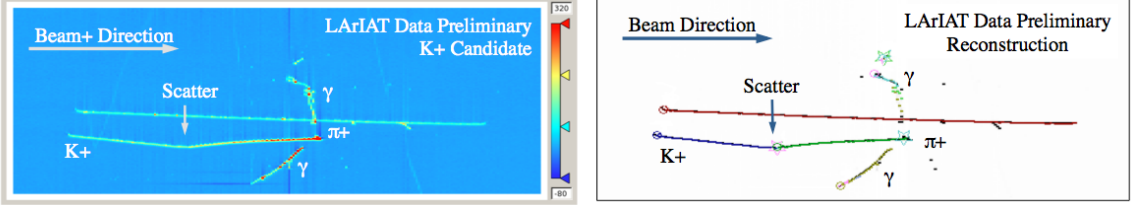


Figure 4.3: Kaon candidate event: on the right, event display showing raw quantities; on the left, event display showing reconstructed tracks. In the reconstructed event display, different colors represent different track objects. A kink is visible in the kaon ionization, signature of a hadronic interaction: the tracking correctly stops at the kink position and two tracks are formed. An additional pile-up track is so present in the event (top track in red).

1921 of pile up particles during the triggered TPC readout time, as shown in figure 4.3.

1922 We attempt to uniquely match one wire chamber track (see Section 3.2.2) to one  
 1923 and only one reconstructed TPC track. In order to determine if a match is present,  
 1924 we apply a geometrical selection on the relative position of the wire chamber and  
 1925 TPC tracks. We start by considering only TPC tracks whose first point is in the first  
 1926 2 cm upstream portion of the TPC for the match. We project the wire chamber track  
 1927 to the TPC front face where we define the coordinates of the projected point as  $x_{FF}$   
 1928 and  $y_{FF}$ . For each considered TPC track, we define  $\Delta X$  as the difference between  
 1929 the  $x$  position of the most upstream point of the TPC track and  $x_{FF}$ .  $\Delta Y$  is defined  
 1930 analogously. We define the radius difference,  $\Delta R$ , as  $\Delta R = \sqrt{\Delta X^2 + \Delta Y^2}$ . We define  
 1931 as  $\alpha$  the angle between the incident WC track and the TPC track in the plane that  
 1932 contains them. If  $\Delta R < 4$  cm,  $\alpha < 8^\circ$ , a match between WC-track and TPC track is  
 1933 found. We describe how we determine the value for the radius and angular selection  
 1934 in Section ???. We discard events with multiple WC2TPC matches. We use only those  
 1935 TPC tracks that are matched to WC tracks in the cross section calculation. Line 6  
 1936 in Table 4.1 shows the number of events where a unique WC2TPC match was found.

1937 In MC, we mimic the matching between the WC and the TPC track by construct-  
 1938 ing an artificial WC track using truth information at wire chamber four. We then  
 1939 apply the same WC to TPC matching algorithm as in data.

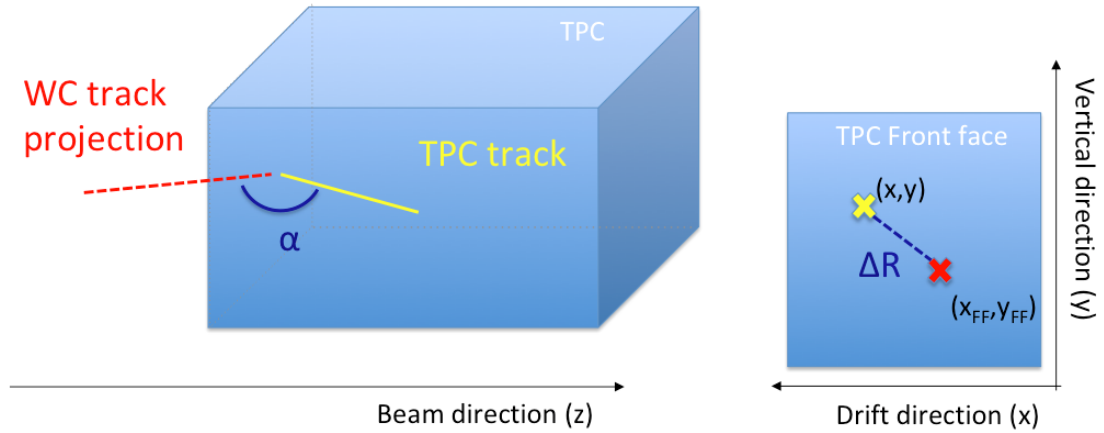


Figure 4.4: Visual rendering of the wire chamber to TPC match.

## 1940 4.3 The Thin Slice Method

1941 Once we have selected the 40841 beamline pion candidates and the 1081 beamline  
1942 kaon candidates, and we have identified the TPC corresponding track, we apply the  
1943 thin slice method to measure the cross section, as the following sections describe.

### 1944 4.3.1 Cross Sections on Thin Target

1945 Cross section measurements on a thin target have been the bread and butter of  
1946 nuclear and particle experimentalists since the Geiger-Marsden experiments [67]. At  
1947 their core, this type of experiments consists in shooting a beam of particles with a  
1948 known flux on a thin slab of material and recording the outgoing flux.

1949 In general even in the case of thin target, the target is not a single particle,  
1950 but rather a slab of material containing many diffusion centers. The so-called “thin  
1951 target” approximation assumes that the target centers are uniformly distributed in  
1952 the material and that the target is thin compared to the projectile interaction length,  
1953 so that no center of interaction sits in front of another. In this approximation, the  
1954 ratio between the number of particles interacting in the target  $N_{\text{Int}}$  and the number of  
1955 incident particles  $N_{\text{Inc}}$  on the target estimates the interaction probability  $P_{\text{Interacting}}$ ,

1956 which is the complementary to one of the survival probability  $P_{Survival}$ . Equation 4.2

$$P_{Survival} = 1 - P_{Interacting} = 1 - \frac{N_{Int}}{N_{Inc}} = e^{-\sigma_{TOT} n \delta X} \quad (4.2)$$

1957 describes the probability for a particle to survive the thin target. This formula relates  
1958 the interaction probability to the total hadronic cross section ( $\sigma_{TOT}$ ), the density of  
1959 the target centers ( $n$ )<sup>1</sup> and the thickness of the target along the incident hadron  
1960 direction ( $\delta X$ ). If the target is thin compared to the interaction length of the process  
1961 considered, we can Taylor expand the exponential function in equation 4.2 and find  
1962 a simple proportionality relationship between the cross section and the number of  
1963 incident and interacting particles, as shown in equation 4.3:

$$1 - \frac{N_{Int}}{N_{Inc}} = 1 - \sigma_{TOT} n \delta X + O(\delta X^2). \quad (4.3)$$

1964 Solving for the cross section, we find:

$$\sigma_{TOT} = \frac{1}{n \delta X} \frac{N_{Int}}{N_{Inc}}. \quad (4.4)$$

### 1965 4.3.2 Not-so-Thin Target: Slicing the Liquid Argon Volume

1966 The interaction length of pions and kaons in liquid argon is expected to be of the  
1967 order of 50 cm for pions and 100 cm for kaons. Thus, the LArIAT TPC, with its 90  
1968 cm of length, is not a thin target. However, the fine-grained tracking of the LArIAT  
1969 LArTPC allows us to treat the argon volume as a sequence of many adjacent thin  
1970 targets.

1971 As described in Chapter 3, LArIAT induction and collection planes consist of 240  
1972 wires each at 4 mm spacing. The wires are oriented at +/- 60° from the vertical

---

1. The scattering center density in the target,  $n$ , relates to the argon density  $\rho$ , the Avogadro number  $N_A$  and the argon molar mass  $m_A$  as  $n = \frac{\rho N_A}{m_A}$ .

1973 direction, while the beam direction is oriented 3 degrees off the  $z$  axis in the  $XZ$   
 1974 plane. The collection wires collect signals proportional to the energy deposited by  
 1975 the hadron along its path in a  $\delta X = 4 \text{ mm}/(\sin(60^\circ)\cos(3^\circ)) \approx 4.7 \text{ mm}$  slab of liquid  
 1976 argon. Thus, one can think to slice the TPC into many thin targets of  $\delta X = 4.7 \text{ mm}$   
 1977 thickness along the direction of the incident particle, making a measurement at each  
 1978 wire along the path.

1979 Considering each slice  $j$  a “thin target”, we can apply the cross section calculation  
 1980 from Equation 4.4 iteratively, evaluating the kinetic energy of the hadron as it enters  
 1981 each slice,  $E_j^{kin}$ . For each WC2TPC matched particle, the energy of the hadron  
 1982 entering the TPC is known thanks to the momentum and mass determination by the  
 1983 tertiary beamline,

$$E_{FrontFace}^{kin} = \sqrt{p_{Beam}^2 - m_{Beam}^2} - m_{Beam} - E_{loss}, \quad (4.5)$$

1984 where  $E_{loss}$  is a correction for the kinetic energy loss in the uninstrumented material  
 1985 between the beamline and the TPC front face. While propagating through the target,  
 1986 the kinetic energy of the hadron at each slab is determined by subtracting the energy  
 1987 deposited by the particle in the previous slabs. For example, at the  $j^{th}$  slab of a track,  
 1988 the kinetic energy will be

$$E_j^{kin} = E_{FrontFace}^{kin} - \sum_{i < j} E_{Dep,i}, \quad (4.6)$$

1989 where  $E_{Dep,i}$  is the energy deposited at each argon slice before the  $j^{th}$  point as mea-  
 1990 sured by the calorimetry associated with the tracking.

1991 If the particle enters a slice, it contributes to the  $N_{Inc}(E^{kin})$  distribution in the  
 1992 energy bin corresponding to its kinetic energy in that slice. While into the slice, a  
 1993 hadron may or may not interact. If it interacts in the slice, it contributes also to the  
 1994  $N_{Int}(E^{kin})$  distribution in the appropriate energy bin; this occurrence corresponds to

	min	max
X	1 cm	46 cm
Y	-15 cm	15 cm
Z	0 cm	86 cm

Table 4.2: Fiducial volume boundaries used to determine cross section interaction point.

the end of the hadron tracking. If the hadron does not interact, it will enter the next slice and the interaction evaluation starts again. The process is applied to all the hadrons in the sample; the cross section as a function of kinetic energy,  $\sigma_{TOT}(E^{kin})$  is then evaluated to be proportional to the ratio  $\frac{N_{Int}(E^{kin})}{N_{Inc}(E^{kin})}$  – bin by bin ratio.

Our goal is to measure the total interaction cross section, independently from the topology of the interaction. Thus, we determine that a hadron interacted simply by requiring that the last point of the WC2TPC matched track lies in a slice within the fiducial volume, whose boundaries are defined in Table 4.2. If the TPC track ends within the fiducial volume, its last point will be the interaction point; if the track crosses the boundaries of the fiducial volume, the track will be considered “through going” and no interaction point will be found. The only points of the hadronic candidate track considered to fill the  $N_{Int}$  and  $N_{Inc}$  distributions are the ones contained in the fiducial volume.

A notable background pertinent only to the  $N_{Int}$  distribution are cases in which the hadrons decays inside the TPC. In those cases in fact, the tracking ends inside the TPC but the interaction is not hadronic. The handling of decay background is treated in a slightly different way for the pion and kaon section, details can be found in sections 5.3 and 7.1 respectively.

### 4.3.3 Corrections to the Raw Cross Section

Equation 4.4 is a prescription for measuring the cross section in case of a pure beam of the hadron of interest and 100% efficiency in the determination of the interaction

2016 point. For example, if LArIAT had a beam of pure pions and were 100% efficient in  
 2017 determining the interaction point within the TPC, the pion cross section as a function  
 2018 of kinetic energy (estimated at the central value of the energy bin  $E_i$ ) would be given  
 2019 by

$$\sigma_{TOT}^{\pi^-}(E_i) = \frac{1}{n\delta X} \frac{N_{Int}^{\pi^-}(E_i)}{N_{Inc}^{\pi^-}(E_i)}. \quad (4.7)$$

2020 Unfortunately, this is not the case. In fact, the selection used to isolate pions in  
 2021 the LArIAT beam allows for the presence of some muons and electrons as background,  
 2022 while the kaon selection allows for a small contamination of protons (see Section 5.2.1).  
 2023 Also, the LArIAT TPC tracking algorithm is not 100% efficient in determining the  
 2024 interaction point. Therefore we need to apply two corrections evaluated on the MC in  
 2025 order to extract the final cross section from LArIAT data: i) a background subtraction  
 2026 and ii) a correction for reconstruction effects. Still using the pion case as example,  
 2027 we estimate the pion cross section in each energy bin changing Equation 4.7 into

$$\sigma_{TOT}^{\pi^-}(E_i) = \frac{1}{n \delta X} \frac{N_{Int}^{\pi^-}(E_i)}{N_{Inc}^{\pi^-}(E_i)} = \frac{1}{n \delta X} \frac{\epsilon^{Inc}(E_i)[N_{Int}^{TOT}(E_i) - B_{Int}(E_i)]}{\epsilon^{Int}(E_i)[N_{Inc}^{TOT}(E_i) - B_{Inc}(E_i)]}, \quad (4.8)$$

2028 where  $N_{Int}^{TOT}(E_i)$  and  $N_{Inc}^{TOT}(E_i)$  is the measured content of the interacting and  
 2029 incident histograms for events that pass the event selection,  $B_{Int}(E_i)$  and  $B_{Inc}(E_i)$   
 2030 represent the contributions from the background to the interacting and incident his-  
 2031 tograms respectively, and  $\epsilon^{Int}(E_i)$  and  $\epsilon^{Inc}(E_i)$  are the corrections for reconstruction  
 2032 effects.

2033 As we will show in section 5.3, the background subtraction for the interacting and  
 2034 incident histograms can be translated into corresponding relative pion content factors  
 2035  $C_{Int}^{\pi MC}(E_i)$  and  $C_{Inc}^{\pi MC}(E_i)$  and the cross section re-written as follows

$$\sigma_{TOT}^{\pi^-}(E_i) = \frac{1}{n \delta X} \frac{\epsilon^{Inc}(E_i)}{\epsilon^{Int}(E_i)} \frac{C_{Int}^{\pi MC}(E_i)}{C_{Inc}^{\pi MC}(E_i)} \frac{N_{Int}^{TOT}(E_i)}{N_{Inc}^{TOT}(E_i)}. \quad (4.9)$$

## 2036 4.4 Procedure testing with MC truth quantities

2037 The  $(\pi^-, \text{Ar})$  and  $(K^+, \text{Ar})$  total hadronic cross section implemented in Geant4 can  
2038 be used as a tool to validate the measurement methodology. We describe here a  
2039 closure test done on Monte Carlo to prove that the methodology of slicing the TPC  
2040 retrieves the underlying cross section distribution implemented in Geant4 within the  
2041 MC statistical uncertainty.

2042 For pions and kaons in the considered energy range, the Geant4 inelastic model  
2043 adopted is “BertiniCascade”; the pion elastic cross sections are tabulated from Chips,  
2044 while the kaon elastic cross sections are tabulated on Gheisha and Chips.

2045 For the validation test, we fire a sample of pions and a sample of kaons inside  
2046 the LArIAT TPC active volume using the Data Driven Monte Carlo, a procedure  
2047 described in Section 5.2.2. We apply the thin-sliced method using only true quantities  
2048 to calculate the hadron kinetic energy at each slab in order to decouple reconstruction  
2049 effects from possible issues with the methodology. For each slab of 4.7 mm length  
2050 along the path of the hadron, we integrate the true energy deposition as given by  
2051 the Geant4 transport model. Then, we recursively subtracted it from the hadron  
2052 kinetic energy at the TPC front face to evaluate the kinetic energy at each slab until  
2053 the true interaction point is reached. Since the MC is a pure beam of the hadron of  
2054 interest and truth information is used to retrieve the interaction point, no background  
2055 correction or reconstruction effects correction is applied. Doing so, we obtain the true  
2056 interacting and incident distributions for the considered hadron, whose ratio leads to  
2057 the true MC cross section as a function of the hadron kinetic energy.

2058 Figure 4.5 shows the total hadronic cross section for argon implemented in Geant4  
2059 10.03.p1 (solid lines) overlaid with the true MC cross section as obtained with the  
2060 sliced TPC method (markers) for pions on the left and kaons on the right; the total  
2061 cross section is shown in green. For completeness, we also report the contributions  
2062 from the elastic cross section (in blue) and the inelastic cross section (in red), available

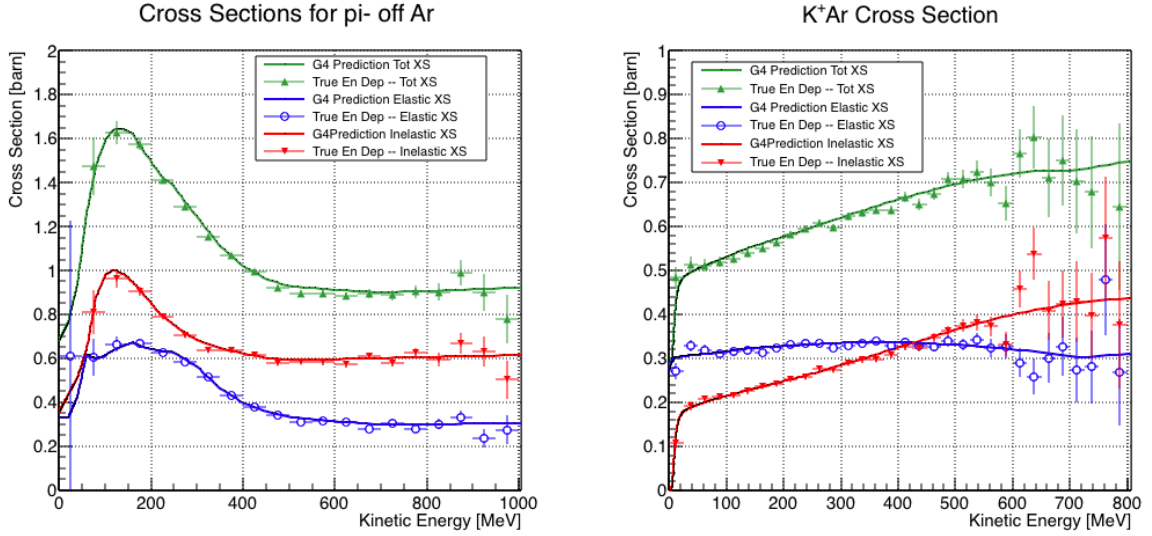


Figure 4.5: Hadronic cross sections for  $(\pi^-, \text{Ar})$  on the left and  $(K^+, \text{Ar})$  on the right as implemented in Geant4 10.03.p1 (solid lines) overlaid the true MC cross section as obtained with the sliced TPC method (markers). The total cross section is shown in green, the elastic cross section in blue and the inelastic cross section in red.

at the MC level. The nice agreement with the Geant4 distribution and the cross section obtained with the sliced TPC method gives us confidence in the validity of the methodology.

2066 **Chapter 5**

2067 **Data and MC preparation for the**  
2068 **Cross Section Measurements**

2069 “*Il dolce non lo mangi mai, ma qualche volta ti rifai.*  
2070 *Abbracciami*”  
2071 – Pietro Ciampi, 1971 –

2072 This chapter describes the work done on the data and Monte Carlo samples in  
2073 preparation for the cross section analyses. This entails the choice of the datasets  
2074 and the production of the information needed to construct the Monte Carlo Simula-  
2075 tion (Section 5.1), the construction and use of said Monte Carlo simulation (section  
2076 5.2), the study of backgrounds for the pion cross section (Section 5.3), the study of  
2077 the energy loss between WC4 and TPC (Section 5.4), the study of the tracking in the  
2078 TPC (Section 5.5), and study of the calorimetry response (Section 5.6).

2079 **5.1 Cross Section Analyses Data Sets**

2080 We choose LArIAT Run-II as the data period for the ( $\pi^-$ ,Ar) and ( $K^+$ ,Ar) total  
2081 hadronic cross section analyses. Data taking for the this period started on 03/15/2016

2082 and ended on 07/31/2016. Since we are interested in beamline and TPC information,  
2083 we ask basic requirements on the operational status of the time of flight counters, wire  
2084 chambers and TPC to form the good run list for this period, which we informally call  
2085 “lovely runs”.

2086 The subset of lovely runs chosen for the ( $\pi^-$ ,Ar) total hadronic cross section  
2087 analysis includes only the -60A and -100A magnet configurations in negative polarity,  
2088 even if LArIAT explored several other beamline configurations during Run-II. The -  
2089 60A and -100A combined data set accounts for approximately 90% of the total Run-II  
2090 negative polarity runs. The choice of these two main beamline settings limits the need  
2091 for the production of many different MC sets and related corrections, still maintaining  
2092 a high number of events.

2093 Similarly, the subset of lovely runs chosen for the ( $K^+$ ,Ar) total hadronic cross  
2094 section analysis includes only the +60A and +100A magnet configurations in positive  
2095 polarity. It should be noted that kaons are extremely rare in the +60A sample, thus  
2096 the data sample for the ( $K^+$ ,Ar) cross section after the mass selection is about 90%  
2097 +100A runs, as shown in Table 5.1.

2098 For these first measurements that make use of both the LArIAT beamline and  
2099 TPC information, we choose strict requirements on the reconstruction of the WC  
2100 tracks, the so-called “Picky Track” sample (see Section 3.2.2), where we require a  
2101 single hit in each and every wire chamber detector to reconstruct the WC track. This  
2102 choice presents two advantages: the uncertainty on the momentum reconstruction  
2103 for the “Picky Tracks” sample is smaller compared to the “High Yield” sample, and  
2104 the comparison with the beamline MC results is straightforward. A possible future  
2105 update and cross check of these analysis would be the use of the High Yield sample,  
2106 where the statistics is about three times higher.

2107 The breakdown of beamline events as a function of the magnets settings is shown  
2108 in Table 5.1. The choice of the data sets determines the production of beamline MC

2109 and serves as basis for the production of Data Driven MC, as shown in the next  
2110 sections.

## 2111 **5.2 Construction of a Monte Carlo Simulation for** 2112 **LArIAT**

2113 For the simulation of LArIAT events and for the simulation of the datasets' particle  
2114 make up, we use a combination of two MC generators: the G4Beamline Monte Carlo  
2115 and the Data Driven single particle Monte Carlo (DDMC). We use the G4Beamline  
2116 MC to simulate the particle transport in the LArIAT tertiary beamline and calculate  
2117 the particle composition of the beam just after the last Wire Chamber (WC4). We  
2118 use the DDMC to simulate the particles after WC4 along the beamline, close to the  
2119 beam window in the LAr cryostat and in the TPC.

### 2120 **5.2.1 G4Beamline**

2121 G4Beamline simulates the beam collision at the LArIAT secondary target, the energy  
2122 deposited by the particles in the LArIAT beamline detectors, and the action of the  
2123 LArIAT magnets, effectively accounting for particle transport through the beamline  
2124 from the LArIAT target until “Big Disk”, a fictional, void detector located just before  
2125 the LArIAT cryostat. At the moment of this writing, G4Beamline does not simulated  
2126 the responses of the beamline detectors. It is possible to interrogate the truth level  
2127 information of the simulated particles in several points of the geometry. In order

	I = 60 A	I = 100 A	Total
Data Events after $\pi/\mu/e$ Mass Selection	67068	71413	138481
Data Events after $K$ Mass Selection	274	2563	2837

Table 5.1: Number of data events which fit the  $\pi/\mu/e$  or  $K$  mass hypothesis as a function of magnet settings.

2128 to ease the handshake between G4Beamline and the DDMC, we ask for the beam  
2129 composition just after WC4. Since LArIAT data are taken under different beam  
2130 conditions, we need to simulate separately the beam composition according to the  
2131 magnets' settings and the secondary pion beam intensity with G4Beamline. For the  
2132 pion cross section analysis the relevant beam conditions are secondary pion beam  
2133 energy of 64 GeV, negative polarity magnet with current of 100 A and 60 A. For the  
2134 kaon cross section analysis the relevant beam conditions is a secondary pion beam  
2135 energy of 64 GeV, positive polarity magnet with current of 100 A.

2136 **Beam Composition for Negative Pion Cross Section**

2137 Even if pions are by far the biggest beam component in negative polarity runs, the  
2138 LArIAT tertiary beam is not a pure pion beam. While useful to discriminate between  
2139 pions, kaons, and (anti)protons, the beamline detectors are not sensitive enough to  
2140 discriminate among the lighter particles in the beam: electrons, muons and pions  
2141 fall under the same mass hypothesis. Thus, we need to assess the contamination  
2142 from beamline particles other than pions in the event selections used for the pion  
2143 cross section analysis and correct for this background. The first step of this process is  
2144 assessing the percentage of electrons and muons in the  $\pi/\mu/e$  beamline candidates via  
2145 the G4Beamline MC, as we deem the percentage of kaons and antiprotons negligible  
2146 after the mass selection ( $\pm 1\%$ ). Since the beamline composition is a function of  
2147 the magnet settings, we simulate separately events for magnet current of -60A and  
2148 -100A. Figure 5.1 shows the momentum predictions from G4Beamline overlaid with  
2149 data for the 60A runs (left) and for the 100A runs (right). The predictions for  
2150 electrons, muons and pions have been staggered and their sum is area normalized  
2151 to data. Albeit not perfect, these plots show a reasonable agreement in momentum  
2152 shapes between data and MC. We attribute the difference in shape (longer tail in  
2153 data) to a two approximations performed in the MC. Firstly, G4Beamline lacks the

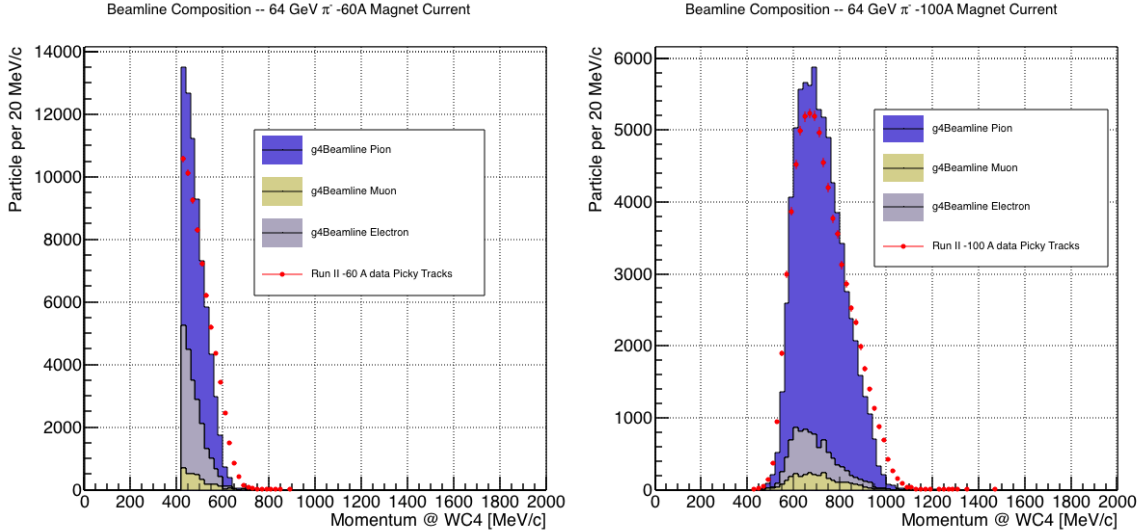


Figure 5.1: Beam composition for the -60A runs (left) and -100A runs (right). The solid blue plot represents the simulated pion content, the yellow plot represents the simulated muon content and the grey plot represents the simulated electron content. The plots are area normalized to the number of data events, shown in red.

	I = -60 A	I = -100 A
G4Pions	68.8 %	87.4 %
G4Muons	4.6 %	3.7 %
G4Electrons	26.6 %	8.9 %

Table 5.2: Simulated beamline composition per magnet settings

simulation of the WC efficiency which is momentum dependent and leads to enhance the number events in the center of the momentum distribution. Secondly, G4Beamline stop tracking pions and their products if they decay after WC1; in data, pion decays in flight can still create a trigger if the produced muon travels thought the beamline detectors. In the pion cross section analysis, these differences between data and the G4Beamline prediction are accounted for as a systematic uncertainty related to the beam composition (see Section 6.2.1).

Table 5.2 shows the beam composition per magnet setting after the mass selection according to the G4Beamline simulation.

The estimated beam composition is used as a basis to estimate the background contamination in the ( $\pi^-$ ,Ar) cross section measurement, whose full treatment is

2165 described in section 5.3.

## 2166 Beam Composition for Positive Kaon Cross Section

2167 In the positive polarity runs, the tertiary beam composition is mainly pions and  
2168 protons. The left side of Figure 5.2 shows the predictions for the momentum spectra  
2169 for the 100A positive runs according to G4Beamline (solid colors) overlaid with data  
2170 (black points). Since the LArIAT beamline detectors can discriminate between kaons  
2171 and other particles, we do not rely on the G4Beamline simulation to estimate the  
2172 beamline contamination in the pool of kaon candidates (as in the case of the pion  
2173 cross section), but rather we use a data driven approach. The basic idea of this data  
2174 driven approach is to estimate the bleed over from high and low mass peaks under  
2175 the kaon peak by fitting the tails of the  $\pi/\mu/e$  and proton mass distributions, as  
2176 shown in Figure 5.2 right side. Since the shape of the tails is unknown, the estimate  
2177 is done multiple times varying the range and shape for reasonable functions. For  
2178 example, to estimate the proton content under the kaon peak, we start by fitting the  
2179 left tail of the proton mass distribution with a gaussian function between  $650 \text{ MeV}/c^2$   
2180 and  $750 \text{ MeV}/c^2$ . We extend the fit function under the kaon peak and integrate the  
2181 extended fit function between  $350-650 \text{ MeV}/c^2$ . We integrate the mass histogram  
2182 in the same range and calculate the proton contamination as the ratio between the  
2183 two integrals. We repeat this procedure for several fit shapes (gaussian, linear and  
2184 exponential functions) and tail ranges. Finally, we calculate the contamination as  
2185 the weighted average of single estimates, where the weights are calculated to be the  
2186  $1./|1 - \chi^2|$  of the tail fits. The procedure is repeated for lighter particles mass peak  
2187 independently. With 12 iterations of this method we find a proton contamination of  
2188  $5.0 \pm 2.0 \%$  and a contamination from the lighter particles of  $0.2 \pm 0.5 \%$ . The  
2189 estimate of the proton background is currently not used in the kaon cross section  
2190 analysis, but it is a fundamental step to retrieve the true kaon cross section which

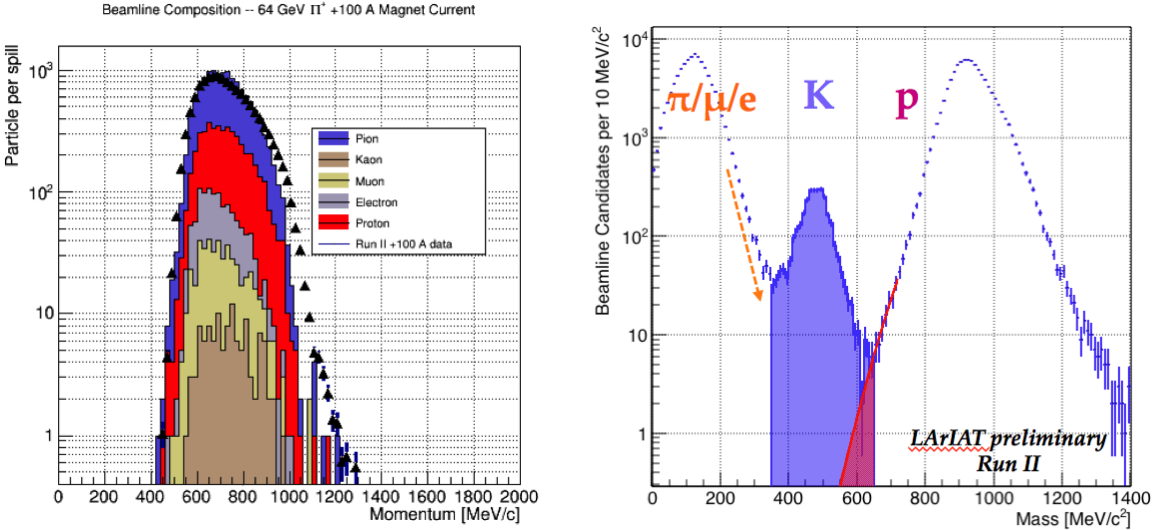


Figure 5.2: *Left:* Beam composition for the +100A runs after WC4 (no mass selection applied). The solid colors represent the contributions from the G4Beamline simulated particles: blue plot represents the simulated pion content, the yellow plot represents the simulated muon content and the grey plot represents the simulated positron content, the red the proton content and the mustard the kaon content. The plots are area normalized to the number of data events, shown in black. *Right:* Mass distribution for the Run-II positive runs, where the area under the kaon mass peak is highlighted in purple. The area under the extension of a possible fit for the proton tail is highlighted in red.

2191 will be implemented in the further development of the analysis.

## 2192 5.2.2 Data Driven MC

2193 The Data Driven single particle Monte Carlo (DDMC) is a single particle gun which  
 2194 simulates the particle transport from WC4 into the TPC leveraging on the beamline  
 2195 data information. The DDMC uses the data momentum and position at WC4 to  
 2196 derive the event generation: a general sketch of the DDMC workflow is shown in  
 2197 Figure 5.3.

2198 When producing a DDMC sample, beamline data from a particular running pe-  
 2199 riod and/or running condition are selected first. For example, data for the negative  
 2200 60A runs and for the negative 100A runs inform the event generation stage of two  
 2201 different DDMC samples. Figure 5.4 schematically shows the data quantities of in-

terest leveraged from data: the momentum ( $P_x, P_y, P_z$ ) and position ( $X, Y$ ) at WC4.  
For each data event, we obtain the particle position ( $X, Y$ ) at WC4 directly from the  
data measurement; we calculate the components of the momentum using the beam-  
line measurement of the momentum magnitude in conjunction with the hits on WC3  
and WC4 to determine the direction of the momentum vector, as described in section  
3.2.2. The momentum and position of the selected data events form a 5-dimensional  
series of tuples. The DDMC event generator samples from the joint distribution  
of these five quantities using a 5-dimensional hit-or-miss sampling procedure. This  
sampling generates MC events with the same momentum and position distributions  
as data, with the additional benefit of accounting for the correlations between the  
 $P_x, P_y, P_z, X, Y$  variables. As an example, the results of the DDMC generation com-  
pared to data for the kaon +100A sample are shown in figure 5.5 for the  $P_z, X$  and  $Y$   
distributions; as expected, MC and data agree within the statistical uncertainty by  
construction. A LArSoft simulation module then launches single particle MC from  
 $z = -100$  cm (the location of the WC4) using the generated events. The particles  
are free to decay and interact in their path from WC4 to the TPC according to the  
Geant4 simulation.

Using the DDMC technique ensures that the MC and data particles have very  
similar momentum, position and angular distributions at WC4 and allows us to use  
the MC sample in several occasions: to estimate the background contamination to  
the pion cross section (see Section 5.3), to calibrate the energy loss upstream of the  
TPC (see Section 5.4), and to study the tracking and the calorimetric performance  
in the LArTPC (sections 5.5 and 5.6). A small caveat is in order here: the DDMC is  
a single particle Monte Carlo, which means that the beam pile-up is not simulated.

We generate six samples for the pion cross section measurement: three samples  
of  $\sim 330000$  pions, muons and electrons to simulate the negative 60A runs, and three  
samples of  $\sim 340000$  pions, muons and electrons for the negative 100A runs. We

2229 generate a sample of 195000 kaons for the kaon cross section analysis.

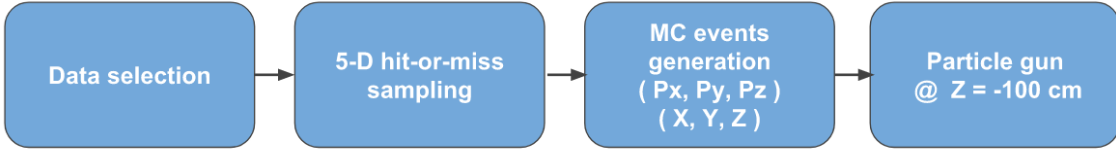


Figure 5.3: Workflow for Data Driven single particle Monte Carlo production.

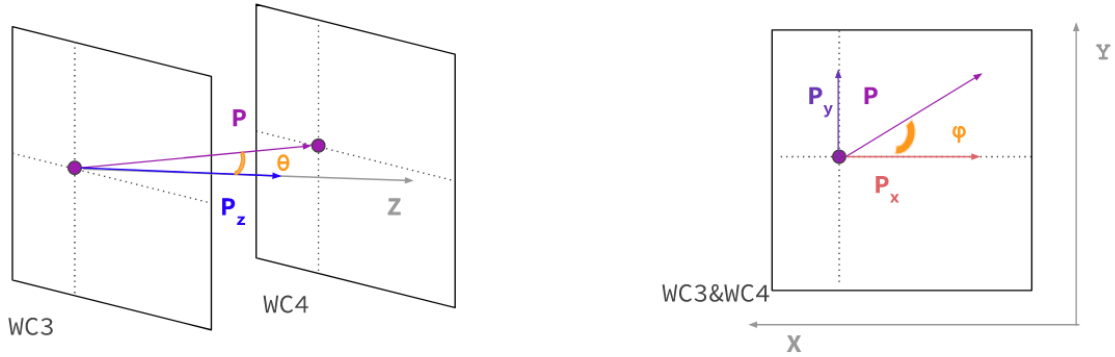


Figure 5.4: Scheme of the quantities of interest for the DDMC event generation:  $P_x, P_y, P_z, X, Y$  at WC4.

## 2230 5.3 Estimate of Backgrounds in the Pion Cross Section

2231 We use the beamline simulation and the DDMC simulation to estimate the background in the total hadronic pion cross section. Two categories of background exists for the negative pion cross section measurement: the background related to the pion alternative processes to hadronic interaction inside the LArTPC, discussed in Section 5.3.1 and the background related to the beamline contamination, discussed in Section 5.3.2.

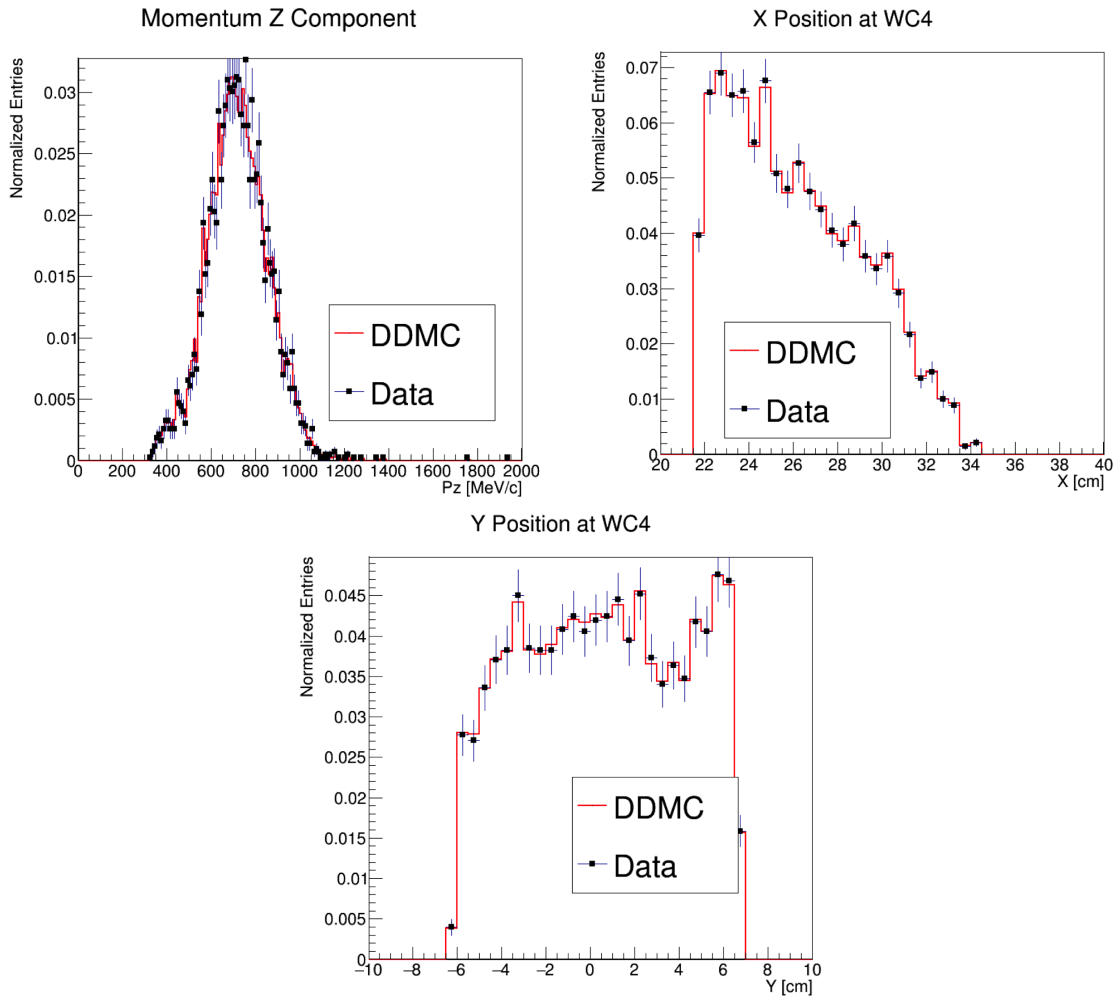


Figure 5.5: Comparison between generated quantities and data distributions for the 100A kaon sample: Z component of the momentum at WC4 (top left), X position at Wire Chamber 4 (top right), Y position at Wire Chamber 4 (bottom).

2238 **5.3.1 Background from Pion Capture and Decay**

2239 Our goal is to measure the total hadronic cross section for negative pions in argon.  
2240 Since pion capture can be classified as an electromagnetic process and pion decay is a  
2241 weak process (as discussed in Section 1.4.1), capture and decay represent alternative  
2242 processes to the hadronic interaction, resulting therefore into a background for the  
2243 cross section analysis. We present here a study of capture and decay in Monte Carlo  
2244 and the solution we adopted to remove their occurrence in the data sample.

2245 For this MC study, we use a sample of MC pions generated according to the  
2246 –60A beam profile with the DDMC (see Section 5.2.2). It is important to notice  
2247 that capture occurs predominantly at rest, while decay may occur both in flight  
2248 and at rest. Thus, we can highly mitigate capture and decay at rest by removing  
2249 pions whose kinetic energy at the TPC front face is low enough to be completely  
2250 released by ionization in the TPC, eventually bringing the pion to stop within the  
2251 fiducial volume. This translates into a beam momentum selection, where we keep  
2252 only events whose WC momentum is above a certain threshold. Figure 5.6 shows the  
2253 true momentum distribution for the primary pions<sup>1</sup> that arrive to the TPC (pink),  
2254 that capture (green) or decay (blue) inside the TPC, on a linear scale (left) and on a  
2255 log scale (right) vertical axis.

2256 In order to choose the selection value for the wire chamber momentum, it is  
2257 beneficial to estimate the fraction of MC capture and decay events that survive the  
2258 momentum selection as a function of the momentum threshold, and compare it with  
2259 the survival fraction for all the 60A events. This is done in figure 5.7. We define the  
2260 survival ratio simply as the number of events surviving the true momentum selection  
2261 divided by the number of events of that category. We calculate the survival ratio

---

1. We use here the Geant4 denomination “primary” to indicate that the pion considered does not undergo interactions modifying its energy before getting to the TPC. In fact, not every pion shot from wire chamber four will arrive to the TPC as primary, some will decay or interact before the TPC.

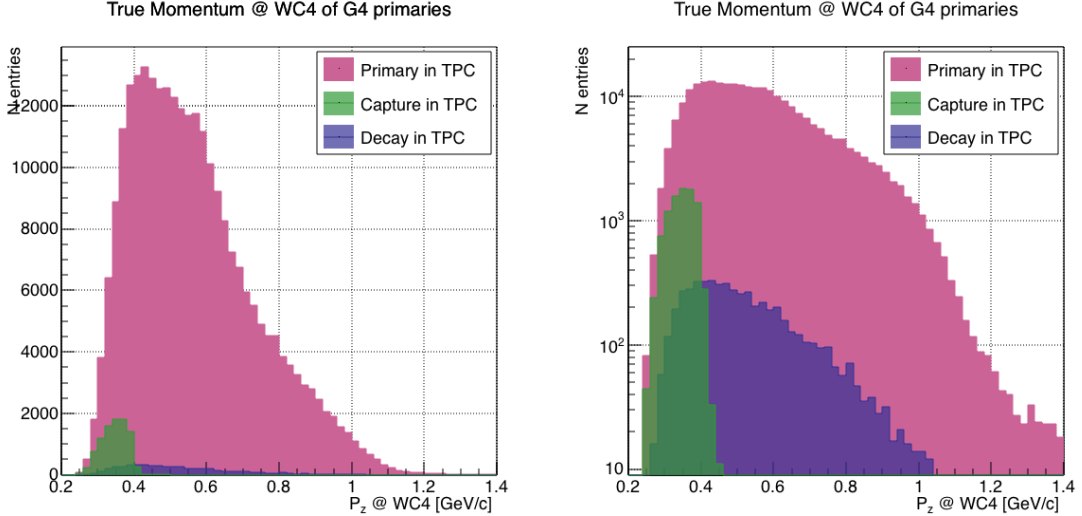


Figure 5.6: MC momentum distribution at wire chamber 4 for every simulated pion arriving in the TPC (pink), ending its life in capture (green) or in decay (blue) in the TPC, linear vertical axis on the left, logarithmic on the right.

2262 separately for the three event categories explained above: total (pink), capture (green)  
 2263 and decay (blue). Selecting pions with momentum greater than 420 MeV/c removes  
 2264  $\sim 99\%$  the capture events while maintaining about 80% of the 60A data sample and  
 2265 almost the entire 100A sample. Figure 5.8 shows the ratio of events which end their  
 2266 life in capture (green) or decay (blue) over the total number of events as a function  
 2267 of the true MC momentum at WC4. This ratio is slightly dependent on the inelastic  
 2268 cross section implemented in Geant4, as we are able to register a pion capture (or  
 2269 decay) only if it did not interact inelastically in the TPC. We choose a momentum  
 2270 threshold of 420 MeV/c because the percentage of capture events drops below 1% and  
 2271 the percentage of decays is never above 2% for momenta greater than 420 MeV/c.  
 2272 After the momentum selection, we evaluate the contribution of capture and decay to  
 2273 be a negligibly small background to the cross section measurement compared to the  
 2274 background related to the beamline which we will address in the next section.

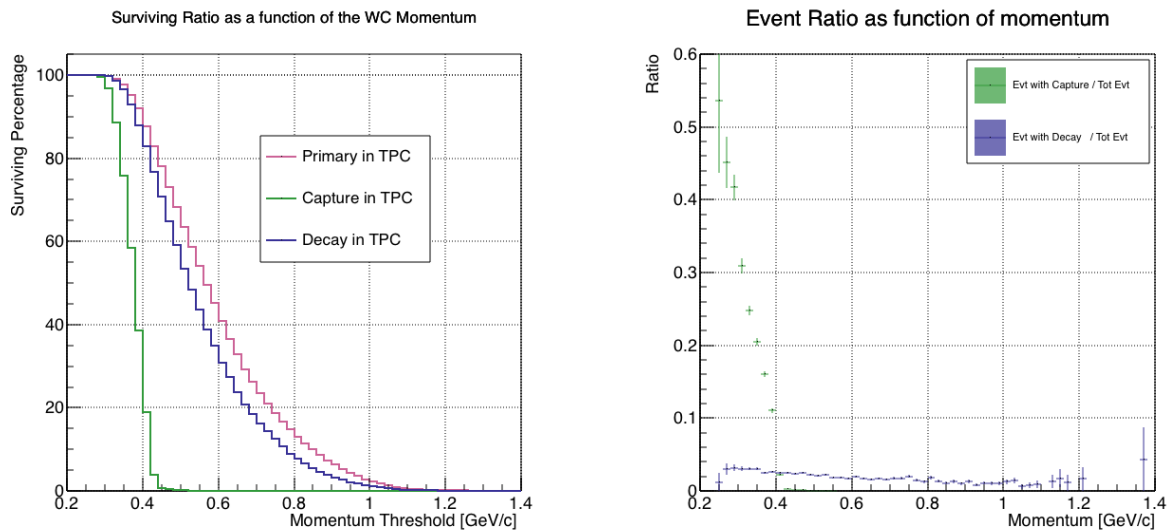


Figure 5.7: Survival ratio as a function of selection threshold on MC momentum at wire chamber four for every simulated pion arriving in the TPC (pink), capture (green) or in decay (blue).

Figure 5.8: Ratio between the capture (green) and decay (blue) events over the total number of events as a function of the MC momentum at wire chamber four.

2275 **5.3.2 Contributions from the Beamline Background**

2276 We define beamline background every TPC track matched to the WC track which is  
2277 not a primary pion. Potentially, there are 4 different types of beamline background:

2278 1) electrons,

2279 2) muons,

2280 3) secondaries from pion interactions in beamline elements,

2281 4) matched pile up events.

2282 The first step to quantify the effect of the beamline background on the pion cross  
2283 section is to estimate what percentage of events used in the cross section calculation is  
2284 not a primary pion. We start by noting that the last type of background, the “matched  
2285 pile up” events, is a negligible fraction, because of the definition of the WC2TPC  
2286 match: we deem the probability of a single match with a halo particle in the absence of  
2287 a beamline particle<sup>2</sup> negligibly small. As shown in Section 5.2.1, we use G4Beamline  
2288 to estimate the percentage of pions, muons and electrons at WC4, obtaining the  
2289 composition shown in Table 5.2. The next step is to simulate those pions, muons and  
2290 electrons from WC4 to the TPC with the DDMC and evaluate their contribution to  
2291 the cross section. To do so, we start by generating the same number of electrons,  
2292 muons and pions with the DDMC and we apply the same selection chain applied in  
2293 data (i.e. track multiplicity rejection, WC2TPC match and shower rejection) on the  
2294 three samples. The number of events per particle species surviving this selection is  
2295 shown on table 5.3. In order to reproduce the data beamline composition, we weight  
2296 each event of a given particle species according to the estimated content for that  
2297 species as found with the G4Beamline simulation. In case of 60A runs, for example,  
2298 the weights are 0.688 for pions, 0.046 for muons and 0.266 for electrons.

---

2. Events with multiple WC2TPC matches are always rejected.

	Magnet Current -60A			Magnet Current -100 A		
	MC $\pi^-$	MC $\mu^-$	MC $e^-$	MC $\pi^-$	MC $\mu^-$	MC $e^-$
Total Initial events	334500	334500	334500	344500	344500	344500
After Multiplicity Rejection	330668	333420	198065	326576	344208	201380
After WC2TPC Selection	218239	296333	91139	230418	300228	98834
Evts After Shower Rejection	208063	288914	20293	219882	293585	17780
Selection Survival Rate	62.2%	86.4%	6.1%	63.8%	85.2%	5.2%
Beam Composition @WC4	68.8%	4.6 %	26.6 %	87.4 %	3.7 %	8.9 %
Expected Composition in XS sample	88.5%	8.2%	3.3 %	94.0%	5.3%	0.7%

Table 5.3: MC selection flow per particle species.

2299 It should be noted that pions may interact hadronically in the steel (cryostat wall)  
 2300 or in the non-instrumented argon upstream to the TPC front face while traveling the  
 2301 length of between WC4 and the TPC. Or, they could decay in flight between WC4  
 2302 and the TPC. One of the interaction or decay products can leak into the TPC and  
 2303 be matched with the WC track, contributing to the pool of events used for the cross  
 2304 section calculation. We call this type of particles “secondaries” from pion events,  
 2305 with a terminology inspired by Geant4. We estimate the number of secondaries using  
 2306 the DDMC pion sample. The percentage of secondaries is given by the number of  
 2307 matched WC2TPC tracks whose corresponding particle is not flagged as primary by  
 2308 Geant4. The secondary particles to primary pion ratio is 4.9% in the 60A sample and  
 2309 4.3% in the 100A sample.

2310 We evaluate the beamline background contribution to the cross section by pro-  
 2311 ducing the interacting and incident histograms for the signal and background events  
 2312 surviving the selection, staggering the contributions for each particle species, as shown  
 2313 in Figure 5.9 for the -60A case and in Figure 5.10 for the -100A case. From those  
 2314 histograms, we are able to evaluate the contribution of pions and beamline back-  
 2315 grounds to each bin of the interacting and incident histograms separately and obtain

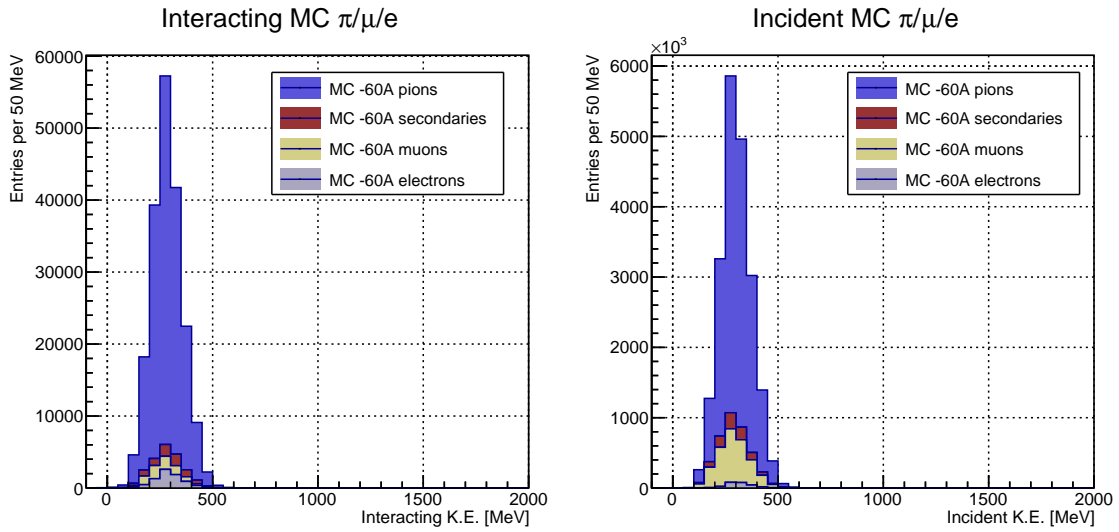


Figure 5.9: Left: staggered contributions to the interacting kinetic energy distribution for electron (grey), muons (yellow) and pion (blue) in the 60A simulation sample. Right: staggered contributions to the incident kinetic energy distribution for electron (grey), muons (yellow) and pion (blue) in the 60A simulation sample.

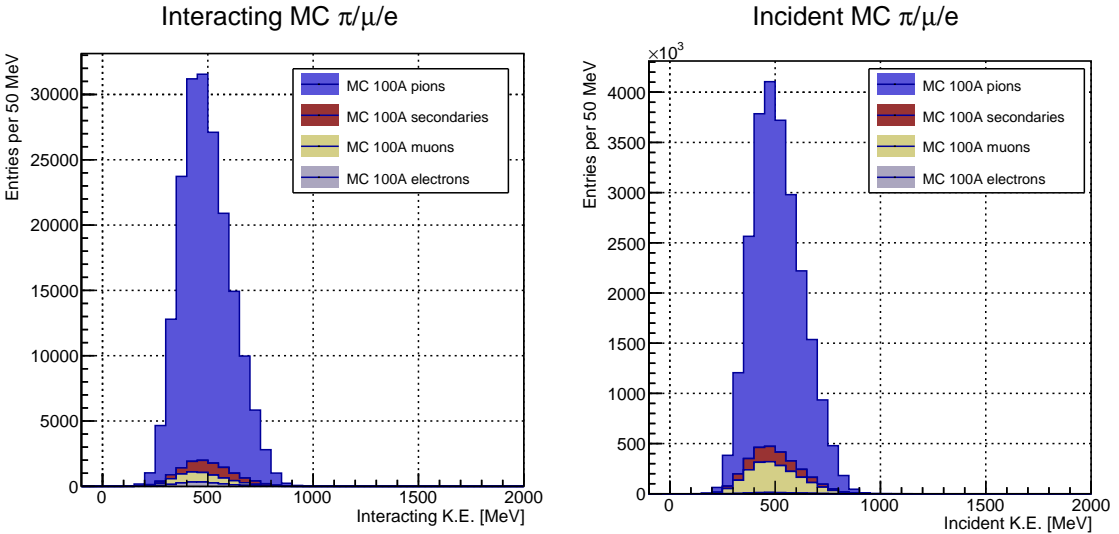


Figure 5.10: Left: staggered contributions to the interacting kinetic energy distribution for electron (grey), muons (yellow) and pion (blue) in the 100A simulation sample. Right: staggered contributions to the incident kinetic energy distribution for electron (grey), muons (yellow) and pion (blue) in the 100A simulation sample.

2316 the relative pion content. The relative pion content in each bin for the interacting  
 2317 and incident histograms represents the correction applied to data. We take here the  
 2318 interacting histogram as example, noting that the derivation of the correction for the  
 2319 incident histogram is identical. The number of entries in each bin of the interacting  
 2320 histogram (Figure 5.9 left) is  $N_{\text{Int}}^{\text{TOT}}(E_i)$ , equal to the sum of the pions and beamline  
 2321 backgrounds flagged as interacting in that bin, namely

$$N_{\text{Int}}^{\text{TOT}}(E_i) = N_{\text{Int}}^{\pi}(E_i) + \underbrace{N_{\text{Int}}^{\mu}(E_i) + N_{\text{Int}}^e(E_i) + N_{\text{Int}}^{\text{Secondary}}(E_i)}_{B_{\text{Int}}(E_i)}. \quad (5.1)$$

2322 Thus, the relative pion content to each bin in MC can be calculated as follows

$$C_{\text{Int}}^{\pi MC}(E_i) = \frac{N_{\text{Int}}^{\pi MC}}{N_{\text{Int}}^{\text{TOTMC}}(E_i)} = \frac{N_{\text{Int}}^{\text{TOTMC}}(E_i) - B_{\text{Int}}^{\text{MC}}(E_i)}{N_{\text{Int}}^{\text{TOTMC}}(E_i)}. \quad (5.2)$$

2323 In order to evaluate the pion content of each bin in data, we scale the measured  
 2324 bin by the corresponding relative pion content found in MC, as follows

$$N_{\text{Int}}^{\pi \text{RecoData}} = N_{\text{Int}}^{\text{TOTData}}(E_i) - B_{\text{Int}}^{\text{Data}}(E_i) = C_{\text{Int}}^{\pi MC}(E_i)N_{\text{Int}}^{\text{TOTData}}(E_i). \quad (5.3)$$

2325 The pion content is evaluated separately in the interacting and incident his-  
 2326 tograms. Their ratio determines a correction to the measured raw cross section.  
 2327 For example, the measured raw cross section of a sample with enhanced muons con-  
 2328 tent will tend to be lower than the raw cross section of a muon free sample. This is  
 2329 because most of the muons will cross the TPC without stopping, thus contributing  
 2330 almost exclusively to the incident histogram, forcing the pion content to be lower in  
 2331 the incident histogram than in the interacting; thus, the correction will tend to en-  
 2332 hance the cross section. We present the estimation of  $C_{\text{Int}}^{\pi MC}(E_i)$  and  $C_{\text{Inc}}^{\pi MC}(E_i)$  and  
 2333 their associated systematic uncertainty in chapter discussing the pion cross section  
 2334 measurement (Figure 6.4).

## 2335 5.4 Estimate of Energy Loss before the TPC

2336 The beamline particles travel a path from where their momentum is measured in  
2337 the beamline until they are tracked again inside the TPC. In the LArIAT geometry,  
2338 a particle leaving the WC4 will encounter the materials listed in Table 5.4 before  
2339 being registered again. The energy lost by the particle in this non-instrumented  
2340 material modifies the particle's kinetic energy and directly affects the cross section  
2341 measurement, as shown in equation 4.5.

Material	density [g/cm <sup>3</sup> ]	width [cm]
Fiberglass laminate (G10)	1.7	1.28
Liquid Argon	1.4	3.20
Stainless Steel	7.7	0.23
Titanium	4.5	0.04
Air	$1.2 \cdot 10^{-3}$	89.43
Plastic Scintillator	1.03	1.20 (+ 1.30)

Table 5.4: LArIAT material budget from WC4 to the TPC Front Face.

We derive an estimate of the energy loss between the beamline momentum measurement and the TPC ( $E_{loss}$ ) from the pion and kaon DDMC samples, since this quantity is not measurable directly on data. The  $E_{loss}$  distribution for the 60A and 100A pion sample is shown in figure 5.11, left and right respectively. The  $E_{loss}$  distribution for the whole kaon sample is shown in figure 5.12. A clear double peaked structure is visible. After a long investigation on the origin of this unexpected shape, we determined that its origin is due to the particles either missing or hitting the HALO paddle (see Section 3.2.4 for the HALO paddle description): a schematic rendering of this occurrence is shown in figure 5.13. The kinematic at WC4 determines the trajectory of a particle and indicates whether or not it will hit the halo paddle, whose positioning and central hole size were not sufficiently well defined when the beamline instrumentation was installed. In figure 5.14 , we plot the true horizontal component of the momentum  $P_x$  versus the true  $X$  position at WC4 for pions missing

the halo paddle (left) and for pions hitting the halo paddle (right) for the -60A MC simulation runs – analogous plots are obtained with the -100A pion simulation and with the kaon simulation. These distributions can be separated drawing a line in this position-momentum space. We use a logistic regression [13] as a classifier to find the best separating line, shown in both plots as the red line. We classify as “hitting the halo paddle” all pions whose  $P_x$  and  $X$  are such that

$$P_x + 0.02 * X - 0.4 < 0$$

and as “missing the halo paddle” all pions whose  $P_x$  and  $X$  are such that

$$P_x + 0.02 * X - 0.4 > 0,$$

where the coefficients of the line are empirically found by the logistic regression estimation. Overall, this simple method classifies in the right category (hit or miss) about 86% of the pion events. In MC, we assign  $E_{loss} = 32 \pm 4$  MeV for pion events classified as “hitting the halo paddle”; we assign  $E_{loss} = 24 \pm 3$  MeV for pion events classified as “missing the halo paddle”. These values are the average and width of the two landau distributions underneath the double peaked distribution. We apply the same classifier on data.

A late scan of the simulated geometry showed an excess of 3 cm of uninstrumented argon compared with the surveyed detector geometry. This excess has an effect on the  $E_{loss}$ : MC particles traverse more uninstrumented material (i.e. loose more energy in the argon before the TPC front face) than data particles. We account for this difference by assigning in data  $E_{loss} = 24 \pm 6$  MeV for pion events classified as “hitting the halo paddle” and  $E_{loss} = 17 \pm 6$  MeV for pion events classified as “missing the halo paddle”, where the uncertainty is derived as the standard deviation of the double peaked distribution.

2357     The summary of the values for used for  $E_{Loss}$  for the pion sample is listed in table  
 2358     5.5 with the analogous results for the study on the kaon case.

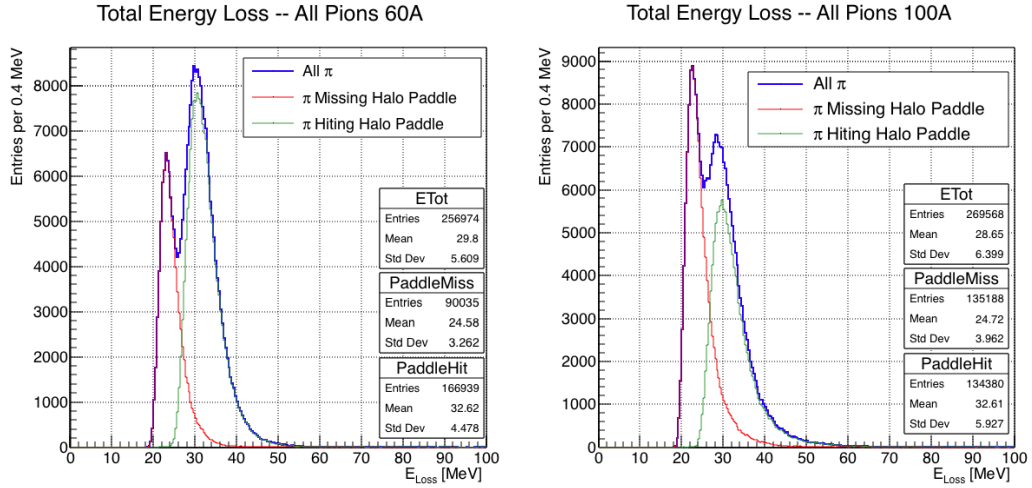


Figure 5.11: True energy loss between WC4 and the TPC front face according to the MC simulation of negative pions of the 60A runs (left) and of the 100A runs (right). The distribution for the whole data sample is shown in blue, the distribution for the pions missing the halo is shown in red, and the distribution for the pions hitting the halo is shown in green.

## 2359     5.5 Tracking Studies

2360     The tracking of hadrons in the TPC determines both the beamline to TPC hand-  
 2361     shake and the identification of the interaction point within the TPC. Thus, it plays  
 2362     a fundamental role in the cross section measurements. We performed several studies  
 2363     geared towards the optimization of the LArSoft software package for tracking in the  
 2364     TPC. In particular, we studied a suitable set of parameters for the WC2TPC match

	$E_{loss}$ [MeV]	
	Hitting Halo	Missing Halo
Pion MC	$32 \pm 4$	$24 \pm 3$
Pion Data	$25 \pm 6$	$17 \pm 6$
Kaon MC	$38 \pm 6$	$31 \pm 5$
Kaon Data	$26 \pm 7$	$22 \pm 7$

Table 5.5: Energy loss for pions and kaons.

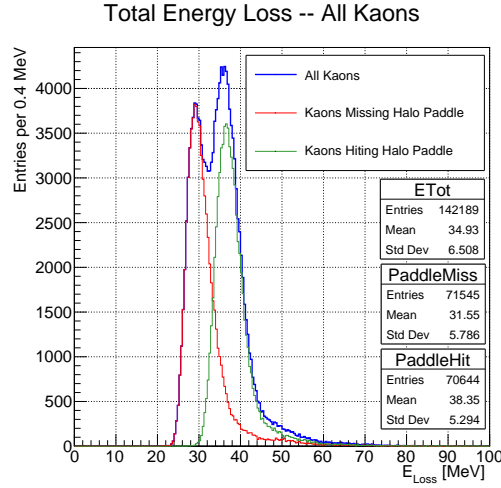


Figure 5.12: True energy loss between WC4 and the TPC front face according to the MC simulation of positive kaons in the 60A and 100A combined sample. The distribution for the whole data sample is shown in blue, the distribution for the kaons missing the halo is shown in red, and the distribution for the kaons hitting the halo is shown in green.

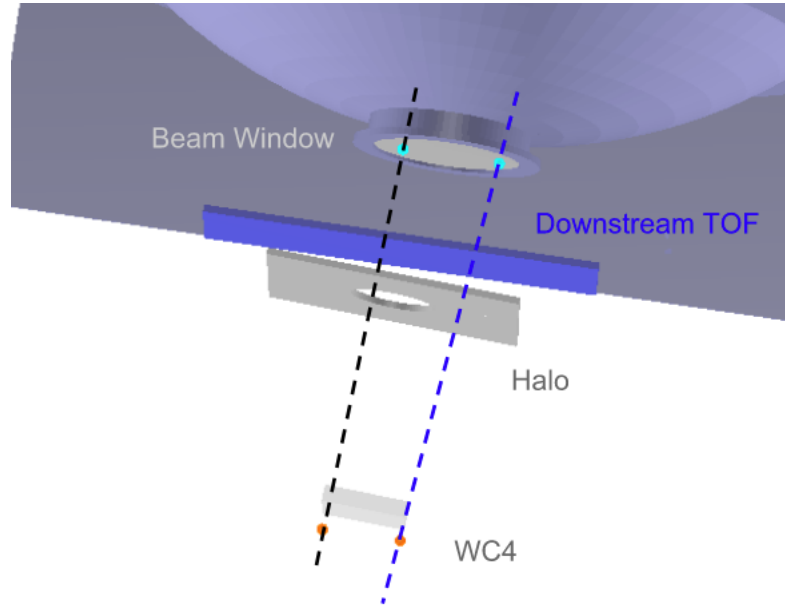


Figure 5.13: Schematic rendering of the particle path between WC4 and the TPC front face. The paddle with the hollow central circle represents the Halo paddle. We illustrate two possible trajectories: in black, a trajectory that miss the paddle and goes through the hole in the Halo, in blue a trajectory that hits the Halo paddle and goes through the scintillation material.

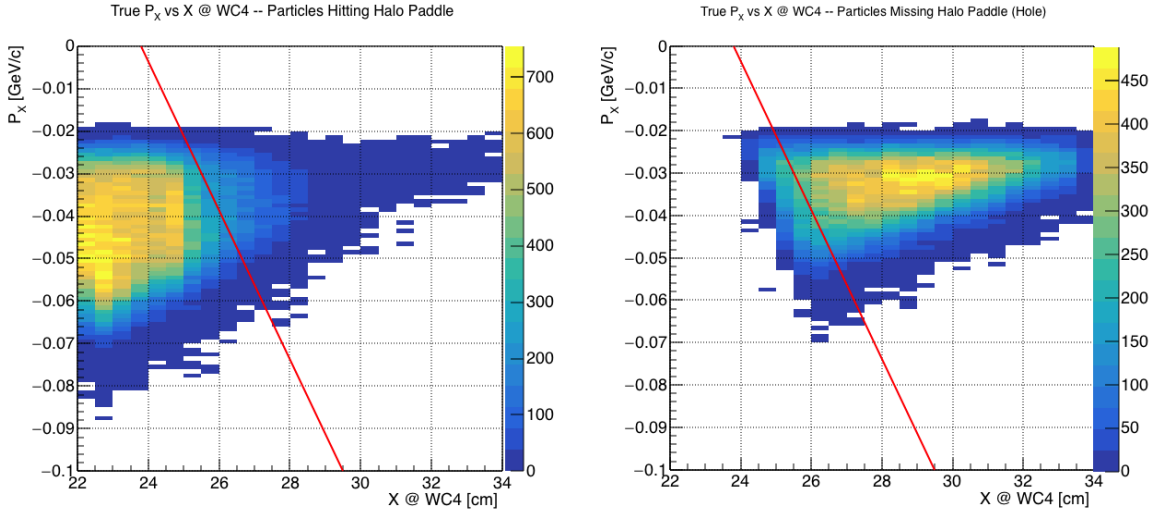


Figure 5.14: Horizontal component of the true momentum vs the horizontal position at WC4 for MC simulated pions of the 60A runs. The plot on the left shows the distribution for pion that miss the halo paddle and the plot on the right shows the distributions for pions that hit the halo. The form of the classifier is overlaid to both plots (red line).

and we optimized the clustering algorithm to maximize the efficiency of finding the interaction point on MC. Given the technical nature of these studies, we report them in Appendix B. We only report here the evaluation of the angular resolution of the tracking algorithm in data and MC, due to its important implications on the physics measurement.

### 5.5.1 Angular Resolution

Scope of this study is to understand and compare the tracking performances and the angular resolution of the TPC tracking on data and MC. We use the angular resolution of the tracking to determine the value of smallest angle that the tracking algorithms allow to reconstruct with a non-zero efficiency, effectively determining a selection on the distribution of the scattering angle of hadronic interaction entering the cross section measurement.

We start by selecting all the WC2TPC matched tracks used for the cross sec-

2378 tion analysis. These tracks can contain from a minimum of 3 3D-space points to a  
2379 maximum of 240 3D-space points. We fit a straight line to all the 3D-space points  
2380 associated with the track. For each track we calculate the average distance between  
2381 each point in space and the fit line as follows

$$\bar{d} = \frac{\sum_i^N d_i}{N}, \quad (5.4)$$

2382 where  $N$  is the number of 3D-space points of the track and  $d_i$  is the distance of the  
2383  $i$ -th space point to the line fit. Several tests to compare the goodness of fit between  
2384 data and MC have been considered. We decided to use  $\bar{d}$  for its straightforward  
2385 interpretation. The  $\bar{d}$  distribution for data and MC is shown in Figure 5.17 for pions  
2386 and in Figure 5.19 for kaons and shows a relatively good agreement between data and  
2387 MC.

2388 A visual representation of the procedure used to evaluate the angular resolution is  
2389 shown in Figure 5.15. For each track, we order the space points according to their Z  
2390 position along the positive beam direction (panel a) and we split them in two sets: the  
2391 first set contains all the points belonging to the first half of the track and the second  
2392 set contains all the points belonging the second half of the track. We remove the last  
2393 four points in the first set and the first four points in the second set, so to have a  
2394 gap in the middle of the original track (panel b). We fit the first and the second set  
2395 of points with two lines (panel c). We then calculate the angle between the fit of the  
2396 first and second half  $\alpha$  (panel d). The angle  $\alpha$  determines the angular resolution of  
2397 the tracking. The distributions for data and MC for  $\alpha$  are given in Figure 5.18 for  
2398 pions and in Figure 5.20 for kaons. The mean of the data and MC angular resolution  
2399 are reported in Table 5.6 for pions and kaons in data and MC.

2400 Interaction angles smaller than the angular resolution are indistinguishable for  
2401 the reconstruction. Therefore, we assess our ability to measure the cross section

2402 to be limited to interaction angles greater than 5.0 deg. More accurate studies of  
 2403 the angular resolution as a function of the kinetic energy and track length, albeit  
 2404 interesting, are left for an improvement of the analysis.

2405 As we discussed in Section 1.4.1, several different interaction topologies are in-  
 2406 cluded as signal in the total hadronic cross section. The ability to detect a minimum  
 2407 interaction angle and to stop the tracking accordingly mainly effects two interaction  
 2408 channels: the pion elastic interaction (see Table 1.4, second line) and the pion in-  
 2409 elastic interaction in case of neutral particle emission (see Table 1.4, fourth line); the  
 2410 overall effect of this limitation is to reduced the cross section measurement to the  
 2411 measurement of the cross section relative to interaction angles greater than a  $\sim 5.0$   
 2412 deg . It is beneficial to take a moment to describe the definition of interaction angle.  
 2413 In case of elastic scattering, the definition is straightforward: the interaction angle is  
 2414 the angle between the incoming and outgoing hadron, i.e.

$$\theta = \cos^{-1} \left( \frac{\vec{p}_{\text{incoming}} \cdot \vec{p}_{\text{outgoing}}}{|\vec{p}_{\text{incoming}}| |\vec{p}_{\text{outgoing}}|} \right). \quad (5.5)$$

2415 In case of the reaction channel, the presence of several topologies requires a more  
 2416 complex definition, as shown in figure 5.16. We define the scattering angle as the  
 2417 biggest of the angles between the incoming hadron and the visible daughters, where  
 2418 the visible daughters are charged particles that travel more than the average pitch  
 2419 length ( $\delta X = 47$  mm) in the detector (see panel a); in case all the daughters are  
 2420 invisible, the angle is assigned to be 90 deg (see panel b). We chose this working  
 2421 definition of scattering angle for inelastic scattering keeping in mind how our tracking  
 2422 reconstruction works: the tracking will stop correctly if none of the daughters is visible

	Data	MC
Pions	$\bar{\alpha}_{Data} = (5.0 \pm 4.5)$ deg	$\bar{\alpha}_{MC} = (4.5 \pm 3.9)$ deg
Kaons	$\bar{\alpha}_{Data} = (4.3 \pm 3.7)$ deg	$\bar{\alpha}_{MC} = (4.4 \pm 3.6)$ deg

Table 5.6: Angular resolution for Pion and Kaon tracking in both data and MC.

2423 in the detector and it is likely to stop correctly if multiple visible daughters form  
2424 an interaction vertex. The only “dangerous” case is the production of one charged  
2425 daughter plus neutrals, which we can study with this working definition of scattering  
2426 angle (see panel c).

2427 Once we fix the scattering angle definition, we can study the effects of the angular  
2428 resolution on the cross section by plotting the true Geant4 total hadronic cross section  
2429 for interaction angles greater than a minimum interaction angle. The left side of  
2430 Figure 5.21 shows the true Geant4 cross section for interaction angles greater than 0  
2431 deg (green), 4.5 deg (red) corresponding to the MC angular resolution, 5.0 deg (blue)  
2432 corresponding to the data angular resolution, and 9.0 deg (yellow). A small 0.5 deg  
2433 systematic shift between the mean of the data and MC angular resolution is present,  
2434 which has a negligible impact on the cross section. The right side of Figure 5.21 shows  
2435 the ratio between the true cross section for interaction angles greater than 5 deg and  
2436 the true interaction cross section for all angles; the cross section for angles greater  
2437 than 5° accounts for more than 80% than the total cross section in every energy bin.

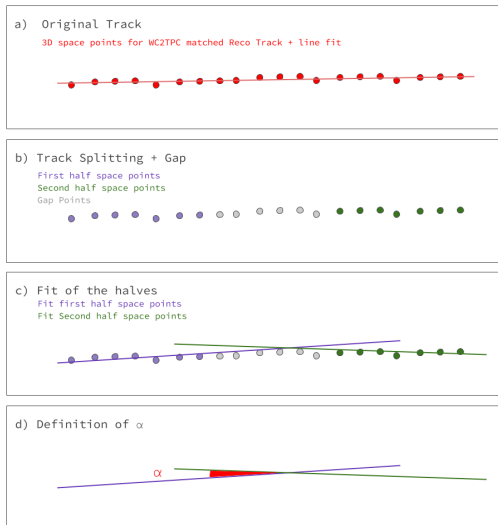


Figure 5.15: A visual representation of the procedure used to evaluate the angular resolution.

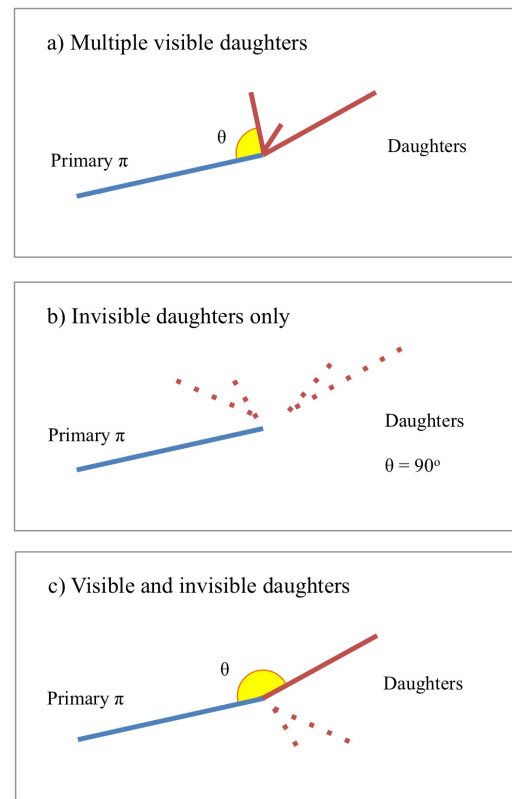


Figure 5.16: A visual representation of the scattering angle definition in case of inelastic scattering.

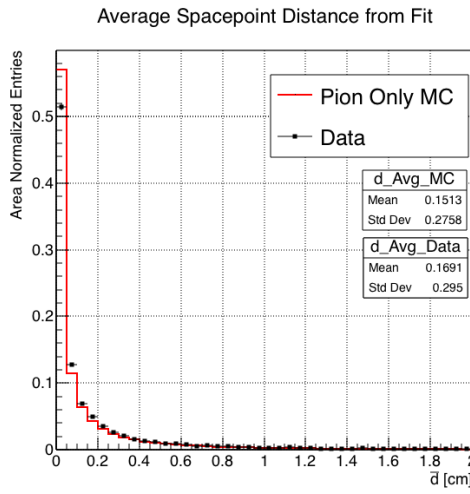


Figure 5.17: Distributions of the average distance between each 3D point in space and the fit line,  $\bar{d}$  for the data used in the pion cross section analysis and the pion only DDMC. The distributions are area normalized.

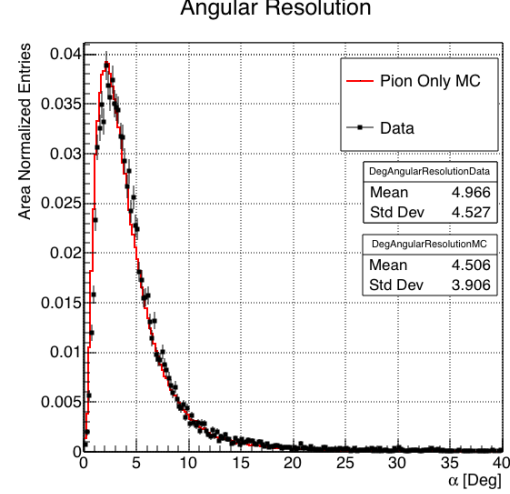


Figure 5.18: Distributions of angular resolution  $\alpha$  for data used in the pion cross section analysis and pion only DDMC. The distributions are area normalized.

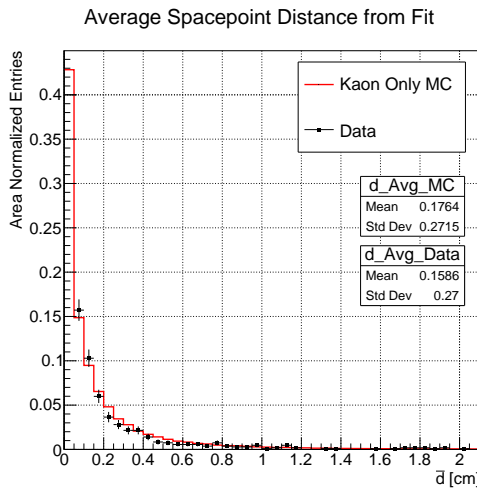


Figure 5.19: Distributions of the average distance between each 3D point in space and the fit line,  $\bar{d}$  for the data used in the kaon cross section analysis and the kaon only DDMC. The distributions are area normalized.

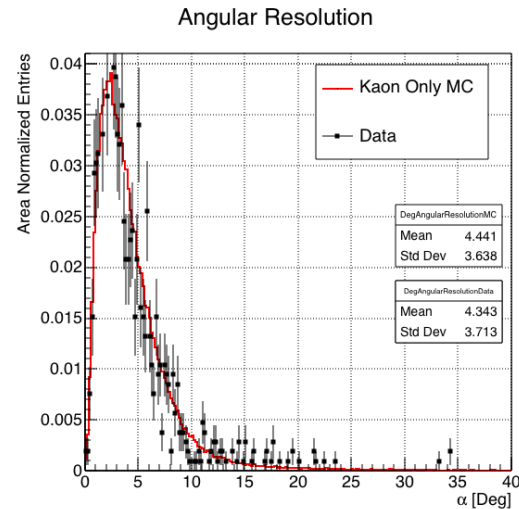


Figure 5.20: Distributions of angular resolution  $\alpha$  for data used in the kaon cross section analysis and kaon only DDMC. The distributions are area normalized.

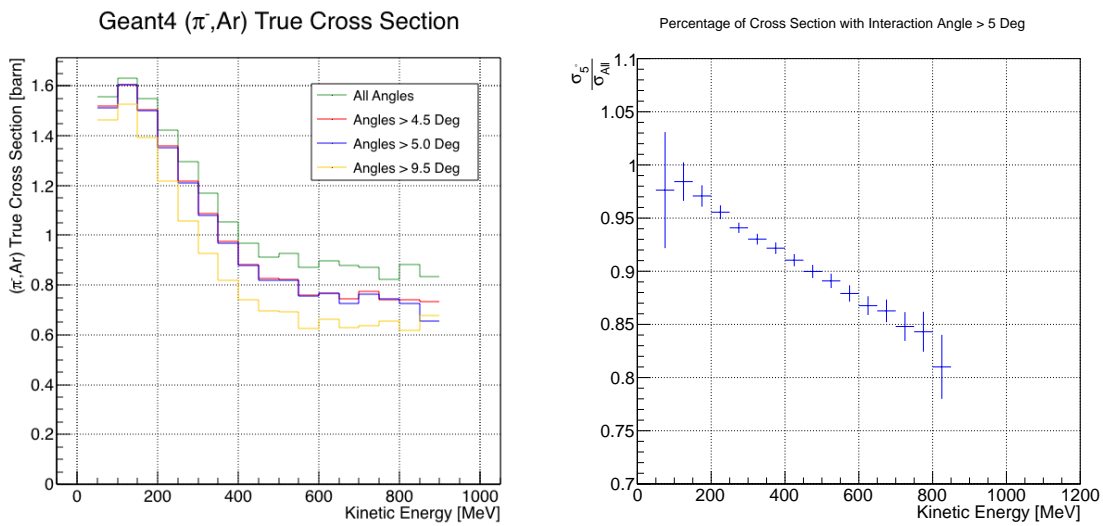


Figure 5.21: *Left:* True ( $\pi^-$ , Ar) cross section for interaction angles greater than 0 deg (green), 4.5 deg (red), 5.0 deg (blue) and 9.0 deg (yellow). *Right:* Ratio between the true cross section for interaction angles greater than 5 deg and the true interaction cross section for all angles.

## 2438 5.6 Calorimetry Studies

2439 The measured kinetic energy of a hadron candidate at each argon slab determines  
2440 which bins of the interacting and incident histograms a selected event is going to fill.  
2441 Thus, the energy measurement provided by the LArTPC is fundamental for the cross  
2442 section analysis. In Appendix C, we describe how we calibrate the TPC calorimetric  
2443 response. In this section, we describe how we measure the kinetic energy of the  
2444 hadrons in the TPC.

### 2445 5.6.1 Kinetic Energy Measurement

2446 In this section, we define the measurement on the kinetic energy and determine the  
2447 related uncertainty. We will propagate this uncertainty into the cross section mea-  
2448 surement, as discussed in Section 6.1.2 for the pion cross section and in Section ??  
2449 for the kaon cross section.

2450 The kinetic energy of a hadron at the  $j^{\text{th}}$  slice of argon in the TPC is given by

$$KE_j = \sqrt{p_{Beam}^2 + m_{Beam}^2} - m_{Beam}^2 - E_{Loss} - E_{FF-j}, \quad (5.6)$$

2451 where  $p_{Beam}$  is the momentum measured by the beamline detectors,  $m_{Beam}$  is the  
2452 mass of the hadron as reported in the PDG,  $E_{Loss}$  is the energy loss between the  
2453 beamline and the TPC, and  $E_{FF-j}$  is the energy that the hadron deposited from the  
2454 TPC front face until the  $j^{\text{th}}$  slice. The uncertainty on  $KE_j$  is then given by

$$\delta KE_j = \sqrt{\delta p_{Beam}^2 + \delta E_{Loss}^2 + \delta E_{dep\ FF-j}^2}, \quad (5.7)$$

2455 where we have dropped the uncertainty on the mass, since it is orders of magnitude  
2456 smaller than the other uncertainties. We assume the relative uncertainty on  $p_{Beam}$  to  
2457 be 2%, and the uncertainty on the energy loss upstream to be 7 MeV, as calculated

2458 in Section 5.4. We describe the estimate of the uncertainty on  $E_{\text{FF-j}}$  in the rest of  
2459 this section.

2460 The energy deposited by the hadron from the TPC front face until the  $j^{\text{th}}$  slice is  
2461 the sum of the measured energy deposited in each previous slabs  $E_i$ , i.e.

$$E_{\text{FF-j}} = \sum_{i < j} E_i, \quad (5.8)$$

2462 where  $E_i$  is measured in each slab as the product of the stopping power,  $dE/dX_i$ ,  
2463 and the track pitch for that point. Since the measurements of the energy deposited  
2464 in each slab rely on the same global calorimetric procedure and tracking algorithms,  
2465 we assume conservatively that the measurements of  $E_i$  are not independent from  
2466 one another; thus, the uncertainty on  $E_{\text{FF-j}}$  becomes

$$\delta E_{\text{FF-j}} = \sum_{i < j} \delta E_i = (j - 1) \delta E_i, \quad (5.9)$$

2467 where  $\delta E_i$  is the uncertainty on the energy loss in one slab of argon.

2468 The left side of Figure 5.22 shows the distribution of the energy deposited in each  
2469 slab of argon, for the 60A negative pion dataset in black and for the pion only MC  
2470 in blue. The analogous plot for the -100A negative pion data set is show on the right  
2471 side of Figure 5.22. The distributions are fitted with a landau displayed in red for  
2472 data and in teal for MC. The uncertainty on  $E_i$  is given by the width of the Landau  
2473 fit to the data. A small systematic uncertainty is given by a 1.0% difference between  
2474 the most probable value of the landau fits in data and MC.

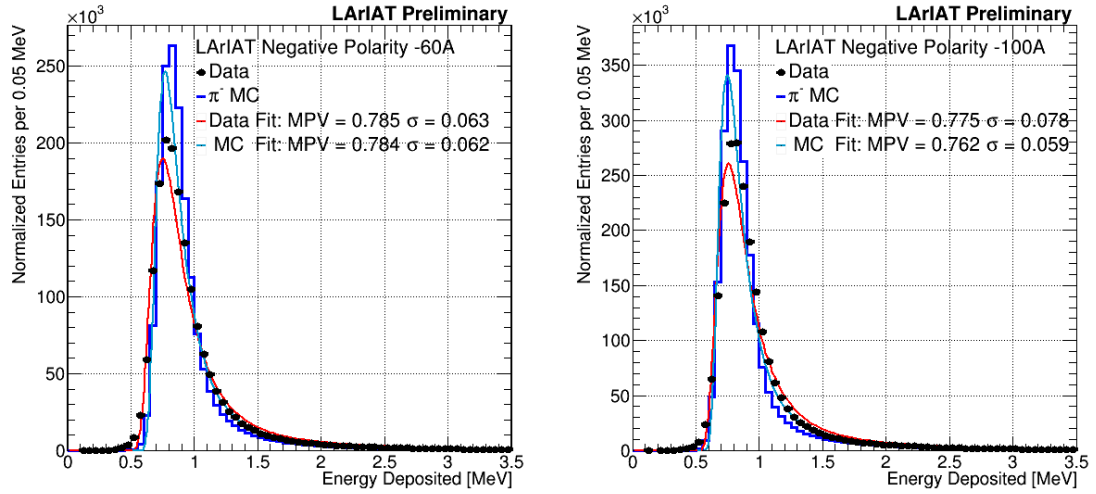


Figure 5.22: Energy deposited  $E_i$  in a single slab of argon for the pion -60A runs (left) and -100A runs (right). The data is shown in black, the MC in blue. The distributions are fitted with a landau displayed in red for data and in teal for MC.

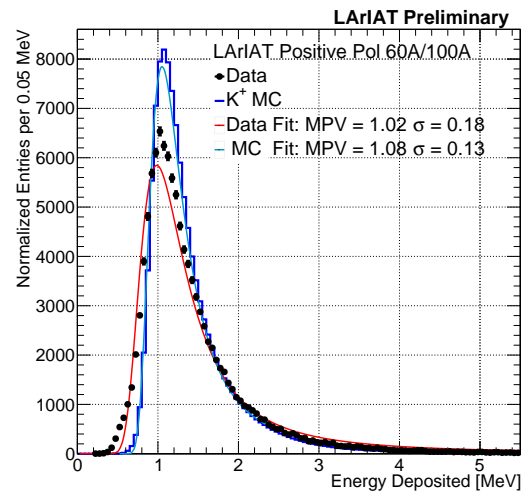


Figure 5.23: Energy deposited  $E_i$  in a single slab of argon for the kaons of the +60A runs and +100A runs. The data is shown in black, the MC in blue. The distributions are fitted with a landau displayed in red for data and in teal for MC.

2475 **Chapter 6**

2476 **Negative Pion Cross Section**

2477 **Measurement**

2478 “*Y ella es flama que se eleva, Y es un pájaro a volar.*

2479 *En la noche que se incendia, estrella de oscuridad*  
2480 *que busca entre la tiniebla, la dulce hoguera del beso.”*

2481 – Lila Downs, 2002 –

2482 In this chapter, we show the result of the thin slice method to measure the ( $\pi^-$ -  
2483 Ar) total hadronic cross section. In Section 6.1, we start by measuring the raw cross  
2484 section, i.e. the cross section obtained exclusively using data reconstruction, without  
2485 any additional corrections. In Section 6.2, we apply the statistical subtraction of the  
2486 background contributions based on simulation and the correction for reconstruction  
2487 effects. The final results are presented in Section 6.3.

2488 **6.1 Raw Cross Section**

2489 We measure the raw ( $\pi^-$ -Ar) total hadronic cross section as a function of the kinetic  
2490 energy in the two chosen data sets, the -60A and -100A negative runs. As we will

clarify in Section 6.2, the corrections to the raw cross section depend on the beam settings and need to be calculated independently for the two datasets. Thus, we present here the measurement of the raw cross section on the two datasets separately.

As stated in section 4.3.2, the raw cross section is given by the equation 4.4

$$\sigma_{TOT}(E_i) = \frac{1}{n \delta X} \frac{N_{Int}^{TOT}(E_i)}{N_{Inc}^{TOT}(E_i)}, \quad (4.4)$$

where  $N_{Int}^{TOT}$  is the measured number of particles interacting at kinetic energy  $E_i$ ,  $N_{Inc}^{TOT}$  is the measured number of particles incident on an argon slice at kinetic energy  $E_i$ ,  $n$  is the density of the target centers and  $\delta X$  is the thickness of the argon slice. The density of the target centers and the slab thickness are  $n = 0.021 \cdot 10^{24} \text{ cm}^{-3}$  and  $\delta X = 0.47 \text{ cm}$ , respectively.

Figure 6.1 shows the distribution of  $N_{Int}^{TOT}$  as a function of the kinetic energy for the 60A dataset on the left and for the 100A dataset on the right. The data central points are represented by black dots, the statistical uncertainty is shown in black, while the systematic uncertainty is shown in red. Data is displayed over the  $N_{Int}^{TOT}$  distribution obtained with a MC sample of pions, muon and electrons weighted by the beam composition (additional details on the composition will be provided in Section ??). The contribution from the simulated pions is shown in blue, the one from secondaries in red, the one from muons in yellow and the ones from electrons in gray. The simulated pion's and backgrounds' contributions are stacked; the sum of the integrals from each particle species is normalized to the integral of the data.

Figure 6.2 shows the distribution of  $N_{Inc}^{TOT}$  for the 60A dataset on the left and for the 100A dataset on the right. Data is displayed over the MC. The same color scheme and normalization procedure is used for both the interacting and incident histograms.

Figure 6.3 shows the raw cross section for the 60A dataset on the left and for the 100A dataset on the right, statistical uncertainty in black and systematic uncertainty

2515 in red. The raw data cross section is overlaid to the reconstructed cross section for the  
 2516 MC sample, displayed in azure. Since the background contributions and the detector  
 2517 effects for the 60A and 100A sample are different, it is premature to compare the raw  
 2518 cross sections obtained from the two samples at this point.

2519 We describe the calculation of the statistical uncertainty for the interacting, in-  
 2520 cident and cross section distributions in Section 6.1.1; we describe the procedure to  
 2521 calculate the corresponding systematics uncertainty on Section 6.1.2.

### 2522 6.1.1 Statistical Uncertainty

2523 The statistical uncertainty for a given kinetic energy bin of the cross section is cal-  
 2524 culated by error propagation from the statistical uncertainty on  $N_{\text{Inc}}^{\text{TOT}}$  and  $N_{\text{Int}}^{\text{TOT}}$   
 2525 correspondent bin. Since the number of incident particles in each energy bin is given  
 2526 by a simple counting, we assume that  $N_{\text{Inc}}^{\text{TOT}}$  is distributed as a poissonian with mean  
 2527 and variance equal to  $N_{\text{Inc}}^{\text{TOT}}$  in each bin. On the other hand,  $N_{\text{Int}}^{\text{TOT}}$  follows a bino-  
 2528 mial distribution: a particle in a given energy bin might or might not interact. The  
 2529 variance for the binomial is given by

$$\text{Var}[N_{\text{Int}}^{\text{TOT}}] = \mathcal{N}P_{\text{Interacting}}(1 - P_{\text{Interacting}}). \quad (6.1)$$

2530 Since the interaction probability  $P_{\text{Interacting}}$  is estimated by  $\frac{N_{\text{Int}}^{\text{TOT}}}{N_{\text{Inc}}^{\text{TOT}}}$  and the number  
 2531 of tries  $\mathcal{N}$  is  $N_{\text{Inc}}^{\text{TOT}}$ , equation 6.1 translates into

$$\text{Var}[N_{\text{Int}}^{\text{TOT}}] = N_{\text{Inc}}^{\text{TOT}} \frac{N_{\text{Int}}^{\text{TOT}}}{N_{\text{Inc}}^{\text{TOT}}} \left(1 - \frac{N_{\text{Int}}^{\text{TOT}}}{N_{\text{Inc}}^{\text{TOT}}}\right) = N_{\text{Int}}^{\text{TOT}} \left(1 - \frac{N_{\text{Int}}^{\text{TOT}}}{N_{\text{Inc}}^{\text{TOT}}}\right). \quad (6.2)$$

2532  $N_{\text{Inc}}^{\text{TOT}}$  and  $N_{\text{Int}}^{\text{TOT}}$  are not independent. In fact, the population of a given bin for  
 2533 the interacting histogram always implies at least the population of the same bin in  
 2534 the incident histogram (and possibly other incidents bins at higher energies). Thus,

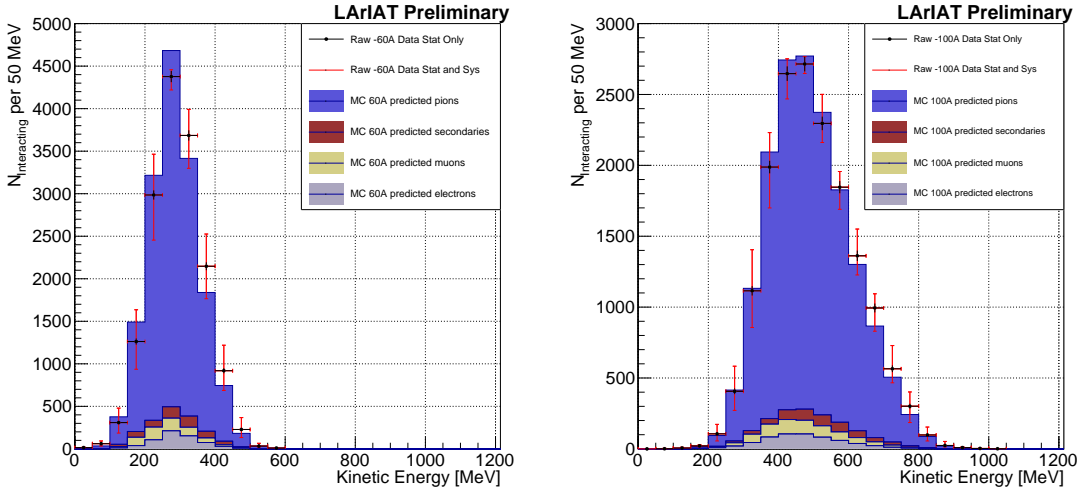


Figure 6.1: Raw number of interacting pion candidates as a function of the reconstructed kinetic energy for the 60A runs (left) and for the 100A runs (right). The statistical uncertainties are shown in black, the systematic uncertainties in red.

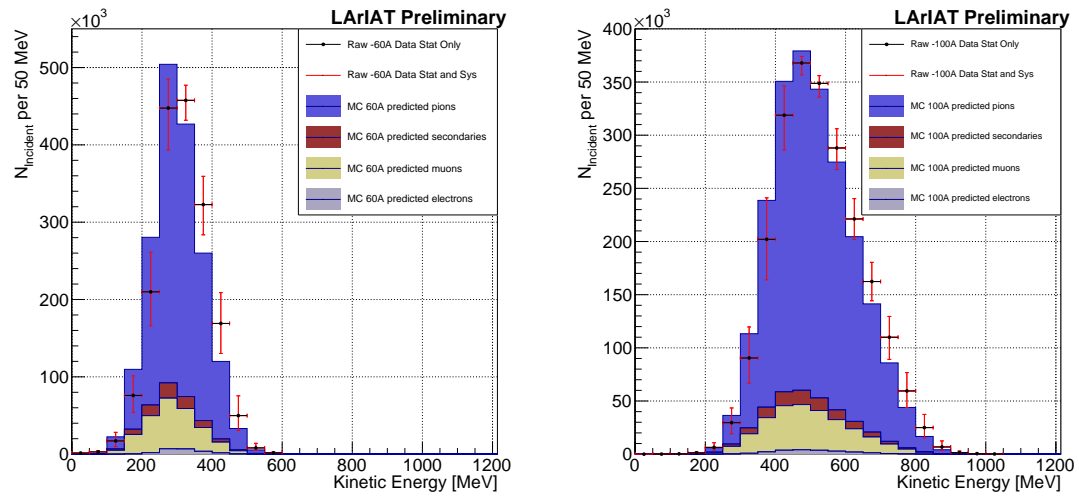


Figure 6.2: Raw number of incident pion candidates as a function of the reconstructed kinetic energy for the 60A runs (left) and for the 100A runs (right). The statistical uncertainty is shown in black, the systematic uncertainties in red.

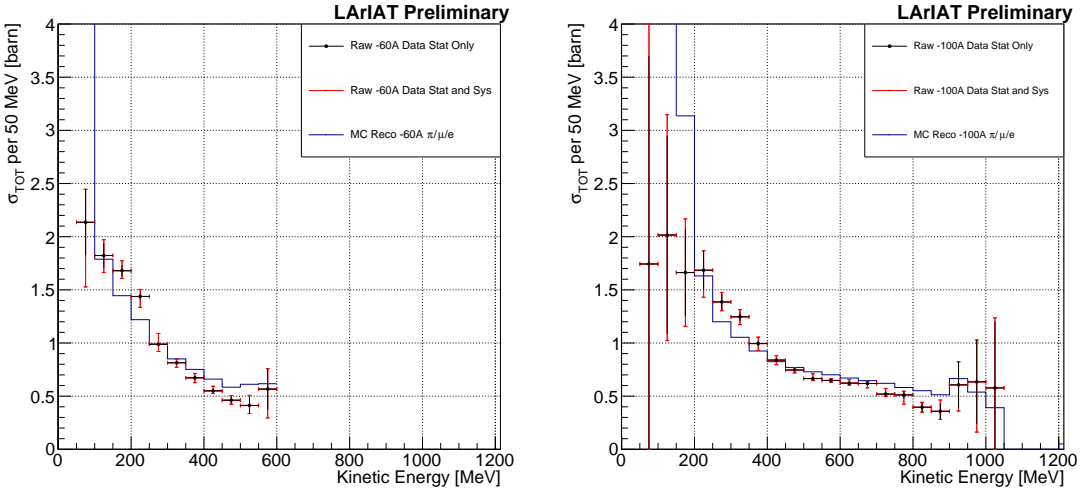


Figure 6.3: Raw ( $\pi^-$ -Ar) total hadronic cross section for the 60A runs (left) and for the 100A runs (right). The statistical uncertainty is shown in black, the systematic uncertainties in red. The raw cross section obtained with a MC mixed sample of pions, muon and electrons in the percentage predicted by G4Beamline is shown in azure.

2535 we conservatively calculate the statistical uncertainty on the cross section as

$$\delta\sigma_{TOT}(E) = \sigma_{TOT}(E) \left( \frac{\delta N_{Int}^{TOT}}{N_{Int}^{TOT}} + \frac{\delta N_{Inc}^{TOT}}{N_{Inc}^{TOT}} \right) \quad (6.3)$$

2536 where:

$$\delta N_{Inc}^{TOT} = \sqrt{N_{Inc}^{TOT}} \quad (6.4)$$

$$\delta N_{Int}^{TOT} = \sqrt{N_{Int}^{TOT} \left( 1 - \frac{N_{Int}^{TOT}}{N_{Inc}^{TOT}} \right)}. \quad (6.5)$$

### 2537 6.1.2 Treatment of Systematics

2538 The only systematic effect considered in the measurement of the raw cross section  
 2539 results from the propagation of the uncertainty associate with the measurement of  
 2540 the kinetic energy at each argon slab. As shown in Section 5.6.1, the uncertainty on  
 2541 the kinetic energy of a pion candidate at the  $j^{th}$  slab of argon is given by

$$\delta KE_j = \sqrt{\delta p_{Beam}^2 + \delta E_{Loss}^2 + \delta E_{dep\ FF-j}^2} \quad (6.6)$$

$$= \sqrt{(2\% p_{Beam})^2 + (6 [\text{MeV}])^2 + (j - 1)^2 (\sim 0.08 [\text{MeV}])^2}. \quad (6.7)$$

2542 We propagate this uncertainty by varying the energy measurement  $KE_j$  at each  
 2543 argon slab. We measure  $N_{Inc}^{TOT}$ ,  $N_{Int}^{TOT}$  and the cross section in three cases: first  
 2544 assigning the measured  $KE_j$  at each kinetic energy sampling, then assigning  $KE_j +$   
 2545  $\delta KE_j$ , and finally assigning  $KE_j - \delta KE_j$ . The difference between the values obtained  
 2546 using the  $KE_j$  sampling and the maximum and minimum values in each kinetic energy  
 2547 bin determines the systematic uncertainty.

## 2548 6.2 Corrections to the Raw Cross Section

2549 As described in section 4.3.3, we need to apply a background correction and an  
 2550 efficiency correction in order to derive the pion cross section from the raw cross  
 2551 section. The cross section is given in equation 4.9,

$$\sigma_{TOT}^{\pi^-}(E_i) = \frac{1}{n \delta X} \frac{\epsilon^{Inc}(E_i)}{\epsilon^{Int}(E_i)} \frac{C_{Int}^{\pi MC}(E_i)}{C_{Inc}^{\pi MC}(E_i)} \frac{N_{Int}^{TOT}(E_i)}{N_{Inc}^{TOT}(E_i)}. \quad (4.9)$$

2552 Section 6.2.1 describes the evaluation of pion content in the interacting and inci-  
 2553 dent histograms, ( $C_{Int}^{\pi MC}(E_i)$  and  $C_{Inc}^{\pi MC}(E_i)$ ) and the propagation to the cross section  
 2554 measurement of the relative systematic uncertainties.

2555 Section 6.2.2 describes the procedure employed to obtain the efficiency corrections  
 2556  $\epsilon^{Int}(E_i)$  and  $\epsilon^{Inc}(E_i)$  and the propagation to the cross section measurement of the  
 2557 relative uncertainties.

2558 **6.2.1 Background subtraction**

2559 We use the procedure described in 5.3.2 to evaluate the relative pion content in  
2560 the interacting histogram  $C_{\text{Int}}^{\pi MC}(E_i)$  and the relative pion content in the incident  
2561  $C_{\text{Inc}}^{\pi MC}(E_i)$ . We start by evaluating the relative pion content assuming the beamline  
2562 composition simulated by G4Beamline, whose pion, muon and electron percentages  
2563 per beam setting are reported again in the first line of Table 6.1. The left side of  
2564 Figure 6.4 shows the MC estimated relative pion content for the interacting histogram  
2565 as function of kinetic energy for the 60A runs (top) and 100A runs (bottom). The  
2566 right side of the same figure shows the MC estimated relative pion content for the  
2567 incident histogram as function of kinetic energy for the 60A runs (top) and 100A  
2568 runs (bottom). In Figure 6.4 the central curves displayed in light blue are obtained  
2569 using the beamline composition as predicted by G4Beamline: these are the correction  
2570 curves for the relative pion content applied to data in equation 4.9.

2571 So, the question now becomes: how well do we know the beamline composition?  
2572 In absence of additional data constraints, we take a 100% systematic uncertainty on  
2573 the electron content, reported in lines 3 and 4 of Table 6.1. The effect of doubling or  
2574 halving the electron percentage in the beam on the pion relative content is displayed  
2575 in red in Figure 6.4. We reserve a slightly different treatment for the muon content.  
2576 Since G4Beamline tracks only particles which cross all the wire chambers, pion events  
2577 that decay in flight from WC1 to WC4 are not recorded by G4Beamline. Pion decays  
2578 in the beamline could trigger the beamline detectors in data, if the produced muon  
2579 propagates forward along the beamline. Thus, we take the G4Beamline prediction  
2580 for muons as a lower bound in the composition: the effect of doubling the muon  
2581 content (line 2 in Table 6.1) is shown in blue on Figure 6.4. A future study of data  
2582 from additional beamline detectors such as the Aerogel Chernkov detectors [43] or the  
2583 muon range stack (see Section 3.2.4) has the potential of narrowing the systematics  
2584 uncertainty coming from the beamline composition.

2585 We propagate the uncertainty on the beamline composition as a systematic un-  
2586 certainty to the cross section by varying the beam composition for all the cases listed  
2587 in Table 6.1 and evaluating variation of obtained data cross sections in each bin. This  
2588 systematic uncertainty is summed in quadrature with the statistical uncertainty and  
2589 the systematic uncertainty related to the kinetic energy measurement.

### 2590 6.2.2 Correction for Reconstruction Effects

2591 The interaction point for a particle in the selected sample for the total hadronic cross  
2592 section analysis is the last point of its track that lies inside the LArTPC fiducial  
2593 volume. This definition holds regardless the type of the interaction, i.e. if the TPC  
2594 track ends within the fiducial volume, its last point will be the interaction point, no  
2595 matter what the products of the interaction look like; on the other hand, if the track  
2596 crosses the boundaries of the fiducial volume, the particle will be considered “through  
2597 going” and no interaction point will be found. Given this definition, it is evident that  
2598 we rely on the tracking algorithm to discern where the interaction occurred in the  
2599 TPC and correctly end the tracking. The tracking algorithm has an intrinsic angle  
2600 resolution as shown in section 5.5.1, which limits its efficiency, especially in the case  
2601 of elastic scattering occurring at low angles. **Plus, there are instances where INSERT**  
2602 **HERE THE STUFF ABOUT THE MIGRATION** Thus, we need to apply a correction  
2603 accounting for mis-reconstruction of the interaction point in order to retrieve the true  
2604 cross section. This correction is evaluated separately for the interacting and incident  
2605 histograms bin by bin, namely  $\epsilon^{\text{int}}(E_i)$  and  $\epsilon^{\text{inc}}(E_i)$ , and applied in the cross section  
2606 formula as shown in equation 4.9.

#### 2607 Reconstruction Effects Correction: Procedure

2608 We describe here the procedure to calculate the mis-reconstruction correction taking  
2609 the interacting distribution as example and noting that the procedure is identical for

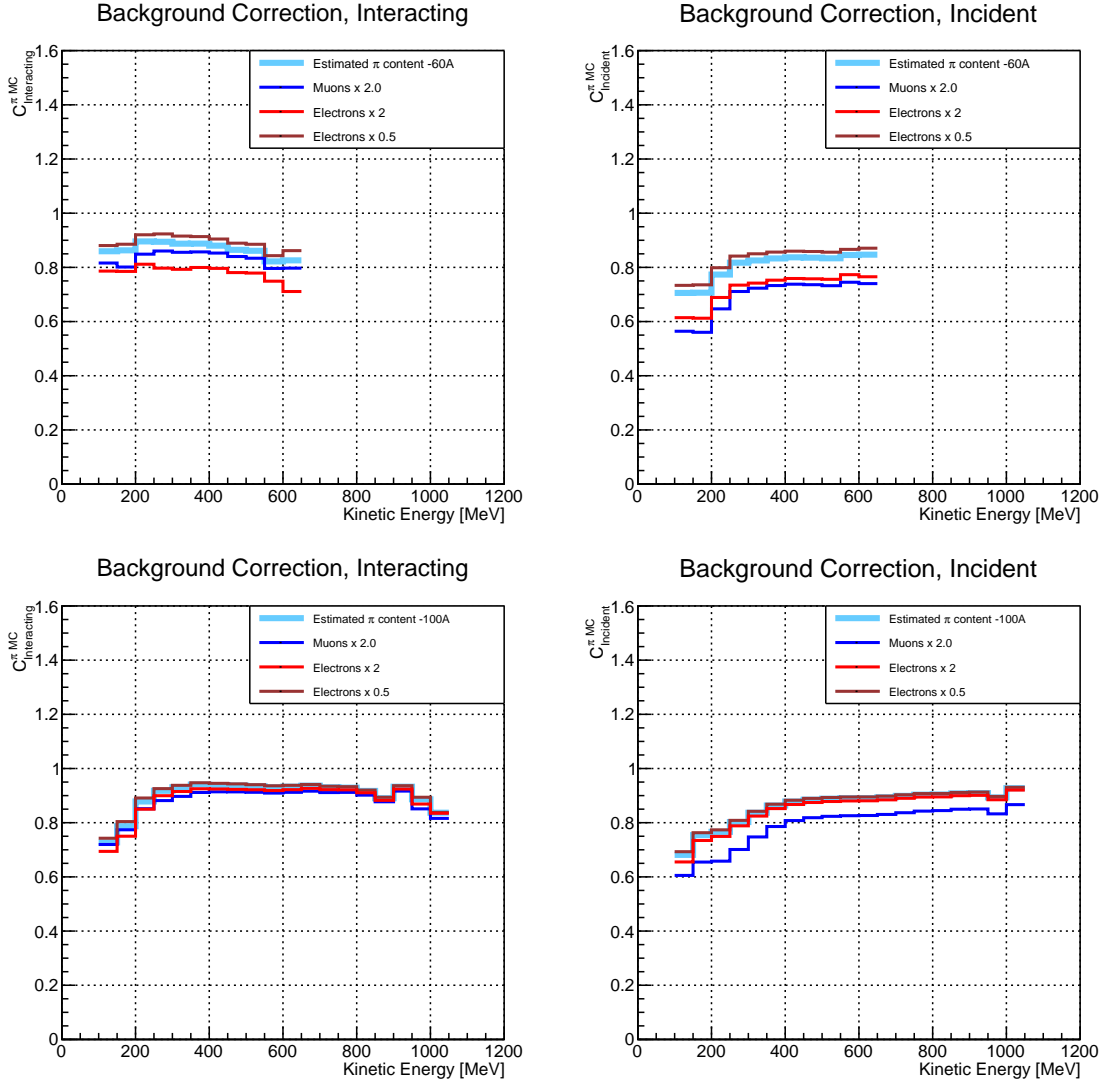


Figure 6.4: *Left:* MC estimated relative pion content for interacting histogram a function of kinetic energy for the 60A runs (top) and 100A runs (bottom), predicted background content in azure and muon and electron content variation in blue and red. *Right:* MC estimated relative pion content for incident histogram a function of kinetic energy for the 60A runs (top) and 100A (bottom), predicted background content in azure and muon and electron content variation in blue and red

2610 the incident distribution.

2611 In section 5.5.1, we estimated the angular resolution for data and MC to be  
2612  $\bar{\alpha}_{Data} = (5.0 \pm 4.5)$  deg and  $\bar{\alpha}_{MC} = (4.5 \pm 3.9)$  deg, respectively. Most interaction  
2613 angles smaller than the angular resolution will thus be indistinguishable for the re-  
2614 construction. Thus, we claim we are able to measure the cross section for interaction  
2615 angles greater than 5.0 deg. Geant4 simulates interactions at all angles, as shown in  
2616 figure 6.7. In order to calculate the correction for reconstruction effects, we select  
2617 events which have an interaction angle greater than a given  $\alpha_{res}$  to construct the true  
2618 interacting and incident histograms (the denominator of the correction).

2619 We derive the correction  $\epsilon^{int}(E_i)$  on a set of pure pion MC, calculating its value bin  
2620 by bin as the ratio between the true bin content and the correspondent reconstructed  
2621 bin content. The true interacting distribution is obtained applying the thin slice  
2622 method on true MC energy deposition up to the MC flagged true interaction point  
2623 for interaction angles greater than  $5^\circ$ . The reconstructed MC interacting distribution  
2624 is obtained treating the MC events through the same reconstruction process as data:  
2625 the interaction point is given by the end of the tracking and its energy is given by  
2626 the reconstructed calorimetric information. The correction is then applied to in data  
2627 bin by bin. In formulae, the correction is calculated to be

$$\epsilon^{Int}(E_i) = \frac{N_{\text{Interacting}}^{\pi \text{ Reco MC}}(E_i)}{N_{\text{Interacting}}^{\pi \text{ True MC}}(E_i)}, \quad (6.8)$$

2628 where  $N_{\text{Int}}^{\pi \text{ True MC}}(E_i)$  is the content of the  $i$ -th bin in the true interacting his-  
2629 togram, and  $N_{\text{Int}}^{\pi \text{ Reco MC}}(E_i)$  is the content of the  $i$ -th bin in the reconstructed inter-  
2630 acting histogram. The correction is applied to data as follows

$$N_{\text{Int}}^{\pi \text{ Data}}(E_i) = \frac{N_{\text{Int}}^{\pi \text{ Reco Data}}(E_i)}{\epsilon^{Int}(E_i)} = N_{\text{Int}}^{\pi \text{ Reco Data}}(E_i) \frac{N_{\text{Int}}^{\pi \text{ True MC}}(E_i)}{N_{\text{Int}}^{\pi \text{ Reco MC}}(E_i)}. \quad (6.9)$$

2631 where  $N_{\text{Int}}^{\pi \text{ Reco Data}}(E_i)$  is the background subtracted bin content of the  $i$ -th bin in  
2632 for the reconstructed interacting histogram for data, i.e.

$$N_{\text{Int}}^{\pi \text{ Reco Data}}(E_i) = N_{\text{Int}}^{\text{TOT Data}}(E_i) - B_{\text{Int}}^{\text{Data}}(E_i) = C_{\text{Int}}^{\pi \text{ MC}}(E_i) N_{\text{Int}}^{\text{TOT Data}}(E_i). \quad (6.10)$$

2633 The systematics on this correction is estimated by varying the value of  $\alpha_{res}$  be-  
2634 tween 0 deg and 4.5 deg and propagating the uncertainty on the cross section.

2635 Figure 6.5 shows  $\epsilon^{\text{Int}}(E_i)$  in the left side and  $\epsilon^{\text{Inc}}(E_i)$  on the right as a function of  
2636 the kinetic energy for the 60A runs and their systematic uncertainty. Similarly, figure  
2637 6.6 shows  $\epsilon^{\text{Int}}(E_i)$  in the left side and  $\epsilon^{\text{Inc}}(E_i)$  on the right as a function of the kinetic  
2638 energy for the 100A runs and their systematic uncertainty.

	Magnet Current -60A			Magnet Current -100 A		
	MC $\pi^-$	MC $\mu^-$	MC $e^-$	MC $\pi^-$	MC $\mu^-$	MC $e^-$
Expected Composition	68.8 %	4.6 %	26.6 %	87.4 %	3.7 %	8.9 %
Composition 2x Muons	64.2 %	9.2 %	26.6 %	83.7 %	7.4 %	8.9 %
Composition 2x Electrons	42.2 %	4.6 %	53.2 %	78.5 %	3.7 %	17.8 %
Composition 0.5x Electrons	82.1 %	4.6 %	13.3 %	91.9 %	3.7 %	4.4 %

Table 6.1: Beam composition variation for the study of systematics due to beam contamination.

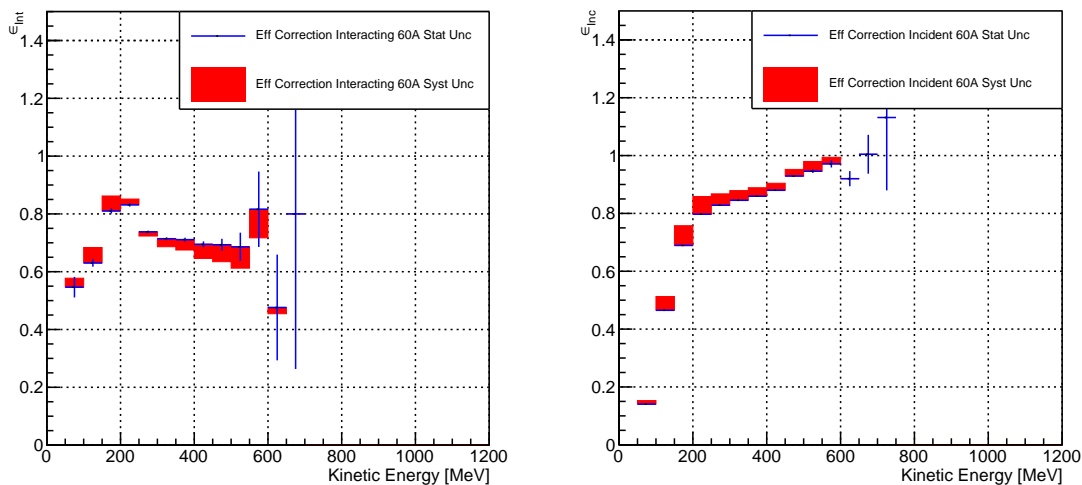


Figure 6.5: *Left:* Reconstruction effects correction on the 60A interacting histogram, statistical uncertainty in blue, systematic uncertainty in red. *Right:* Reconstruction effects correction on the 60A incident histogram, statistical uncertainty in blue, systematic uncertainty in red.

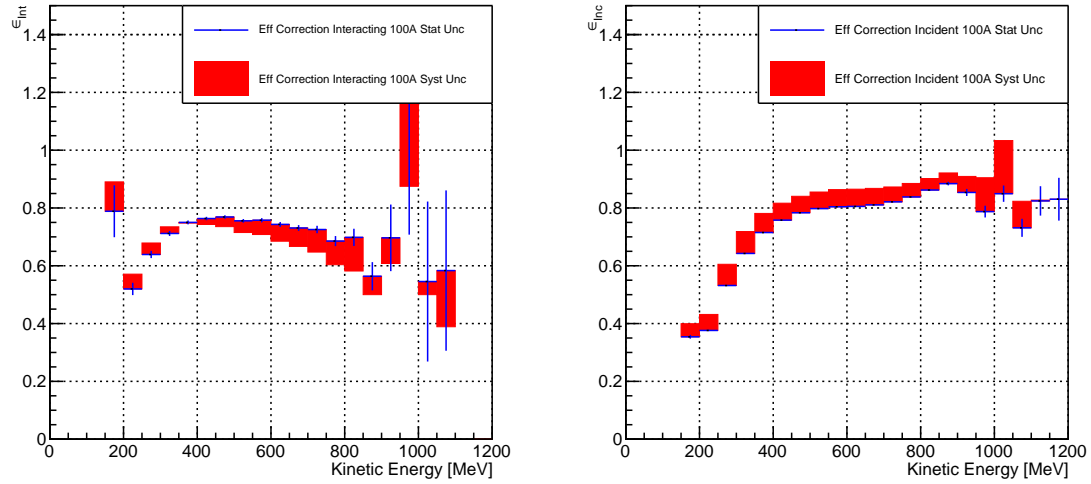


Figure 6.6: *Left*: Reconstruction effects correction on the 100A interacting histogram, statistical uncertainty in blue, systematic uncertainty in red. *Right*: Reconstruction effects correction on the 100A incident histogram, statistical uncertainty in blue, systematic uncertainty in red.

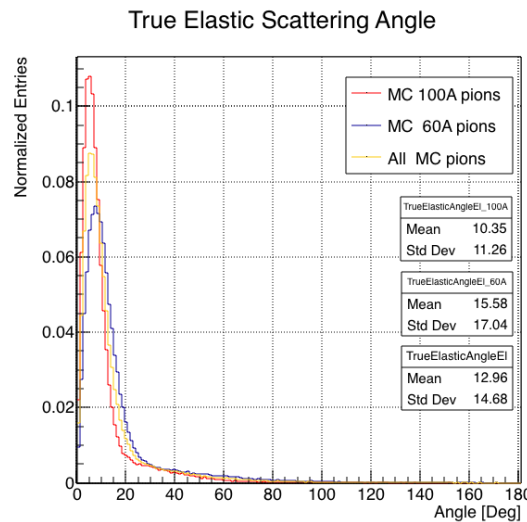


Figure 6.7: Distribution of the true scattering angle for a pion elastic scattering off the argon nucleus as simulated by Geant4.

2639 **6.3 Results**

2640 Figure 6.8 show the measurement of the ( $\pi^-$ -Ar) total hadronic cross section for  
2641 scattering angles greater than  $5^\circ$ , as the result of the background subtraction and  
2642 reconstruction effects correction to the raw cross section. The top left plot is the  
2643 measurement obtained on the 60A data, statistical uncertainty in black and system-  
2644 atic uncertainty in red. The top right plot is the measurement obtained on the 100A  
2645 data, statistical uncertainty in black and systematic uncertainty in blue. The bottom  
2646 plot shows the two measurements overlaid. In all three plot, the Geant4 prediction  
2647 for the total hadronic cross section for angle scattering greater than  $5^\circ$  is displayed  
2648 in green.

2649 The systematic uncertainty on the cross section is the sum in quadrature of the  
2650 statistical uncertainty, the systematic uncertainty related to the kinetic energy mea-  
2651 surement, the systematic uncertainty related to the beam composition and the sys-  
2652 tematic uncertainty related to the reconstruction effects correction.

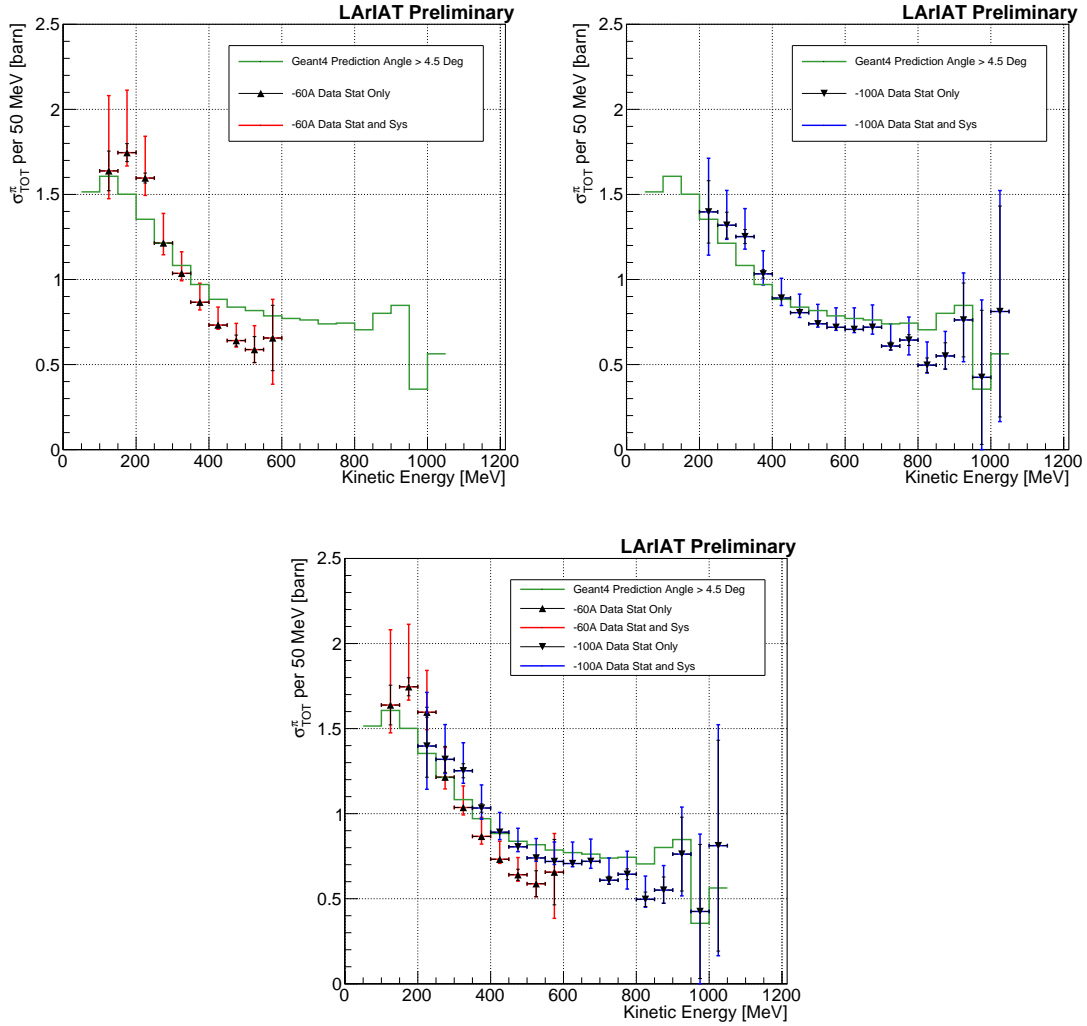


Figure 6.8: *Top Left:* ( $\pi^-$ -Ar) total hadronic cross section for scattering angles greater than  $5^\circ$  measured in the 60A sample, statistical uncertainty in black and systematic uncertainty in red. The Geant4 prediction for the total hadronic cross section for angle scattering greater than  $5^\circ$  is displayed in green.

*Top Right:* ( $\pi^-$ -Ar) total hadronic cross section for scattering angles greater than  $5^\circ$  measured in the 100A sample, statistical uncertainty in black and systematic uncertainty in blue. The Geant4 prediction for the total hadronic cross section for angle scattering greater than  $5^\circ$  is displayed in green.

*Bottom:* ( $\pi^-$ -Ar) total hadronic cross section measurements in the 60A and 100A samples overlaid with the Geant4 prediction (green).

2653 **Chapter 7**

2654 **Positive Kaon Cross Section**

2655 **Measurement**

2656 “Beat-up little seagull, on a marble stair  
2657 Tryin’ to find the ocean, lookin’ everywhere.”  
2658 – Nina Simone, 1978 –

2659 In this chapter, we show the result of the thin slice method to measure the ( $K^+$ -  
2660 Ar) total hadronic cross section. In Section 7.1, we start by measuring the raw  
2661 cross section. In Section 7.2, we apply a statistical subtraction of the background  
2662 contributions based on simulation and a correction for reconstruction effects. The  
2663 final results are presented in Section 7.3.

2664 **7.1 Raw Cross Section**

2665 We measure the raw ( $K^+$ -Ar) total hadronic cross section as a function of the kinetic  
2666 energy in the combined +60A and +100A dataset.

2667 Similar to the pion case, the raw cross section is given by the equation 4.4

$$\sigma_{TOT}(E_i) = \frac{1}{n\delta X} \frac{N_{Int}^{TOT}(E_i)}{N_{Inc}^{TOT}(E_i)}, \quad (4.4)$$

2668 where  $N_{Int}^{TOT}$  is the measured number of particles interacting at kinetic energy  $E_i$ ,  
2669  $N_{Inc}^{TOT}$  is the measured number of particles incident on an argon slice at kinetic energy  
2670  $E_i$ ,  $n$  is the density of the target centers and  $\delta X$  is the thickness of the argon slice.  
2671 The density of the target centers and the slab thickness are  $n = 0.021 \cdot 10^{24} \text{ cm}^{-3}$  and  
2672  $\delta X = 0.47 \text{ cm}$ , respectively.

2673 As in the case of pions, kaons might decay or interact between WC4 and the TPC  
2674 front face. Some of the interaction products may be wrongly matched to the WC  
2675 track, forming the “secondary” particle’s background in the kaon sample. We estimate  
2676 the effect of the contamination of secondaries through the DDMC kaon sample. Figure  
2677 7.1 shows the distribution of  $N_{Int}^{TOT}$  as a function of the kinetic energy. The data  
2678 central points are represented by black dots, the statistical uncertainty is shown in  
2679 black, while the systematic uncertainty is shown in red. Data is displayed over the  
2680  $N_{Int}^{TOT}$  distribution obtained with a DDMC sample of kaons shot from WC4. The  
2681 contribution from the simulated kaons which interact hadronically is shown in pink,  
2682 the contributions from kaon decay is shown in orange and the one from secondaries  
2683 in red. The simulated kaon’s and secondaries’ contributions are stacked; the sum of  
2684 their integrals is normalized to the integral of the data.

2685 Figure 7.2 shows the distribution of  $N_{Inc}^{TOT}$ . Data is displayed over the MC. For  
2686 the  $N_{Inc}^{TOT}$  distribution we do not make a distinction between kaons that decay or  
2687 interact hadronically because any kaon contributes to the flux of incident particles at  
2688 given kinetic energy independently from its final interaction. The same normalization  
2689 procedure is used for both the interacting and incident histograms.

2690 Figure 7.3 shows the raw cross section, statistical uncertainty in black and system-

atic uncertainty in red. The raw data cross section is overlaid to the reconstructed cross section for the MC mixed sample, displayed in azure. We calculate the statistical uncertainty for the interacting, incident and cross section distributions in a similar fashion to the pion case as described in Section 6.1.1.

As in the pion case, the only systematic effect considered in the measurement of the raw cross section results from the propagation of the uncertainty associate with the measurement of the kinetic energy at each argon slab. For kaons, the uncertainty on the kinetic energy of a candidate at the  $j^{th}$  slab of argon is given by

$$\delta KE_j = \sqrt{\delta p_{Beam}^2 + \delta E_{Loss}^2 + \delta E_{dep\ FF-j}^2} \quad (7.1)$$

$$= \sqrt{(2\% p_{Beam})^2 + (7\text{ [MeV]})^2 + (j - 1)^2(\sim 0.18\text{ [MeV]})^2}. \quad (7.2)$$

We propagate this uncertainty by varying the energy measurement  $KE_j$  at each argon slab. We measure  $N_{Inc}^{TOT}$ ,  $N_{Int}^{TOT}$  and the cross section in three cases: first assigning the measured  $KE_j$  at each kinetic energy sampling, then assigning  $KE_j + \delta KE_j$ , and finally assigning  $KE_j - \delta KE_j$ . The difference between the values obtained using the  $KE_j$  sampling and the maximum and minimum values in each kinetic energy bin determines the systematic uncertainty.

## 7.2 Corrections to the Raw Cross Section

As described in section 4.3.3, we need to apply a background correction and a correction for reconstruction effects in order to derive the kaon cross section from the raw cross section. The cross section is given in equation 4.9,

$$\sigma_{TOT}^{K^+}(E_i) = \frac{1}{n\delta X} \frac{\epsilon^{Inc}(E_i)}{\epsilon^{Int}(E_i)} \frac{C_{Int}^{KMC}(E_i)}{C_{Inc}^{KMC}(E_i)} \frac{N_{Int}^{TOT}(E_i)}{N_{Inc}^{TOT}(E_i)}. \quad (4.9)$$

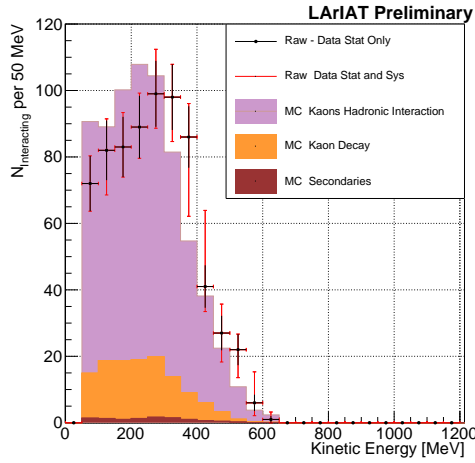


Figure 7.1: Raw number of interacting kaon candidates as a function of the reconstructed kinetic energy. The statistical uncertainties are shown in black, the systematic uncertainties in red.

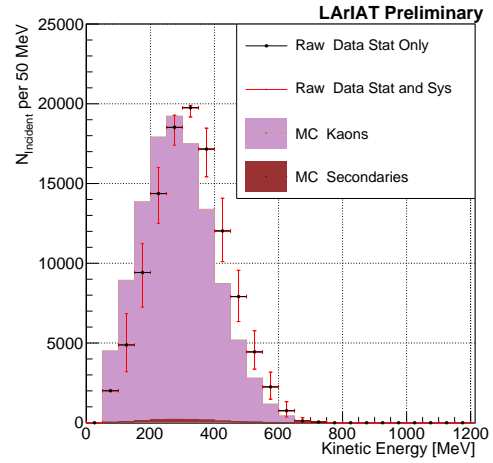


Figure 7.2: Raw number of incident kaon candidates as a function of the reconstructed kinetic energy. The statistical uncertainty is shown in black, the systematic uncertainties in red.

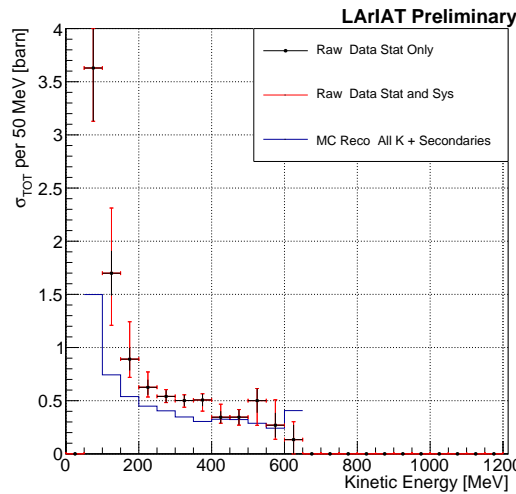


Figure 7.3: Raw ( $K^+$ -Ar) total hadronic cross section. The statistical uncertainty is shown in black, the systematic uncertainties in red. The raw cross section obtained with a MC sample of kaons is shown in blue. For the MC cross section, we include the contributions from secondaries.

2709     Currently, the only background considered for the kaon hadronic cross section  
2710   comes from the presence of secondaries and decay interaction points. A further de-  
2711   velopment of the analysis will need to account for the presence of a small proton  
2712   contamination. Figure 7.4 shows the relative kaon content suitable for the hadronic  
2713   cross section for the interacting and incident histograms.

2714     As described in 6.2.2 for the pion case, we derive the correction on a set of pure  
2715   kaon MC, calculating its value bin by bin as the ratio between the true bin content  
2716   and the correspondent reconstructed bin content. The correction is then applied  
2717   to the relevant bin in data. The correction for reconstruction effects is evaluated  
2718   separately for the interacting and incident histograms, namely  $\epsilon^{\text{int}}(E_i)$  and  $\epsilon^{\text{inc}}(E_i)$ ,  
2719   and propagated to the cross section as shown in equation 4.9.

2720     In section 5.5.1, we estimated the angular resolution for data and MC to be  
2721    $\bar{\alpha}_{\text{Data}} = (4.3 \pm 3.7) \text{ deg}$  and  $\bar{\alpha}_{\text{MC}} = (4.4 \pm 3.6) \text{ deg}$ , respectively. Most interaction  
2722   angles smaller than the angular resolution will thus be indistinguishable for the re-  
2723   construction. Thus, we claim we are able to measure the cross section for interaction  
2724   angles greater than 4.5 deg. Geant4 simulates interactions at all angles: in order  
2725   to calculate the correction for reconstruction effects, we select events which have an  
2726   interaction angle greater than a  $\alpha_{\text{res}}$  to construct the true interacting and incident  
2727   histograms (the denominator of the correction). The systematics on this correction  
2728   is estimated by varying the value of  $\alpha_{\text{res}}$  between 0 deg and 4.5 deg and propagating  
2729   the uncertainty on the cross section.

2730     Figure 7.5 shows  $\epsilon^{\text{Int}}(E_i)$  in the left side and  $\epsilon^{\text{Inc}}(E_i)$  on the right as a function of  
2731   the kinetic energy for the kaon sample and their systematic uncertainty.

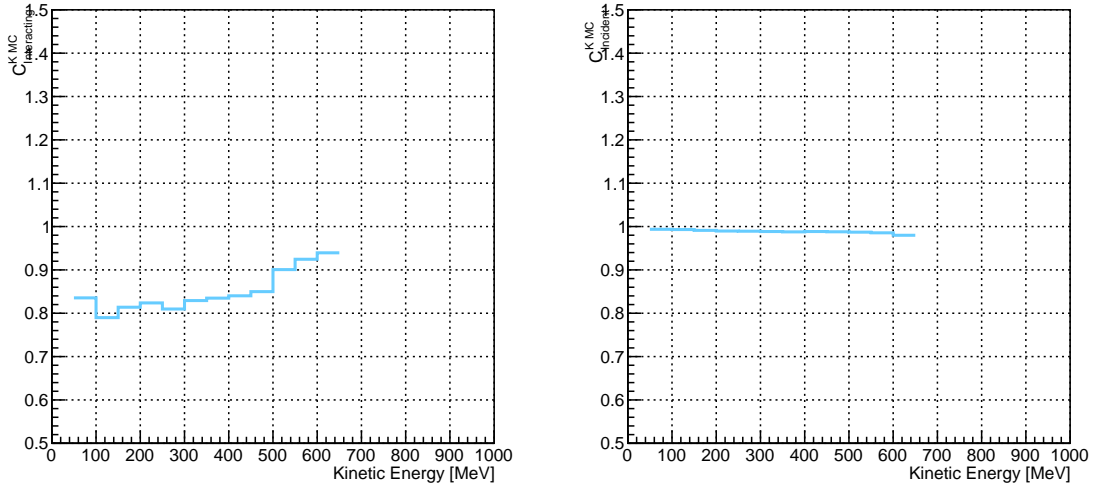


Figure 7.4: *Left:* MC estimated relative kaon content for kaons interacting hadronically as function of kinetic energy. *Right:* MC estimated relative kaon content for incident histogram a function of kinetic energy.

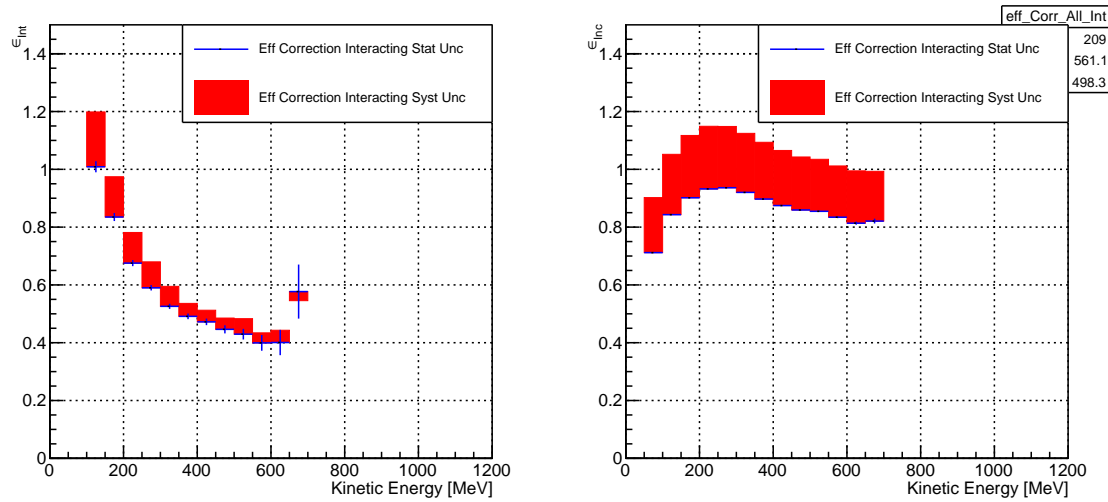


Figure 7.5: *Left:* Reconstruction effects correction on the interacting histogram, statistical uncertainty in blue, systematic uncertainty in red. *Right:* Reconstruction effects correction on the incident histogram, statistical uncertainty in blue, systematic uncertainty in red.

## 2732 7.3 Results

2733 Figure 7.6 show the measurement of the ( $K^+$ -Ar) total hadronic cross section for  
2734 scattering angles greater than  $5^\circ$ , as the result of the background subtraction and  
2735 reconstruction effects correction to the raw cross section. The plot shows the mea-  
2736 surement obtained on the full dataset, statistical uncertainty in black and systematic  
2737 uncertainty in red. The Geant4 prediction for the total hadronic cross section for  
2738 angle scattering greater than  $5^\circ$  is displayed in green.

2739 The systematic uncertainty on the cross section is the sum in quadrature of the  
2740 statistical uncertainty, the systematic uncertainty related to the kinetic energy mea-  
2741 surement and the systematic uncertainty related to the reconstruction effects correc-  
2742 tion.

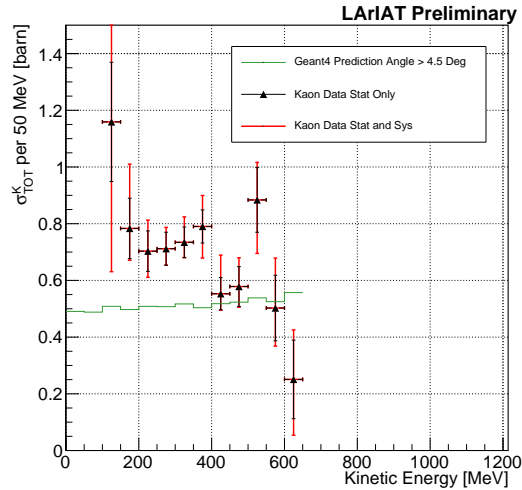


Figure 7.6: ( $K^+$ -Ar) total hadronic cross section for scattering angles greater than  $5^\circ$  measured in the 60A sample, statistical uncertainty in black and systematic un-  
certainty in red. The Geant4 prediction for the total hadronic cross section for angle scat-  
tering greater than  $5^\circ$  is displayed in green.

<sup>2743</sup> **Chapter 8**

<sup>2744</sup> **Conclusions**

<sup>2745</sup> In the era of neutrino precision measurements, of huge liquid argon detectors and  
<sup>2746</sup> of massive amount of information from LArTPCs, a renewed interest for an ancient  
<sup>2747</sup> measurement arises: the measurement of hadronic interactions with matter. With  
<sup>2748</sup> this work, we presented the first ever ( $\pi^-$ -Ar) and ( $K^+$ -Ar) total hadronic cross  
<sup>2749</sup> section measurements as a function of the hadron kinetic energy. These analyses are  
<sup>2750</sup> the first physics analyses developed by the LArIAT experiment. Both the analysis  
<sup>2751</sup> follow a similar workflow and they rely on beam line detector information as well as  
<sup>2752</sup> both calorimetry and tracking in the TPC.

<sup>2753</sup> In order to measure ( $\pi^-$ -Ar) total hadronic argon cross sections, we start by  
<sup>2754</sup> selecting pion beamline candidates through a series of selections on the beamline  
<sup>2755</sup> and TPC information apt to maximize the number of pions in the selection over  
<sup>2756</sup> the number of muons and electrons. We use the LArIAT beamline MC to estimate  
<sup>2757</sup> the beam composition of the selected beamline candidates and we propagate them  
<sup>2758</sup> to the LArIAT TPC constructing a properly weighted sample with the DDMC. We  
<sup>2759</sup> apply the thin slice method on the pion candidates and obtain the raw cross section  
<sup>2760</sup> measurement. From the simulated sample, we obtain two corrections accounting for  
<sup>2761</sup> the beamline background contamination and for detector effects. Finally, we apply

2762 the corrections to data and measure the true cross section.

2763 In order to measure ( $K^+$ -Ar) total hadronic argon cross sections, we follow a  
2764 similar procedure, i.e. we apply the thin slice method on kaon candidates identified  
2765 in the beamline to obtain the raw cross section. We apply a background correction and  
2766 a correction for detector effects to the raw cross section. The background correction  
2767 accounts for the presence of secondary particles in both the interacting and incident  
2768 histograms and for the presence of decay events in the interacting plot.

2769 The final results for the ( $\pi^-$ -Ar) and ( $K^+$ -Ar) total hadronic cross section are  
2770 shown side by side in figure 8.1.

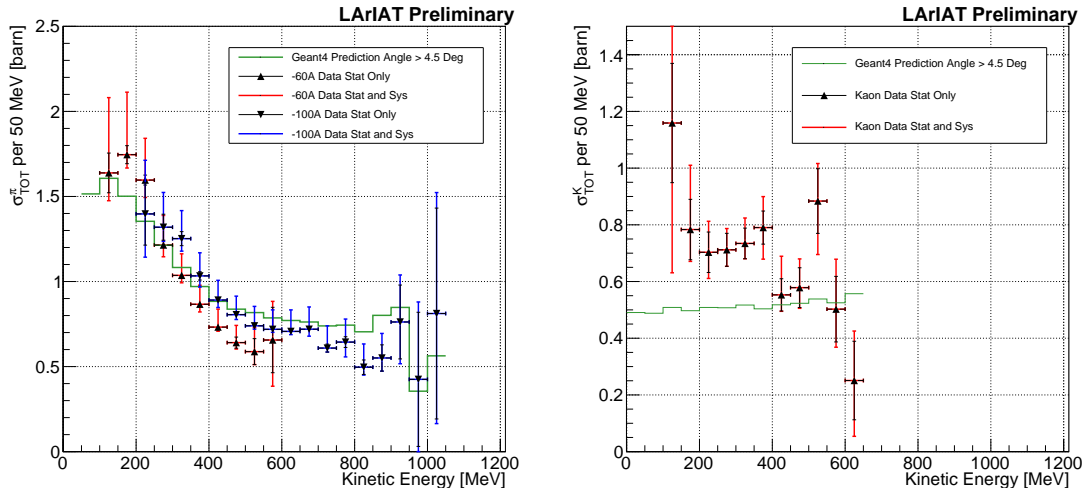


Figure 8.1: *Left:* ( $\pi^-$ -Ar) total hadronic cross section measurements in the 60A and 100A samples overlaid with the Geant4 prediction (green). *Right:* ( $K^+$ -Ar) total hadronic cross section for scattering angles greater than  $5^\circ$  measured in the 60A sample, statistical uncertainty in black and systematic uncertainty in red. The Geant4 prediction for the total hadronic cross section for angle scattering greater than  $5^\circ$  is displayed in green.

2771 These analyses' will serve as a basis for the future cross section measurements of  
2772 pions and kaons for the exclusive channels in LArIAT.

2773 **Appendix A**

2774 **Measurement of LArIAT Electric  
2775 Field**

2776 The electric field of a LArTPC in the drift volume is a fundamental quantity for  
2777 the proper functionality of this technology, as it affects almost every reconstructed  
2778 quantity such as the position of hits or their collected charge. Given its importance,  
2779 we calculate the electric field for LArIAT with a single line diagram from our HV  
2780 circuit and we cross check the obtained value with a measurement relying only on  
2781 TPC data.

2782 Before getting into the details of the measurement procedures, it is important to  
2783 explicit the relationship between some quantities in play. The electric field and the  
2784 drift velocity ( $v_{drift}$ ) are related as follows

$$v_{drift} = \mu(E_{field}, T)E_{field}, \quad (\text{A.1})$$

2785 where  $\mu$  is the electron mobility, which depends on the electric field and on the  
2786 temperature (T). The empirical formula for this dependency is described in [115]  
2787 and shown in Figure A.1 for several argon temperatures.

2788 The relationship between the drift time ( $t_{drift}$ ) and the drift velocity is trivially

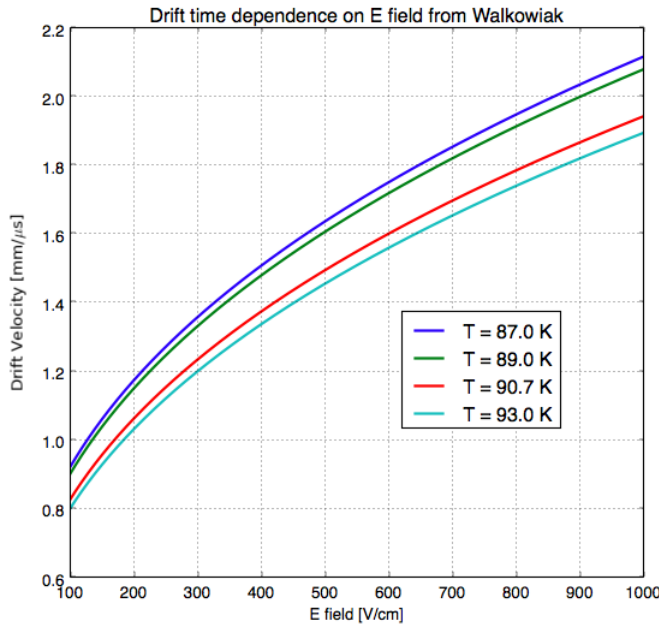


Figure A.1: Drift velocity dependence on electric field for several temperatures. The slope of the line at any one point represents the electron mobility for that given temperature and electric field.

Table A.1: Electric field and drift velocities in LArIAT smaller drift volumes

	Shield-Induction	Induction-Collection
$E_{field}$	700.63 V/cm	892.5 V/cm
$v_{drift}$	1.73 mm/μs	1.90 mm/μs
$t_{drift}$	2.31 μs	2.11 μs

2789 given by

$$t_{drift} = \Delta x / v_{drift}, \quad (\text{A.2})$$

2790 where  $\Delta x$  is the distance between the edges of the drift region. Table A.1 reports the  
2791 values of the electric field, drift velocity, and drift times for the smaller drift volumes.

2792 With these basic parameters established, we can now move on to calculating the  
2793 electric field in the main drift region (between the cathode and the shield plane).

2794 **Single line diagram method**

2795 The electric field strength in the LArIAT main drift volume can be determined know-  
 2796 ing the voltage applied to the cathode, the voltage applied at the shield plane, and the  
 2797 distance between them. We assume the distance between the cathode and the shield  
 2798 plane to be 470 mm and any length contraction due to the liquid argon is negligibly  
 2799 small ( $\sim 2$  mm).

2800 The voltage applied to the cathode can be calculated using Ohm's law and the  
 2801 single line diagram shown in Figure A.2. A set of two of filter pots for emergency  
 2802 power dissipation are positioned between the Glassman power supply and the cathode,  
 2803 one at each end of the feeder cable, each with an internal resistance of  $40 \text{ M}\Omega$ .

2804 Given the TPC resistor chain, the total TPC impedance is  $6 \text{ G}\Omega$ . Since the total  
 2805 resistance on the circuit is driven by the TPC impedance, we expect the resulting  
 2806 current to be

$$I = V_{PS}/R_{tot} = -23.5 \text{ kV}/6 \text{ G}\Omega \sim 4 \mu\text{A}, \quad (\text{A.3})$$

2807 which we measure with the Glassman power supply, shown in Figure A.3.

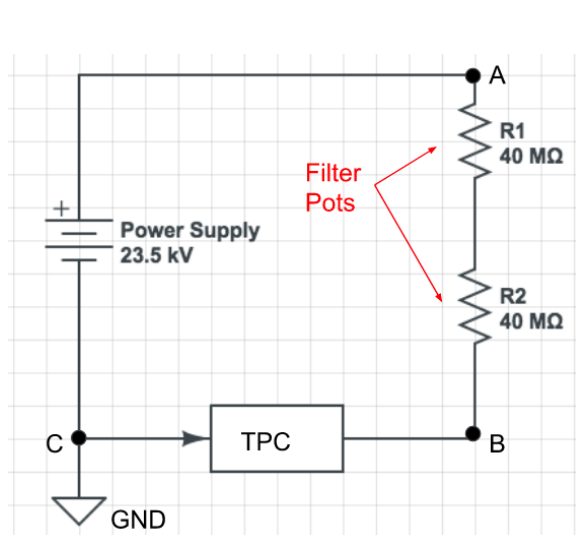


Figure A.2: LArIAT HV simple schematics.

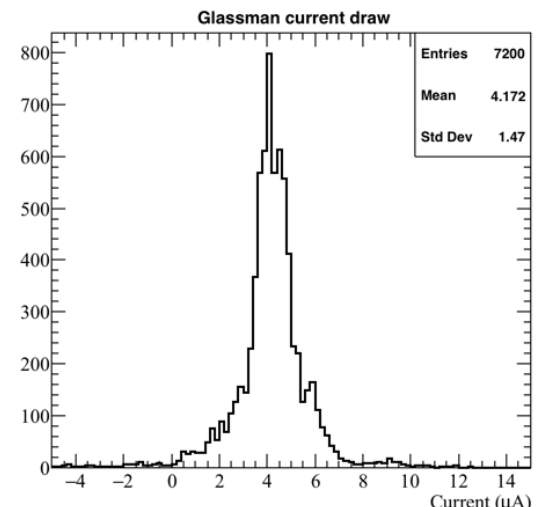


Figure A.3: Current reading from the Glassman between May 25th and May 30th, 2016 (typical Run-II conditions).

2808 Using this current, the voltage at the cathode is calculated as

$$V_{BC} = V_{PS} - (I \times R_{eq}) = -23.5 \text{ kV} + (0.00417 \text{ mA} \times 80 \text{ M}\Omega) = -23.17 \text{ kV}, \quad (\text{A.4})$$

2809 where  $I$  is the current and  $R_{eq}$  is the equivalent resistor representing the two filter  
2810 pots. The electric field is then calculated to be

$$E_{\text{field}} = \frac{V_{BC} - V_{\text{shield}}}{\Delta x} = 486.54 \text{ V/cm}. \quad (\text{A.5})$$

2811 **E field using cathode-anode piercing tracks**

2812 We devise an independent method to measure the drift time (and consequently drift  
2813 velocity and electric field) using TPC cathode to anode piercing tracks. We use this  
2814 method as a cross check to the single line method. The basic idea is simple:

- 2815 0. Select cosmic ray events with only 1 reconstructed track
- 2816 1. Reduce the events to the one containing tracks that cross both anode and cath-
- 2817 ode
- 2818 2. Identify the first and last hit of the track
- 2819 3. Measure the time difference between these two hits ( $\Delta t$ ).

2820 This method works under the assumptions that the time it takes for a cosmic particle  
2821 to cross the chamber ( $\sim \text{ns}$ ) is small compared to the charge drift time ( $\sim \text{hundreds}$   
2822 of  $\mu\text{s}$ ).

2823 We choose cosmic events to allow for a high number of anode to cathode piercing  
2824 tracks (ACP tracks), rejecting beam events where the particles travel almost perpen-  
2825 dicularly to drift direction. We select events with only one reconstructed track to  
2826 maximize the chance of selecting a single crossing muon (no-michel electron). We  
2827 utilize ACP tracks because their hits span the full drift length of the TPC, see figure

2828 A.4, allowing us to define where the first and last hit of the tracks are located in space  
2829 regardless of our assumption of the electric field.

2830 One of the main features of this method is that it doesn't rely on the measurement  
2831 of the trigger time. Since  $\Delta t$  is the time difference between the first and last hit of a  
2832 track and we assume the charge started drifting at the same time for both hits, the  
2833 measurement of the absolute beginning of drift time  $t_0$  is unnecessary. We boost the  
2834 presence of ACP tracks in the cosmic sample by imposing the following requirements  
2835 on tracks:

- 2836 • vertical position (Y) of first and last hits within  $\pm 18$  cm from TPC center  
2837 (avoid Top-Bottom tracks)
- 2838 • horizontal position (Z) of first and last hits within 2 and 86 cm from TPC front  
2839 face (avoid through going tracks)
- 2840 • track length greater than 48 cm (more likely to be crossing)
- 2841 • angle from the drift direction (phi in figure A.5) smaller than 50 deg (more  
2842 reliable tracking)
- 2843 • angle from the beam direction (theta in figure A.5) greater than 50 deg (more  
2844 reliable tracking)

2845 Tracks passing all these selection requirements are used for the  $\Delta t$  calculation.

2846 For each track passing our selection, we loop through the associated hits to retrieve  
2847 the timing information. The analysis is performed separately on hits on the collection  
2848 plane and induction plane, but lead to consistent results. As an example of the time  
2849 difference, figures A.6 and A.7 represent the difference in time between the last and  
2850 first hit of the selected tracks for Run-II Positive Polarity sample on the collection  
2851 and induction plane respectively. We fit with a Gaussian to the peak of the  $\Delta t$   
2852 distributions to extract the mean drift time and the uncertainty associated with it.

2853 The long tail at low  $\Delta t$  represents contamination of non-ACP tracks in the track  
2854 selection. We apply the same procedure to Run-I and Run-II, positive and negative  
2855 polarity alike.

2856 To convert  $\Delta t$  recorded for the hits on the induction plane to the drift time we  
2857 employ the formula

$$t_{drift} = \Delta t - t_{S-I} \quad (\text{A.6})$$

2858 where  $t_{drift}$  is the time the charge takes to drift in the main volume between the  
2859 cathode and the shield plane and  $t_{S-I}$  is the time it takes for the charge to drift from  
2860 the shield plane to the induction plane. In Table A.1 we calculated the drift velocity  
2861 in the S-I region, thus we can calculate  $t_{S-I}$  as

$$t_{S-I} = \frac{l_{S-I}}{v_{S-I}} = \frac{4mm}{1.73mm/\mu s} \quad (\text{A.7})$$

2862 where  $l_{S-I}$  is the distance between the shield and induction plane and  $v_{S-I}$  is the drift  
2863 velocity in the same region. A completely analogous procedure is followed for the hits  
2864 on the collection plane, taking into account the time the charge spent in drifting from  
2865 shield to induction as well as between the induction and collection plane. The value  
2866 for  $\Delta t_{drift}$ , the calculated drift velocity ( $v_{drift}$ ), and corresponding drift electric field  
2867 for the various run periods is given in Table A.2 and are consistent with the electric  
2868 field value calculated with the single line diagram method.

### Delta $t_{drift}$ , drift v and E field with ACP tracks

Data Period	$\Delta t_{Drift}$ [ $\mu s$ ]	Drift velocity [mm/ $\mu s$ ]	E field [V/cm]
RunI Positive Polarity Induction	$311.1 \pm 2.4$	$1.51 \pm 0.01$	$486.6 \pm 21$
RunI Positive Polarity Collection	$310.9 \pm 2.6$	$1.51 \pm 0.01$	$487.2 \pm 21$
RunII Positive Polarity Induction	$315.7 \pm 2.8$	$1.49 \pm 0.01$	$467.9 \pm 21$
RunII Positive Polarity Collection	$315.7 \pm 2.7$	$1.49 \pm 0.01$	$467.9 \pm 21$
RunII Negative Polarity Induction	$315.9 \pm 2.6$	$1.49 \pm 0.01$	$467.1 \pm 21$
RunII Negative Polarity Collection	$315.1 \pm 2.8$	$1.49 \pm 0.01$	$470.3 \pm 21$
Average Values	314.1	$1.50 \pm 0.01$	$474.3 \pm 21$

Table A.2:  $\Delta t$  for the different data samples used for the Anode-Cathode Piercing tracks study.

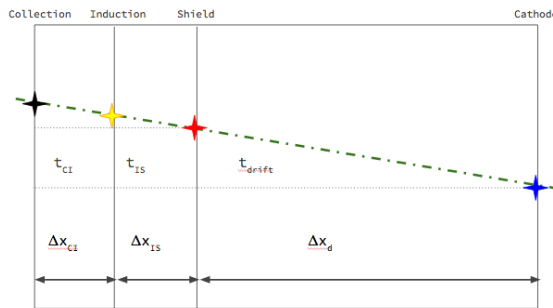


Figure A.4: Pictorial representation of the YX view of the TPC. The distance within the anode planes and between the shield plane and the cathode is purposely out of proportion to illustrate the time difference between hits on collection and induction. An ACP track is shown as an example.

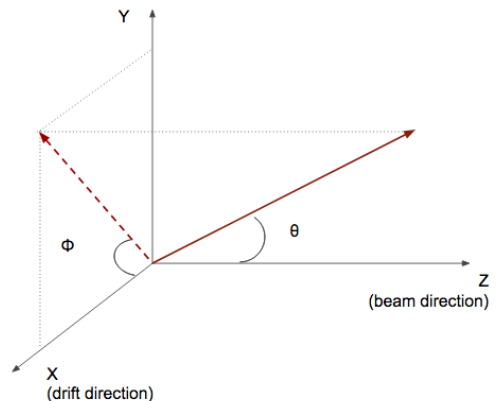


Figure A.5: Angle definition in the context of LArIAT coordinate system.

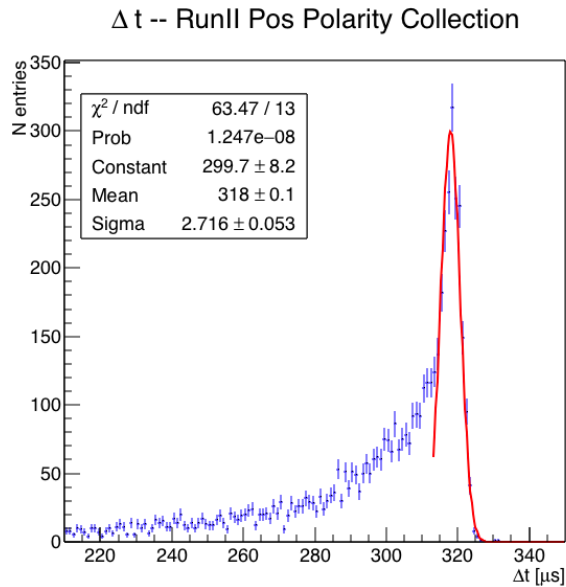


Figure A.6: Collection plane  $\Delta t$  fit for Run II positive polarity ACP data selected tracks.

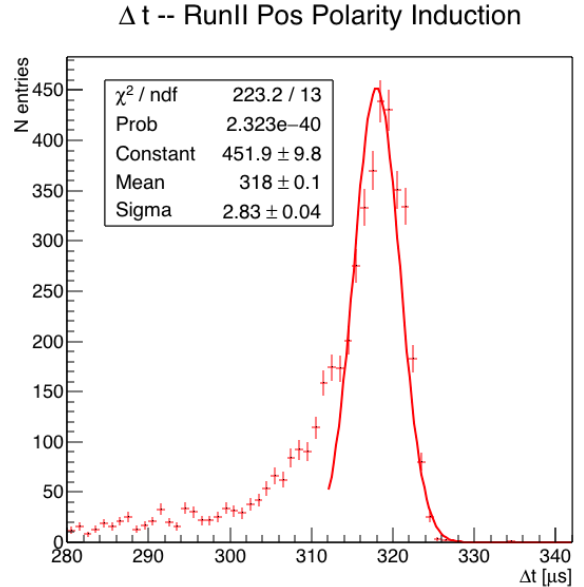


Figure A.7: Induction plane  $\Delta t$  fit for Run II positive polarity ACP data selected tracks.

2869 **Appendix B**

2870 **Additional Tracking Studies for**  
2871 **LArIAT Cross Section Analyses**

2872 In this section, we describe two studies. The first is a justification of the selection  
2873 criteria for the beamline handshake with the TPC information. We perform this  
2874 study to boost the correct identification of the particles in the TPC associated with  
2875 the beamline information, while maintaining sufficient statistics for the cross section  
2876 measurement. The second study is an optimization of the tracking algorithm, with  
2877 the scope of maximizing the identification of the hadronic interaction point inside the  
2878 TPC. These two studies are related, since the optimization of the tracking is per-  
2879 formed on TPC tracks which have been matched to the wire chamber track; in turn,  
2880 the tracking algorithm for TPC tracks determines the number of reconstructed tracks  
2881 in each event used to try the matching with the wire chamber track. Starting with  
2882 a sensible tracking reconstruction, we perform the WC2TPC matching optimization  
2883 first, then the tracking optimization. The WC2TPC match purity and efficiency are  
2884 then calculated again with the optimized tracking.

2885    **B.0.1   Study of WC to TPC Match**

2886   Scope of this study is assessing the performances of the WC2TPC match on Monte  
2887   Carlo (see Section 4.2 ) and decide the selection values we will use on data. A  
2888   word of caution is necessary here. With this study, we want to minimize pathologies  
2889   associated with the presence of the primary hadron itself, e.g. the incorrect association  
2890   between the beamline hadron and its decay products inside the TPC. Assessing the  
2891   contamination from pile-up<sup>1</sup>, albeit related, is beyond the scope of this study.

2892       In MC, we are able to define a correct WC2TPC match using the Geant4 truth  
2893   information. We are thus able to count how many times the WC tracks is associated  
2894   with the wrong TPC reconstructed track.

2895       We define a correct match if the all following conditions are met:

- 2896       - the length of the true primary Geant4 track in the TPC is greater than 2 cm,  
2897       - the length of the reconstructed track length is greater than 2 cm,  
2898       - the Z position of the first reconstructed point is within 2 cm from the TPC  
2899           front face  
2900       - the distance between the reconstructed track and the true entering point is the  
2901           minimum compared with all the other reconstructed tracks.

2902       In order to count the wrong matches, we consider all the reconstructed tracks  
2903   whose Z position of the first reconstructed point lies within 2 cm from the TPC front  
2904   face. Events with true length in TPC < 2 cm are included. Since hadrons are shot  
2905   100 cm upstream from the TPC front face, the following two scenarios are possible  
2906   from a truth standpoint:

2907       [Ta ] the primary hadron decays or interact strongly before getting to the TPC,

---

1. We remind the reader that the DDMC is a single particle Monte Carlo, where the beam pile up is not simulated.

2908 [Tb ] the primary hadron enters the TPC.

2909 As described in Section 4.2, we define a WC2TPC match according to the relative  
2910 position of the WC and TPC track parametrized with  $\Delta R$  and the angle between  
2911 them, parametrized with  $\alpha$ . Once we choose the selection values  $r_T$  and  $\alpha_T$  to de-  
2912 termine a reconstructed WC2TPC match, the following five scenarios are possible in  
2913 the truth to reconstruction interplay :

- 2914 1) only the correct track is matched  
2915 2) only one wrong track is matched  
2916 3) the correct track and one (or more) wrong tracks are matched  
2917 4) multiple wrong tracks matched.  
2918 5) no reconstructed tracks are matched

2919 Since we keep only events with one and only one match, we discard cases 3), 4)  
2920 and 5) from the events used in the cross section measurement. For each set of  $r_T$  and  
2921  $\alpha_T$  selection value, we define purity and efficiency of the selection as follows:

$$\text{Efficiency} = \frac{\text{Number of events correctly matched}}{\text{Number of events with primary in TPC}}, \quad (\text{B.1})$$

$$\text{Purity} = \frac{\text{Number of events correctly matched}}{\text{Total number of matched events}}. \quad (\text{B.2})$$

2922 Figure B.1 shows the efficiency (left) and purity (right) for WC2TPC match as  
2923 a function of the radius,  $r_T$ , and angle,  $\alpha_T$ , selection value. It is apparent how both  
2924 efficiency and purity are fairly flat as a function of the radius selection value at a  
2925 given angle. This is not surprising. Since we are studying a single particle gun Monte  
2926 Carlo sample, the wrong matches can occur only for mis-tracking of the primary or

for association with decay products; decay products will tend to be produced at large angles compared to the primary, but could be fairly close to the in  $x$  and  $y$  projection of the primary. The radius cut would play a key role in removing pile up events.

For LArIAT cross section measurements, we generally prefer purity over efficiency, since a sample of particles of a pure species will lead to a better measurement. Obviously, purity should be balanced with a sensible efficiency to avoid rejecting the whole sample.

We choose  $(\alpha_T, r_T) = (8 \text{ deg}, 4 \text{ cm})$  and get a MC 85% efficiency and 98% purity for the kaon sample and a MC 95% efficiency and 90% purity for the pion sample.

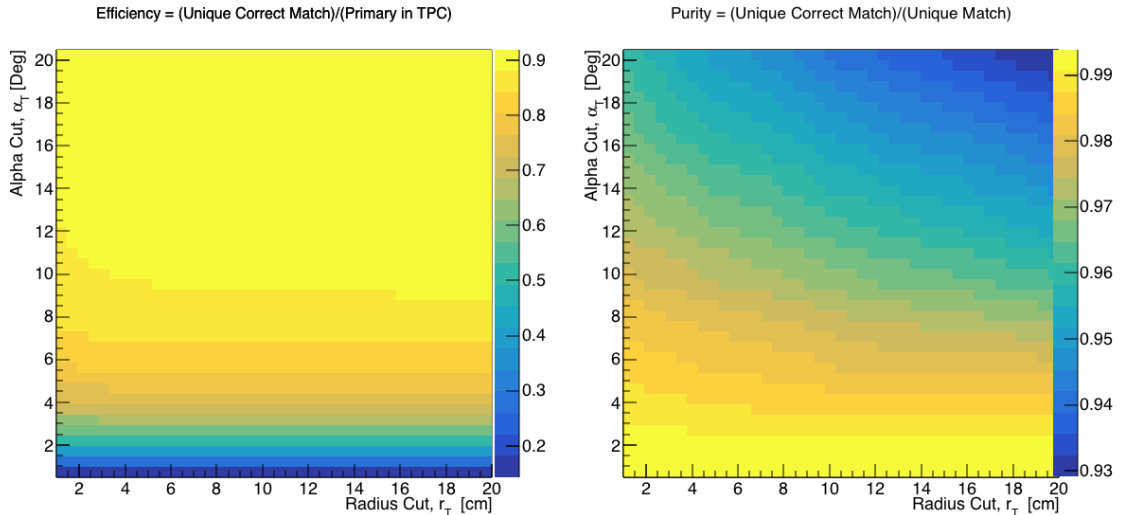


Figure B.1: Efficiency (left) and purity (right) for WC2TPC match as a function of the radius and angle selections for the kaon sample.

## B.0.2 Tracking Optimization

We perform an optimization of the clustering algorithm (see Section 2.1.5) with the scope of maximizing the efficiency of finding the interaction point for the total hadronic cross section measurements. We define as the interaction point the most downstream point of a WC2TPC matched TPC tracks within the TPC fiducial volume. Since all the WC2TPC tracks are by definition beam particles, tracks travel

2942 from upstream to downstream in the TPC; thus, identifying the interaction point  
2943 means to stop the tracking correctly.

2944 TrajCluster is the package used to cluster hits in LArIAT; this package counts more  
2945 than 20 tunable parameters. A standard method to develop clustering algorithms and  
2946 checking their performances is to “hand scan”, which means recognizing the effect of  
2947 parameters tuning by looking at a series of data event displays. Albeit we recognize  
2948 the importance of hand scanning as a great diagnosis tool, we developed a fully  
2949 automated optimization package which compares MC reconstructed information to  
2950 MC truth.

2951 We start by defining a figure of merit in order to discern what makes a parameter  
2952 configuration better than an other. We chose the percentage of events whose recon-  
2953 structed and true length differ less than 2 cm. We then identify the parameters in  
2954 TrajCluster that are most important to correctly stop the tracking and an appropriate  
2955 range of values for each of them. We chose to optimize the parameters that leverage  
2956 on the angle between consecutive groups of hits, the number of hits use in the cluster  
2957 fit and the average hit charge to stop the tracking. We define a configuration space  
2958 with all possible combination of values for the chosen parameters and we perform  
2959 reconstruction one combination at a time: the combination with the highest figure of  
2960 merit determines the optimized tracking reconstruction.

2961 We chose construct the combination space using a total of 5 parameters, 3 values  
2962 each and two iterations of the method (for a total of 486 combinations). We run the  
2963 combinations on a sample of 100000 pion events. After the optimization, the most  
2964 upstream point of the tracking is correctly identified 99.5% of the times, the most  
2965 downstream point is correctly identified 62.5% of the times, the tracking stops short  
2966 about 15% of the times and misses the interaction point 22.5% of the times. Hand  
2967 scanning confirmed that the missed interaction points happen in the vast majority of  
2968 cases for very shallow angles, as shown in the event display in Figure, or in the case

2969 of angles visible only in one projection plane. We also noticed that the premature  
2970 stopping of the tracks is often related to the presence of delta rays parallel to the  
2971 track. We see room of improvement, such as the delta ray removal and a forced track  
2972 breaking in case of a kink present in a single plane, for a future analysis. **ADD evd**

2973 The procedure behind this optimization package is virtually applicable to any  
2974 LArSoft module where it is possible to define figure of merit.

2975 **Appendix C**

2976 **Energy Calibration**

2977 Scope of the energy calibration is to identify the factors which convert the charge  
2978 collected ( $dQ$ ) to energy deposited in the chamber ( $dE$ ). As described in section  
2979 2.1.5, this is a multi-step procedure. In LArIAT, we first correct the raw charge by  
2980 the electronic noise on the considered wire [103], then by the electron lifetime [104],  
2981 and then by the recombination using the ArgoNeut recombination values. Lastly, we  
2982 apply overall calibration of the energy, i.e. we determine the “calorimetry constants”  
2983 using the procedure described in this section.

2984 We independently determine the calorimetry constants for Data and Monte Carlo  
2985 in the LArIAT Run-II Data samples using a parametrization of the stopping power  
2986 (a.k.a. energy deposited per unit length,  $dE/dX$ ) as a function of momentum. This is  
2987 done by comparing the stopping power measured on reconstructed quantities against  
2988 the Bethe-Bloch theoretical prediction for various particle species (see Equation 2.1).  
2989 We obtain the theoretical expectation for the  $dE/dX$  most probable value of pions  
2990 ( $\pi$ ), muons ( $\mu$ ), kaons ( $K$ ), and protons ( $p$ ) in the momentum range most relevant  
2991 for LArIAT (Figure C.1) using the tables provided by the Particle Data Group [101]  
2992 for liquid argon [1].

2993 The basic idea of this calibration technique is to utilize a sample of beamline

2994 events with known particle species and momentum to measure the  $dE/dX$  of the  
2995 corresponding tracks in the TPC. In particular, we decided to use positive pions as  
2996 calibration sample and samples from all the other particle species as cross check. Once  
2997 the  $dE/dX$  of the positive pion sample has been measured at various momenta, we  
2998 tune to calorimetry constants within the reconstruction software to align the measured  
2999 values to match the theoretical ones found in Figure C.1.

3000 In data, we start by selecting a sample of beamline positive pion beamline can-  
3001 didates without any restriction on their measured momentum<sup>1</sup>. We then apply the  
3002 WC2TPC match and subtract the energy loss upstream to the TPC front face, de-  
3003 termining the momentum at the TPC front face. For each surviving pion candidate,  
3004 we measure the  $dE/dx$  at each of the first 12 spacepoints associated the 3D recon-  
3005 structed track, corresponding to a  $\sim 5$  cm portion. These  $dE/dX$  measurements are  
3006 then put into a histogram that corresponds to measured momentum of the track.  
3007 The  $dE/dX$  histograms are sampled every 50 MeV/c in momentum (e.g. 150 MeV/c  
3008  $< P < 200$  MeV/c, 200 MeV/c  $< P < 250$ /c MeV, etc...). This process of selecting,  
3009 sampling, and recording the  $dE/dX$  for various momentum bins is repeated over the  
3010 entire sample of events, allowing us to collect sufficient statistic in most of the mo-  
3011 mentum bins between 150 MeV/c and 1100 MeV/c. On average, pions and muons  
3012 only lose  $\sim 10$  MeV in this 5 cm section of the track and protons lose  $\sim 20$  MeV. Thus  
3013 choosing 50 MeV/c size bins for our histograms covers the energy spread within those  
3014 bins due to energy loss from ionization for all the particle species identifiable in the  
3015 beamline. Each 50 MeV/c momentum binned  $dE/dX$  histogram is now fit with a  
3016 simple Landau function. The most probable value (MPV) and the associated error  
3017 on the MPV from the fit are extracted and plotted against the theoretical prediction  
3018 Figure C.1. Depending on the outcome of the data-prediction comparison, we modify  
3019 the calorimetry constants and we repeat the procedure until a qualitative agreement

---

1. it should be noted that some muon and position contamination is present in the  $\pi^+$  sample

3020 is achieved. We perform this tuning for the collection and induction plane separately.  
 3021 As a cross check to the calorimetry constants determined using the positive pions,  
 3022 we lock the constants and plot the  $dE/dx$  versus momentum distribution of all the  
 3023 other particle species identifiable in the beamline data ( $\pi/\mu/e$ , K , p, in both polarities)  
 3024 against the corresponding Beth-Bloch prediction. The agreement between data  
 3025 from the other particle species and the predictions is the expected result of this cross  
 3026 check. The results of the tuning and cross check for Run-II data on the collection  
 3027 plane is shown in Figure C.2 negative polarity data on top, positive polarity data on  
 3028 the bottom.

3029 In MC, we simulate the corresponding positive pion sample with the DDMC (see  
 3030 section 5.2.2) and follow the same steps as in data. More details on the calorimetry  
 3031 tuning can be found in [79].

3032 **Add agreement between data and MC for dedx for pions**

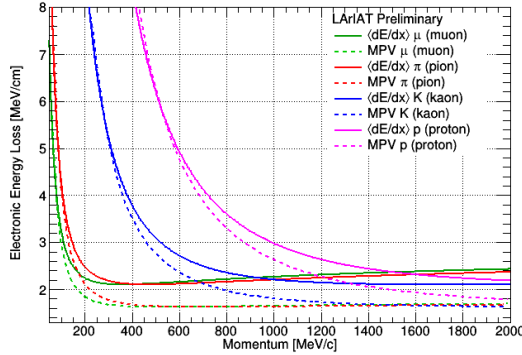


Figure C.1: Stopping power for pions, muons, kaons, and protons in liquid argon over the momentum range most relevant for LArIAT according to the Beth-Bloch equation. The solid lines represent the prediction for the mean energy  $dE/dX$ , while the dashed lines are the predictions for the MPV.

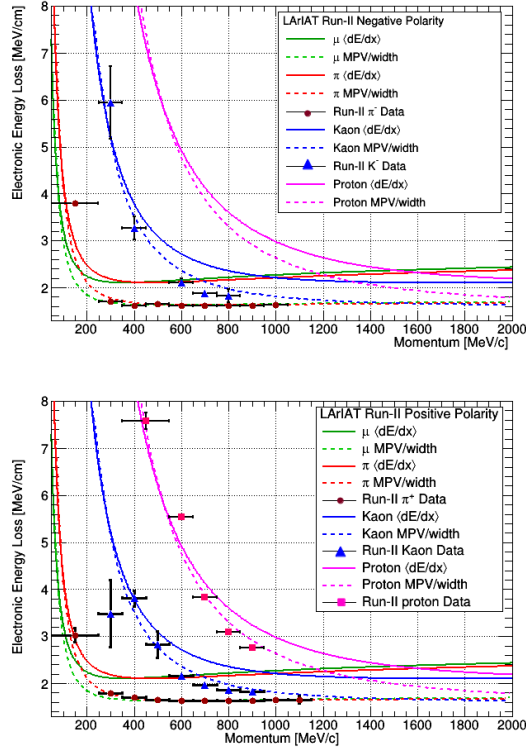


Figure C.2: Stopping power versus Momentum for Run-II negative (top) and positive (bottom) polarity data. We achieve the agreement between the Bethe-Bloch predictions and the distribution obtained with of the positive pions (top plot, red dots) by tuning the calorimetry constants. Once the calorimetry constants are locked in, the agreement between the other particle species and the Bethe-Bloch predictions follows naturally.

3033    **Bibliography**

- 3034    [1] PDG Tables for Liquid Argon. . Technical report.
- 3035    [2] Precision electroweak measurements on the  $Z$  resonance. *Physics Reports*,  
3036                          427(5):257 – 454, 2006.
- 3037    [3] K. Abe, J. Amey, C. Andreopoulos, M. Antonova, S. Aoki, A. Ariga, D. Au-  
3038        tiero, S. Ban, M. Barbi, G. J. Barker, G. Barr, C. Barry, P. Bartet-Friburg,  
3039        M. Batkiewicz, V. Berardi, S. Berkman, S. Bhadra, S. Bienstock, A. Blondel,  
3040        S. Bolognesi, S. Bordoni, S. B. Boyd, D. Brailsford, A. Bravar, C. Bronner,  
3041        M. Buizza Avanzini, R. G. Calland, T. Campbell, S. Cao, S. L. Cartwright,  
3042        M. G. Catanesi, A. Cervera, C. Checchia, D. Cherdack, N. Chikuma,  
3043        G. Christodoulou, A. Clifton, J. Coleman, G. Collazuol, D. Coplowe, A. Cudd,  
3044        A. Dabrowska, G. De Rosa, T. Dealtry, P. F. Denner, S. R. Dennis, C. Densham,  
3045        D. Dewhurst, F. Di Lodovico, S. Di Luise, S. Dolan, O. Drapier, K. E. Duffy,  
3046        J. Dumarchez, M. Dziewiecki, S. Emery-Schrenk, A. Ereditato, T. Feusels,  
3047        A. J. Finch, G. A. Fiorentini, M. Friend, Y. Fujii, D. Fukuda, Y. Fukuda,  
3048        V. Galymov, A. Garcia, C. Giganti, F. Gizzarelli, T. Golan, M. Gonin, D. R.  
3049        Hadley, L. Haegel, M. D. Haigh, D. Hansen, J. Harada, M. Hartz, T. Hasegawa,  
3050        N. C. Hastings, T. Hayashino, Y. Hayato, R. L. Helmer, A. Hillairet, T. Hiraki,  
3051        A. Hiramatsu, S. Hirota, M. Hogan, J. Holeczek, F. Hosomi, K. Huang, A. K.  
3052        Ichikawa, M. Ikeda, J. Imber, J. Insler, R. A. Intonti, T. Ishida, T. Ishii, E. Iwai,  
3053        K. Iwamoto, A. Izmaylov, B. Jamieson, M. Jiang, S. Johnson, P. Jonsson,

3054 C. K. Jung, M. Kabirnezhad, A. C. Kaboth, T. Kajita, H. Kakuno, J. Kameda,  
3055 D. Karlen, T. Katori, E. Kearns, M. Khabibullin, A. Khotjantsev, H. Kim,  
3056 J. Kim, S. King, J. Kisiel, A. Knight, A. Knox, T. Kobayashi, L. Koch, T. Koga,  
3057 A. Konaka, K. Kondo, L. L. Kormos, A. Korzenev, Y. Koshio, K. Kowalik,  
3058 W. Kropp, Y. Kudenko, R. Kurjata, T. Kutter, J. Lagoda, I. Lamont, M. Lam-  
3059 oureux, E. Larkin, P. Lasorak, M. Laveder, M. Lawe, M. Licciardi, T. Lindner,  
3060 Z. J. Liptak, R. P. Litchfield, X. Li, A. Longhin, J. P. Lopez, T. Lou, L. Ludovici,  
3061 X. Lu, L. Magaletti, K. Mahn, M. Malek, S. Manly, A. D. Marino, J. F. Martin,  
3062 P. Martins, S. Martynenko, T. Maruyama, V. Matveev, K. Mavrokordis, W. Y.  
3063 Ma, E. Mazzucato, M. McCarthy, N. McCauley, K. S. McFarland, C. McGrew,  
3064 A. Mefodiev, C. Metelko, M. Mezzetto, P. Mijakowski, A. Minamino, O. Mi-  
3065 neev, S. Mine, A. Missent, M. Miura, S. Moriyama, Th. A. Mueller, J. Myslik,  
3066 T. Nakadaira, M. Nakahata, K. G. Nakamura, K. Nakamura, K. D. Nakamura,  
3067 Y. Nakanishi, S. Nakayama, T. Nakaya, K. Nakayoshi, C. Nantais, C. Nielsen,  
3068 M. Nirko, K. Nishikawa, Y. Nishimura, P. Novella, J. Nowak, H. M. O'Keeffe,  
3069 K. Okumura, T. Okusawa, W. Oryszczak, S. M. Oser, T. Ovsyannikova, R. A.  
3070 Owen, Y. Oyama, V. Palladino, J. L. Palomino, V. Paolone, N. D. Patel,  
3071 P. Paudyal, M. Pavin, D. Payne, J. D. Perkin, Y. Petrov, L. Pickard, L. Pick-  
3072 ering, E. S. Pinzon Guerra, C. Pistillo, B. Popov, M. Posiadala-Zezula, J.-M.  
3073 Poutissou, R. Poutissou, P. Przewlocki, B. Quilain, T. Radermacher, E. Radi-  
3074 cioni, P. N. Ratoff, M. Ravonel, M. A. Rayner, A. Redij, E. Reinherz-Aronis,  
3075 C. Riccio, P. A. Rodrigues, E. Rondio, B. Rossi, S. Roth, A. Rubbia, A. Rychter,  
3076 K. Sakashita, F. Sánchez, E. Scantamburlo, K. Scholberg, J. Schwehr, M. Scott,  
3077 Y. Seiya, T. Sekiguchi, H. Sekiya, D. Sgalaberna, R. Shah, A. Shaikhiev,  
3078 F. Shaker, D. Shaw, M. Shiozawa, T. Shirahige, S. Short, M. Smy, J. T.  
3079 Sobczyk, H. Sobel, M. Sorel, L. Southwell, J. Steinmann, T. Stewart, P. Stowell,  
3080 Y. Suda, S. Suvorov, A. Suzuki, S. Y. Suzuki, Y. Suzuki, R. Tacik, M. Tada,

- 3081 A. Takeda, Y. Takeuchi, H. K. Tanaka, H. A. Tanaka, D. Terhorst, R. Terri,  
3082 T. Thakore, L. F. Thompson, S. Tobayama, W. Toki, T. Tomura, C. Touramani,  
3083 T. Tsukamoto, M. Tzanov, Y. Uchida, M. Vagins, Z. Vallari, G. Vasseur,  
3084 T. Vladislavljevic, T. Wachala, C. W. Walter, D. Wark, M. O. Wascko, A. We-  
3085 ber, R. Wendell, R. J. Wilkes, M. J. Wilking, C. Wilkinson, J. R. Wilson, R. J.  
3086 Wilson, C. Wret, Y. Yamada, K. Yamamoto, M. Yamamoto, C. Yanagisawa,  
3087 T. Yano, S. Yen, N. Yershov, M. Yokoyama, K. Yoshida, T. Yuan, M. Yu, A. Za-  
3088 lewska, J. Zalipska, L. Zambelli, K. Zaremba, M. Ziembicki, E. D. Zimmerman,  
3089 M. Zito, and J. Źmuda. Combined analysis of neutrino and antineutrino oscil-  
3090 lations at t2k. *Phys. Rev. Lett.*, 118:151801, Apr 2017.
- 3091 [4] K. Abe, Y. Haga, Y. Hayato, M. Ikeda, K. Iyogi, J. Kameda, Y. Kishimoto,  
3092 M. Miura, S. Moriyama, M. Nakahata, T. Nakajima, Y. Nakano, S. Nakayama,  
3093 A. Orii, H. Sekiya, M. Shiozawa, A. Takeda, H. Tanaka, T. Tomura, R. A. Wen-  
3094 dell, R. Akutsu, T. Irvine, T. Kajita, K. Kaneyuki, Y. Nishimura, E. Richard,  
3095 K. Okumura, L. Labarga, P. Fernandez, J. Gustafson, C. Kachulis, E. Kearns,  
3096 J. L. Raaf, J. L. Stone, L. R. Sulak, S. Berkman, C. M. Nantais, H. A.  
3097 Tanaka, S. Tobayama, M. Goldhaber, W. R. Kropp, S. Mine, P. Weatherly,  
3098 M. B. Smy, H. W. Sobel, V. Takhistov, K. S. Ganezer, B. L. Hartfiel, J. Hill,  
3099 N. Hong, J. Y. Kim, I. T. Lim, R. G. Park, A. Himmel, Z. Li, E. O’Sullivan,  
3100 K. Scholberg, C. W. Walter, T. Wongjirad, T. Ishizuka, S. Tasaka, J. S. Jang,  
3101 J. G. Learned, S. Matsuno, S. N. Smith, M. Friend, T. Hasegawa, T. Ishida,  
3102 T. Ishii, T. Kobayashi, T. Nakadaira, K. Nakamura, Y. Oyama, K. Sakashita,  
3103 T. Sekiguchi, T. Tsukamoto, A. T. Suzuki, Y. Takeuchi, T. Yano, S. V. Cao,  
3104 T. Hiraki, S. Hirota, K. Huang, T. Kikawa, A. Minamino, T. Nakaya, K. Suzuki,  
3105 Y. Fukuda, K. Choi, Y. Itow, T. Suzuki, P. Mijakowski, K. Frankiewicz, J. Hig-  
3106 night, J. Imber, C. K. Jung, X. Li, J. L. Palomino, M. J. Wilking, C. Yanag-  
3107 isawa, D. Fukuda, H. Ishino, T. Kayano, A. Kibayashi, Y. Koshio, T. Mori,

- 3108 M. Sakuda, C. Xu, Y. Kuno, R. Tacik, S. B. Kim, H. Okazawa, Y. Choi,  
3109 K. Nishijima, M. Koshiba, Y. Totsuka, Y. Suda, M. Yokoyama, C. Bronner,  
3110 M. Hartz, K. Martens, Ll. Marti, Y. Suzuki, M. R. Vagins, J. F. Martin, A. Kon-  
3111 aka, S. Chen, Y. Zhang, and R. J. Wilkes. Search for proton decay via  $p \rightarrow e^+ \pi^0$   
3112 and  $p \rightarrow \mu^+ \pi^0$  in 0.31 megaton · years exposure of the super-kamiokande water  
3113 cherenkov detector. *Phys. Rev. D*, 95:012004, Jan 2017.
- 3114 [5] R Acciarri, C Adams, J Asaadi, B Baller, T Bolton, C Bromberg, F Ca-  
3115 vanna, E Church, D Edmunds, A Ereditato, S Farooq, B Fleming, H Greenlee,  
3116 G Horton-Smith, C James, E Klein, K Lang, P Laurens, D McKee, R Mehdiyev,  
3117 B Page, O Palamara, K Partyka, G Rameika, B Rebel, M Soderberg, J Spitz,  
3118 A M Szelc, M Weber, M Wojcik, T Yang, and G P Zeller. A study of electron  
3119 recombination using highly ionizing particles in the argoneut liquid argon tpc.  
3120 *Journal of Instrumentation*, 8(08):P08005, 2013.
- 3121 [6] R Acciarri, M Antonello, B Baibussinov, M Baldo-Ceolin, P Benetti,  
3122 F Calaprice, E Calligarich, M Cambiaghi, N Canci, F Carbonara, F Cavanna,  
3123 S Centro, A G Cocco, F Di Pompeo, G Fiorillo, C Galbiati, V Gallo, L Grandi,  
3124 G Meng, I Modena, C Montanari, O Palamara, L Pandola, G B Piano Mortari,  
3125 F Pietropaolo, G L Raselli, M Roncadelli, M Rossella, C Rubbia, E Segreto,  
3126 A M Szelc, S Ventura, and C Vignoli. Effects of nitrogen contamination in  
3127 liquid argon. *Journal of Instrumentation*, 5(06):P06003, 2010.
- 3128 [7] R. Acciarri et al. Demonstration and Comparison of Operation of Photomulti-  
3129 plier Tubes at Liquid Argon Temperature. *JINST*, 7:P01016, 2012.
- 3130 [8] R. Acciarri et al. Design and Construction of the MicroBooNE Detector. *JINST*,  
3131 12(02):P02017, 2017.

- 3132 [9] R. Acciarri et al. First Observation of Low Energy Electron Neutrinos in a  
3133 Liquid Argon Time Projection Chamber. *Phys. Rev.*, D95(7):072005, 2017.  
3134 [Phys. Rev.D95,072005(2017)].
- 3135 [10] M Adamowski, B Carls, E Dvorak, A Hahn, W Jaskierny, C Johnson, H Jostlein,  
3136 C Kendziora, S Lockwitz, B Pahlka, R Plunkett, S Pordes, B Rebel, R Schmitt,  
3137 M Stancari, T Tope, E Voirin, and T Yang. The liquid argon purity demon-  
3138 strator. *Journal of Instrumentation*, 9(07):P07005, 2014.
- 3139 [11] C. Adams et al. The Long-Baseline Neutrino Experiment: Exploring Funda-  
3140 mental Symmetries of the Universe. 2013.
- 3141 [12] P. Adamson, L. Aliaga, D. Ambrose, N. Anfimov, A. Antoshkin, E. Arrieta-  
3142 Diaz, K. Augsten, A. Aurisano, C. Backhouse, M. Baird, B. A. Bambah,  
3143 K. Bays, B. Behera, S. Bending, R. Bernstein, V. Bhatnagar, B. Bhuyan,  
3144 J. Bian, T. Blackburn, A. Bolshakova, C. Bromberg, J. Brown, G. Brunetti,  
3145 N. Buchanan, A. Butkevich, V. Bychkov, M. Campbell, E. Catano-Mur, S. Chil-  
3146 dress, B. C. Choudhary, B. Chowdhury, T. E. Coan, J. A. B. Coelho, M. Colo,  
3147 J. Cooper, L. Corwin, L. Cremonesi, D. Cronin-Hennessy, G. S. Davies, J. P.  
3148 Davies, P. F. Derwent, R. Dharmapalan, P. Ding, Z. Djurcic, E. C. Dukes,  
3149 H. Duyang, S. Edayath, R. Ehrlich, G. J. Feldman, M. J. Frank, M. Gabrielyan,  
3150 H. R. Gallagher, S. Germani, T. Ghosh, A. Giri, R. A. Gomes, M. C. Goodman,  
3151 V. Grichine, R. Group, D. Grover, B. Guo, A. Habig, J. Hartnell, R. Hatcher,  
3152 A. Hatzikoutelis, K. Heller, A. Himmel, A. Holin, J. Hylen, F. Jediny, M. Judah,  
3153 G. K. Kafka, D. Kalra, S. M. S. Kasahara, S. Kasetti, R. Keloth, L. Kolupaeva,  
3154 S. Kotelnikov, I. Kourbanis, A. Kreymer, A. Kumar, S. Kurbanov, K. Lang,  
3155 W. M. Lee, S. Lin, J. Liu, M. Lokajicek, J. Lozier, S. Luchuk, K. Maan, S. Mag-  
3156 ill, W. A. Mann, M. L. Marshak, K. Matera, V. Matveev, D. P. Méndez, M. D.  
3157 Messier, H. Meyer, T. Miao, W. H. Miller, S. R. Mishra, R. Mohanta, A. Moren,

- 3158 L. Mualem, M. Muether, S. Mufson, R. Murphy, J. Musser, J. K. Nelson,  
3159 R. Nichol, E. Niner, A. Norman, T. Nosek, Y. Oksuzian, A. Olshevskiy, T. Ol-  
3160 son, J. Paley, P. Pandey, R. B. Patterson, G. Pawloski, D. Pershey, O. Petrova,  
3161 R. Petti, S. Phan-Budd, R. K. Plunkett, R. Poling, B. Potukuchi, C. Principato,  
3162 F. Psihas, A. Radovic, R. A. Rameika, B. Rebel, B. Reed, D. Rocco, P. Rojas,  
3163 V. Ryabov, K. Sachdev, P. Sail, O. Samoylov, M. C. Sanchez, R. Schroeter,  
3164 J. Sepulveda-Quiroz, P. Shanahan, A. Sheshukov, J. Singh, J. Singh, P. Singh,  
3165 V. Singh, J. Smolik, N. Solomey, E. Song, A. Sousa, K. Soustruznik, M. Strait,  
3166 L. Suter, R. L. Talaga, M. C. Tamsett, P. Tas, R. B. Thayyullathil, J. Thomas,  
3167 X. Tian, S. C. Tognini, J. Tripathi, A. Tsaris, J. Urheim, P. Vahle, J. Vasel,  
3168 L. Vinton, A. Vold, T. Vrba, B. Wang, M. Wetstein, D. Whittington, S. G. Wo-  
3169 jcicki, J. Wolcott, N. Yadav, S. Yang, J. Zalesak, B. Zamorano, and R. Zwaska.  
3170 Constraints on oscillation parameters from  $\nu_e$  appearance and  $\nu_\mu$  disappearance  
3171 in nova. *Phys. Rev. Lett.*, 118:231801, Jun 2017.
- 3172 [13] Alan Agresti. *Categorical Data Analysis*. Wiley Series in Probability and Statis-  
3173 tics. Wiley, 2013.
- 3174 [14] A. Aguilar-Arevalo et al. Evidence for neutrino oscillations from the observation  
3175 of anti-neutrino(electron) appearance in a anti-neutrino(muon) beam. *Phys.*  
3176 *Rev.*, D64:112007, 2001.
- 3177 [15] A. A. Aguilar-Arevalo et al. Improved Search for  $\bar{\nu}_\mu \rightarrow \bar{\nu}_e$  Oscillations in the  
3178 MiniBooNE Experiment. *Phys. Rev. Lett.*, 110:161801, 2013.
- 3179 [16] S. Amoruso et al. Study of electron recombination in liquid argon with the  
3180 ICARUS TPC. *Nucl. Instrum. Meth.*, A523:275–286, 2004.
- 3181 [17] C. Anderson et al. The ArgoNeuT Detector in the NuMI Low-Energy beam  
3182 line at Fermilab. *JINST*, 7:P10019, 2012.

- 3183 [18] C. Andreopoulos et al. The GENIE Neutrino Monte Carlo Generator. *Nucl.*  
3184        *Instrum. Meth.*, A614:87–104, 2010.
- 3185 [19] Timofei Bolshakov Andrey Petrov. Java synoptic toolkit. Technical report,  
3186        Sept 2010.
- 3187 [20] M. Antonello, B. Baibussinov, P. Benetti, E. Calligarich, N. Canci, S. Cen-  
3188        tro, A. Cesana, K. Cieslik, D. B. Cline, A. G. Cocco, A. Dabrowska, D. De-  
3189        qual, A. Dermenev, R. Dolfini, C. Farnese, A. Fava, A. Ferrari, G. Fiorillo,  
3190        D. Gibin, S. Gninenko, A. Guglielmi, M. Haranczyk, J. Holeczek, A. Ivashkin,  
3191        J. Kisiel, I. Kochanek, J. Lagoda, S. Mania, A. Menegolli, G. Meng, C. Monta-  
3192        nari, S. Otwinowski, A. Piazzoli, P. Picchi, F. Pietropaolo, P. Plonski, A. Rap-  
3193        poldi, G. L. Raselli, M. Rossella, C. Rubbia, P. Sala, A. Scaramelli, E. Seg-  
3194        reto, F. Sergiampietri, D. Stefan, J. Stepaniak, R. Sulej, M. Szarska, M. Ter-  
3195        rani, F. Varanini, S. Ventura, C. Vignoli, H. Wang, X. Yang, A. Zalewska,  
3196        and K. Zaremba. Precise 3d track reconstruction algorithm for the ICARUS  
3197        t600 liquid argon time projection chamber detector. *Advances in High Energy*  
3198        *Physics*, 2013:1–16, 2013.
- 3199 [21] M. Antonello et al. A Proposal for a Three Detector Short-Baseline Neutrino  
3200        Oscillation Program in the Fermilab Booster Neutrino Beam. 2015.
- 3201 [22] D. Ashery, I. Navon, G. Azuelos, H. K. Walter, H. J. Pfeiffer, and F. W.  
3202        Schlepütz. True absorption and scattering of pions on nuclei. *Phys. Rev. C*,  
3203        23:2173–2185, May 1981.
- 3204 [23] C. Athanassopoulos et al. Evidence for  $\nu(\mu) \rightarrow \nu(e)$  neutrino oscillations  
3205        from LSND. *Phys. Rev. Lett.*, 81:1774–1777, 1998.

- 3206 [24] Borut Bajc, Junji Hisano, Takumi Kuwahara, and Yuji Omura. Threshold  
3207 corrections to dimension-six proton decay operators in non-minimal {SUSY}  
3208  $\text{su}(5)$  {GUTs}. *Nuclear Physics B*, 910:1 – 22, 2016.
- 3209 [25] B. Baller. Trajcluster user guide. Technical report, apr 2016.
- 3210 [26] Gary Barker. Neutrino event reconstruction in a liquid argon TPC. *Journal of*  
3211 *Physics: Conference Series*, 308:012015, jul 2011.
- 3212 [27] BASF Corp. 100 Park Avenue, Florham Park, NJ 07932 USA.
- 3213 [28] R. Becker-Szendy, C. B. Bratton, D. R. Cady, D. Casper, R. Claus, M. Crouch,  
3214 S. T. Dye, W. Gajewski, M. Goldhaber, T. J. Haines, P. G. Halverson, T. W.  
3215 Jones, D. Kielczewska, W. R. Kropp, J. G. Learned, J. M. LoSecco, C. Mc-  
3216 Grew, S. Matsuno, J. Matthews, M. S. Mudah, L. Price, F. Reines, J. Schultz,  
3217 D. Sinclair, H. W. Sobel, J. L. Stone, L. R. Sulak, R. Svoboda, G. Thornton,  
3218 and J. C. van der Velde. Search for proton decay into  $e^+ + \pi^0$  in the imb-3  
3219 detector. *Phys. Rev. D*, 42:2974–2976, Nov 1990.
- 3220 [29] J B Birks. Scintillations from organic crystals: Specific fluorescence and relative  
3221 response to different radiations. *Proceedings of the Physical Society. Section A*,  
3222 64(10):874, 1951.
- 3223 [30] A. Bodek and J. L. Ritchie. Further studies of fermi-motion effects in lepton  
3224 scattering from nuclear targets. *Phys. Rev. D*, 24:1400–1402, Sep 1981.
- 3225 [31] Mark G. Boulay and A. Hime. Direct WIMP detection using scintillation time  
3226 discrimination in liquid argon. 2004.
- 3227 [32] D. V. Bugg, R. S. Gilmore, K. M. Knight, D. C. Salter, G. H. Stafford, E. J. N.  
3228 Wilson, J. D. Davies, J. D. Dowell, P. M. Hattersley, R. J. Homer, A. W. O'dell,

- 3229 A. A. Carter, R. J. Tapper, and K. F. Riley. Kaon-nucleon total cross sections  
3230 from 0.6 to 2.65 gev/ *c. Phys. Rev.*, 168:1466–1475, Apr 1968.
- 3231 [33] W. M. Burton and B. A. Powell. Fluorescence of tetraphenyl-butadiene in the  
3232 vacuum ultraviolet. *Applied Optics*, 12(1):87, jan 1973.
- 3233 [34] CAEN. Caen v1495 data sheet. Technical report, jan 2018.
- 3234 [35] CAEN. Caen v1740 data sheet. Technical report, jan 2018.
- 3235 [36] A. S. Carroll, I. H. Chiang, C. B. Dover, T. F. Kycia, K. K. Li, P. O. Mazur,  
3236 D. N. Michael, P. M. Mockett, D. C. Rahm, and R. Rubinstein. Pion-nucleus  
3237 total cross sections in the (3,3) resonance region. *Phys. Rev. C*, 14:635–638,  
3238 Aug 1976.
- 3239 [37] D. Casper. The nuance neutrino physics simulation, and the future. *Nuclear  
3240 Physics B - Proceedings Supplements*, 112(1-3):161–170, nov 2002.
- 3241 [38] F. Cavanna et al. LArIAT: Liquid Argon In A Testbeam. 2014.
- 3242 [39] A. Cervera, A. Donini, M.B. Gavela, J.J. Gomez Cádenas, P. Hernández,  
3243 O. Mena, and S. Rigolin. Golden measurements at a neutrino factory. *Nu-  
3244 clear Physics B*, 579(1-2):17–55, jul 2000.
- 3245 [40] E. Church. LArSoft: A Software Package for Liquid Argon Time Projection  
3246 Drift Chambers. 2013.
- 3247 [41] ATLAS Collaboration. Observation of a new particle in the search for the  
3248 standard model higgs boson with the ATLAS detector at the LHC. *Physics  
3249 Letters B*, 716(1):1–29, sep 2012.
- 3250 [42] CMS Collaboration. Observation of a new boson at a mass of 125 gev with the  
3251 cms experiment at the lhc. *Physics Letters B*, 716(1):30 – 61, 2012.

- 3252 [43] The LArIAT Collaboration. The liquid argon in a testbeam (lariat) experiment.  
3253 Technical report, In Preparation 2018.
- 3254 [44] Stefano Dell’Oro, Simone Marcocci, Matteo Viel, and Francesco Vissani. Neu-  
3255 trinoless double beta decay: 2015 review. *Advances in High Energy Physics*,  
3256 2016:1–37, 2016.
- 3257 [45] S.E. Derenzo, A.R. Kirschbaum, P.H. Eberhard, R.R. Ross, and F.T. Solmitz.  
3258 Test of a liquid argon chamber with 20 m rms resolution. *Nuclear Instruments  
3259 and Methods*, 122:319 – 327, 1974.
- 3260 [46] Savas Dimopoulos, Stuart Raby, and Frank Wilczek. Proton Decay in Super-  
3261 symmetric Models. *Phys. Lett.*, B112:133, 1982.
- 3262 [47] D. Drakoulakos et al. Proposal to perform a high-statistics neutrino scattering  
3263 experiment using a fine-grained detector in the NuMI beam. 2004.
- 3264 [48] A Ereditato, C C Hsu, S Janos, I Kreslo, M Messina, C Rudolf von Rohr,  
3265 B Rossi, T Strauss, M S Weber, and M Zeller. Design and operation of  
3266 argontube: a 5 m long drift liquid argon tpc. *Journal of Instrumentation*,  
3267 8(07):P07002, 2013.
- 3268 [49] Torleif Ericson and Wolfram Weise. *Pions and Nuclei (The International Series  
3269 of Monographs on Physics)*. Oxford University Press, 1988.
- 3270 [50] A.A. Aguilar-Arevalo et al. The miniboone detector. *Nuclear Instruments and  
3271 Methods in Physics Research Section A: Accelerators, Spectrometers, Detectors  
3272 and Associated Equipment*, 599(1):28 – 46, 2009.
- 3273 [51] Antonio Bueno et al. Nucleon decay searches with large liquid argon TPC de-  
3274 tectors at shallow depths: atmospheric neutrinos and cosmogenic backgrounds.  
3275 *Journal of High Energy Physics*, 2007(04):041–041, apr 2007.

- 3276 [52] A.S. Clough et al. Pion-nucleus total cross sections from 88 to 860 MeV. *Nuclear*  
3277 *Physics B*, 76(1):15–28, jul 1974.
- 3278 [53] B.W. Allardycce et al. Pion reaction cross sections and nuclear sizes. *Nuclear*  
3279 *Physics A*, 209(1):1 – 51, 1973.
- 3280 [54] C Athanassopoulos et al. The liquid scintillator neutrino detector and LAMPF  
3281 neutrino source. *Nuclear Instruments and Methods in Physics Research Section*  
3282 *A: Accelerators, Spectrometers, Detectors and Associated Equipment*, 388(1-  
3283 2):149–172, mar 1997.
- 3284 [55] F. Binon et al. Scattering of negative pions on carbon. *Nuclear Physics B*,  
3285 17(1):168 – 188, 1970.
- 3286 [56] L. Aliaga et al. Minerva neutrino detector response measured with test beam  
3287 data. *Nuclear Instruments and Methods in Physics Research Section A: Ac-*  
3288 *celerators, Spectrometers, Detectors and Associated Equipment*, 789:28 – 42,  
3289 2015.
- 3290 [57] M Adamowski et al. The liquid argon purity demonstrator. *Journal of Instru-*  
3291 *mentation*, 9(07):P07005, 2014.
- 3292 [58] P. Vilain et al. Coherent single charged pion production by neutrinos. *Physics*  
3293 *Letters B*, 313(1-2):267–275, aug 1993.
- 3294 [59] R. Acciarri et al. Convolutional neural networks applied to neutrino events  
3295 in a liquid argon time projection chamber. *Journal of Instrumentation*,  
3296 12(03):P03011, 2017.
- 3297 [60] R. Acciarri et al. Design and construction of the MicroBooNE detector. *Journal*  
3298 *of Instrumentation*, 12(02):P02017–P02017, feb 2017.

- 3299 [61] C. E. Aalseth et al.l. DarkSide-20k: A 20 tonne two-phase LAr TPC for direct  
3300 dark matter detection at LNGS. *The European Physical Journal Plus*, 133(3),  
3301 mar 2018.
- 3302 [62] H Fenker. Standard beam pwc for fermilab. Technical report, Fermi National  
3303 Accelerator Lab., Batavia, IL (USA), 1983.
- 3304 [63] H Fesbach. Theoretical nuclear physics: Nuclear reactions. 1992.
- 3305 [64] J. A. Formaggio and G. P. Zeller. From ev to eev: Neutrino cross sections across  
3306 energy scales. *Rev. Mod. Phys.*, 84:1307–1341, Sep 2012.
- 3307 [65] E. Friedman et al. K+ nucleus reaction and total cross-sections: New analysis  
3308 of transmission experiments. *Phys. Rev.*, C55:1304–1311, 1997.
- 3309 [66] V.M. Gehman, S.R. Seibert, K. Rielage, A. Hime, Y. Sun, D.-M. Mei,  
3310 J. Maassen, and D. Moore. Fluorescence efficiency and visible re-emission  
3311 spectrum of tetraphenyl butadiene films at extreme ultraviolet wavelengths.  
3312 *Nuclear Instruments and Methods in Physics Research Section A: Accelerators,*  
3313 *Spectrometers, Detectors and Associated Equipment*, 654(1):116 – 121, 2011.
- 3314 [67] H. Geiger and E. Marsden. On a diffuse reflection of the formula-particles.  
3315 *Proceedings of the Royal Society A: Mathematical, Physical and Engineering*  
3316 *Sciences*, 82(557):495–500, jul 1909.
- 3317 [68] Howard Georgi and S. L. Glashow. Unity of all elementary-particle forces. *Phys.*  
3318 *Rev. Lett.*, 32:438–441, Feb 1974.
- 3319 [69] D.Y. Wong (editor) G.L. Shaw (Editor). *Pion-nucleon Scattering*. John Wiley  
3320 & Sons Inc, 1969.
- 3321 [70] Glassman High Voltage, Inc., Precision Regulated High Voltage DC Power Sup-  
3322 ply.

- 3323 [71] D S Gorbunov. Sterile neutrinos and their role in particle physics and cosmology.  
3324       *Physics-Uspekhi*, 57(5):503, 2014.
- 3325 [72] C. Green, J. Kowalkowski, M. Paterno, M. Fischler, L. Garren, and Q. Lu. The  
3326       Art Framework. *J. Phys. Conf. Ser.*, 396:022020, 2012.
- 3327 [73] S. Hansen, D. Jensen, G. Savage, E. Skup, and A. Soha. Fermilab test beam  
3328       multi-wire proportional chamber tracking system upgrade. June 2014. Interna-  
3329       tional Conference on Technology and Instrumentation in Particle Physics (TIPP  
3330       2014).
- 3331 [74] J. Harada. Non-maximal  $\theta_{23}$  , large  $\theta_{13}$  and tri-bimaximal  $\theta_{12}$  via quark-  
3332       lepton complementarity at next-to-leading order. *EPL (Europhysics Letters)*,  
3333       103(2):21001, 2013.
- 3334 [75] Peter W. Higgs. Broken symmetries and the masses of gauge bosons. *Physical  
3335       Review Letters*, 13(16):508–509, oct 1964.
- 3336 [76] P.W. Higgs. Broken symmetries, massless particles and gauge fields. *Physics  
3337       Letters*, 12(2):132–133, sep 1964.
- 3338 [77] H J Hilke. Time projection chambers. *Reports on Progress in Physics*,  
3339       73(11):116201, 2010.
- 3340 [78] N. Ishida, M. Chen, T. Doke, K. Hasuike, A. Hitachi, M. Gaudreau, M. Kase,  
3341       Y. Kawada, J. Kikuchi, T. Komiyama, K. Kuwahara, K. Masuda, H. Okada,  
3342       Y.H. Qu, M. Suzuki, and T. Takahashi. Attenuation length measurements of  
3343       scintillation light in liquid rare gases and their mixtures using an improved  
3344       reflection suppresser. *Nuclear Instruments and Methods in Physics Research  
3345       Section A: Accelerators, Spectrometers, Detectors and Associated Equipment*,  
3346       384(2-3):380–386, jan 1997.

- 3347 [79] G. Pulliam J. Asaadi, E. Gramellini. Determination of the electron lifetime in  
3348 lariat. Technical report, August 2017.
- 3349 [80] George Jaffé. Zur theorie der ionisation in kolonnen. *Annalen der Physik*,  
3350 347(12):303–344, 1913.
- 3351 [81] C. Jarlskog. A basis independent formulation of the connection between quark  
3352 mass matrices, CP violation and experiment. *Zeitschrift für Physik C Particles  
3353 and Fields*, 29(3):491–497, sep 1985.
- 3354 [82] B J P Jones, C S Chiu, J M Conrad, C M Ignarra, T Katori, and M Toups. A  
3355 measurement of the absorption of liquid argon scintillation light by dissolved ni-  
3356 trogen at the part-per-million level. *Journal of Instrumentation*, 8(07):P07011,  
3357 2013.
- 3358 [83] Benjamin J. P. Jones. *Sterile Neutrinos in Cold Climates*. PhD thesis, MIT,  
3359 2015.
- 3360 [84] Cezary Juszczak, Jarosław A. Nowak, and Jan T. Sobczyk. Simulations from  
3361 a new neutrino event generator. *Nuclear Physics B - Proceedings Supplements*,  
3362 159:211–216, sep 2006.
- 3363 [85] D. I. Kazakov. Beyond the standard model: In search of supersymmetry. In  
3364 *2000 European School of high-energy physics, Caramulo, Portugal, 20 Aug-2  
3365 Sep 2000: Proceedings*, pages 125–199, 2000.
- 3366 [86] Dae-Gyu Lee, R. N. Mohapatra, M. K. Parida, and Merostar Rani. Predic-  
3367 tions for the proton lifetime in minimal nonsupersymmetric  $so(10)$  models: An  
3368 update. *Phys. Rev. D*, 51:229–235, Jan 1995.

- 3369 [87] M A Leigui de Oliveira. Expression of Interest for a Full-Scale Detector Engi-  
3370 neering Test and Test Beam Calibration of a Single-Phase LAr TPC. Technical  
3371 Report CERN-SPSC-2014-027. SPSC-EOI-011, CERN, Geneva, Oct 2014.
- 3372 [88] W. H. Lippincott, K. J. Coakley, D. Gastler, A. Hime, E. Kearns, D. N. McK-  
3373 insey, J. A. Nikkel, and L. C. Stonehill. Scintillation time dependence and pulse  
3374 shape discrimination in liquid argon. *Phys. Rev. C*, 78:035801, Sep 2008.
- 3375 [89] Jorge L. Lopez and Dimitri V. Nanopoulos. Flipped SU(5): Origins and re-  
3376 cent developments. In *15th Johns Hopkins Workshop on Current Problems*  
3377 *in Particle Theory: Particle Physics from Underground to Heaven Baltimore,*  
3378 *Maryland, August 26-28, 1991*, pages 277–297, 1991.
- 3379 [90] Vincent Lucas and Stuart Raby. Nucleon decay in a realistic so(10) susy gut.  
3380 *Phys. Rev. D*, 55:6986–7009, Jun 1997.
- 3381 [91] Ettore Majorana. Teoria simmetrica dell'elettrone e del positrone. *Il Nuovo*  
3382 *Cimento*, 14(4):171–184, apr 1937.
- 3383 [92] Hisakazu Minakata and Alexei Yu. Smirnov. Neutrino mixing and quark-lepton  
3384 complementarity. *Phys. Rev. D*, 70:073009, Oct 2004.
- 3385 [93] M. Mooney. The microboone experiment and the impact of space charge effects.  
3386 2015.
- 3387 [94] E. Morikawa, R. Reininger, P. Gürtler, V. Saile, and P. Laporte. Argon, kryp-  
3388 ton, and xenon excimer luminescence: From the dilute gas to the condensed  
3389 phase. *The Journal of Chemical Physics*, 91(3):1469–1477, aug 1989.
- 3390 [95] FM Newcomer, S Tedja, R Van Berg, J Van der Spiegel, and HH Williams.  
3391 A fast, low power, amplifier-shaper-discriminator for high rate straw tracking  
3392 systems. *IEEE Transactions on Nuclear Science*, 40(4):630–636, 1993.

- 3393 [96] Emmy Noether. Invariant variation problems. *Transport Theory and Statistical*  
3394 *Physics*, 1(3):186–207, jan 1971.
- 3395 [97] I. Nutini. Study of charged particles interaction processes on ar in the 0.2 - 2.0  
3396 GeV energy range through combined information from ionization free charge  
3397 and scintillation light. Technical report, jan 2015.
- 3398 [98] D. R. Nygren. The time projection chamber: A new  $4\pi$  detector for charged  
3399 particles. Technical report, 1974.
- 3400 [99] L. Onsager. Initial recombination of ions. *Phys. Rev.*, 54:554–557, Oct 1938.
- 3401 [100] S. Pascoli, S.T. Petcov, and A. Riotto. Leptogenesis and low energy cp-violation  
3402 in neutrino physics. *Nuclear Physics B*, 774(1):1 – 52, 2007.
- 3403 [101] C. Patrignani et al. Review of Particle Physics. *Chin. Phys.*, C40(10):100001,  
3404 2016.
- 3405 [102] B. Pontecorvo. Neutrino Experiments and the Problem of Conservation of  
3406 Leptonic Charge. *Sov. Phys. JETP*, 26:984–988, 1968. [Zh. Eksp. Teor.  
3407 Fiz.53,1717(1967)].
- 3408 [103] T. Yang R. Acciarri. Investigation of the non-uniformity observed in the wire  
3409 response to charge in lariat run 1. Technical report, February 2017.
- 3410 [104] T. Yang R. Acciarri, M. Stancari. Determination of the electron lifetime in  
3411 lariat. Technical report, March 2016.
- 3412 [105] Martti Raidal. Relation between the neutrino and quark mixing angles and  
3413 grand unification. *Phys. Rev. Lett.*, 93:161801, Oct 2004.
- 3414 [106] Steve Ritz et al. Building for Discovery: Strategic Plan for U.S. Particle Physics  
3415 in the Global Context. 2014.

- 3416 [107] C. Rubbia. The Liquid Argon Time Projection Chamber: A New Concept for  
3417 Neutrino Detectors. 1977.
- 3418 [108] L.M. Saunders. Electromagnetic production of pions from nuclei. *Nucl. Phys.*,  
3419 *B7*: 293-310(1968).
- 3420 [109] Qaisar Shafi and Zurab Tavartkiladze. Neutrino democracy, fermion mass hier-  
3421 archies, and proton decay from 5d su(5). *Phys. Rev. D*, 67:075007, Apr 2003.
- 3422 [110] Sigma-Aldrich, P.O. Box 14508, St. Louis, MO 63178 USA.
- 3423 [111] R. K. Teague and C. J. Pings. Refractive index and the lorentz–lorenz function  
3424 for gaseous and liquid argon, including a study of the coexistence curve near the  
3425 critical state. *The Journal of Chemical Physics*, 48(11):4973–4984, jun 1968.
- 3426 [112] J. Thomas and D. A. Imel. Recombination of electron-ion pairs in liquid argon  
3427 and liquid xenon. *Phys. Rev. A*, 36:614–616, Jul 1987.
- 3428 [113] D.R.O. Morrison N. Rivoire V. Flaminio, W.G. Moorhead. Compilation of  
3429 Cross Sections I:  $\pi^+$  and  $\pi^-$  Induced Reactions. *CERN-HERA*, pages 83–01,  
3430 1983.
- 3431 [114] D.R.O. Morrison N. Rivoire V. Flaminio, W.G. Moorhead. Compilation of  
3432 Cross Sections II:  $K^+$  and  $K^-$  Induced Reactions. *CERN-HERA*, pages 83–02,  
3433 1983.
- 3434 [115] W. Walkowiak. Drift velocity of free electrons in liquid argon. *Nuclear Instru-*  
3435 *ments and Methods in Physics Research Section A: Accelerators, Spectrometers,*  
3436 *Detectors and Associated Equipment*, 449(1-2):288–294, jul 2000.
- 3437 [116] Hermann Weyl. Gravitation and the electron. *Proceedings of the National  
3438 Academy of Sciences of the United States of America*, 15(4):323–334, 1929.

- 3439 [117] Colin et al Wilkin. A comparison of pi+ and pi- total cross-sections of light  
3440 nuclei near the 3-3 resonance. *Nucl. Phys.*, B62:61–85, 1973.
- 3441 [118] D. H. Wright and M. H. Kelsey. The Geant4 Bertini Cascade. *Nucl. Instrum.*  
3442 *Meth.*, A804:175–188, 2015.
- 3443 [119] C. S. Wu, E. Ambler, R. W. Hayward, D. D. Hoppes, and R. P. Hudson.  
3444 Experimental test of parity conservation in beta decay. *Phys. Rev.*, 105:1413–  
3445 1415, Feb 1957.
- 3446 [120] N Yahlali, L M P Fernandes, K Gonzlez, A N C Garcia, and A Soriano. Imaging  
3447 with sipms in noble-gas detectors. *Journal of Instrumentation*, 8(01):C01003,  
3448 2013.
- 3449 [121] T. Yanagida. Horizontal symmetry and masses of neutrinos. *Progress of Theo-*  
3450 *retical Physics*, 64(3):1103–1105, sep 1980.